TECHNISCHE UNIVERSITÄT
BERGAKADEMIE FREIBERG
Die Ressourcenuniversität. Seit 1765.

DROPWISE CONDENSATION IN THE PRESENCE OF NON-CONDENSABLE GAS

To the Faculty of Mechanical, Process and Energy Engineering
of the Technische Universität Bergakademie Freiberg
approved

THESIS

to attain the academic degree of
Doktor-Ingenieur
(Dr. Ing.)

submitted

by **M.Sc. Shaofei Zheng**

born on the 6 May 1990 in Anhui, China

Reviewers: **Prof. Dr.-Ing. habil. Ulrich Groß**
Technische Universität Bergakademie Freiberg

Prof. Dr.-Ing. habil. Rüdiger Schwarze
Technische Universität Bergakademie Freiberg

Date of the award: 16 December 2019

Declaration

I hereby declare that I completed this work without any improper help from a third party and without using any aids other than those cited. All ideas derived directly or indirectly from other sources are identified as such.

In the selection and in the use of materials and in the writing of the manuscript I received support from the following persons:

Prof. Dr.-Ing. habil. Ulrich Groß

Persons other than those above did not contribute to the writing of this thesis. I did not seek the help of a professional doctorate-consultant. Only persons identified as having done so received any financial payment from me for any work done for me.

This thesis has not previously been submitted to another examination authority in the same or similar form in Germany or abroad.

10 July 2019 Shaofei Zheng

Versicherung

Hiermit versichere ich, dass ich die vorliegende Arbeit ohne unzulässige Hilfe Dritter und ohne Benutzung anderer als der angegebenen Hilfsmittel angefertigt habe; die aus fremden Quellen direkt oder indirekt übernommenen Gedanken sind als solche kenntlich gemacht.

Bei der Auswahl und Auswertung des Materials sowie bei der Herstellung des Manuskripts habe ich Unterstützungsleistungen von folgenden Personen erhalten:

Prof. Dr.-Ing. habil. Ulrich Groß

Weitere Personen waren an der Abfassung der vorliegenden Arbeit nicht beteiligt. Die Hilfe eines Promotionsberaters habe ich nicht in Anspruch genommen. Weitere Personen haben von mir keine geldwerten Leistungen für Arbeiten erhalten, die nicht als solche kenntlich gemacht worden sind.

Die Arbeit wurde bisher wederim Inland noch im Ausland in gleicher oder ähnlicher Form einer anderen Prüfungsbehörde vorgelegt.

10 July 2019 Shaofei Zheng

Acknowledgement

The work of this thesis is carried out at the Chair of Technical Thermodynamics (TTD) of the Technische Universität Bergakademie Freiberg where I study for PhD since September 2015.

Firstly, I would like to express my sincere appreciation and thanks to my supervisor Prof. Dr.-Ing habil. Ulrich Groß for giving me the opportunity to work at his group. Thank you very much for your continuous support and confidence during the time. Furthermore, I am thankful to Prof. Dr.-Ing Tobias Fieback for supporting me and discussing about the work.

In addition, special thanks give to all my colleagues at our group for their help and understanding. Specifically, I would like to say "Thanks" to Dr.-Ing C. Philipp and Mr. F. Eimann for the help in experiments. There is one colleague I would like to thank him again, for his kind discussion and help in my work and life, for inviting me to visit your family and city "Tharandt": Mr. Eimann. Here, I would like to say "good luck in dropwise condensation" for you. And I am also thankful to my Chinese friends for helping me during my life in our "village" Freiberg. Thank you all!!

There is no doubt that this thesis could not be produced without the financial support from the Chinese Scholarship Council (CSC) and German Research Foundation (DFG). Special thanks to CSC and DFG. I would also like to thank the HPC in the university for the computing support.

Especially, I would like to dedicate this thesis to my parents even they know nothing. Without their support, I cannot overcome all the obstacles.

Abstract

Dropwise condensation, which collects the condensate liquid in the form of droplets on the cold substrate, has attracted a growing interest due to much higher heat transfer coefficient since the first discovery. One important and challenging issue in dropwise condensation is the presence of non-condensable gas (NCG) which drastically reduces its heat transfer performance. Thanks to the complex coupled heat and mass transfer accompanied by the complicated droplet dynamics behaviors, dropwise condensation with considering NCG is still far from being complete in spite of much progresses achieved. Concerning the mechanistic understanding, the purpose of this thesis is to investigate dropwise condensation in case of NCG by combining the experiments, analytical method and numerical simulation.

First of all, dropwise condensation out of humid air is experimentally investigated in a feasible facility that allows visualization of the condensation process under the controllable condition. The roles of NCG and the forced convection are seriously studied by experiments. By using the microscope camera, the size distribution and growth rate of droplets are additionally carried out during measurements. The experimental investigations construct a solid foundation for this work.

The critical aspects in dropwise condensation considering NCG include the coupled heat and mass transfer during droplet growth, the multi-scale feature of droplet size, the blocking effects of neighboring droplets for vapor diffusion (i.e. the interaction effects between droplets), the influence of convective mass transfer and the droplet dynamics characteristics. About those concerned issues, different ideas are launched. Based on the isolated growth, a single droplet growth model is developed to cover the simultaneous heat and mass transfer across the droplet from the free stream to the cold wall. For the multi-scale feature of droplet size, the Knudsen layer as a bridge between the continuum and kinetic limits is included into the present model. Correspondingly, other kinds of growth models are also presented and the comparison between them is further carried out. For dropwise condensation having a larger number of droplets and the closer inter-droplet spacing, a distributed point sink method (DPSM) is proposed to capture the strong interaction effects between droplets. Correspondingly, the correction factors reflecting the interaction effects of droplets can be solved by DPSM. Furthermore, the influence of convective mass transfer is considered by the droplet Sherwood number. Even though the droplet growth rate is depended on its size, the droplet interactions are strongly sensitive to the droplet spatial distribution. Therefore, a mathematical algorithm is developed to simulate the droplet spatio-temporal dynamics behaviors, including nucleation, growth, coalescence, slide-off/fall-off and re-nucleation. Combining all those aspects, for a certainly re-constructed droplet spatial distribution, the relative condensation characteristics is modeled for coupled heat and mass transfer driven dropwise condensation. Last but not the least, the comparison between the experiments and modeling is implemented for evaluation. And mechanistic understanding about dropwise condensation in case of NCG is simultaneously and conclusively discussed.

Dropwise condensation collects a set of challenge topics, e.g., vapor-liquid phase change,

free surface flow, coupled heat and mass transfer, multi-scale feature, interfacial behavior. As those issues, it is still great challenging to make the directly numerical simulation of dropwise condensation in progress. For advancing that, a multi-component multi-phase thermal pseudopotental-based lattice Boltzmann (LB) model as a mesoscopic method is developed for thermal multi-component multi-phase flow with phase change. The present LB model is firstly verified using some benchmarks. After that, droplet condensation considering NCG is numerically investigated using the present LB method, which presents our efforts in direct numerical simulation and qualitative investigations for dropwise condensation with the presence of NCG.

Contents

Nomenclatures

The description and unit for common symbols are listed here, whereas more details can be found in the corresponding part. The symbols having the unit l.u. means it is a variable in LB method. In LB simulation, the lattice unit (l.u.) is used for all quantities.

***Latin symbols**:*

Symbol	Description	Unit
$\boldsymbol{A}$	coefficient matrix in DPSM	-
A_s	area of the condensation substrate	m^2
B	constant in calculation of droplet Sh	-
b	distance between the new point sink and the droplet center	m
C	normalized vapor concentration	-
C_{ds}	normalized vapor concentration on the droplet surface	-
C_∞	normalized vapor concentration on the far field	-
c	vapor concentration	kg/m^3
c_{ds}	vapor concentration on the droplet surface	kg/m^3
c_v	specific heat at constant volume	l.u.
c_∞	vapor concentration in the far field	kg/m^3
D	diffusion coefficient of vapor in moist air	m^2/s
D_c	hydraulic diameter of the flow channel	m
d	distance between droplets	m
$\boldsymbol{e}$	discrete lattice velocity vector	l.u.
F'	forcing term in the discrete velocity space	l.u.
$\boldsymbol{F}=(F_x, F_y)$	body force	l.u.
f	density distribution function	l.u
$\mathbf{f}$	column vector of distribution function at velocity space	l.u.
f^*	density distribution function after streaming	l.u.
fc	function described the concentration contributed by one point sink	-
fc^*	mean value of the function fc at the same order	-
fd	function described the reciprocal of the distance between the point sink and the interesting point	-
fi	function described the condensation rate contributed by one point sink	-
fi^*	mean value of the function fi at the same order	-
G	interaction strength between components	l.u.
h^*	mean heat transfer coefficient	W/m^2K
h_{ma}	specific enthalpy of moist air	J/Kg
h_{int}	interfacial heat transfer coefficient	W/m^2K

$\mathbf{I}$	unit tensor	-
k_d	thermal conductivity of liquid water	$W/m{\cdot}K$
k_{ma}	thermal conductivity of moist air	$W/m{\cdot}K$
k_s	thermal conductivity of the block sensor	$W/m{\cdot}K$
L	latent heat	J/kg
L_s	length of the condensation substrate	m
l	distance between the point sink and the droplet center	m
lc	lattice constant	l.u.
lc_s	lattice sound speed	l.u.
M	number of the point sink for one droplet	-
$\mathbf{M}$	orthogonal transformation matrix	l.u.
M_{vw}	vapor molecular weight	g/mol
m	mass flow rate for one droplet	kg/s
$\mathbf{m}$	distribution function at the moment space	l.u.
$\mathbf{m}^*$	collision process at the moment space	l.u.
m_{iso}	droplet condensation rate within an isolated growth	kg/s
m_{sys}	droplet condensation rate within the droplets system	kg/s
m_t	total condensation rate over the whole sunstrate	kg/s
m_t^*	average of total condensation rate	kg/s
m_{-v}	incoming mass flow rate of vapor molecules	kg/s
m_{+v}	outgoing mass flow rate of vapor molecules	kg/s
N	droplet number	-
Nd	size distribution density of big droplets	$m^{-2}\mu m^{-1}$
N_t	total number of the point sink	-
nd	size distribution density of small droplets	$m^{-2}\mu m^{-1}$
O	order number in MOI	-
P_{ma}	pressure of moist air	bar
P_v	partial pressure of water vapor	bar
$P_{v,ds}$	partial pressure of water vapor on the droplet surface	bar
$P_{v,i}$	partial pressure of water vapor between the Knudsen layer and continuum region	bar
p	pressure	l.u.
p_c	critical pressure	l.u.
Q	heat flow rate for single droplet	W
Q_t	total heat flow rate by all droplets	W
q_{fc}	total heat flux due to the forced convection	W/m^2
q_s	total heat flux due to condensation	W/m^2
q_t	total heat flux over the whole substrate	W/m^2

R	droplet radius	μm
Ra	ratio of the mean value of function *fc* between two neighboring orders in MOI	-
R_{cr}	capillary resistance	-
R_{dr}	conduction resistance of liquid droplet	-
R_e	critical droplet radius	μm
R_i	radius of the Knudsen layer	μm
R_{ir}	interficial resistance	-
R_{is}	radius of the imaginary sphere in DPSM	μm
R_{ma}	specific gas constant of moist air	-
R_{max}	maximum droplet radius	μm
R_{min}	minimum droplet radius	μm
R_{sr}	conduction resistance of the condensation substrate	-
R_u	universal gas constant	-
R_v	specific gas constant of vapor	-
R_{vr}	diffusion resistance of vapor	-
r	radial distance in spherical coordinate system	μm
$\boldsymbol{r}$	location vector in spherical coordinate system	-
$\mathbf{S}$	adjustable vector	l.u.
s	entropy	l.u.
T	temperature	l.u.
T_{bs}^*	averaged temperature at the back side of block sensor	K
T_c	critical temperature	l.u.
T_{cs}	temperature on cooling side	K
T_d	dew point temperature	K
T_{ds}	temperature on the droplet surface	K
T_{fs}^*	averaged temperature at the front side of block sensor	K
T_i	temperature on the interface between the Knudsen layer and continuum region	K
T_{ma}	temperature of moist air	K
T^{sat}	saturation temperature of water vapor	K
T_w	temperature on the condensation wall	K
t	time	s or l.u.
$\boldsymbol{u}=(u_x, u_y)$	velocity vector	l.u.
u_b	radial bulk velocity	m/s
v_v	relative velocity of vapor with respcet to the bulk	m/s
v_a	relative velocity of dry air with respcet to the bulk	m/s
W_{NCG}	mass fraction of NCG	l.u.

W_v	mass fraction of vapor	l.u.
w	weighting coefficient	l.u.
$\boldsymbol{x}=(x,y)$	location vector in rectangular coordinate system	l.u.

***Greek symbols**:*

Symbol	description	Unit
α	accommodation coefficient	-
α_c	condensation coefficient	-
α_e	evaporation coefficient	-
γ	correction factor for canceling the lateral heat flow into the block sensor	-
δ_s	distance between the front side and back side in block sensor	*m*
δ_t	time spacing	l.u.
δ_x	lattice spacing	l.u.
ε	pseudopotential for different components	l.u.
η	correction factor for the interaction effects between droplets	-
θ	droplet contact angle	°
θ_w	simulated contact angle	l.u.
θ_w^a	prescribed contact angle	l.u.
κ	parameter in the adjustable vector	l.u.
$\boldsymbol{\Lambda}$	diagonal matrix	l.u.
λ	thermal conductivity	l.u.
λ_{ma}	mean free path of moist air	*nm*
μ_{ma}	dynamic viscosity of moist air	*Pa·s*
ξ	polar angle in spherical coordinate system	°
ρ	density	l.u.
ρ_a	partial density of dry air	kg/m^3
ρ_d	density of liquid water	kg/m^3
ρ_{ma}	density of moist air	kg/m^3
ρ_v	partial density of water vapor	kg/m^3
$\rho_{v,ds}$	partial density of water vapor on the droplet surface	kg/m^3
$\rho_{v,i}$	partial density of water vapor between the knudsen layer and continuum region	kg/m^3
$\rho_{v,ma}$	partial density of water vapor in moist air	kg/m^3
σ	intensity of the point sink	-
σ_d	surface tension of liquid water	*N/m*
τ	relaxation time	l.u.
υ	kinematic viscosity	l.u.
ϕ	quantity	l.u.

φ	anzimuthal angle in spherical coordinate system	°
χ	thermal diffusivity	l.u.
ψ	pseudopotential for the same components	l.u.
ω	surface fraction covered by droplets	%

***Non-dimensional number**:*

Symbol	Description
Kn	Knudsen number
Nu^*	mean Nusselt number
Pr	Prandtl number
Re	bulk Reynolds number
Re_d	droplet Reynolds number
Sc	Schmidt number
Sh_d	droplet Sherwood number
Sh_0	droplet Sherwood number due to natural convection

***Abbreviations**:*

Symbol	Description
B. C.	boundary condition
BGK	Bhatnagar-Gross-Ktook
D2Q9	two-dimensional nine-velocity scheme
DPSM	distributed point sink method
EOS	equation of state
GPBiCG	Generalized product-type bi-conjugate gradient
LB	lattice Boltzmann
l.u.	lattice unit
MOI	method of image
MRT	multi-relaxation-time
NCG	non-condensable gas
PSM	point sink method
RH	relative humidity
ΔT	temperature difference
ΔT_{aw}	temperature difference T_{ma}-T_w
ΔT_{dw}	temperature difference T_d-T_w

***Subscripts**:*

Symbol	Description
a	dry air
bs	the back side of block sensor

c	condensation/channel
cr	capillary resistance
cs	cooling side
d	droplet
dr	diffusion resistance
ds	droplet surface
e	evaporation
fc	forced convection
fs	the front side of block sensor
i	interface between the Knudsen layer and continuum region
i, j, k, l	indices
ir	interficial resistance
is	imaginary sphere
iso	growth by isolated form
ma	moist air
max	maximum
min	minimum
s	condensation substrate
sr	conduction resistance of substrate
sys	growth within droplets system
t	total
v	water vapor
vr	vapor diffusion
w	wall
∞	far field/infinite

***Superscripts**:*

Symbol	Description
eq	equilibrium state
sat	saturation state
*	averaging

Chapter 1 Introduction

Dropwise condensation is a common natural phenomenon in daily life and many industrial applications (e.g., the dews on grass leaves in the morning (see Figure 1.1(a)) [1], the cooling system of the nuclear power plants [2]). To survive in extreme environments, animals (e.g., desert beetles) and plants such as the desert cactus have adapted to harvest the water by condensation [3].

Dropwise condensation collects the liquid in the form of drops over the cold substrate by vapor/liquid phase change. The drops at nanometer scale are firstly formed at preferred nucleation sites. Then these tiny drops grow by direct condensation, until they approach the neighbors and a coalescence-dominated growth begins accompanied with direct condensation. Because of the external force (e.g., the gravity force), the drops reaching a critical size will leave from the substrate. The blank substrate exposed via coalescence and sliding permits new nucleation drops to become available [4]. Finally, a complicated spatio-temporal distribution of drops is formed on the surfaces, as shown in Figure 1.1(b) [5].

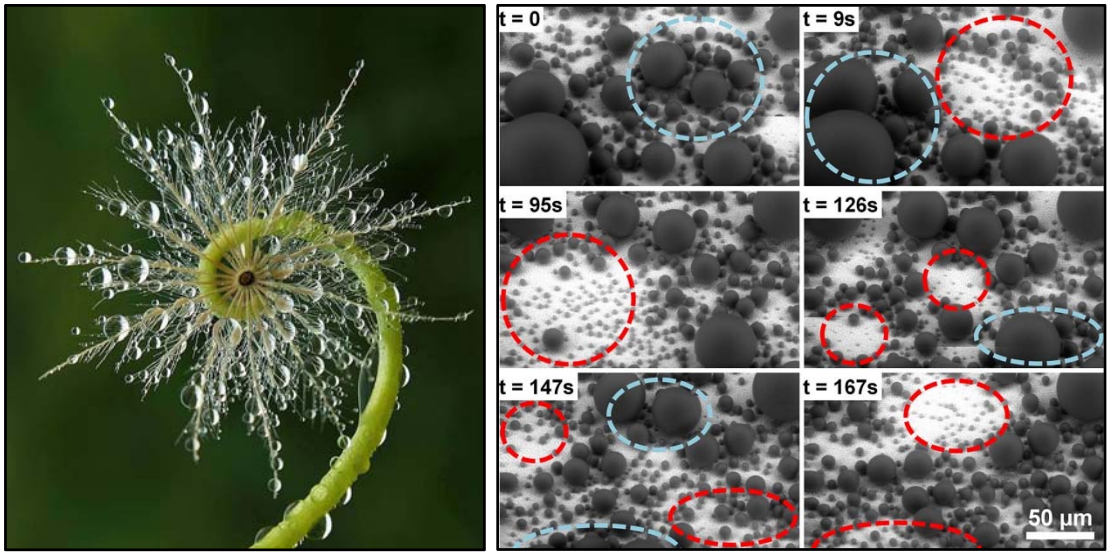

Figure 1.1 (a) the dews on grass leaves in the morning [1]; (b) dropwise condensation over a CuO surface captured by the environmental scanning electron microscopy (ESEM): reproduced with permission [5] (copyright 2012, American chemical society).

As because of the complex droplet dynamics, the heat transfer coefficient during dropwise condensation is a few order of magnitude higher than for filmwise condensation [6], which attracts a growing interest since the first discovery by Schmidt et al. [7]. In heat transfer community, continuously considerable efforts have been carried out for understanding its physical mechanism and the successful application [6, 8]. Nevertheless, dropwise condensation is still far from being complete.

1.1 Promoting dropwise condensation

Since its discovery nine decades ago, significant interests for dropwise condensation are concentrated on the following issues: longtime sustainability, heat transfer measurement, substrate property, forming mechanism, controllability and multiscale phenomenon [4, 6, 8]. And the classical thermal resistance model [4, 9] for heat transfer across the droplet has clearly figured out the influencing factors for promoting dropwise condensation. Therefore, the mainly attention in nearly twenty years is given to the substrate. The chemical and physical technology changing the substrate properties (e.g., the surface energy and the wetting characteristics) or special substrate materials can be used to promote dropwise condensation by reducing droplet departure size and enabling faster cleaning of the surface for re-nucleation [10-15]. It is noteworthy that the development of bioinspired engineering has a significant potentials in promoting dropwise condensation. In nature, the directional and spontaneous transports of drops by animals and plants provide more advanced functions, including drops harvesting and storage, locomotion, antifogging, self-cleaning and adhesion [3, 16-20]. Based on the principles derived from Namib desert beetles, cacti and pitcher plants, a slippery asymmetric bump as shown in Figure 1.2 is designed by Park et al. [16] for enabling drops to grow faster and to shed as quickly as possible. In spite of much progresses achieved, a number of technical advances are still required for longtime sustainability and high efficiency of dropwise condensation heat transfer.

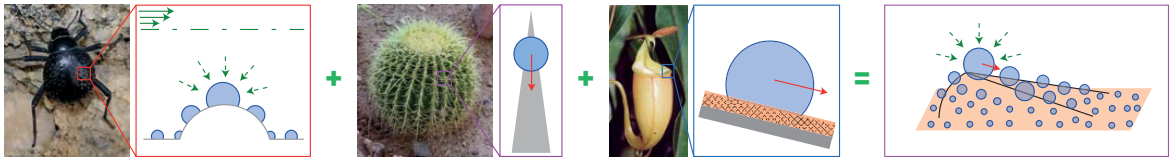

Figure 1.2 Dropwise Condensation on slippery asymmetric bump: reproduced with permission [16] (copyright 2016, Nature publishing group).

1.2 Effect of non-condensable gas

In dropwise condensation community, researches are mostly carried out under pure vapor condition in the labor. However, one important and challenging issue in dropwise condensation is that the presence of non-condensable gas (NCG) will reduce its heat transfer coefficient drastically [6]. Many researchers had experimentally found that even a small concentration of NCG brings a significant reduction in the heat transfer performance of dropwise condensation [21-25]. In some conditions, dropwise condensation and filmwise condensation in case of NCG fell in a similar range of the heat transfer rate [23]. The conclusion is that, NCG goes against the heat transfer of dropwise condensation losing its advantage over the filmwise condensation. It is widely accepted that the presence of NCG drops down the saturation temperature of the bulk because of the partial pressure reduced. In addition, the impermeable vapor/liquid interface leads to NCG accumulation during a non-condensable diffusion layer formed. About dropwise condensation with NCG, due to the

coupled vapor diffusion barrier and quite complex dynamics of drops, research stays in the experimental stage and the mechanistic understanding is far from being complete so far.

1.3 Object and outline of the thesis

Considering the significant impact of NCG on dropwise condensation, the primary object of this thesis is going to understand the reduction mechanism of NCG for dropwise condensation heat transfer in depth. It is desirable that the concerned methodologies should be comprehensive and universal for the future researches of dropwise condensation community. Accordingly, the research is carried out by combining the experiments, analytical method and numerical simulation. Over this work, the working fluid is moist air and the dry air is considered as the non-condensable gas. And the droplet is seen as a semi-sphere with the contact angle 90°.

Correspondingly, the thesis is mainly comprised by three parts: the experiments, modeling by the semi-analytical method and the numerical simulation, which are distributed as following:

Chapter 2: This chapter is mainly dedicated on the experimental investigation. The influence of the laminar forced convection and the droplet growth rate over the substrate during dropwise condensation of humid air are provided experimentally.

Chapter 3: This chapter presents a multiscale growth model of isolated droplet and its corresponding simplified version, including a mostly adopted model in literatures. To figure out the role of the vapor diffusion, those three isolated droplet growth models for the case of NCG is totally compared with the classical thermal resistance model in the condition of pure steam.

Chapter 4: The interaction effects between droplets over the substrate is the core of this chapter. Facing a strong interaction effect during dropwise condensation, a distributed point sink method is developed and compared with the point sink method and the method of images.

Chapter 5: In this chapter, a mathematical numerical is developed for re-constructing the droplet dynamics behaviors and the droplet Sherwood number is added to consider the influence of convective mass transfer. Combining all those aspects, modeling of heat and mass transfer for dropwise condensation of moist air is launched in this chapter. Additionally, the predicted results are compared with the experimental investigations in the second chapter for understanding the influencing mechanism of NCG.

Chapter 6: Aiming to simulate droplet condensation with NCG numerically, this chapter is trying to construct a multi-component multi-phase thermal lattice Boltzmann model.

Chapter 7: The present work is summarized and the possible extension in the future work is also provided.

Chapter 2 Experimental Investigation of Dropwise Condensation out of moist air

In this chapter, dropwise condensation of moist air promoted by a polymer substrate is experimentally investigated in a feasible facility that allows visualization of the condensation process at a controlled condition. The roles of the NCG (dry air in this work) and the forced convection are seriously investigated for dropwise condensation. For that, measurements are carried out at a constant relative humidity (RH) with a variety of sub-cooling degree and Reynolds numbers. By the microscope camera, the size distribution and growth rate of droplets are launched additionally. The experimentally defined droplet size distribution density presents a good agreement with the existing theoretical models. Significantly, the monitored droplet growth rate dispersedly spread a wide range, which indicates that the droplet growth rate is not only depended on its size. The results also demonstrate that the convective flow even at a quite small Reynolds number should be regarded as a vital factor to promote dropwise condensation with NCG.

2.1 Literature review

In contrast to the pure vapor, the vapor partial pressure is reduced due to the presence of NCG and subsequently, the saturation temperature of bulk drops down. Furthermore, the vapor/liquid interface is actually impermeable to the NCG and close to it the NCG accumulate during the condensation process forming a non-condensable diffusion layer. The latter one is responsible for the creation of a temperature difference between the bulk and the liquid/vapor interface, acting as a diffusion barrier for the vapor molecular moving to the interface [8].

Since the first attention by Othmer [26], many experimental studies [21-25] have been done for dropwise condensation in the presence of NCG so far. Tanner and his coworkers [21, 22] reported an experimental comparison of dropwise condensation with and without NCG at atmospheric pressure and low pressure. The results demonstrated that the heat transfer performance of dropwise condensation with NCG strongly depends upon the concentration, the steam pressure and the NCG composition. The experimental comparison of filmwise and dropwise condensation of steam with the presence of NCG was performed by Chung et al. [23]. They concluded that dropwise and filmwise condensation fell in similar range of the heat transfer rates in the presence of air. For the solutal Marangoni condensation, Wang and Utaka [24] found that the effect of NCG was remarkable for the domain controlled by dropwise

condensation. Ma et al. [25] measured the heat transfer characteristics of dropwise condensation for a variety of NCG concentration, saturation pressure and surface sub-cooling degree. The results showed that dropwise-condensation heat transfer coefficients of steam with air concentrations of 0.5-5% can be increased by 30-80% compared with those for filmwise condensation.

In recent decades, the researchers focus on understanding its influencing mechanism in depth and try to improve the heat transfer performance under suffering NCG. Based on an apparatus with controlled removel of condensation droplets, Grooten and van der Geld [27-28] experimental measured the diffusion resistance in different droplet removal frequency and the surface property effects on heat transfer for dropwise condensation from flowing air-steam mixture. The effect of relative humidity on droplets dynamics is investigated by Castillo et al. [29]. Danilo et al. [30] studied the coupling between fully developed turbulent convection and dropwise condensation of unsaturated humid air, and the role of the relative humidity level. Also for convective dropwise condensation flow, Eimann et al. [31] revealed the condensate heat transfer resistance assuming the droplet pattern into an equivalent film. Recently, Zhao et al. [32] investigated the geometric effect on dropwise condensation with and without NCG.

The main research conclusion is that, like filmwise condensation, the presence of NCG brings a significant reduction for heat transfer performance of dropwise condensation. Because the mechanism of dropwise condensation is quite contradictory and the presence of NCG complicates it again, the understanding of mechanism and theory of dropwise condensation suffering NCG is far from being complete in spite of many efforts made [8].

The scope of this chapter is to perform experiments of dropwise condensation out of humid air. A feasible apparatus allows dropwise condensation at a controlled sub-cooling temperature, air flow velocity and relative humidity. And the droplets dynamic characteristic (the distribution characteristic and growth behavior of droplets) can be captured the microscope camera.

2.2 Experimental setup and procedures

2.2.1 Experimental setup

The experimental set-up is generally shown in Figure 2.1. A closed loop system filled by moist air is constructed. A fan is used to drive the closed loop of moist air and control the air speed by adjusting its frequency. A rectangle channel (12×32×750 *mm*) is centrally placed into two concentric tubes, as shown by the dashed rectangle in Figure 2.1(a) and the cross-section view in Figure 2.1(b). For dropwise condensation, a block sensor made from stainless steel (sized 9×6×10 *mm*, the blue block shown in Figure 2.1(a)) is assembled on vertical side wall of the test channel 500 *mm* downstream from the inlet. Facing the block sensor, a viewing window made by the sapphire is constructed to visualize dropwise condensation using a microscope camera in Figure 2.1(b). An electrical heating wrap is placed on the upstream for controlling the air temperature. And a wetted wick fed with liquid water is inserted into the

outer tube for humidification of the air. The entire measuring system is encapsulated by a temperature controlling house, as the part closed by the dashed rectangle in Figure 2.1(a). The heated air flow from the outer annular tube is forced to return to the left side and separated into two parts (indicated by the red arrows in Figure 2.1(a) and Figure 2.1(b)). The main part enters the test channel, the other one flows through the bypass tube. This design can make sure a homogeneous spatial temperature distribution along the test channel wall which prevents condensation in the upstream of the block sensor.

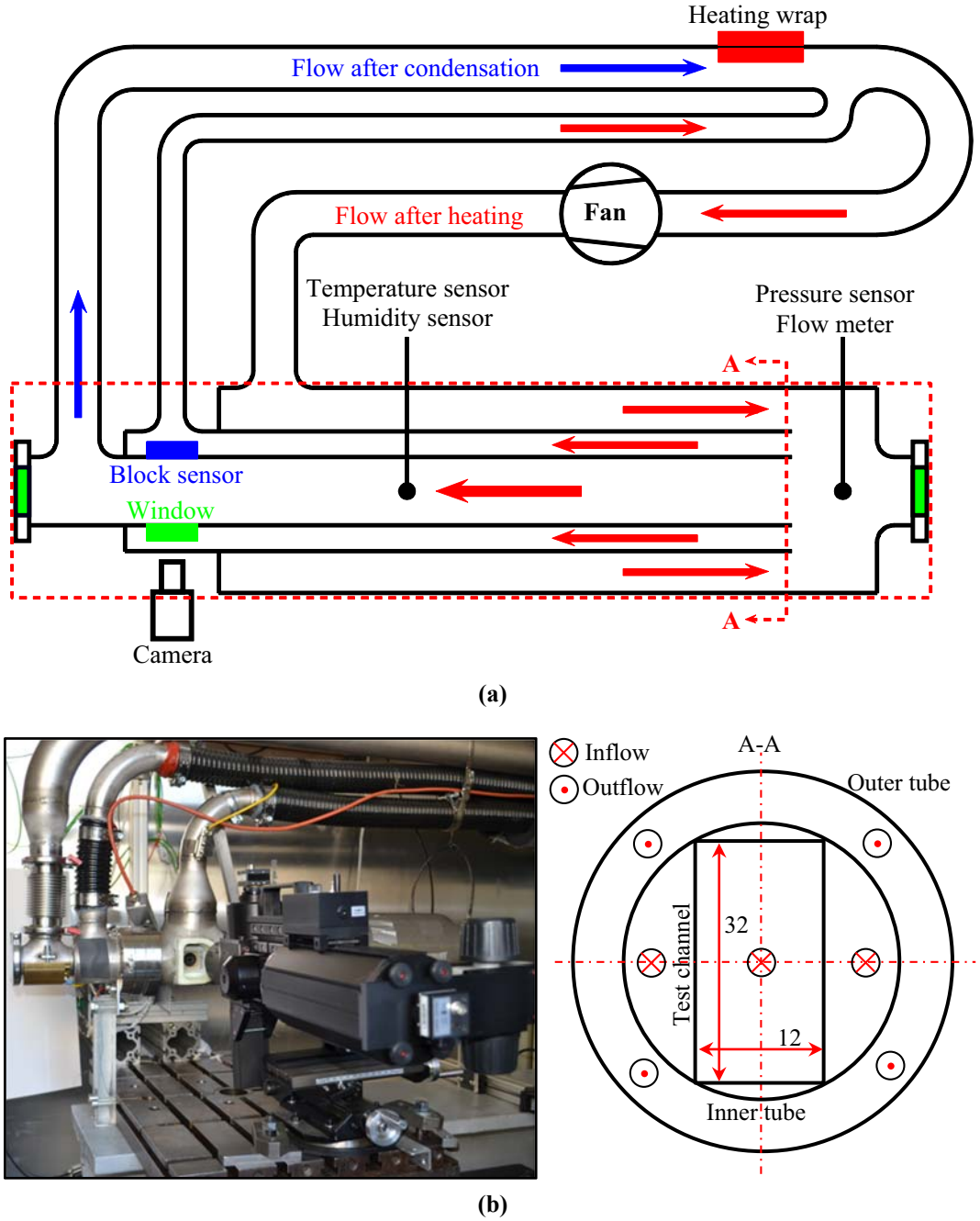

Figure 2.1 (a) Schematic of experimental set-up; (b) Camera and cross-section view of the test section (unit: *mm*).

The mass flow rate of the air is measured by a mass flow meter ST-98 (Fluid components Ltd., USA). For defining the relative humidity, a Vaisala HMT 334 transmitter having the

uncertainty ±0.4 ºC for a dew point of 21.5 ºC is employed to quantify the dew point. And the uncertainty increases up to ±0.9 ºC for increased dew point. The air temperature is measured by multiple thermocouples (Type K) inside the flow channel.

The block sensor shown in Figure 2.2 is flush mounted in the vertical wall of the test channel. Using it, dropwise condensation is realized and the corresponding heat flux can be evaluated. Eleven holes with 0.28 mm diameter and 5 mm depth are drilled into the block for the thermocouples having 0.25 mm diameter which are flush mounted with the front and back surfaces. Seven thermocouples (spacing 0.5, 1.25, 2, 3, 4.5, 6.5 and 8.5 *mm* from the flow side) distributed at the condensation side and four thermocouples (spacing 0.5, 2, 4.5 and 8.5 *mm* from the flow side) installed at the cooling side are used to measure the wall temperature of block. The measurement uncertainty is controlled within ±0.1 ºC.

In order to ensure a homogeneous thermal emissivity, the front side of the block sensor is firstly covered by camera paint (thickness 0.024 *mm*). Next, a polyethylene foil with a thickness of 0.009 *mm* is affixed for promoting dropwise condensation. The polyethylene foil has 90º static contact angle approximately. And the advancing and receding contact angles are about 111º and 74º respectively. Throughout this work, we neglect the contact angle hysteresis and take the contact angle as 90º. The block sensor is cooled by a thermoelectric cooler at its backside. And an aluminum block between the block sensor and the cooler is arranged for a best possible homogeneous temperature distribution. For minimization of the lateral heat flow, the block sensor is thermally insulated by a 1.5 *mm* air-gap from the inner channel wall.

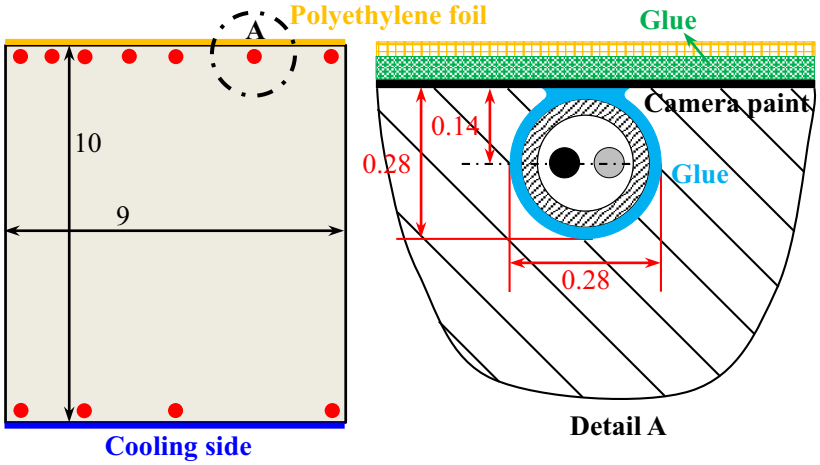

Figure 2.2 Experimental block sensor with 11 K-type thermocouples and the mounting schematic (unit: *mm*).

The heat flux across the block is determined by the reading temperatures of thermocouples. At each time interval, the averaged temperature at the back side T_{bs}^{*} is calculated using arithmetic averaging for the temperature recorded by four thermocouples. Because of the convective flow, there will be a large streamwise temperature gradient on the condensation side. Consequently, averaging of the front side temperature T_{fs}^{*} is calculated by a third grade polynomial using the reading temperature of seven thermocouples [31]. Finally, using two averaged temperature the heat flux can be calculated by the Fourier's law:

$$q_t = k_s / \delta_s \left(T_{fs}^* - T_{bs}^* \right) \gamma \tag{2.1}$$

where k_s is the thermal conductivity of the block sensor, δ_s is the distance between the front and back side thermocouples. As mentioned above, an air gap between the block and the wall is arranged for diminishing the lateral heat flow. Nevertheless, it is also significant for the total heat flux. The total heat flux through the block sensor includes the heat flows from top and side. For canceling the lateral heat flow, a correction factor γ in Eq. (2.1) is introduced. Subsequently, a CFD model covering the convective flow inside the channel and the conduction inside the walls and the block sensor is set up for defining the correction factor. In CFD model, the heat flow released by condensation is accounted by adding a heat source terms on the front surface. And the magnitude of the heat source is manually iterated until the thermocouple readings is successfully reached. Figure 2.3 validates the CFD simulation by using the experimentally obtained temperatures by the front-side seven thermocouples. It shows a good agreement. Finally, the heat flux entering the block sensor from top and side quantified by the CFD simulation can be related to the measured heat flux, which results in the correction factor γ. Several tests covering the considered parameter range state that the correction factor γ is dependence of the driving force for mass transfer and the temperature difference between the bulk and the substrate. For strong condensation behavior, the correction factor is reaching unit corresponding to an approximately neglected lateral heat flow. Based on the obtained correction factors, a polynomial regression model is developed to describe the dependencies of the correction factor γ [31]. Herein, this polynomial regression function is added into Eq. (2.1) for canceling the lateral heat flow.

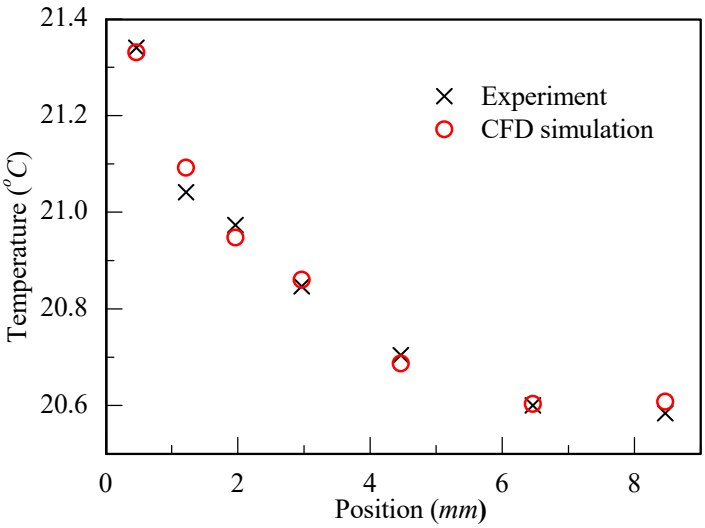

Figure 2.3 Comparison of the experimental temperature recorded by the front-side seven thermocouples and that from CFD simulation [31].

Then, considering the thermal resistance from the extra layer (the camera paint, the glue and the polyethylene foil), the wall temperature at the air-side of the polyethylene foil is got by extrapolating the temperature gradient to the condensation surface.

2.2.2 Experimental procedure and visualization

The present experimental investigation aims to examine the dependency of the dropwise condensation heat transfer on the bulk-flow Reynolds number *Re* (800-2800) over the laminar flow range. Dropwise condensation experiments are conducted at a constant bulk temperature (303.15 *K*) and NCG concentration (RH = 94%) with varied bulk velocity (0.79-2.8 *m/s*) and the sub-cooling degree of the substrate (0-10 *K*). The experimental system is running with respect to the given fan frequency (*Re*), moist air temperature and relative humidity. Dropwise condensation happens by setting the substrate temperature below the dew point temperature. When a steady state is reached having the fluctuating error within 2%, the measurement is started with the time at least a droplet life circle. Next, the substrate temperature is stepwise decreased by using the Peltier cooler. After changing sub-cooling, a steady state must be regained and maintained for restarting the measurement. Finally, temporal averaging is conducted for the heat flux. The uncertainty analysis for the measured heat flux is also performed [33], as shown in APPENDIX A.

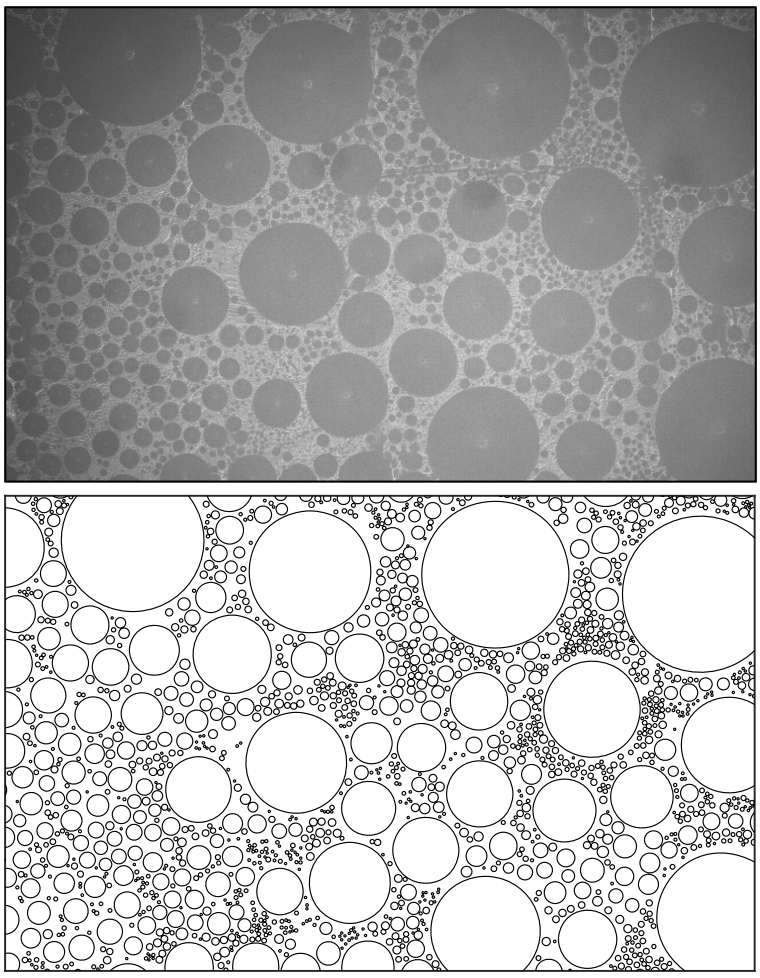

Figure 2.4 Checking of the droplet distribution image from camera.

During the measurements, the snapshots of the droplets spatial distribution over the condensation substrate are recorded simultaneously by the microscope camera (TSO Thalheim Spezialoptik GmbH). The recording time for the snapshot is flexible. The magnification is fixed to capture the whole substrate (9×6 *mm*). And the resolution is 2592×1944 pixels with the calibrated spatial resolution 4.22±0.1 μm/pixel. In addition, a

zoom-in mode using a large magnification makes it possible to visualize the droplets distribution on a small region of the substrate. At the zoom-in mode, the spatial resolution is 0.98±0.01 μm/pixel with the same resolution 2592×1944 pixels.

An automated image post-processing script is developed in MATLAB to recognize the droplet and characterize its size. The processing steps mainly include the contrast enhancement, binary segmentation and droplet boundary detection. And then each droplet boundary is recognized as a circle using the Hough transform technique. Herein, the droplet deformation due to the external force is neglected and the droplet is assumed as a spherical cap with a constant angle 90 degrees. Figure 2.4 presents a gray-scale image of droplet distribution by the camera and the correspondingly detected result.

2.2.3 Forced-convection flow heat transfer

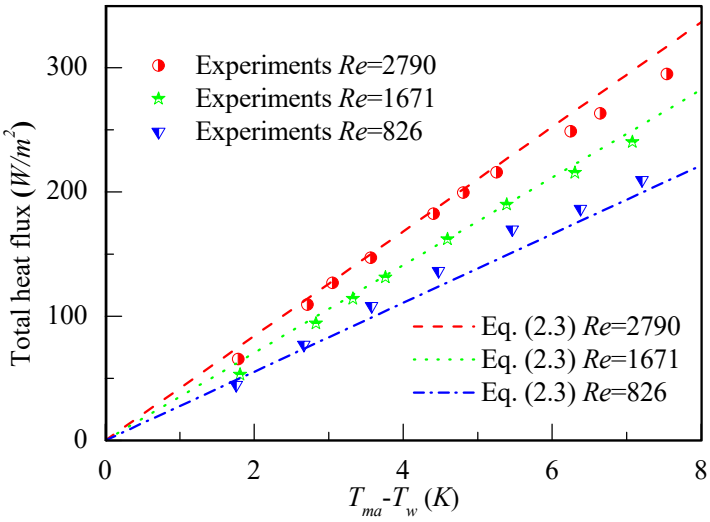

Figure 2.5 Heat flux of the convection measurement and theory evaluation versus the driving force.

For validating the measurement system and the experimental data reduction, the single phase laminar convection experiments are also carried out. In this work, the convection flow with the considered Reynolds number up to 2800 is assumed as laminar. In the test rectangle channel, just the condensation substrate (9×6 *mm*) is cooled. Correspondingly, the thermal boundary layer is only developed over the entire condensation substrate within the fully developed laminar flow. Consequently, the present system can be seen as a fully developed laminar flow heat transfer over condensation substrate in a duct. Historically, based on a large amount of experimental data, different empirical correlations have been developed for forced convection heat transfer [34-35]. Here, the mean Nusselt number Nu^* over the entire length of block sensor can be calculated as [35]:

$$Nu^* = \left\{ 3.66^3 + 0.7^3 + \left[1.615 \left(\frac{RePrD_c}{L_s} \right)^{1/3} - 0.7 \right]^3 \right\}^{1/3} \tag{2.2}$$

where Pr is the Prandtl number, the bulk Reynolds number Re is calculated using the

hydraulic diameter of the channel D_c, L_s is the length of condensation substrate along the flow direction. After that, the average heat flux over the condensation substrate can be evaluated. Finally, the heat flux obtained by the correlation and the measurements is compared in Figure 2.5. As expected, no more words is necessary for forced-convection flow heat transfer. Additionally this part also provides the base for next dropwise condensation under a fully developed laminar flow.

2.3 Results and discussion

2.3.1 Droplets size distribution density

As an important dynamic characteristic, the droplet size distribution density has to be taken. This issue has been studied experimentally at different sub-cooling conditions.

For the recorded snapshot, an extracted rectangle area is selected to count the droplets and their radius, as shown in Figure 2.4. The counting size range used to calculate the droplet size distribution density is 0.8R - 1.2R. Droplets located on the boundary of the inspection zone are considered proportionally area ratio parameter ranging from 0 to 1, which reflects the area of each droplet lying within the statistical region. Due to the restriction of the camera resolution and the checking difference, the considered minimum radius in this work is approximately set at 13.5 μm corresponding to the minimum pixelated area of 32 pixels.

The droplet distribution on the cooling substrate has a complex dynamic characteristic. An accurate evaluation of this dynamic behavior is the droplet size distribution density averaged by the time. The time-series characteristics of dropwise condensation have been investigated experimentally and theoretically [29, 36-37]. The time-average means the analysis of each instantaneous droplet distribution during the whole measuring process being the time consuming. The goal of this study for the droplets size distribution density is to define a best-possible nucleation density for the simulation using the experimental results. Hence the time-averaged characteristics are not the research topic. The transient droplet size distribution density after reaching a steady-state is investigated for different sub-cooling conditions, as shown in Figure 2.6. Two representative existing theoretical models (Fractal model [37] and Le Revre & Rose model [38]) for droplet size distribution density are also included.

Le Fevre and Rose were the first to introduce the concept of droplet size distribution density and they derived a power-law equation as a function of the droplet radius based on the concept of geometrically similar structure:

$$Nd\left(R\right) = 1/3\pi R^2 R_{max}\left(R/R_{max}\right)^{-2/3} \tag{2.3}$$

where $Nd(R)$ is the droplets size distribution density, R means the droplet radius, R_{max} is the maximum radius in the condensation substrate.

Based on the fractal geometry theory, Mei et al. [37] derived the following expression for the droplet size distribution density:

$$Nd\left(R\right) = ((2-d_f)\omega)/(\pi(1-\omega))\, R_{max}{}^{-(2-d_f)} R^{-(1+d_f)} \tag{2.4}$$

where ω is the surface fraction covered by droplets, d_f is the fractal dimension ($0 < d_f < 2$). The maximum radius R_{max} can be considered as the departing droplet radius, which is approximately in the range 1.44 - 1.74 *mm* observed from the present experiments. For different sub-cooling conditions in the experiments, the surface fraction ranges from 0.63 to 0.74. In this work, the maximum radius, the fraction of surface coverage and the fractal dimension are set as 1.6 *mm*, 0.7 and 1.95 respectively.

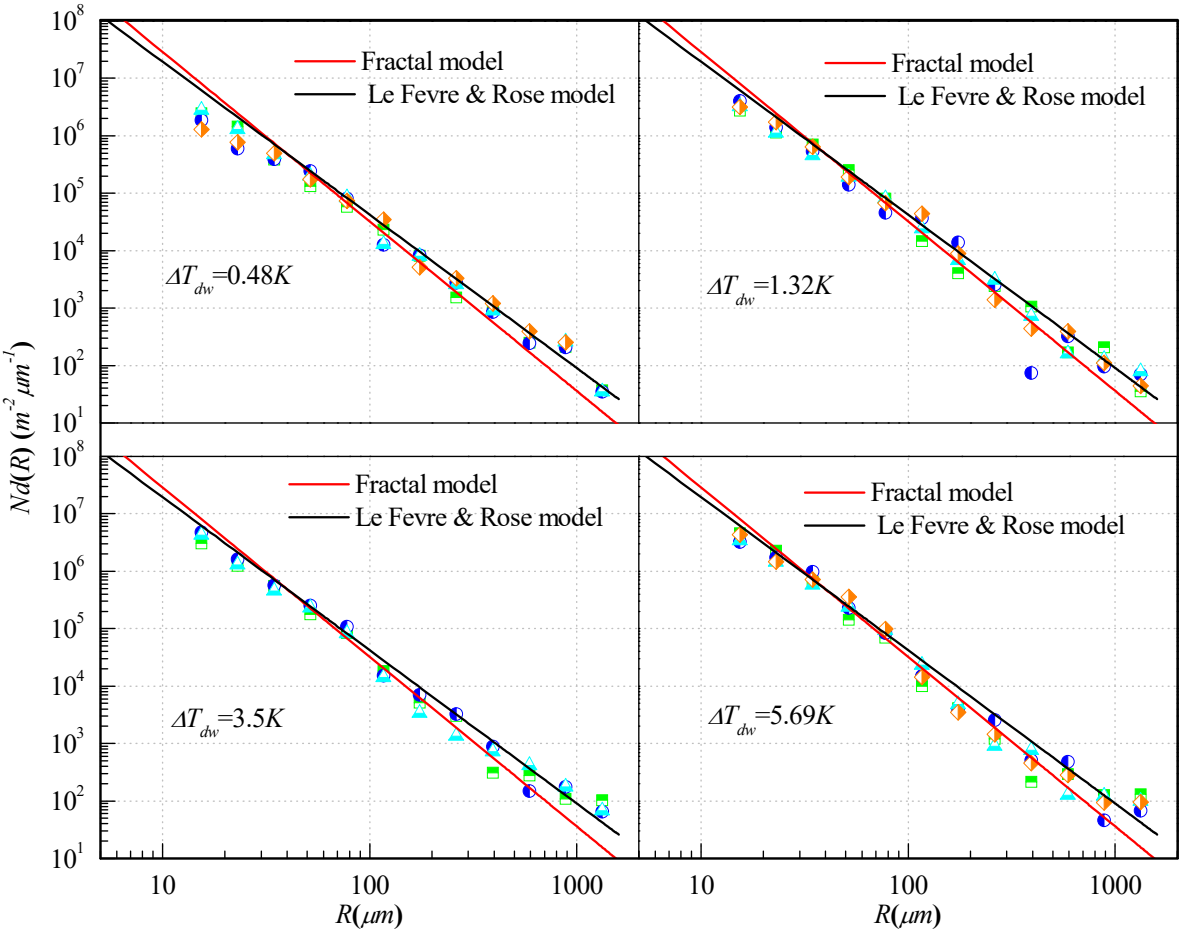

Figure 2.6 Droplet size distribution density depending on sub-cooling in 94% RH. Different symbol means the droplet-size distribution at different measuring time.

In Figure 2.6, the droplet size distribution density (divide the droplets number per area by the counting range) from the measurements is depicted against the geometric mean radius in the counting range. As presented in the figures, the droplet size distribution densities given by Le Revre & Rose model and Fractal model are good agreement with that of the experimental data. Additionally, the difference between the correlations and the measurements is more due to the experimental transient distribution. As shown in Figure 2.6, a discontinuity of the droplets population density can be found with decreasing droplet size, especially at lower sub-cooling. This is because of the beginning of coalescence when the droplet radius reaches a critical size decided by the nucleation site density. For this reason, a pronounced effect shown in Figure 2.6 is that the nucleation site density increases with increasing sub-cooling, which has been reported earlier by McCormick and Westwater [39]. Furthermore, the existing

correlations including the above mentioned models just can work for droplets having the radius larger than the critical size, not for small droplet before coalescence.

2.3.2 Droplet growth rate

Over the condensation substrate, the complicated droplet dynamics behaviors are characterized by the droplet growth thanks to the direct condensation and the coalescence events. While the direct condensation on the droplet surface releases the main heat flow, the droplet growth behavior plays a vital role for dropwise condensation. To quantify the growth rates, the droplet growth by direct condensation between coalescence events is monitored by the camera. Figure 2.7 illustrates the process to define the droplet growth rate experimentally. Turning to the zoom-in mode, the camera having the view field 2.53×1.90 mm^2 focuses on the condensation substrate. Video measurements are made during dropwise condensation. Finally, the growth of individual droplet without coalescence events can be captured by checking the video, as the droplet marked by green circle in the top of Figure 2.7. Then the sizes of the interesting droplet during growth, which is plotted in the bottom of Figure 2.7, are detected by the image post processing for sequential images. The detecting error of the droplet size is within 1 pixel (0.98 μm). The slope of the best linear fitting line is then regarded as the growth rate of the interesting droplet at the mean radius. The uncertainties of the obtained growth rate are defined by the simple linear regression with the confidence level 95% [40].

Repeating the above process, the droplet growth rates at different size can be experimentally figured out. In order to minimize the coalescence events, the measurements are carried out at a low bulk-flow velocity (Re = 826) and sub-cooling ($\Delta T_{dw}=T_d-T_w \approx 1.0\ K$). Considering the generality, both of the center and edge regions of the substrate are all measured by moving the camera. The droplets without coalescence during a period of time is considered to determine the growth rate only by direct condensation. While the coalescence events occur frequently for larger size droplets, the size of the considered droplet spreads in the range 20-80 μm. Figure 2.8 plots the experimentally defined droplet growth rate with its radius. It is surprised that the growth rate of droplet is not a strong function of its size and dispersedly spread in a wide range. Nevertheless, the smaller droplets grow faster than the larger one as a whole. The difference of the growth rate for the equal size droplets is up to 300%. What we find here keeps consistent with the previous experiments [41-42]. Leach et al. [41] experimentally tracked three small droplets have the approximately same size and locate different positions. The varying radius during time demonstrated that the droplet far away from the large droplet grows 20% faster than another two droplets closing to large drops. From the works by Medici et al. [42], growth enhancement by the droplets on substrate edges or corners can reach nearly 500% comparing with these drops locating on the center of the substrate. That is because of different effects of the local depletion of the vapor concentration field. In conclusion, the droplet growth rates are significantly affected by its neighbors. The spatio-temporal-dependent dynamics of the droplets are responsible for this varying growth rate.

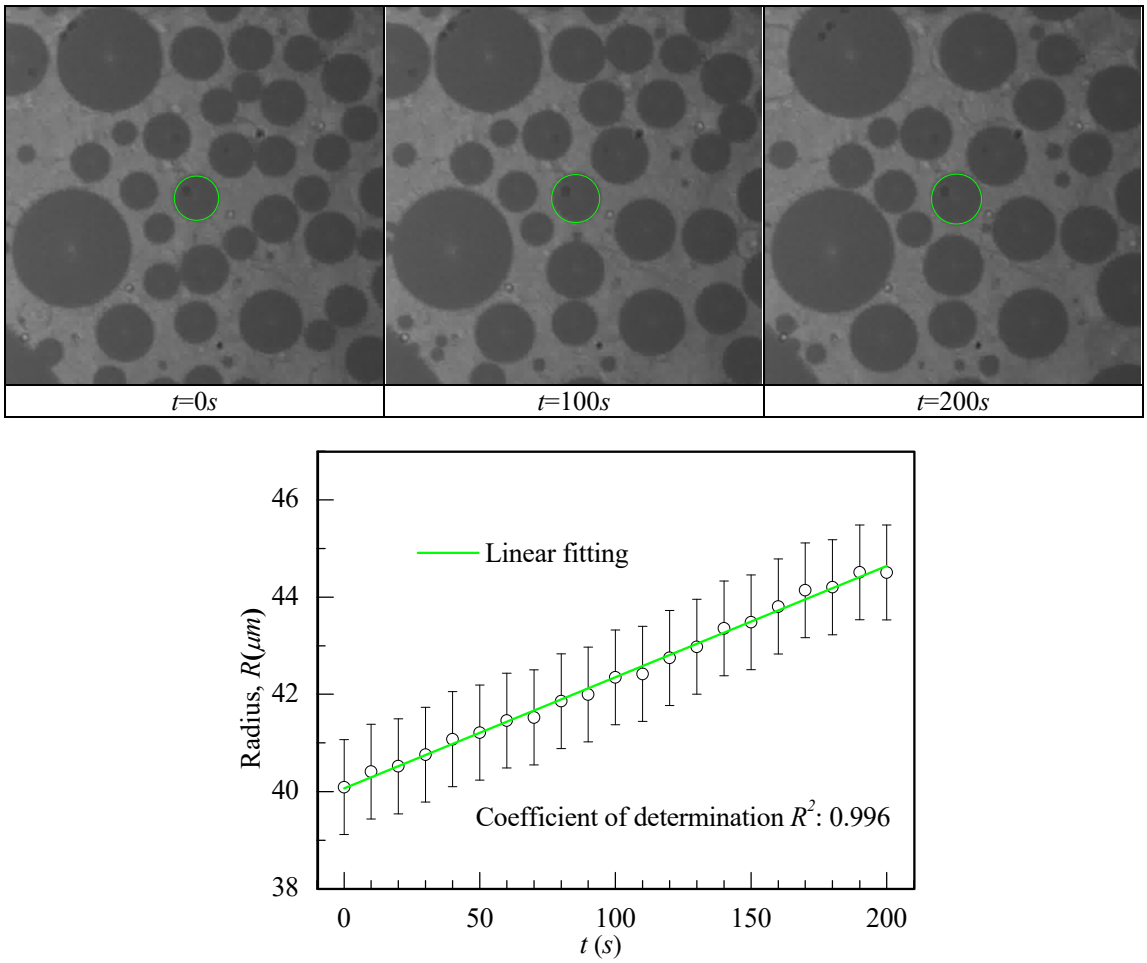

Figure 2.7 Illustration of experimentally defining growth rate of droplet.

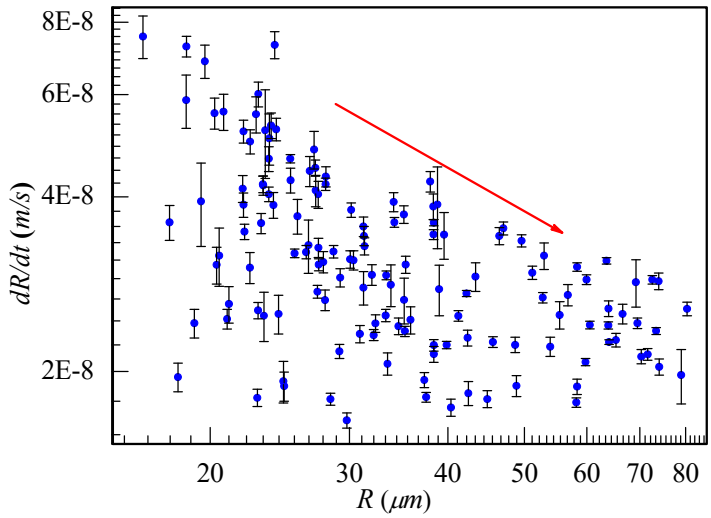

Figure 2.8 Experimentally defined growth rate versus droplet radius.

2.3.3 Overall heat flux

Under the forced convection laminar flow, dropwise condensation experiments at different Reynolds numbers are carried out and the measured overall heat flux has been plotted in Figure 2.9. Dropwise condensation occurs when the wall temperature (T_w) is lower than the dew point temperature (T_d). At current experimental conditions (T_{ma}=303.15 K and RH=94%),

the dew point temperature is approximately at T_d=302.1 *K*. Therefore, it is single phase forced convection if the wall temperature is higher than the dew point temperature, and is said to be convective dropwise condensation flow at lower temperature. As because of the fluctuating RH during experiments, the critical temperature difference ($\Delta T_{aw}=T_{ma}-T_w$) distinguishing single phase convection and convective dropwise condensation locates over a range. As shown in Figure 2.9, the critical region for present experiments is marked by two vertical dashed line. In current *Re* range, the dragging force of the bulk flow is neglected for droplets dynamics. Within convective dropwise condensation flow, the heat flow is comprised of sensible heat and latent heat. The sensible heat transfer by forced convection is governed by the thermal driving temperature difference (ΔT_{aw}). Otherwise, the diffusion driving temperature difference (ΔT_{dw}) is responsible for latent heat of condensation. In Figure 2.5, the forced convection heat transfer is enhanced by increasing *Re*. By comparison, the enhancement effect is expanded for convective dropwise condensation flow. The answer is that in addition to the enhanced convection heat transfer, vapor condensation is extremely enhanced by convective flow, namely the convective mass transfer. Consequently, heat and mass transfer during convective dropwise condensation with NCG are all promoted by the convective flow as a vital factor.

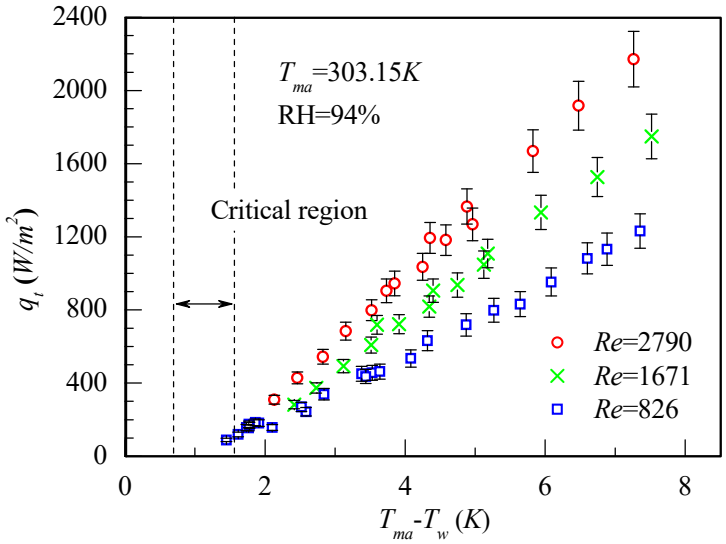

Figure 2.9 Overall heat flux versus sub-cooling at different Reynolds numbers.

2.4 Conclusions

This chapter is focused to experimentally study convective dropwise condensation out of humid air. The dry air is recognized as NCG. Measurements are carried out at a constant relative humidity (RH) with a variety of sub-cooling degree and Reynolds numbers. And the microscope camera is available for visualization. The experimental system and the data reduction are validated by the forced-convection flow heat transfer experiments. After that, the droplet size distribution density during condensation measurements is depicted using the camera and compared with two classical theoretical models. In addition, the camera is employed to determine the droplet growth rate keeping the coalescence events away. The

droplet growth rates which dispersedly locate a wide range demonstrate the local depletion of water vapor affected by each others. Significantly, the measured overall heat flux announces the role of the convection flow on heat and mass transfer during convective dropwise condensation. The experimental results in this chapter construct a solid foundation for next modeling.

Chapter 3 Single Droplet Growth Model

In this chapter, a droplet growth model by an isolated form is developed for modeling heat and mass transfer during dropwise condensation in case of NCG. The condensation process is divided by the droplet surface into two parts. The first step, i.e. the processes of mass transfer from the surroundings to the droplet surface, is modeled by the kinetic theory and the laws of continuum fluid dynamics formulated using the two-region concept (Knudsen layer and continuum region). The second step, i.e. the heat transfer process across the liquid droplet, is governed by Fourier's law of heat conduction. These three regions (the continuum region, the Knudsen layer and the droplet) are incorporated by matching both the mass flow rate and the energy flow rate. This model is named by Model A which considers the multi-scale feature of droplet size by the Knudsen layer bridging the continuum and kinetic limits. Neglecting the multi-scale feature, the droplet growth rate can be solved by matching the mass flow rate of diffusion and the heat flow rate crossing the droplet. A simplified version of Model A is constructed-that is Model B. Furthermore, Model C assumes the droplet surface has the same temperature with the droplet base. As a commonly used model in literatures, Model C only handles the vapor diffusion process. For these three models, more details and the discussion will be given next.

3.1 Literature review

In absence of NCG, the vapor keeps on an equilibrium state and the heat transfer of dropwise condensation depends on the heat resistance from the droplet surface to the cooling side. The classical thermal resistance model [4, 9, 43-44] across a droplet typically comprises the interfacial resistance for molecules transport across the liquid/vapor interface, the capillary resistance of the droplet curvature, the conduction resistance by the liquid droplet, the conduction resistance due to the substrate and the promoter layer. In contrast to the pure vapor, the presence of NCG reduces the vapor partial pressure. Subsequently, the saturation temperature of bulk drops down. Furthermore, the vapor/liquid interface is actually impermeable to the NCG and closing it the NCG accumulate during the condensation process forming a non-condensable diffusion layer. Finally, the diffusion resistance for the vapor molecules moving to the condensing interface is introduced. Figure 3.1 intuitively gives a schematic view of a droplet over a cold substrate with and without NCG.

To account for the influence of NCG, the difference between the dew point temperature of

the bulk and the surface temperature on the droplet was introduced into the classical thermal resistance model of pure steam condensation by Ghosh et al. [45]. This new term acts to reflect the decrease of vapor mass fraction from the free flow to the droplet surface as the driving force for condensation mass transfer rate. As a plausible simplification, a fractional constant reduction of the effective driving temperature difference is assumed to estimate the condensation rate. For simplification, literatures [42, 46-48] assume that the temperature of the droplet surface is equal to the temperature of droplet base. The vapor diffusion is uniquely considered. However, in practice, an exact definition for the surface temperature of droplet and the corresponding condensation rate must be rated on the solution of the coupled mass and energy equations. Because of the contradictory, the heat transfer model of dropwise condensation considering NCG is rarely investigated.

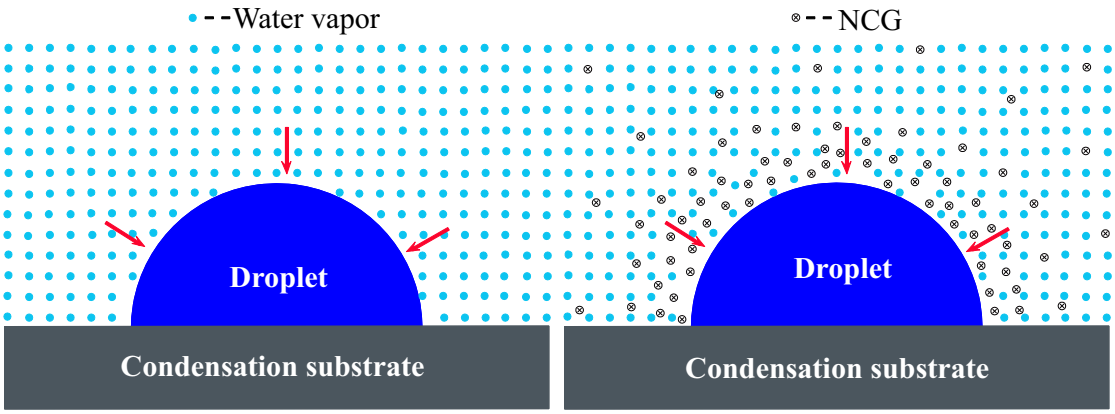

Figure 3.1 Schematic view of condensation droplet on a cold substrate. Left: the pure vapor; right: the presence of NCG.

Basically, the growth process of droplets has a multi-scale feature as the droplet radius spreads from the initial radius of some nanometers to the departure size at millimeter scale. That means the mechanism of the heat and mass transfer processes depends to a large extent on the Knudsen number *Kn*, which is described as the ratio of the mean free path of vapor molecules to the droplet diameter. For very small *Kn* corresponding to the big droplets, the heat and mass transfer process is determined by the laws of continuum fluid dynamics. For very large *Kn* in the initial stage of growth, the continuum hypothesis is not suitable and the kinetic theory is applied to describe the impingement process of vapor molecules. However, the growth processes occur consecutively. Hence, a useful growth model is necessary to consider the intermediate case where $Kn = O(1)$.

For condensation and evaporation of droplets in carrier gases, the Gyarmathy model [49] and the Young model [50-51] are two classic growth models having different descriptions for the transition between the continuum and kinetic regimes. The Gyarmathy model uses an interpolating fit between the continuum and the molecular kinetic regime and those two are independently described. The Young model on the other side incorporates the transition into the growth model based on the well-known two-region concept. Peters and Meyer [52] developed an experiment to investigate the droplets growth of a pure vapor in the transition

regime. They also formulated a model bridging the molecular and continuous heat and mass transfer processes with a minor adjustment factor to cover the evaporation and condensation coefficients. In order to validate the droplet growth model, Peeters et al. [53] compared the Gyarmathy model and the Young model with the growth results obtained from a pulse expansion wave tube. Those two models gave the best results in the different regimes. For the solid surface, Luo et al. [54] developed a droplet growth model based on the two-region concept (Knudsen layer and continuum region) for the quantitative description of the processes of droplet condensation and evaporation on a solid surface in the presence of NCG. The transition between those two regimes was also described by an incorporation method as shown in Young model. The effect of the solid surface was considered by their new kinetic model. Although the effect of solid surface is taken into account, the droplet temperature is identical to that of the solid surface.

In spite of the continuous advance and the wide research for the droplet growth model considering NCG, the considering is just the droplet growth in a carrier gases and the application fields are in aerosol science and cloud physics mostly. In those cases, the latent heat released by the condensation is transferred to the surrounding gases and any heat transfer between the droplets and the solid surface is neglected.

For dropwise condensation on a cold substrate, however, the latent heat of condensation is transferred to the cold substrate through the droplet, which is one of the crucial processes. To our knowledge, very few theoretical investigations for droplet growth are performed about dropwise condensation in the presence of NCG. In this chapter, a single droplet growth model considering the multi-scale feature of droplet size is presented to cover the complex simultaneous heat and mass transfer across the droplet from the free stream to the cold wall. The transition between the continuum and kinetic limit is bridged by the Knudsen layer from Young's model. In addition, another two relatively reduced models ignoring the multi-scale characteristic are given too. And a well-informed discussion about these three models is carried out in this chapter.

3.2 Model development and methods

In this section, a detailed description of the droplet growth model and the calculating method are presented for dropwise condensation of moist air. The theory is simplified by the following assumptions: (i) quasi-steady droplet growth at a specified radius; (ii) uniform pressure; (iii) droplet is hemispherical that means a 90º static contact angle (θ=90º); (iiii) the contact angle hysteresis is not considered. For promoting dropwise condensation, the cold substrate is generally covered by a suitable promoter layer, on which the vapor molecules condensate in the form of discrete liquid droplets. The cooling side of the cold substrate is kept at a constant temperature using some cooling technique. Steady-state 1-D heat conduction is assumed to be passed through the promoter layer and the cold substrate when condensation comes to a stable state. In this model, the wall temperature is assumed to be equally distributed. This assumption is reasonable because the size of substrate is always

much larger than the droplet size for the investigated cases. Actually, the present model is just handling the heat and mass transfer resistances from the bulk to the droplet base, including the diffusion resistance R_{vr}, the interfacial resistance R_{ir}, the capillary resistance R_{cr} and the conduction resistance of liquid droplet R_{dr}, as shown in Figure 3.2.

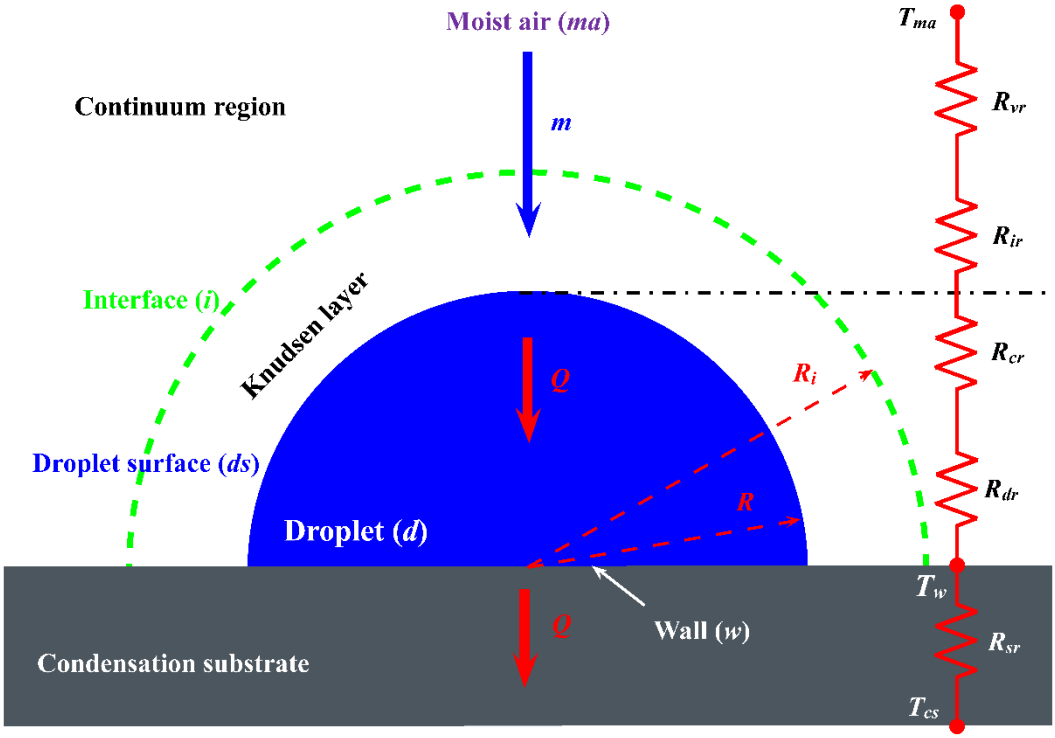

Figure 3.2 Schematic view of droplet growth model under the NCG condition and the corresponding resistance model of heat and mass transfer.

Figure 3.2 gives the schematic view of the droplet growth model over a cold substrate. Three regions (droplet, Knudsen layer, continuum region) are visible with mass flow rate m, the heat flow rate Q as directed. The heat transfer crossing the liquid droplet is governed by the Fourier's law of heat conduction. Within the framework of the Young model, the flow-field surrounding the droplet is presumed to contain two regions (Knudsen layer and continuum region). This simple model was first introduced by Langmuir [55] considering the rarefied gases effect. The hemispherical droplet having radius R is surrounded by the Knudsen layer seen as a semispherical shell, where R and R_i are the radius of the inner sphere and the outer sphere respectively. Similarly, the continuum region is considered as special semispherical shell surrounding the Knudsen layer, and the far field is the outer sphere having an infinity radius. The Knudsen layer having a thickness of the order of the mean free path is also called a collision-free zone because the molecular collisions are supposedly unimportant [56]. So, for the inner Knudsen layer, the free molecule kinetic theory can be applied to describe the transfer processes of vapor molecules onto the droplet and to calculate the mass fluxes. For the outer continuum region, the mass transfer is governed by the binary-gases diffusion law.

Above all, the Knudsen layer (collision-free zone) and the continuum region are combined into the flow-field region outside the droplet. The mass flow rate in those two regions is

matched over the interface of Knudsen layer. Because the NCG do not condense, the heat flow is all from the vapor condensation. Therefore, the flow-field region and the liquid region are incorporated by matching the mass and heat flow rates. The spherical polar coordinate system is used here.

3.2.1 Liquid droplet

Heat conduction through the hemispherical-shaped droplet with radius R can be written as [4]:

$$Q = 4\pi R k_d (T_{ds} - T_w) \tag{3.1}$$

Taking the heat flow rate to be identical with the latent heat of condensation, equation (1) may be rewritten as:

$$Q = m * L = 4\pi R k_d (T_{ds} - T_w) \tag{3.2}$$

where L means the condensation latent heat of water vapor, k_d is the thermal conductivity of liquid droplet and T_{ds} is the temperature of the droplet surface which is also the liquid/vapor interface, m is the mass flow rate due to the mass transfer.

3.2.2 Knudsen layer

The radius of the Knudsen layer is arbitrarily defined with the droplet radius.

$$R_i = R + \beta\lambda_{ma} \tag{3.3}$$

where the experimental coefficient β has a weak influence for the fluxes and a best fit value of 0.75 [51]. The mean free path of moist air (vapor-gas) λ_{ma} is calculated by an explicit expression [54]:

$$\lambda_{ma} = 2\mu_{ma}\sqrt{R_{ma}T_{ma}}\,/P_{ma} \tag{3.4}$$

where all physical parameters are talked for moist air.

It is assumed that all molecules evaporating and reflecting from the droplet surface have a similar Maxwellian velocity distribution at the temperature of droplet surface. In Young's model [51], the Grad velocity function can give a physically more realistic representation of the convective and diffusive heat and mass flow rate near the interface and thus is applied to describe the velocity distribution of the incoming molecules that correspond to the Knudsen interface. The vapor and NCG have an identical distribution.

Since the NCG does not contribute to the net mass flux of condensation, the mass flow rate of vapor across the Knudsen layer can be calculated as:

$$m = \alpha_e m_{+v} - (1-\alpha_c) m_{-v} + m_{-v} = \alpha_e m_{+v} + \alpha_c m_{-v} \tag{3.5}$$

where α_c and α_e respectively denote the condensation and evaporation coefficients. In many studies, the distinguishable difference between those two coefficients is ignored (i.e., $\alpha_c = \alpha_e$) and these two coefficients can be named by accommodation coefficient α. The first term of the middle part represents the mass flux due to the evaporation. The second and third terms in the middle part indicate the reflected and incoming molecules, respectively. Over nearly a century, intensive researches have been made to determine the accommodation coefficient

experimentally. Both evaporation and condensation were investigated under various conditions (different pressure, different water vapor saturation, different temperature and different substrate) and various environments (vacuum, standard air, passive or reactive atmospheres) [57-59]. Due to the complexity of the corresponding physical mechanisms and the limitation of measurement technology, the reported values for both of the coefficients for water span widely from 0.001 to 1 [58]. The choice of coefficient strongly depends on the measurement condition and environment. Actually the accommodation coefficient defines the fraction of the striking vapor molecules that actually condenses on the vapor/liquid interface. The remaining fraction (1-α) represents the reflected vapor molecules that strike the interface but do not condense. Consequently, the accommodation coefficient indirectly defines the interfacial resistance of the interface for condensation [4] (namely, higher α meaning lower interfacial resistance for the molecules transport crossing the interface). As a crucial parameter for defining the interfacial resistance, it will be discussed in depth later. The incoming and outgoing mass flow rate of vapor molecules m_{-v} and m_{+v} (see APPENDIX B), respectively, can be evaluated using the triple integral of the velocity distribution [50-51]:

$$m_{-v} = -2\pi R^2 \left(1-\cos\theta\right) \rho_{v,i} R_v T_i \Big/ \sqrt{2\pi R_v T_i} + R^2 \Big/ 2R_i^2 \, m \tag{3.6}$$

$$m_{+v} = 2\pi R^2 \left(1-\cos\theta\right) \rho_{v,ds} R_v T_{ds} \Big/ \sqrt{2\pi R_v T_{ds}} \tag{3.7}$$

Substitution of Eqs. (3.6) and (3.7) into Eq. (3.5) results in:

$$m = \frac{4\pi R^2 R_i^2 \left(1-\cos\theta\right)}{\left(2R_i^2 - \alpha_c R^2\right)} \left(\frac{\alpha_c \rho_{v,ds} R_v T_{ds}}{\sqrt{2\pi R_v T_{ds}}} - \frac{\alpha_e \rho_{v,i} R_v T_i}{\sqrt{2\pi R_v T_i}} \right) \tag{3.8}$$

where the vapor partial density at the interface between the Knudsen layer and the continuum region can be obtained by the ideal gas equation:

$$\rho_{v,i} = P_{v,i} \big/ R_v T_i \tag{3.9}$$

with R_v is the specific gas constant of vapor, the vapor partial pressure $P_{v,i}$ equals to the saturated vapor pressure $P_{v,i}^{sat}$ at its temperature T_i [60]:

$$P_{v,i}^{sat} = 611.2\exp[6816(1/273.15 - 1/T_i) + 5.1309\ln(273.15/T_i)] \tag{3.10}$$

For the droplet surface, thermodynamic equilibrium at the temperature T_{ds} and pressure $P_{v,ds}$ is assumed. The Kelvin equation, which defines the vapor pressure over a curved liquid/vapor interface, is used to calculate the vapor partial pressure $P_{v,ds}$ of an equilibrium state over the droplet surface [54]:

$$P_{v,ds} = P_{v,ds}^{sat} \exp(2\sigma_d \big/ (\rho_d R_u T_{ds} R)) \tag{3.11}$$

where the surface tension of liquid σ_d and the liquid density ρ_d are defined at the temperature of droplet surface T_{ds}, R_u is the universal gas constant, $P_{v,ds}^{sat}$ denotes the saturated vapor pressure at temperature T_{ds} over a flat liquid/vapor interface by Eq. (3.10). Finally, the vapor partial density on the droplet surface $\rho_{v,ds}$ can be calculated by Eq. (3.9).

3.2.3 Continuum region

In the continuum region, macroscopic laws of continuum fluid mechanics are applicable.

The condensation is assumed as a quasi-steady process: the characteristic time for the state-change of the surrounding is much larger than that which the droplet growth process needs for reaching a steady state. After neglecting the viscous normal stresses, the mass and energy conservation equations (vapor-air mixture and vapor alone) for a spherically symmetric stationary case can be expressed as follows [50-51, 54]:

$$\frac{d}{dr}(r^2\rho_{ma}u_b)=0 \tag{3.12}$$

$$\frac{d}{dr}(r^2\rho_{ma}u_b(h_{ma}+\frac{u_b^2}{2})+r^2q_r)=0 \tag{3.13}$$

where the density of moist air ρ_{ma}, the radial bulk velocity u_b, the specific enthalpy h_{ma} and the outward radial heat flux q_r for the moist air are all depend on the radial coordinate r. The density of moist air ρ_{ma} can be defined with the partial density (vapor density ρ_v and dry air density ρ_a):

$$\rho_{ma}=\rho_v+\rho_a \tag{3.14}$$

It is necessary to take a closer look at the relative velocities when the vapor is condensing at the droplet surface. As a whole, the bulk velocity (u_b) of the mixture points toward the droplet (negative). The relative velocity of vapor with respect to the bulk (v_v) is the inward diffusive velocity of the vapor from the far field to the interface and also negative. While the relative velocity of NCG with respect to the bulk (v_a) is the outward diffusive velocity of the vapor from the interface to the far field, that is positive correspondingly. In condensation case, the net mass flux only attribute to the vapor condensation. The NCG does not contribute to the condensation which implies no net mass flux (ρ_a (u_b+v_a) = 0), or the inward bulk mass flux ($\rho_a u_b$) has the same value with the outward diffusive mass flux ($\rho_a v_a$). Furthermore, by definition we have the sum of diffusive fluxes in steady-state condensation:

$$\rho_v v_v+\rho_a v_a=0 \tag{3.15}$$

The velocity of each component is composed of the bulk velocity u_b and the diffusive velocity (v_a and v_v). So the mass conservation equation (3.12) can be rewritten as:

$$\frac{d}{dr}(r^2\rho_v(u_b+v_v)+r^2\rho_a(u_b+v_a))=\frac{d}{dr}(r^2\rho_v(u_b+v_v))=0 \tag{3.16}$$

Finally, the total mass flow rate can be yielded by the integration of equation (3.12) and (3.16):

$$m=2\pi r^2\left(1-\cos\theta\right)\rho_{ma}u_b=2\pi r^2\left(1-\cos\theta\right)\rho_v(u_b+v_v) \tag{3.17}$$

Simultaneously, Fick's law for diffusion has the form:

$$\rho_v v_v=-\rho_{ma}D\frac{d}{dr}(\frac{\rho_v}{\rho_{ma}}) \tag{3.18}$$

where the diffusion coefficient of water vapor in air D depends on the temperature and pressure [60]:

$$D=2.11\times10^{-5}\ (T_{ma}/273.15)^{1.94}(1/P_{ma}) \tag{3.19}$$

Combining equations (3.17) and (3.18), the following result can be derived:

$$m(1-\frac{\rho_v}{\rho_{ma}}) = 2\pi r^2 \left(1-\cos\theta\right)\rho_{ma} D \frac{d}{dr}(\frac{\rho_v}{\rho_{ma}}) \tag{3.20}$$

Equation (3.20) can be integrated subject to the boundary conditions $\rho_{v,i}/\rho_{ma}$ at $r=R_i$ and $\rho_{v,ma}/\rho_{ma}$ as $r=\infty$, resulting in:

$$m = 2\pi R_i \left(1-\cos\theta\right)\rho_m D \ln\left(\frac{\rho_{ma}-\rho_{v,ma}}{\rho_{ma}-\rho_{v,i}}\right) \approx 2\pi R_i \left(1-\cos\theta\right) D(\rho_{v,i}-\rho_{v,ma}) \tag{3.21}$$

where the vapor partial density of moist air $\rho_{v,ma}$ can be obtained by the ideal gas equation.

3.2.4 Iterative solution

Based on the mass and energy conservation, the heat and mass flow equations in those three regions can be solved. Due to the related physical parameters of droplet and gas mixture depend on two unknown variables (T_i, T_{ds}), the solution would require an iterative method.

For the dropwise condensation of moist air over a cold substrate, there are some input parameters: the wall temperature T_w, droplet radius R, properties of moist air (including vapor density $\rho_{v,ma}$, temperature T_{ma} and pressure P_{ma}). Once the properties of vapor-air mixture are known, the radius of the Knudsen layer R_i can be solved by equations (3.3) and (3.4). With these input parameters, 3 unknown variables (m, T_{ds}, T_i) can be solved by the 3 equations (3.2, 3.8, 3.21).

The iterative procedure has the following five steps: 1) assume an initial temperature at the droplet surface T_{ds}; 2) define the physical properties of droplet using T_{ds}, and then calculate m by solving equation (3.2); 3) calculate vapor pressure and density over the droplet surface by solving equation (3.11) and the ideal gas law (3.9); 4) calculate m and T_i by solving equations (3.8) and (3.21) (the saturated vapor is considered at the Knudsen layer interface); 5) compare the mass flow rate m from step 2 and 4 using a solving deviation Δm, if the absolute mass flux difference of two results is larger than the solving deviation, use a new T_{ds} to repeat step 2-5. The calculation is repeatedly carried out at different droplet sizes from minimum to maximum.

A MATLAB script is developed to follow those solving steps. Once the mass flow rate m is obtained, the droplet growth rate depending on its radius can be computed from the mass conservation:

$$\frac{dR}{dt} = \frac{-m}{2\pi R^2 \left(1-\cos\theta\right)\rho_d} \tag{3.22}$$

In brief, a theoretical model for single droplet growth in dropwise condensation considering NCG has been proposed. This model provides an elaborated solution for the heat and mass transfer processes across the droplet from the flow-field to the wall during dropwise condensation of vapor-NCG mixture. In addition, the nucleation radius of a droplet without growth rate, the temperature at droplet surface and Knudsen layer interface can be obtained by

this model. It is clear that the model is suitable for dropwise condensation with any NCG, any concentration. Derails on this model can be found in Zheng et al. [61].

3.2.5 Model extension

To sum up, a multi-scale droplet growth model presented in sections 3.2.1-3.2.3 is named by **Model A**. Model A covers the complex coupled heat and mass transfer from the mixture to the droplet base and considers the multi-scale feature of droplet size. And the interfacial resistance R_{ir} is considered automatically due to the nature of the Knudsen layer. The employment of the Kelvin equation states the capillary resistance R_{cr} is also handled within this model. Based on model A, another two models are introduced as below.

Model B: Without the Knudsen layer (namely, neglecting the multi-scale feature), the vapor diffusion from the bulk to the droplet surface is defined by:

$$m = 2\pi R\left(1-\cos\theta\right)D(\rho_{v,ds}-\rho_{v,ma}) \tag{3.23}$$

where the vapor partial density on the droplet surface $\rho_{v,ds}$ is also calculated by equations (3.9-3.11) for considering the capillary resistance. The heat flow rate crossing the droplet is calculated by:

$$Q = m^{*}L = 4\pi Rk_{d}(T_{ds}-T_{w}) \tag{3.24}$$

The solution for equations (3.23) and (3.24) can be following the iterative method in section 3.2.4. Clearly, this model may be seen as a simplified version of model A on the macro-scale.

Model C: There is negligible heat conduction through the droplet. The temperature of the droplet surface T_{ds} is equal to the temperature of droplet base T_w. The vapor diffusion is uniquely considered as:

$$m = 2\pi R\left(1-\cos\theta\right)D(\rho_{v,ds}-\rho_{v,ma}) \tag{3.25}$$

where the temperature T_{ds}=T_w is used to calculate the vapor density $\rho_{v,ds}$. Owing to its simplification and the higher proportion of the diffusion resistance in most cases, this model is commonly adopted [42, 46-48].

The considered resistances for heat and mass transfer in three models are listed in Table 3.1. The difference in three models can be found intuitively. Further discussions and comparisons for those three models will be given in depth and detail next.

Table 3.1 Considered resistances in three models.

	Diffusion	Interfacial	Curvature	Droplet	Multi-scale
Model A	Eq. (3.21)	Knudsen layer	Kelvin equation	Eq. (3.2)	Knudsen layer
Model B	Eq. (3.23)	N/A	Kelvin equation	Eq. (3.24)	N/A
Model C	Eq. (3.25)	N/A	N/A	N/A	N/A

3.3 Results and discussion

3.3.1 Minimum radius of droplet

The minimum radius of droplet can possibly grow for a specified wall sub-cooling, where

the droplet is at the meta-stable state of saturated vapor and liquid phase. Based on Gibbs free energy criterion and assuming the saturated vapor at a uniform temperature, the minimum size for dropwise condensation on a sub-cooled substrate is given, e.g., by Graham and Griffith [62]:

$$R_{min} = (2T^{sat}\sigma_d)/(L\rho_d \Delta T) \tag{3.26}$$

where ΔT is the temperature difference between the temperature of saturated vapor (T^{sat}) and the wall temperature (T_w). This equation is universally used to calculate the nucleation radius for dropwise condensation of saturated vapor. In case of an unsaturated vapor, the vapor adjacent to the cooling wall will be also saturated due to the effect of cooling. Hence the minimum droplet at nano-scale is surrounded by saturated vapor for dropwise condensation of an unsaturated vapor and equation (3.26) is valid too.

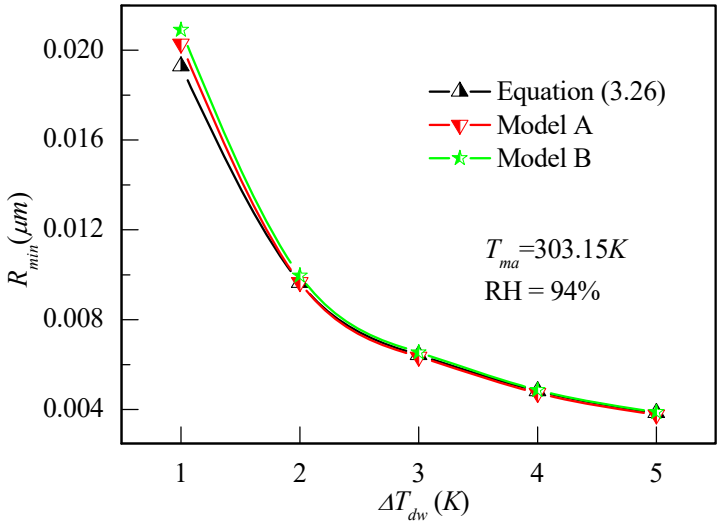

Figure 3.3 Comparison of the obtained minimum radius of droplet from the present models with the equation proposed in pure steam case.

On this point, moist air having the temperature T_{ma} = 303.15 K and the relative humidity 94% is corresponding a dew point temperature T_d = 302.1 K. For model A and model B, the droplet growth rate is solved based on the mass and energy balance. The minimum droplet is versus to the point where the growth rate is zero. It is no doubt that model C cannot give the minimum radius. As plotted in Figure 3.3, at a given condition the minimum radius of a droplet is evaluated as a function of the sub-cooling degree following equation (3.26) and models A and B. The temperature difference ΔT_{dw} between the dew point and the condensation substrate temperature is used as the sub-cooling degree in equation (3.26). The minimum radius predicted from both of the methods shows good agreement, which provides a validation for the present models. The inclination indicates that the minimum radius strongly depends on the sub-cooling ΔT_{dw} in dropwise condensation of moist air.

3.3.2 Temperature of droplet surface

For comparing those three models, investigation is carried out at a given condition. The temperature of moist air is set as T_{ma} = 303.15 K and the difference between the dew point and

the wall temperature ΔT_{dw} = 1.0 K is chosen. The relative humidity RH = 94% is considered with the corresponding dew point (302.1 K).

As described in section 3.2 for three models, the iteration of temperature at droplet surface T_{ds} is used to solve model A and B. Finally, the temperature T_{ds} from three models is evaluated with respect to the droplet radius, as plotted in Figure 3.4. The capital letters index the model. In model A, when the droplet size is getting smaller, the temperature of the droplet surface gradually approaches the wall temperature. This is because the small droplet provides a smaller thermal conduction resistance. As discussed in section 3.2.2, the accommodation coefficient α indirectly reflects the interfacial resistance for the transport of vapor molecules toward the vapor/liquid interface. When the interfacial resistance is increased with smaller accommodation coefficient, the influence of the thermal conduction resistance is getting smaller. Therefore, the size range of droplet, where the temperature of droplet surface gets approaching the wall temperature, is extended with decreasing the accommodation coefficient. For fully thermal accommodation α = 1, model A produces a closing result with model B neglecting the interfacial resistance. In conclusion, the accommodation coefficient in model A can be seen as an adjusting factor for the interfacial resistance. For model C, the temperature of droplet surface is equal to the wall temperature with neglecting conduction resistance through the droplet. It is noted that the temperature difference between the droplet surface and the wall varies in a small range in model A and B. The temperature drop from the bulk to the droplet surface denotes the main part significantly. Therefore, the mass transfer resistance (including the diffusion resistance and the interfacial resistance) for vapor molecules moving to the droplet surface is the key point in present condition.

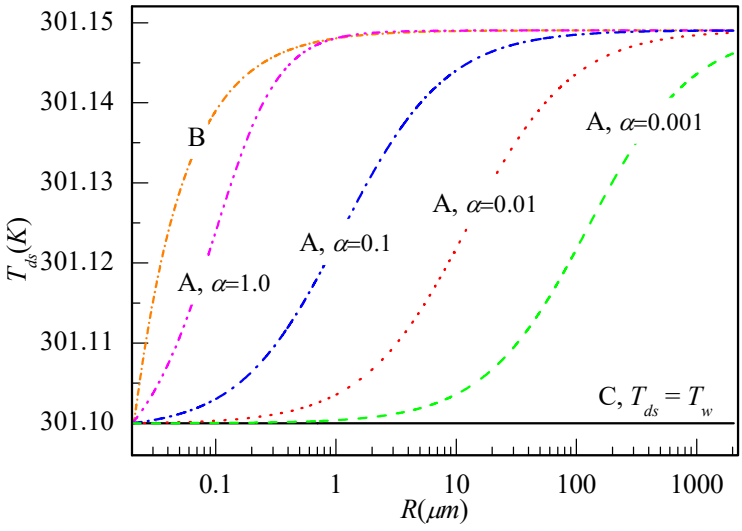

Figure 3.4 The temperature of droplet surface against the droplet radius from three models.

3.3.3 Droplet growth rate

In table 3.1, the considered resistances for heat and mass transfer in three models are listed. The difference between different models can be directly reflected in the droplet growth rate. Figure 3.5 plots the droplet growth rate by three models for single droplet condensation out of

moist air. When the surrounding in Figure 3.2 is the saturated pure steam, the droplet growth rate can be evaluated by the classical thermal resistance model [4, 9, 43-44]:

$$\frac{dR}{dt}=\frac{2\left(T^{sat}-T_w\right)}{\rho_d L}\frac{\left(1-R_{min}/R\right)}{2/h_{\text{int}}+R/k_d} \tag{3.27}$$

where the minimum radius R_{min} can be calculated by Eq. (3.26). The interfacial heat transfer coefficient h_{int} is written as:

$$h_{\text{int}}=\frac{2\alpha}{\left(2-\alpha\right)}\left(\frac{L^2\rho_v}{T^{sat}}\right)\sqrt{\frac{M_{vw}}{2\pi R_v T^{sat}}} \tag{3.28}$$

where M_{vw} is the vapor molecule weight, ρ_v is the vapor density. For pure steam, the accommodation coefficient usually is taken as unity with an assumption of fully thermal accommodation. Here, for comparison, the considered temperature of moist air is used as the saturation temperature under pure steam condition ($T^{sat} = T_{ma} = 303.15\ K$ in Eq. (3.27)). The droplet growth rate in pure steam by equation (3.27) is also plotted in Figure 3.5.

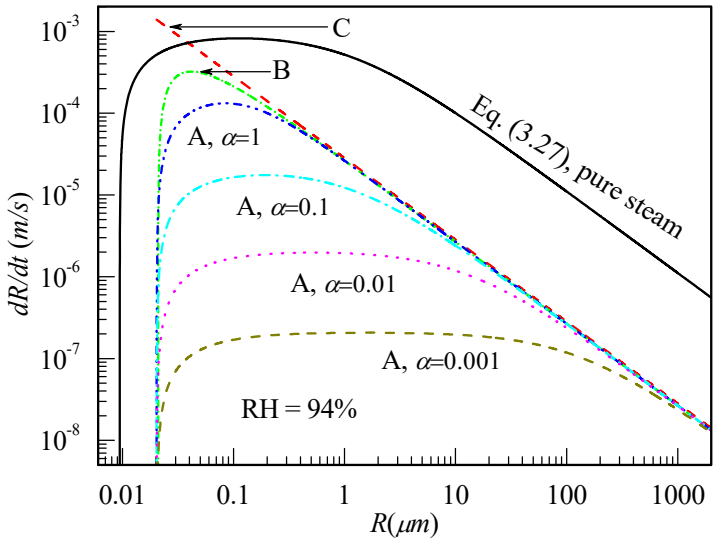

Figure 3.5 The droplet growth rate in full size from different models for single droplet condensation in different conditions (moist air and pure steam).

In Figure 3.5, three letters (A, B and C) denote three model in Table 3.1. In the minimum size (nucleation size), the droplet growth rate is zero due to the metastable state (i.e., the condensation rate is equal to the evaporation rate). Once the droplet size is larger than the minimum radius, the dominant condensation leads to a dramatic increasing of the growth rate. After reaching the maximum, a strong decrease is found due to the increase of the heat conduction resistance by the droplet. Except model C, all models including the growth model in pure steam follow the same tendency described above. Just considering the diffusion resistance, the growth rate by model C shows an inverse proportional relationship with the droplet radius. For model A, the accommodation coefficient adjusting the interfacial resistance has a significant influence on the growth rate. The growth rate varies smoothly over the multi-scale range because of the Knudsen layer. The growth rate predicted by model B is getting close to the result of model A with a unity accommodation coefficient. As a whole,

model B and C without the consideration of the interfacial resistance and the Knudsen layer overestimate the droplet growth rate totally. It is no doubt that model A with a proper α can accurately predict the droplet growth considering NCG.

In addition, as shown in Figure 3.5, the presence of NCG significantly decrease the droplet growth rate under the pure steam. The reduction is significantly depended on the diffusion resistance driven by the vapor concentration difference between the bulk and the droplet surface. For the moist air with RH =94%, the mass fraction of NCG is more than 97%, which urges a strong diffusion resistance responsible for the strong decrease. The main resistance by the liquid conduction resistance under pure steam is switched to the diffusion resistance of vapor in case of NCG. And the minimum radius is increased due to the decreased saturation temperature by the presence of NCG.

3.3.4 Effect of sub-cooling

For those three droplet growth models, the difference from the considered resistance can be seen from Table 3.1 and the predicted growth rate and temperature of droplet surface also is presented in Figure 3.4 and Figure 3.5. Model C as the simplest neglects the droplet conduction resistance which contributes an un-ignorable temperature drop as seen in Figure 3.4. While Model A, on the other hand, considers the heat and mass transfer resistance compressively, imported parameter α which cannot be accurately defined in present brings its weakness. In comparison, Model B is more functional. Therefore, model B is chosen to make modeling dropwise condensation which will be given next soon. In this section, effect of sub-cooling for droplet growth is given based on model B.

Keeping the same conditions of moist air as before, the droplet growth rates at different sizes at different wall temperatures are plotted in Figure 3.6 and correspondingly the temperatures of droplet surface are presented in Figure 3.7. As expected, increasing sub-cooling degree is an active factor for droplet growth because of the increased diffusion driving force. And the increased sub-cooling degree decreases the minimum droplet size, which is consistent with Eq. (3.26). For the growth rate and temperature, the tendency following the droplet size is not changed by the sub-cooling. The temperature drop through the droplet is slightly enlarged with the sub-cooling increasing.

3.4 Conclusions

Aiming to understand the influence of NCG for single droplet growth, a droplet growth model is presented. The present model accurately covers the heat and mass transfer processes across the droplet from the free stream to the droplet base by an elaborate solution of the coupled energy and mass equations. Concerning the multi-scale feature of the droplet size, the transition between the continuum and kinetic limit is incorporated by the Knudsen layer. However, as a crucial parameter the accommodation coefficient is introduced for adjusting the interfacial resistance of the vapor/liquid interface. There is no doubt that the developed model with a proper accommodation coefficient can accurately describe the droplet growth with the

presence of NCG. Due to the complexity of the corresponding physical mechanisms and the limitation of measurement technology, the accommodation coefficient in the presence of NCG component is still a subject of dispute. Therefore, a simplified model is developed neglecting the multi-scale characteristic (also the interfacial resistance). In addition, another model which is mostly adopted in the literatures is presented too. In the third model, there is negligible heat conduction resistance crossing the droplet and only the vapor diffusion is considered. Finally, the temperature of droplet surface and the droplet growth rate from these three models are compared and discussed. And the droplet growth rate out of moist air is also compared with the case of pure steam using the classical thermal resistance model. It is no doubt that the droplet growth rate is significantly slowed down because of the induced diffusion resistance. Furthermore, the diffusion resistance of vapor becomes the main barrier for the case of heat transfer.

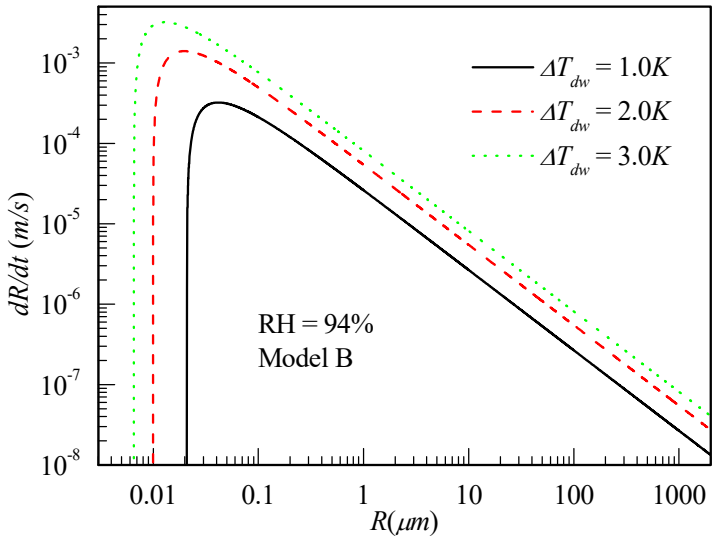

Figure 3.6 The sub-cooling effect for the droplet growth rate.

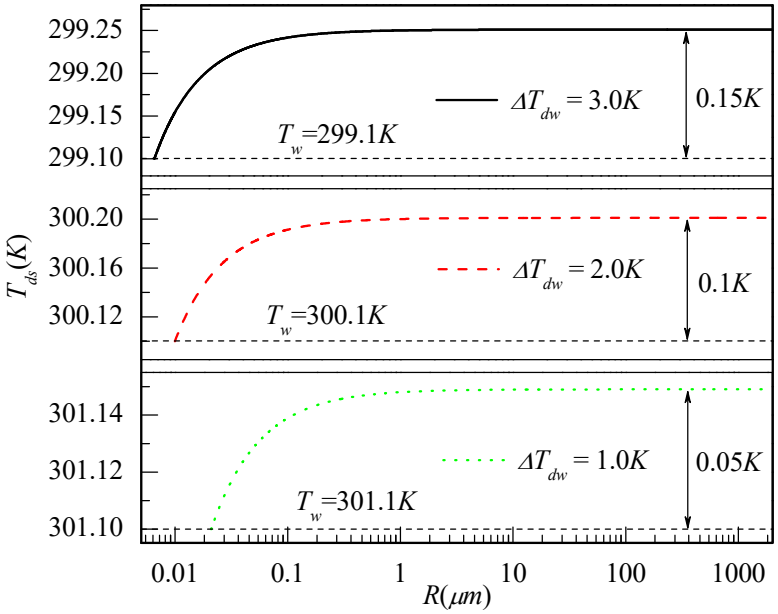

Figure 3.7 The sub-cooling effect on the temperature of droplet surface.

Chapter 4 Interaction Effects between Droplets

With the presence of NCG, the vapor diffusion from ambient to the vapor/liquid interface must be considered during dropwise condensation. Historically, modeling dropwise condensation often makes the assumption that the droplet is growing in an isolated way. However, the blocking effects of surrounding droplets will tremendously influence the spatial distribution of vapor, which finally determines a different condensation rate comparing with that by the isolated-droplet growth model. Consequently, an accurate prediction must include the blocking effects of neighbors (namely the interaction effects between droplets). Some classical semi-analytical methods, including the point sink method (PSM) treating the droplet as single point sink and the method of images (MOI) constructing an infinite series of the point sinks to satisfying certain boundary conditions, are limited to the relatively weak interaction. For capturing the strong interaction during dropwise condensation because of a large number of droplets and the closer inter-droplet spacing, a distributed point sink method (DPSM) as the method of Green's function is proposed here. Considering some simple droplet arrays and a general droplet array, the solutions of DPSM are then compared with those using PSM and MOI. Based on the uniqueness theorem, the exactly satisfied boundary conditions state the ability of DPSM in solving strong interaction.

4.1 Literature review

No matter the presence of NCG or not, the droplet growth during dropwise condensation is a complicated spatiotemporal dynamics equilibrium process which is formed by a series of time- and space-dependent sub-processes (nucleation, growth, coalescence and departure) occurring periodically [4]. Just because of its complexity, the classical methods in developing a theoretical model or correlation are currently making an assumption that the droplets system is considered as a growth of film approximation or isolated growth of droplets. In studying the edge effect on dropwise condensation out of humid air, Medici et al. [42] have addressed these two kinds of growth forms. Transferring the droplets pattern into an equivalent film, a correlation for the condensate heat transfer resistance is proposed by Eimann et al. [31]. For dropwise condensation with pure vapor, the macroscopic mathematical model based on the thermal resistance theory [4, 9] is absolutely dealing with the isolated growth of droplets. Similarly, for dropwise condensation considering NCG, three models presented in chapter 3 are also based on the isolated growth of droplets.

For the diffusion controlled dropwise condensation, some important growth characteristics cannot be captured exactly using the simplification of single droplet growth model. As shown in Figure 4.1, a specific characteristics is the blocking effects of neighboring droplets for the vapor diffusion which can significantly reduce the droplet condensation rate. Leach et al. [41] experimentally found that small drops close to larger drops often grow more slowly because of the local depletion of absorbed vapor. The local depletion of absorbed vapor is exactly attributed to the strong blocking effects by the large neighboring drops. Sokuler et al. [63] experimentally compared the evaporation/condensation rate of an isolated droplet with a similar sized droplet surrounded by droplets. And the finite element method was also used to simulate the evaporation of a droplet array with different inter-droplet distances. The experimental and simulation results state the influence of the interaction effect of droplets for the evaporation rate. The experiments by Ucar et al. [46] have determined that neighboring droplets slow down the condensation rate by 14% to 40% than that of an isolated growing droplet on different substrates. Also, the geometric discontinuities (such as the substrate edges and the corners) can result in a different vapor concentration distribution around the drops which can also affect the droplet growth rate significantly. According to the experiments by Medici et al. [42], in some certain cases, the growth enhancement can dramatically reach 500% for droplets near the edges or corners comparing with the droplets near the substrate center. Actually, that is because that the droplets locating on the geometric discontinuities have more weaker interaction due to more less neighbors comparing with the droplets locating on the substrate center. What deserves to be mentioned is that recently Castillo and Weibel [48, 64] release the prediction of droplet interaction effects during diffusion-driven dropwise condensation using the point sink method. And the predicted droplet growth rates considering the interaction effect using the PSM method present a good agreement with the experimental results. As a whole, the interaction effects between droplets significantly reduces the droplet condensation rate.

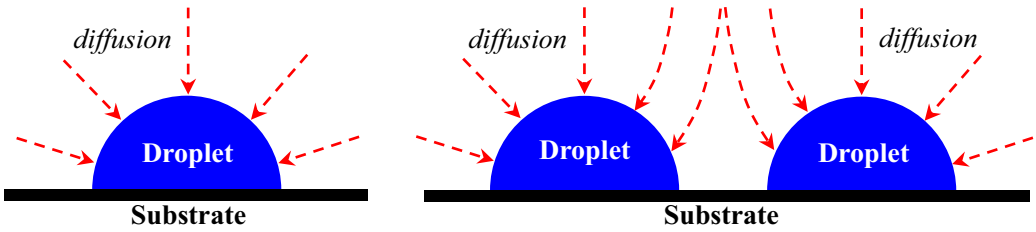

Figure 4.1 Schematic view of the blocking effect of neighbors for the vapor diffusion.

From above discussion, it can be concluded that the isolated droplet growth model will over-predict the growth rate for dropwise condensation. In chapter 3, three different growth models of a single droplet have been presented for dropwise condensation driven by vapor diffusion in humid air. Regrettably, the interaction effects between droplets are not considered into those individual droplet models. Therefore, considering the interaction effects of droplets, the correction factor for the condensation rate is required for accurately predicting dropwise condensation behavior.

For a certain spatial distribution of droplets at a given condensation instant, by solving the diffusion equation the numerical simulation can be applied to determine the condensation rate of each droplet and the vapor concentration field. Nevertheless, numerical simulation for dropwise condensation is still a great challenge due to a large number of droplets in a wide size range. It is no doubt that a simple analytical approach will be welcome. Significantly a semi-analytical method the point sink method (PSM) developed by Annamalai et al. [65-66] for the drop interaction effects during gasification and combustion [67] is applied into dropwise condensation community by Castillo and Weibel [48, 64]. Actually, as a analytical method, the point sink/source method treats each suspended or sessile droplet as a point mass source/sink (PSM), the term "source" and "sink" is corresponding to gasification/combustion and condensation respectively. It can be applied to solve the evaporation/condensation rate of each droplet and the vapor concentration field by superimposing Maxwell's solution of all sources/sinks. In the community of evaporation and combustion, another classical method for dealing with the interaction problems is the method of images (MOI) which is developed for the evaporation of cloud particles by Labowsky [68-69]. An infinite series of point sources/sinks is constructed in MOI for satisfying the favorable boundary conditions. Actually, MOI is a classical tool for solving the boundary-value problems in electrostatics [70]. Out of question, these methods for the droplet interaction in evaporation/combustion are also suitable for multiple condensation droplets, and the difference is just the mass source or the mass sink (hereafter we don't distinguish the terms "sink" and "source", we just consider "sink" for condensation in present work).

During dropwise condensation, a large number of droplets generated over the condensation substrate is accompanied by a strong interaction effect where the droplets approach each other closely. Due to some limitations, these classical semi-analytical methods (MOI and PSM) suffer the problems of the solving accuracy and the computation divergence in handling the strong interaction. As the process in solving these problems (the droplet number considered and strong interaction effect), a creative distributed point sink method (DPSM) is developed. Firstly, the point sinks are averagely distributed on the surface of an imaginary concentric sphere for each spherical droplet and mapped to the droplet surface. After that a highly-efficient matrix operation for determining the strengths of the point sinks is formulated using the discrete target points on the droplet surface for satisfying the boundary conditions. The comparison between these three methods for different droplet arrays states that the proposed DPSM method can accurately capture the strong interaction effect even when the droplets are touching each other. Using less point sinks makes it possible to consider more droplets. Under retaining good accuracy, this new semi-analytical method achieves the accurate predictions for the droplet growth rate and the vapor concentration field, while keeping simplicity compared to the complicated numerical simulation.

4.2 The problem description

During dropwise condensation with the presence of NCG, a large number of droplets having a surface temperature below the dew point temperature of the surrounding mixture are

distributed on the cold substrate, as illustrated in Figure 4.2. Condensation of water vapor over the droplet surface is driven by the concentration difference between the ambient and the droplet surface. For simplification, we assume that all droplets have the same vapor concentration on their surface (c_{ds}, namely the same surface temperature). The normalized vapor concentration, C, is defined as:

$$C = \left(c - c_{ds}\right) / \left(c_{\infty} - c_{ds}\right) \tag{4.1}$$

where c_{∞} is the vapor concentration in the far field, and c represents the vapor concentration at any points of the surrounding. Hereafter, the vapor concentration distribution is normalized. Hence, the dimensionless vapor concentration field outside the droplets obeys the diffusion equation [48]:

$$D\nabla^2 C\left(\boldsymbol{r},t\right) = \frac{\partial C\left(\boldsymbol{r},t\right)}{\partial t} \tag{4.2}$$

with the location vector $\boldsymbol{r}$ and the vapor diffusion coefficient in mixture D. Based on the quasi-stationary assumption, namely much smaller growth rate of the droplet surface comparing with the adjusting rate of the vapor concentration field, the diffusion equation can be reduced to the Laplace equation following [48, 68]:

$$\nabla^2 C\left(\boldsymbol{r}\right) = 0 \tag{4.3}$$

The boundary conditions for solving the Laplace equation satisfy [68]:

B. C. #1: $C_{ds} = 0$ on all droplet surfaces

B. C. #2: $C_{\infty} = 1$ at the far field

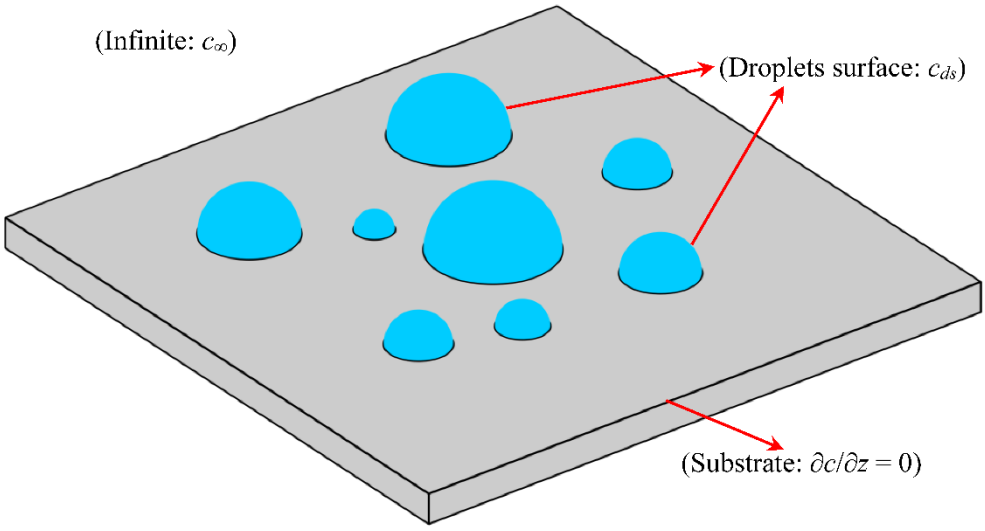

Figure 4.2 Illustration of dropwise condensation over a cold substrate.

Hence, the droplets system in dropwise condensation process is mathematically described by the Laplace equation accompanied by the corresponding boundary conditions. Another point is the zero mass flux normal to the cold wall ($\partial c/\partial z = 0$) as shown in Figure 4.2. For developing a semi-analytical method, this boundary condition is not considered into. In addition, the spherical cap-shaped droplet over a substrate is just a part of corresponding spherical suspended droplet with the contact angle 90°. Thus, the prediction of the vapor

concentration field and the condensation rate of each individual droplet is determined by condensation of the corresponding spherical suspended droplet. The following analytical models have the same processing method for the spherical cap-shaped droplet and the spherical suspended droplet.

For definition of the influence of the interaction effect on the condensation rate, a correction factor is introduced by:

$$\eta = m_{sys} / m_{iso} \tag{4.4}$$

where m_{sys} and m_{iso} denote the condensation rate within the droplet system and the isolated growth, respectively.

Following the above assumption, all of the droplet have the same surface temperature. That means the thermal conduction through the droplet is neglected. In order to keeping consistency in this chapter, model C presented in third chapter can be used to droplet condensation rate in an isolated form:

$$m_{iso} = 2\pi R\left(1-\cos\theta\right) D(C_\infty - C_{ds}) = 2\pi R\left(1-\cos\theta\right) D \tag{4.5}$$

with the droplet radius R.

4.3 Method of solution

4.3.1 The point sink method

Historically, the PSM is a powerful method in studying evaporation of multiple droplets [65-66]. And it has been applied to dropwise condensation community successfully [48, 64]. In PSM, each droplet is concentrated as a mass point sink located at its center [48, 64-66] as presented in Figure 4.3. Thanks to the linearity of the Laplace equation, the vapor concentration field surrounding the droplet array can be solved by superimposing the solution of the Laplace equation for each point sink (i.e. droplet). Using PSM, prediction of droplet interactions during diffusion-driven dropwise condensation has been launched in [48, 64]. Here, the PSM is repeatedly implemented for the droplets interaction during condensation. Next PSM is briefly introduced according previous works [48, 64-66].

For an isolated droplet as a point sink located at its center $\boldsymbol{r} = \boldsymbol{r}_i$, including the mass sink term the governing Laplace equation becomes the Poisson equation:

$$\nabla^2 C(\boldsymbol{r}) = \sigma\delta(\boldsymbol{r} - \boldsymbol{r}_i) \tag{4.6}$$

where $\delta(\boldsymbol{r}\text{-}\boldsymbol{r}_i)$ represents the Dirac-delta function and σ is the intensity of the point sink. For arbitrary point $\boldsymbol{r}$, the normalized vapor concentration induced by the point sink can be solved by integrating Eq. (4.6) [48, 66]:

$$C_\infty - C(\boldsymbol{r}) = \sigma / |\boldsymbol{r} - \boldsymbol{r}_i| \tag{4.7}$$

Concerning the point $\boldsymbol{r}$ at the droplet surface, the sink intensity σ can be defined as:

$$\sigma = m_{iso} / (2\pi D) = R(C_\infty - C_{ds}) \tag{4.8}$$

where R is the droplet radius. It is obvious that the vapor concentration increases at increasing

distance from the point sink. Actually, Eqs. (4.7) and (4.8) give the solution of the vapor concentration around an isolated condensation droplet using PSM.

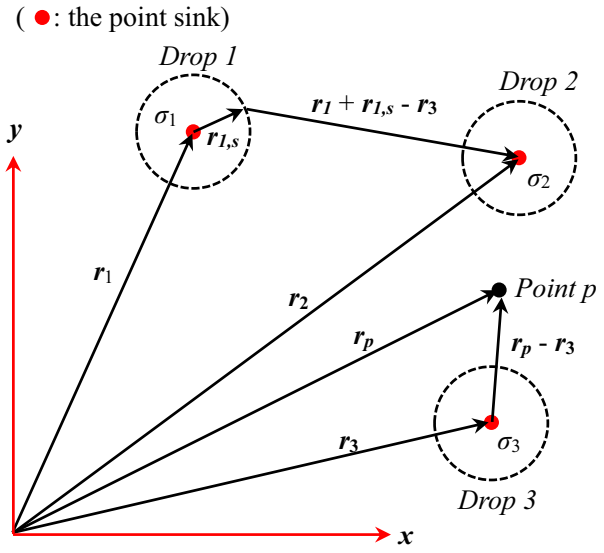

Figure 4.3 Schematic view of the point sink method for three-droplet array.

Turning to a system having N condensation droplets located at $\boldsymbol{r} = \boldsymbol{r}_i$ having the radius R_i, each droplet having the unknown condensation rate $m_{sys,i}$ is treated as a point sink at its center with the strength $\sigma_i = m_{sys,i}/(2\pi D)$ as illustrated in Figure 4.3 for a three-droplets system. For indicating the vapor concentration at location $\boldsymbol{r}$ due to the point sink σ_i, a contribution function is defined as:

$$fc(\boldsymbol{r},\boldsymbol{r}_i,\sigma_i)=\frac{m_{sys,i}}{2\pi D}\frac{1}{|\boldsymbol{r}-\boldsymbol{r}_i|} \tag{4.9}$$

with $|\boldsymbol{r}\text{-}\boldsymbol{r}_i|$ is the distance from the point sink location $\boldsymbol{r}_i$. Finally, the vapor concentration at point $\boldsymbol{r}$ can be obtained by superimposing the contributed concentration of all point sinks:

$$C_\infty - C(\boldsymbol{r})=\sum_{i=1}^{N} fc(\boldsymbol{r},\boldsymbol{r}_i,\sigma_i)=\sum_{i=1}^{N}\frac{m_{sys,i}}{2\pi D}\frac{1}{|\boldsymbol{r}-\boldsymbol{r}_i|} \tag{4.10}$$

Evaluation of the vapor concentration on the surface of the *k-th* droplet, Eq. (4.10) results in:

$$C_\infty - C(\boldsymbol{r}_k+\boldsymbol{r}_{k,s})=\sum_{i=1}^{N}\frac{m_{sys,i}}{2\pi D}\frac{1}{|\boldsymbol{r}_k+\boldsymbol{r}_{k,s}-\boldsymbol{r}_i|} \tag{4.11}$$

where $\boldsymbol{r}_{k,s}$ is the position vector of the droplet surface from its center. Remarkably, PSM assumes the droplet size is much less than the inter-droplet distance:

$$R_k=|\boldsymbol{r}_{k,s}| \ll |\boldsymbol{r}_k-\boldsymbol{r}_i| \tag{4.12}$$

Due to this assumption, PSM derives only an approximate result for strong interaction when the droplets approach closely each other. Additionally, assuming a same vapor concentration on all droplet surfaces, the evaluation equation (4.11) can be rewritten as:

$$1=C_\infty - C_{ds}=\frac{m_{sys,k}}{2\pi R_k D}+\sum_{i=1,i\neq k}^{N}\frac{m_{sys,i}}{2\pi D}\frac{1}{|\boldsymbol{r}_k-\boldsymbol{r}_i|} \tag{4.13}$$

Substituting the definition of the correction factor by Eq. (4.4) and the droplet condensation

rate in the isolated form by Eq. (4.5), the above equation becomes:

$$\eta_k + \sum_{i=1,i\neq k}^{N} \eta_i \frac{R_i}{|\boldsymbol{r}_k - \boldsymbol{r}_i|} = 1 \tag{4.14}$$

Thus, the correction factors for all droplets can be determined by solving N linear equations in Eq. (4.14). After getting the correction factors of all droplets, the normalized vapor concentration distribution using Eq. (4.10) can be expressed as:

$$C(\boldsymbol{r}) = C_\infty - \sum_{i=1}^{N} \frac{m_{sys,i}}{2\pi D} \frac{1}{|\boldsymbol{r} - \boldsymbol{r}_i|} = 1 - \sum_{i=1}^{N} \frac{\eta_i R_i}{|\boldsymbol{r} - \boldsymbol{r}_i|} \tag{4.15}$$

For the solution of the concentration field and the droplet condensation rate within a multi-droplet condensation system, PSM provides a simple and compact analytical tool. However, the simplification in Eq. (4.12) also brings its weakness when handling the strong interaction effect between droplets. About this point, a detailed discussion will be given in next section.

4.3.2 The method of images

In the electrostatics, the method of images (MOI) is a classical method to determine the electric field without solving the differential equation [70-71]. In the exterior region, the image charges are placed to satisfy certain boundary conditions. It is based on the uniqueness theorem which proves that certain boundary conditions determine a unique solution in mathematics. The uniqueness theorem is often expressed by saying that a physical problem can be solved by different methods as long as certain boundary conditions are satisfied. This method has been applied treating the interaction effect on vaporization and burning of droplet array [67-69]. As such, the solution is also constructed by superimposing the fields contributed by all point sources. Here, MOI is extended to studying the interaction effect in condensation of a droplet array. Firstly, a brief view about MOI is given.

Similar to the mathematical problem in Section 4.2, MOI should obey the given boundary conditions that the normalized concentration is zero at all droplet surfaces (B. C. #1) and is unity far from the system (B. C. #2). As seen from Eq. (4.7) suitable for all point sinks, the field due to one point sink is the reciprocal function of the distance. The concentration on the surface of each droplet with the radius R_i is desired to be zero by placing a point sink with the strength $\sigma_i = R_i$ at its center, the *N 0-th* order point sinks are generated for N droplets. However, the born *0-th* order sinks will also raise the concentration at the surface of other droplets and make it deviating the desired zero concentration. In order to negate the effect of *N-1 0-th* order point sinks from the *N-1* neighboring droplets, the *N-1 1-st* order point sinks are suitably placed inside the droplet. The solution for the strengths and positions of these *1*-st order point sinks, as seen in the references [68-71] and Figure 4.4(a), can be determined by:

$$\sigma_{i,j} = -\sigma_i R_j / l \tag{4.16}$$

$$b = R_j^2 / l \tag{4.17}$$

The *2-nd* order point sinks are also needed to cancel the effect from the *1*-st order point

sinks. So forth, this generation process of the point sink is repeated up to an infinite series for making sure the desired boundary conditions on all droplet surface. The strengths and locations of the *0-th* order sinks are decided by the sizes and positions of the *N* droplets. After the *0-th* order, the strengths and positions of the point sinks in any order can be successively determined by the point sinks of the last order using Eqs. (4.16) and (4.17). For the case of three-droplet array, the point sinks of the first three orders are illustrated in Figure 4.4(b).

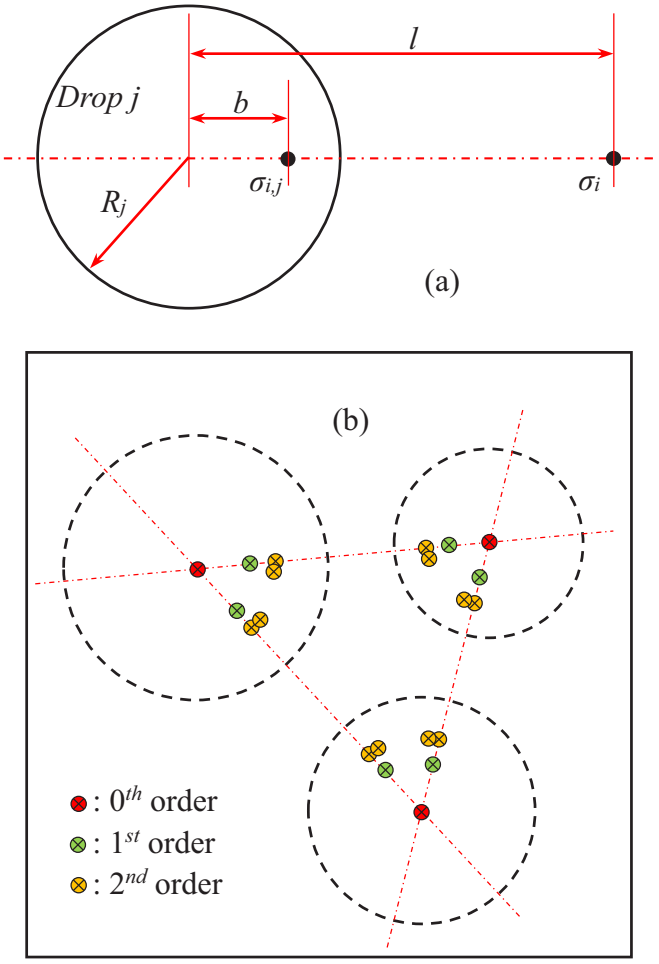

Figure 4.4 (a) Location and strength of the new point sink because of the point sink in last order; (b) Demonstration of the point sinks of the first three order for three droplets.

Finally, based on Eq. (4.7) for one point sink, the normalized vapor concentration at an arbitrary point $\boldsymbol{r}$ can be solved by superimposing the concentration contributed by all generated point sinks:

$$C(\boldsymbol{r}) = 1 - \sum_{i=1}^{N} \sum_{j=0}^{O} \sum_{k=1}^{(N-1)^j} fc(\boldsymbol{r}, \boldsymbol{r}_{i,j,k}, \sigma_{i,j,k}) \tag{4.18}$$

$$fc(\boldsymbol{r}, \boldsymbol{r}_{i,j,k}, \sigma_{i,j,k}) = \sigma_{i,j,k} \Big/ \left| \boldsymbol{r} - \boldsymbol{r}_{i,j,k} \right| \tag{4.19}$$

where i, j and k are respectively the droplet number, the order number and the sink number, $\sigma_{i,j,k}$ and $\boldsymbol{r}_{i,j,k}$ denote the intensity and position vector for the *k-th* sink in the *j-th* order inside the *i-th* droplet. The contribution function *fc* means the concentration contributed by single point sink ($\sigma_{i,j,k}$, $\boldsymbol{r}_{i,j,k}$) for any point $\boldsymbol{r}$. And the total number of the point sinks, N_t, is related to the

droplet number N and the considered order number O by:

$$N_t = N\sum_{j=0}^{O}(N-1)^j \tag{4.20}$$

According to the Gauss's flux theorem, the condensation rate of droplet $m_{sys,p}$ can be defined by the integration of the gradient of the dimensionless concentration field over the closed droplet surface S_p in the spherical coordinate system:

$$m_{sys,p} = -D\oint_{S_p}\nabla C\big|_{R_p}\, dS_p = D\sum_{i=1}^{N}\sum_{j=0}^{O}\sum_{k=1}^{(N-1)^j} fi(R_p,\sigma_{i,j,k},\boldsymbol{r}_{i,j,k}) \tag{4.21}$$

$$fi(R_p,\sigma_{i,j,k},\boldsymbol{r}_{i,j,k}) = \sigma_{i,j,k}\int_0^{2\pi}\int_0^{\theta}\left(\frac{\partial fd\left(r,\xi,\varphi\right)}{\partial r}\right)_{r=R_p} R_p^2\sin\xi d\xi d\varphi \tag{4.22}$$

where p is the droplet number, θ means the droplet contact angle, ξ and φ are the polar angle and the azimuthal angle in the spherical coordinate system respectively. The function fd (r, ξ, φ) is given by:

$$fd(r,\xi,\varphi) = \left(r^2 + r_{i,j,k}^2 - 2rr_{i,j,k}\left(\sin(\xi)\sin(\xi_{i,j,k})\cos(\varphi-\varphi_{i,j,k}) + \cos(\theta)\cos(\theta_{i,j,k})\right)\right)^{-0.5} \tag{4.23}$$

Thus, the function fi represents the contribution of each point sink ($\sigma_{i,\,j,\,k}$, $\boldsymbol{r}_{i,\,j,\,k}$) for the condensation rate of droplet p. The function fd means the reciprocal of the distance between the point (r, ξ, φ) and the point sink ($r_{i,j,k}$, $\xi_{i,j,k}$, $\varphi_{i,j,k}$).

Upon careful observation, the centered point sinks in PSM are just the point sinks in the *0-th* order of MOI [72]. In MOI, not only the centered point sinks but also the off-center point sinks are required in order to satisfy rigorously the boundary conditions; yet, the result will be gradually converging the exact solution. Theoretically, MOI using an infinite number of orders will provide the exact solution for the concentration field and the condensation rate. However, the considered droplet number is limited by the required number of the point sink. For example, the first four orders for an array having ten droplets contain 8200 point sinks. On the other hand, if the interaction effect is strong, more orders should be considered for the solution accuracy. Thus, the original MOI is only working for a relatively small number of droplets and a weak interaction effect. For the application, some improvements have been carried out [68, 71]. In handling the droplet evaporation, Labowsky [68] considered a mean calculated concentration using the first three orders. Considering the electric potential due to a system of conducting spheres, Metzger et al. [71] developed some methods to optimize the location and strength of the image charges. According to our tests, these truncated methods for the infinite series still suffer the limitation in the droplet number and the interaction strength.

During the testing process, a really interesting phenomena is found. The distribution of the point sinks has a fractal characteristic which urges a proposed closed form for the infinite series in Eqs. (4.18) and (4.21) based on the fractal theory. By the case of a five-droplet array having the same size, the point sinks in the first four orders are plotted in Figure 4.5. The

point sink distribution inside each droplet presents a typical fractal characteristic. In the river networks, water is collected from all streams in different orders. As a self-similar structure, the scaling properties of river networks are summarized in some well-known laws, such as the Horton's law of stream lengths and numbers in two neighboring orders [73].

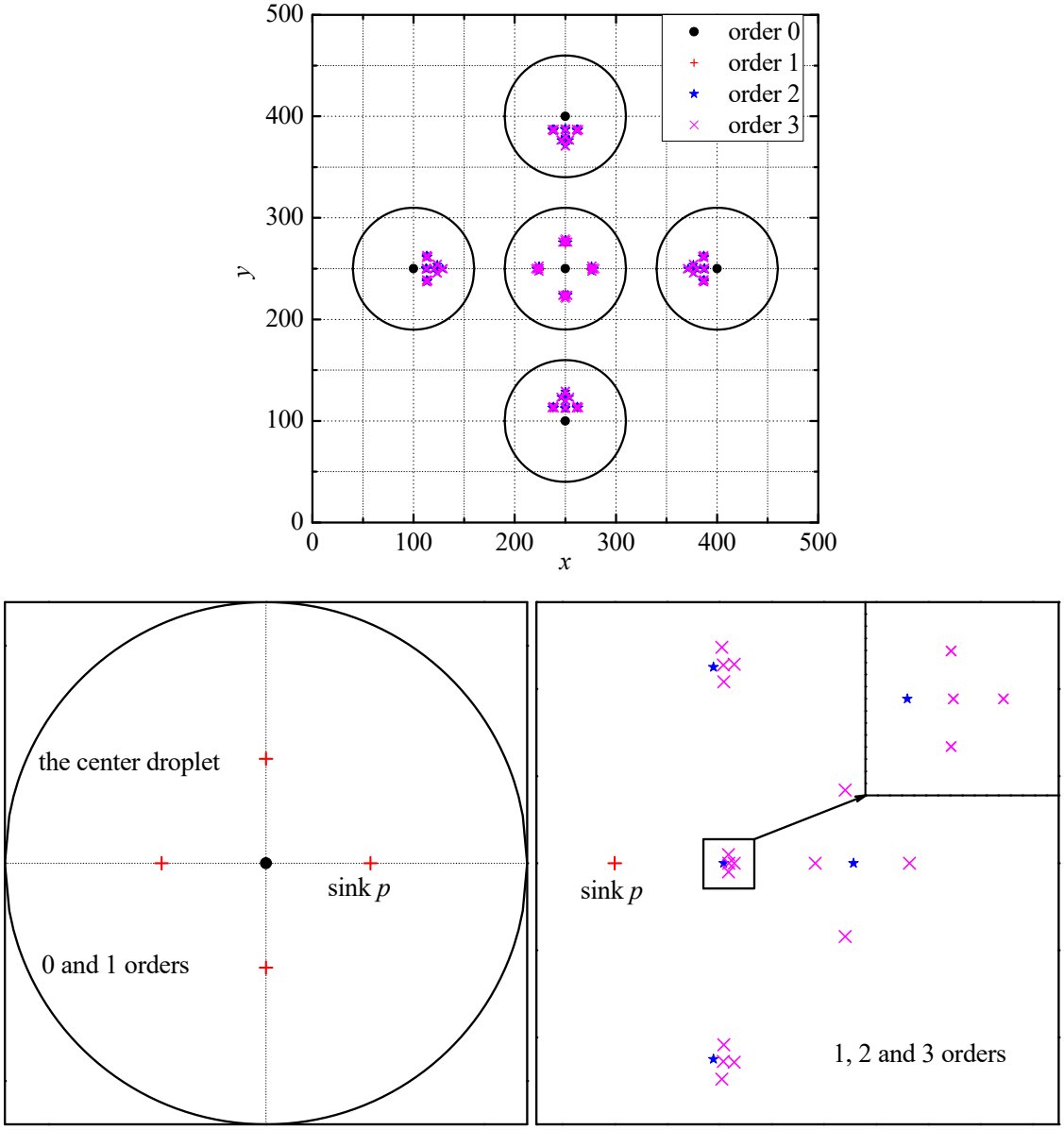

Figure 4.5 Illustration of the fractal characteristic for the distribution of the point sinks.

With this idea in mind, the concentration on each point and the condensation rate of each droplet, as stated by Eqs. (4.18) and (4.21), are the collection of the contribution of all point sinks. Firstly, for any point inside the solving region, the contributed concentration because of each point sink in the center droplet is solved using Eq. (4.19) and averaged in the same order. Considering four different points, Figure 4.6(a) plots the averaged absolute contribution value against the order and a clear power law is presented. If fc_i^* denotes the mean contributed concentration of single point sink in the order i for a point, the ratio between two neighboring orders fc_i^*/fc_{i-1}^* is defined by:

$$fc_i^* / fc_{i-1}^* = Ra_i \tag{4.24}$$

Similarly, the ratio for these point is plotted in Figure 4.6(b). Apparently, the ratio will converge to a negative constant value after the first four orders.

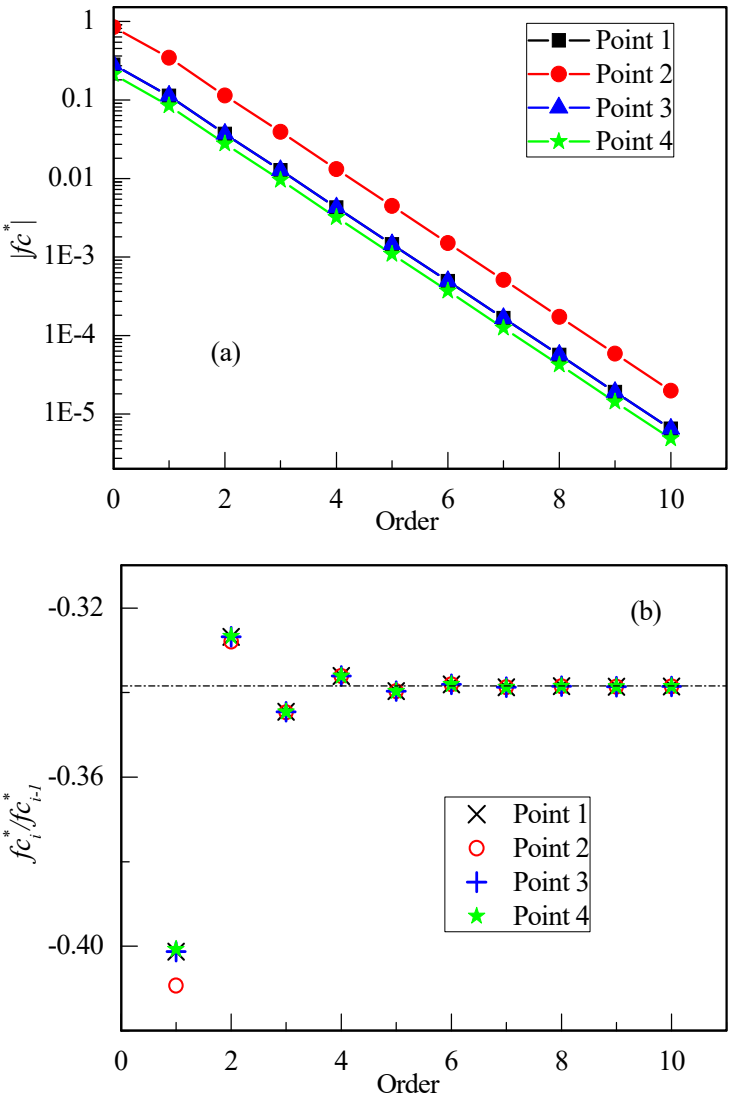

Figure 4.6 (a) the averaged absolute contributed concentration vs order in different points; (b) the ratio of the averaged contributed concentration in two neighboring orders.

Neglecting the ratio fluctuation in the first four orders, the mean contributed concentration of one point pink in two neighboring orders can be described by a geometric progression with a negative common ratio *Ra*. And all point sinks in different droplets are all following this relationship after testing. On the other hand, also, Eq. (4.20) the point sink number in two neighboring orders is a geometric progression with the common ratio (*N*-1). Finally, a closed form of the infinite series Eq. (4.18) can be constructed as following:

$$C(\boldsymbol{r}) = 1 - \sum_{i=1}^{N} \sum_{j=0}^{\infty} fc_{i,0}^{*} \left((N-1)Ra\right)^{j} = 1 - \sum_{i=1}^{N} fc_{i,0}^{*} \frac{1-\left((N-1)Ra\right)^{\infty}}{1-(N-1)Ra} \tag{4.25}$$

where *j* denotes the order number, $fc_{i,0}^{*}$ is the mean concentration contributed by one point sink in the *0-th* order of droplet *i*. The results also state the contributed condensation rate of single point sink by Eq. (4.22) for each droplet follows the same relationship too. The same as above, the closed form for Eq. (4.21) is written:

$$m_{sys,p} = D\sum_{i=1}^{N} fi_{i,0}^{*}\,\frac{1-\left((N-1)Ra\right)^{\infty}}{1-(N-1)Ra} \tag{4.26}$$

with $fi_{i,0}^{*}$ denotes the mean contribution of one point sink of droplet i for the condensation rate of droplet p. Eqs. (4.25) and (4.26) construct a closed form MOI.

Essentially, the geometric progressions for the vapor concentration and droplet condensation rate contributed by single point sink are attributed to the definition equations (4.16) and (4.17) for the sink strength and position. This means also a converging process of the infinite series for touching the desired boundary conditions. Mathematically, Eqs. (4.25) and (4.26) will be convergent if the common ratio (N-1)Ra is greater than minus unity, otherwise divergent. Changing the inter-droplet distance d, the variation of the common ratio (N-1)Ra is plotted in Figure 4.7. With the enhancement of the interaction effect, the absolute common ratio is increased slowly. For the strong interaction effect, the common ratio smaller than minus unity is corresponding to the divergent solution which is also indicated by the tests. That means the closed from MOI cannot work meeting a strong interaction even if it can provide an exact solution in handling the weak interactions.

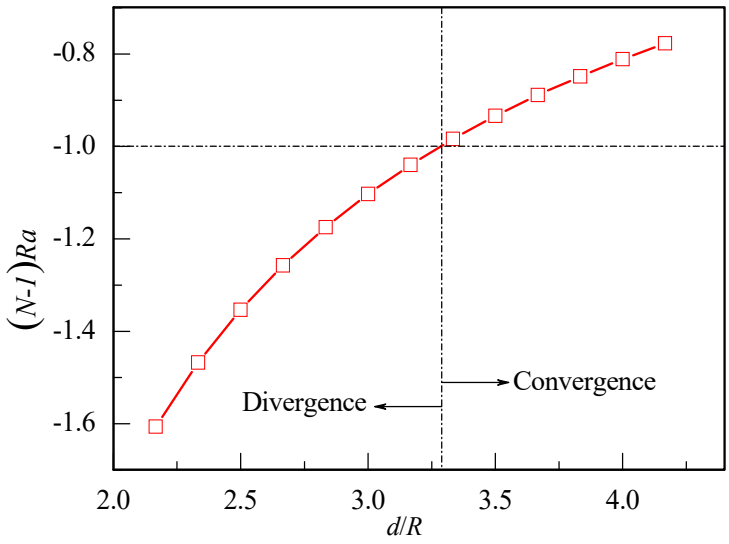

Figure 4.7 Variation of the common ratio (N-1)Ra with the distance ratio d/R.

4.3.3 The distributed point sink method

In general, dropwise condensation meets a strong interaction effect due to the closely-spaced droplets and a large number of droplets. As described above, two classical methods (PSM and MOI) are all limited in dealing with a weak interaction of droplets. In solving the boundary problems that include the magnetic, ultrasonic and electrostatic field, the distributed point source method has historically been developed into a powerful and invaluable analytical tool [74-75]. Without the numerical discretization of the boundary and the interesting domain, the transducer/sensor surface or interface are replaced by the distributed point source for modeling the field. Strengths and positions of the point sources are adjusted such that the total field and the boundary conditions can be satisfied exactly.

With this idea in mind, based on the uniqueness theorem, we propose a distributed point sink method (DPSM) for solving the interaction effect of a multi-droplet condensation system. It should be mentioned here that this method is based on the fact that the Laplace equation is a linear partial differential equation. As such, the superposition method in above two methods is also suitable in this method. For a multi-droplet condensation system, each droplet can be treated as a "source" of the total field denoted as "sensor". The boundary conditions that all droplet surfaces have the same concentration can be called as "target". Here, "sensor" is replaced by the distributed point sinks. Some target points are considered on the droplet surface. The basic principle for the DPSM is illustrated in Figure 4.8. Firstly, an imaginary sphere is generated sharing the same center with the droplet, as shown in the left of Figure 4.8; then the M point sinks are averagely arranged along the longitude and latitude lines of the imaginary sphere, see the right of Figure 4.8. The positions of the point sink are decided by the radius of the imaginary sphere R_{is}. This point sink configuration is considered due to the spherical shape of the droplet.

Considering M point sinks for one droplet, there will be $N*M$ point sinks for N droplets system. For defining the strengths of $N*M$ point sinks, one need $N*M$ number of equations. Thus, the same number of target points on the droplet surface which is mapped from the point sinks is required to construct a solving matrix. The final concentration on each target point is to be solved by superimposing the concentration produced by each point sinks, as given by Eqs. (19) and (20). For $N*M$ target point, this can be summarized by the following matrix equation:

$$\boldsymbol{A}\bullet\begin{pmatrix}\sigma_{1,1}\\ \vdots\\ \sigma_{M,1}\\ \vdots\\ \sigma_{M*(N-1)+1,N}\\ \vdots\\ \sigma_{M*N,N}\end{pmatrix}=\begin{pmatrix}1-C_{ds}^{1,1}\\ \vdots\\ 1-C_{ds}^{M,1}\\ \vdots\\ 1-C_{ds}^{M*(N-1)+1,N}\\ \vdots\\ 1-C_{ds}^{M*N,N}\end{pmatrix} \tag{4.27}$$

$$\boldsymbol{A}=\begin{pmatrix}A_{1,1}^{1,1} & \cdots & A_{M,1}^{1,1} & \cdots & A_{M*(N-1)+1,N}^{1,1} & \cdots & A_{M*N,N}^{1,1}\\ \vdots & \vdots & \vdots & \vdots & \vdots & \vdots & \vdots\\ A_{1,1}^{M,1} & \cdots & A_{M,1}^{M,1} & \cdots & A_{M*(N-1)+1,N}^{M,1} & \cdots & A_{M*N,N}^{M,1}\\ \vdots & \vdots & \vdots & \vdots & \vdots & \vdots & \vdots\\ A_{1,1}^{M*(N-1)+1,1} & \cdots & A_{M,1}^{M*(N-1)+1,N} & \cdots & A_{M*(N-1)+1,N}^{M*(N-1)+1,N} & \cdots & A_{M*N,N}^{M*(N-1)+1,N}\\ \vdots & \vdots & \vdots & \vdots & \vdots & \vdots & \vdots\\ A_{1,1}^{M*N,N} & \cdots & A_{M,1}^{M*N,N} & \cdots & A_{M*(N-1)+1,N}^{M*N,N} & \cdots & A_{M*N,N}^{M*N,N}\end{pmatrix} \tag{4.28}$$

where the right matrix is a unit column vector having the components denoted the boundary conditions (the normalized concentration of target point on the droplet surface); in the superscript, the first term represents the target point on the surface of the droplet indexed by the second term. For the left second term, the component $\sigma_{i,j}$ is the strength of the i point sink on the j imaginary sphere. The coefficient matrix $\boldsymbol{A}$ is a square matrix of order $N*M$. For the

component in matrix $\boldsymbol{A}$, the first and second terms in the superscript mean the mapped point and the droplet hold it respectively; the point sink and its imaginary sphere are respectively indexed by the first and second term in the subscript. And the component of the matrix $\boldsymbol{A}$ can be defined as the reciprocal of the distance between the mapped point (i, j) and the point sink (k, l):

$$A_{k,l}^{i,j} = 1 \Big/ \left| \boldsymbol{r}_{i,j} - \boldsymbol{r}_{k,l} \right| \tag{4.29}$$

After choosing radius of the imaginary sphere, the positions of the point sinks and target points are known. With the known concentration at all target points, the strengths of all point sinks can be solved by:

$$\begin{pmatrix} \sigma_{1,1} \\ \vdots \\ \sigma_{M,1} \\ \vdots \\ \sigma_{M*(N-1)+1,N} \\ \vdots \\ \sigma_{M*N,N} \end{pmatrix} = \boldsymbol{A}^{-1} \bullet \begin{pmatrix} 1 - C_{ds}^{1,1} \\ \vdots \\ 1 - C_{ds}^{M,1} \\ \vdots \\ 1 - C_{ds}^{M*(N-1)+1,N} \\ \vdots \\ 1 - C_{ds}^{M*N,N} \end{pmatrix} \tag{4.30}$$

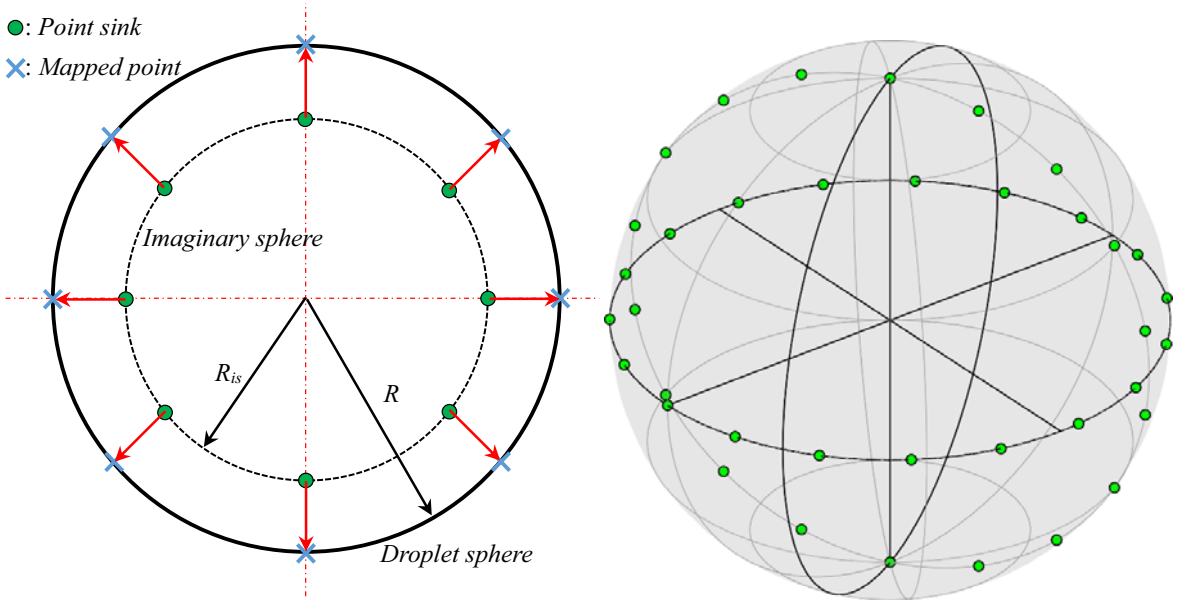

Figure 4.8 Illustration of the distributed point sink method (DPSM).

Once the strengths and positions of all point sinks are known, the concentration at any point $\boldsymbol{r}$ in the interesting domain can be calculated by the superimposing method:

$$C(\boldsymbol{r}) = 1 - \sum_{i=1}^{N} \sum_{j=1}^{M} fc(\boldsymbol{r}, \boldsymbol{r}_{i,j}, \sigma_{i,j}) \tag{4.31}$$

$$fc(\boldsymbol{r}, \boldsymbol{r}_{i,j}, \sigma_{i,j}) = \sigma_{i,j} \Big/ \left| \boldsymbol{r} - \boldsymbol{r}_{i,j} \right| \tag{4.32}$$

Similarly, the condensation rate on the droplet p can be solved by:

$$m_{sys,p} = -D \oint_{S_p} \nabla C \big|_{R_p} \, dS_p = D \sum_{i=1}^{N} \sum_{j=1}^{M} fi(R_p, \sigma_{i,j}, \boldsymbol{r}_{i,j}) \tag{4.33}$$

$$fi(R_p,\sigma_{i,j},\boldsymbol{r}_{i,j})=\sigma_{i,j}\int_0^{2\pi}\int_0^{\theta}\left(\frac{\partial fd\left(r,\xi,\varphi\right)}{\partial r}\right)_{r=R_p}R_p^2\sin\xi d\xi d\varphi \tag{4.34}$$

$$fd(r,\xi,\varphi)=\left(r^2+r_{i,j}^2-2rr_{i,j}\left(\sin(\xi)\sin(\xi_{i,j})\cos(\varphi-\varphi_{i,j})+\cos(\theta)\cos(\theta_{i,j})\right)\right)^{-0.5} \tag{4.35}$$

And these equations are expressed in the spherical coordinate system.

Two parameters including the radius of the imaginary sphere R_{is} and the number of the point sinks for a single droplet M can be adjusted according to the interaction strength for satisfying the boundary conditions. After testing, the radius of the imaginary sphere is chosen as R_{is} = 0.5**R* here. And a few hundred of the point sinks for one droplet is necessary for a strong interaction. In general, the main part in solution is the linear system of equations in Eq. (4.27) and the surface integral from Eq. (4.33). Subsequently, meeting a larger number of droplets the DPSM suffers the solving issue for a huge and dense linear systems and a huge computing number of the surface integral. For example, we consider N = 2000 droplets and M = 200 point sinks for one droplets. Then the dimension of the matrix equation in Eq. (4.27) and the time of the surface integral in Eq. (4.33) are up to N*M = 400,000 and N*M*N = 8,000,000, respectively. The solution meets the problems of the computer memory and the computing time. For the huge and dense linear system, an iterative method the generalized product-type biconjugate gradient method (GPBiCG) [76-78] is utilized and described in APPENDIX C. On the other hand, a classical TwoD algorithm based on the tiled method by Shampine [79] is considered for numerically evaluating the surface integral. Aiming to handle a larger number of considered droplets, a Fortran 90 code implementing the GPBiCG and TwoD algorithms which is paralleled using open MPI for improving the computation efficiency is developed to make the computation possible in a distributed supercomputers.

The discrete target points on the droplet surface are used and their concentration value is known according to the boundary conditions, the calculation of the strengths of all point sinks can be formulated as a matrix operation. After that, the concentration field in the region surrounding the droplet and the condensation rate of each droplet can be defined by the superimposing method. As a result of the strengths of all point sinks solved using the boundary condition, the given boundary condition can be satisfied automatically and exactly. Consequently, according to the uniqueness theorem, the solved concentration field and the condensation rate can be guaranteed in accuracy in DPSM.

In conclusion, these three methods are essentially in commonness: they all belong to the method of Green's function based on the uniqueness theorem. Physically, a mathematic-physical equation means a relationship between a special "field" and the "source" producing it, such as the equation of heat conduction representing the relationship between the temperature field and the heat flow rate (source). Under certain boundary conditions, the "field" can be determined by superimposing the "field" of many "sources" resolved from the initial "source". That is the method of Green's function for solving the mathematic-physical equation. Resolving process of the initial "source" is for constructing the Green's function. For multi-droplet condensation, the condensation droplets can be considered as a total mass

"sink" which results in the vapor concentration field surrounding the droplet. These three methods (PSM, MOI and DPSM) are working to resolve the total mass "sink" into many mass point "sinks" using different ways. For DPSM, constructing the point sinks is based on certain boundary conditions, which can make sure the boundary conditions are satisfied accurately by the generated point sinks.

4.4 Results and discussion

In this section, some simple droplet arrays are first considered in order to determine the ability of these methods (PSM, MOI and DPSM) in the interaction effect of droplet system. Based on the uniqueness theorem, an evaluation criteria whether or not certain boundary condition is satisfied is used to evaluate the solution accuracy.

4.4.1 An isolated droplet

It is no doubt that the DPSM method is also suitable for a single condensation droplet. As presented in chapter 3, the mathematics-based solution of the Laplace equation provides the analytical solution (Eq. (4.5)) for the condensation rate of an isolated growth droplet. For validation, this section compares the predicted condensation rates for a single condensation droplet in different contact angles by the DPSM method against the analytical solutions. The case considers a single droplet on the substrate with the radius $R = 300\ \mu m$. The humid air at the temperature $T_{ma} = 303.15\ K$ has a relative humidity 94%. The temperature of the droplet surface is assumed to be equal to the substrate temperature $T_{ds} = T_w = 300.1\ K$. In DPSM, the number of the point sinks for one droplet is chosen as $M = 200$.

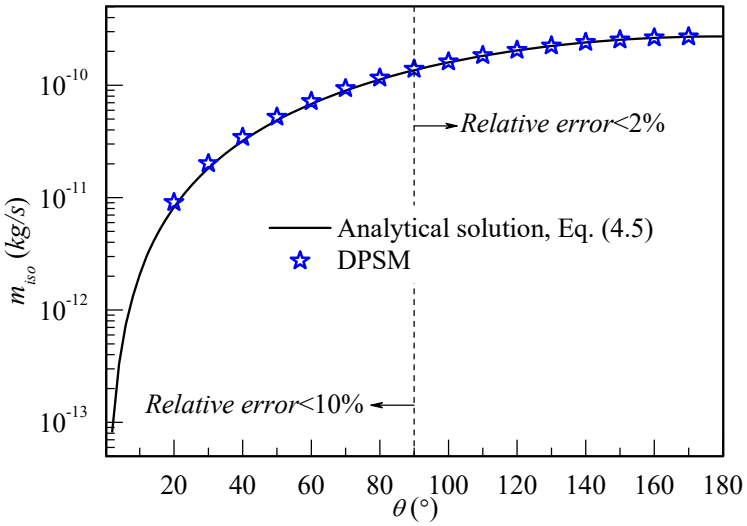

Figure 4.9 The predicted condensation rate by DPSM and the analytical solution for an isolated growth droplet.

Figure 4.9 plots the predicted condensation rate comparing with the analytical solutions by Eq. (4.5). It can be observed that the predictions by DPSM closely match the analytical solutions. The relative error between two manners, for the contact angle greater than 90°, remains below 2%. And the relative error falls within 10% for the smaller contact angle. Furthermore, the

dimensionless concentration distributions of the exterior domain surrounding the droplet are provided by DPSM. For selected three contact angles (60˚, 90˚, 120˚), the dimensionless concentration fields are presented in Figure 4.10 from the cross-sectional view. The red dashed circular line depicts the droplet profiles. Based on the uniqueness theorem, an evaluation criteria whether or not certain boundary conditions is satisfied is utilized to evaluation the accuracy. It is apparent through the zero iso-concentration lines overlapping with the droplet profiles that the desired boundary conditions are satisfied exactly in different contact angles.

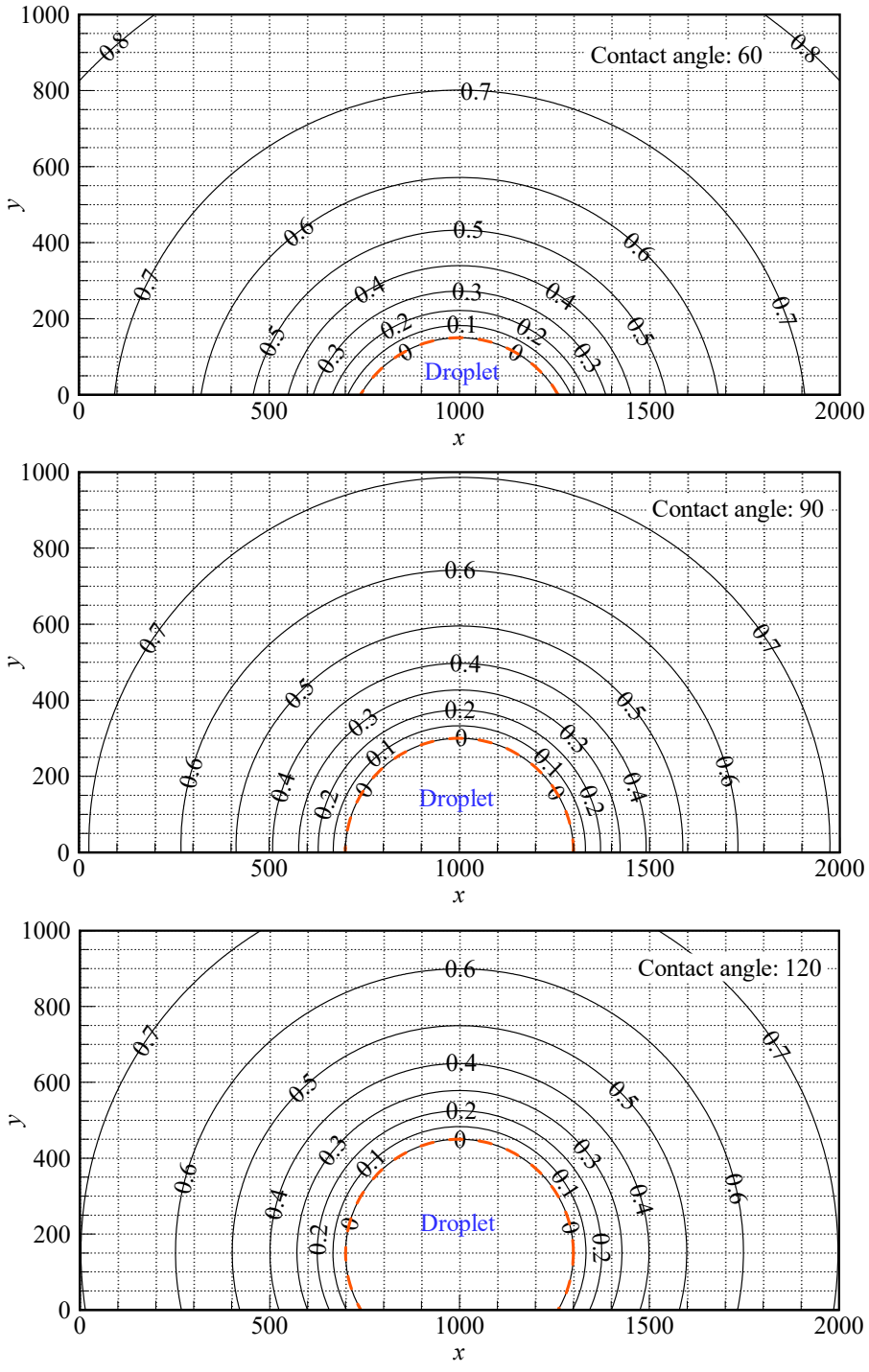

Figure 4.10 The normalized vapor concentration fields for single condensing droplet in different contact angles (unit: μm).

4.4.2 A binary array of droplet

This example considers a binary array of two droplets having the same size $R = 60\ \mu m$ and different inter-spacing d. The droplet is considered as a spherical suspended droplet and all droplets are assumed having the same vapor concentration on their surface. Three methods including PSM, MOI and DPSM are applied to predict the dimensionless concentration field and the correction factor for the droplet growth rate.

First, using PSM the dimensionless concentration fields for there different separation distances are presented in Figure 4.11 from the cross-sectional view. The red dashed circles depict the droplet profiles. It is apparent from the zero iso-concentration line that the desired boundary conditions (B. C. #1) on all droplet surfaces are not satisfied exactly. With increasing the inter-spacing, the zero iso-concentration lines are getting close to the droplet edges. Even at the ratio $d/R = 2.5$, Figure 4.11(a) shows a negative region between two droplets. That is the result of the simplification in Eq. (4.12). The solution deviation of PSM is enlarged with the increasingly approaching droplets. Consequently, PSM is not competent for the strong interaction behavior between droplets.

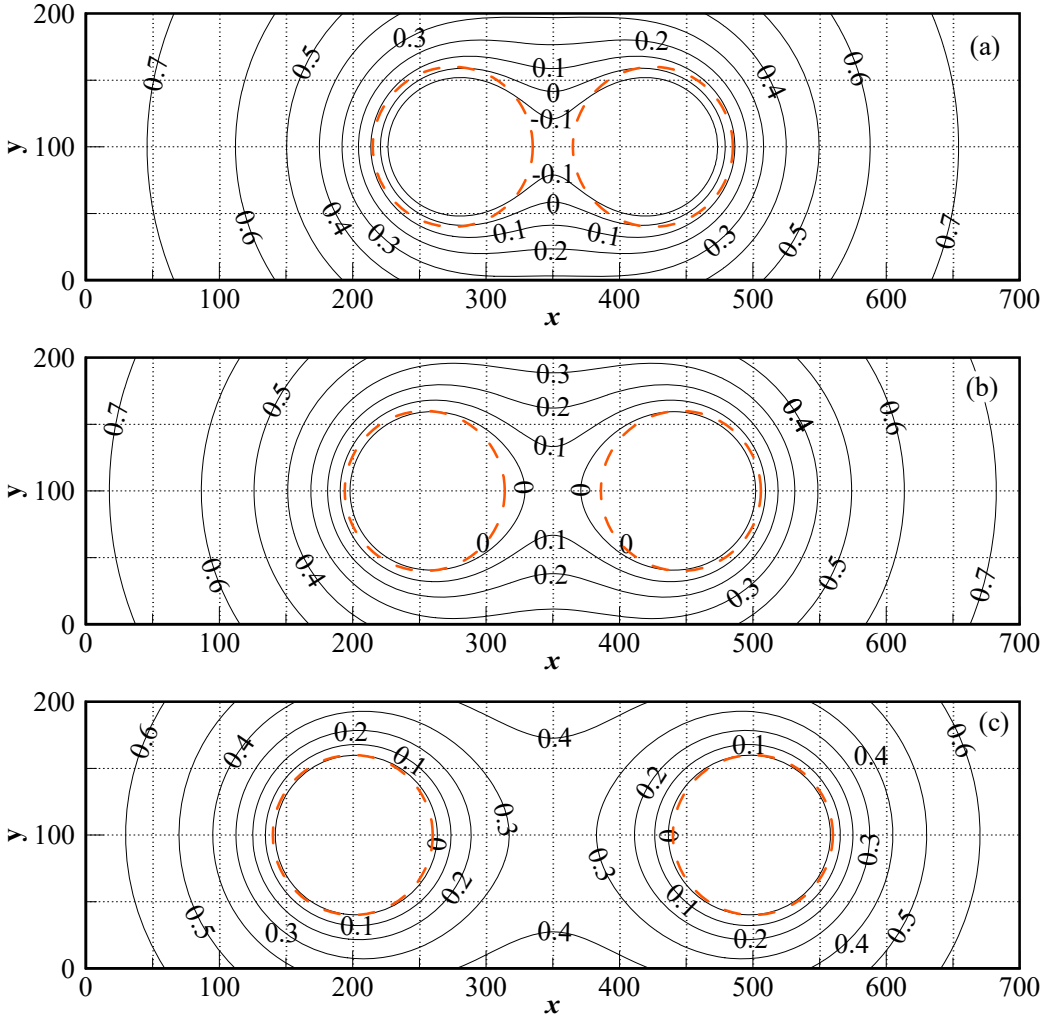

Figure 4.11 The normalized vapor concentration distributions for two condensation droplets predicted by PSM. (a) $d/R = 2.5$; (b) $d/R = 3.2$; (c) $d/R = 5$.

Comparing with PSM, the closed form MOI in section 4.3.2 can be seen as an exact analytical solution when the common ratio (*N*-1)*Ra* has a absolute value smaller than unity. As shown in Figure 4.6(b), there will be a fluctuation in the first few orders. In order to cancel the error due to the fluctuation, the point sinks in the first four orders are kept back, after that the closed form is adopted. As a result, Figure 4.12 gives the dimensionless vapor concentration distributions for the same three cases using the closed form MOI. In three different *d/R*, the satisfied boundary conditions are announced by the zero iso-concentration lines overlapping with the droplet edges, which also means an exact solution based on the uniqueness theorem. Unaffected by the droplet inter-distance, the closed form MOI can accurately predict the inter-droplet interaction so as a converged series in Eq. (4.25).

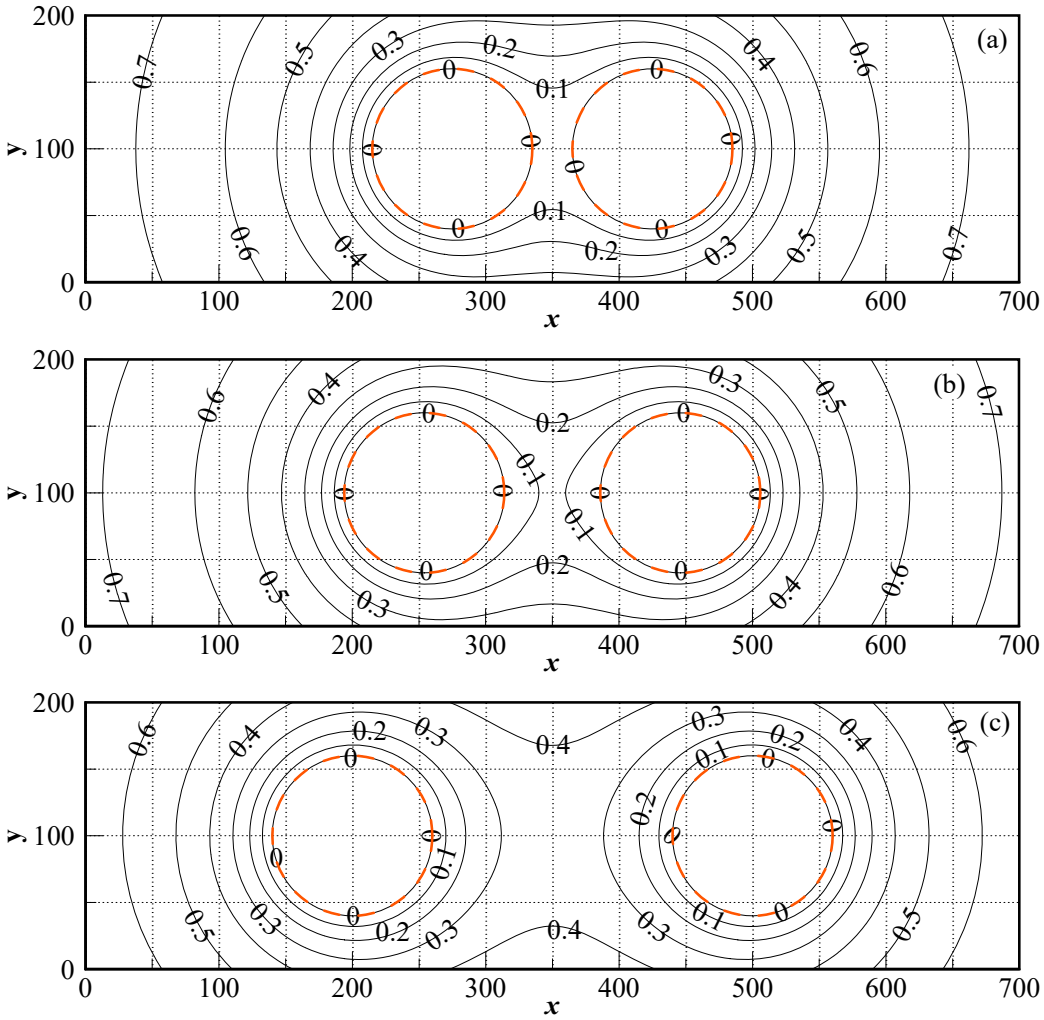

Figure 4.12 The normalized vapor concentration distributions for two condensation droplets using the closed form MOI. (a) *d/R* = 2.5; (b) *d/R* = 3.2; (c) *d/R* = 5.

Similarly, the developed DPSM is also considered. The choices for the two parameters (R_{is} and *M*) depends on the strength of the inter-droplet interaction. Numbers of tests state that the strong interaction (a lot of closing droplets) needs more point sinks and a smaller radius of the imaginary sphere. For those three cases, the radius of the imaginary sphere and the number of the point sinks for one droplet are taken as R_{is} = 0.5**R* and *M* = 200. The corresponding normalized concentration profiles are available in Figure 4.13. Similar as in Figure 4.12, the

boundary conditions are exactly satisfied without doubt using only 200 point sinks for each droplet. From Figure 4.12 and Figure 4.13, the predicted field by the proposed DPSM is closely the same with that from the closed form MOI.

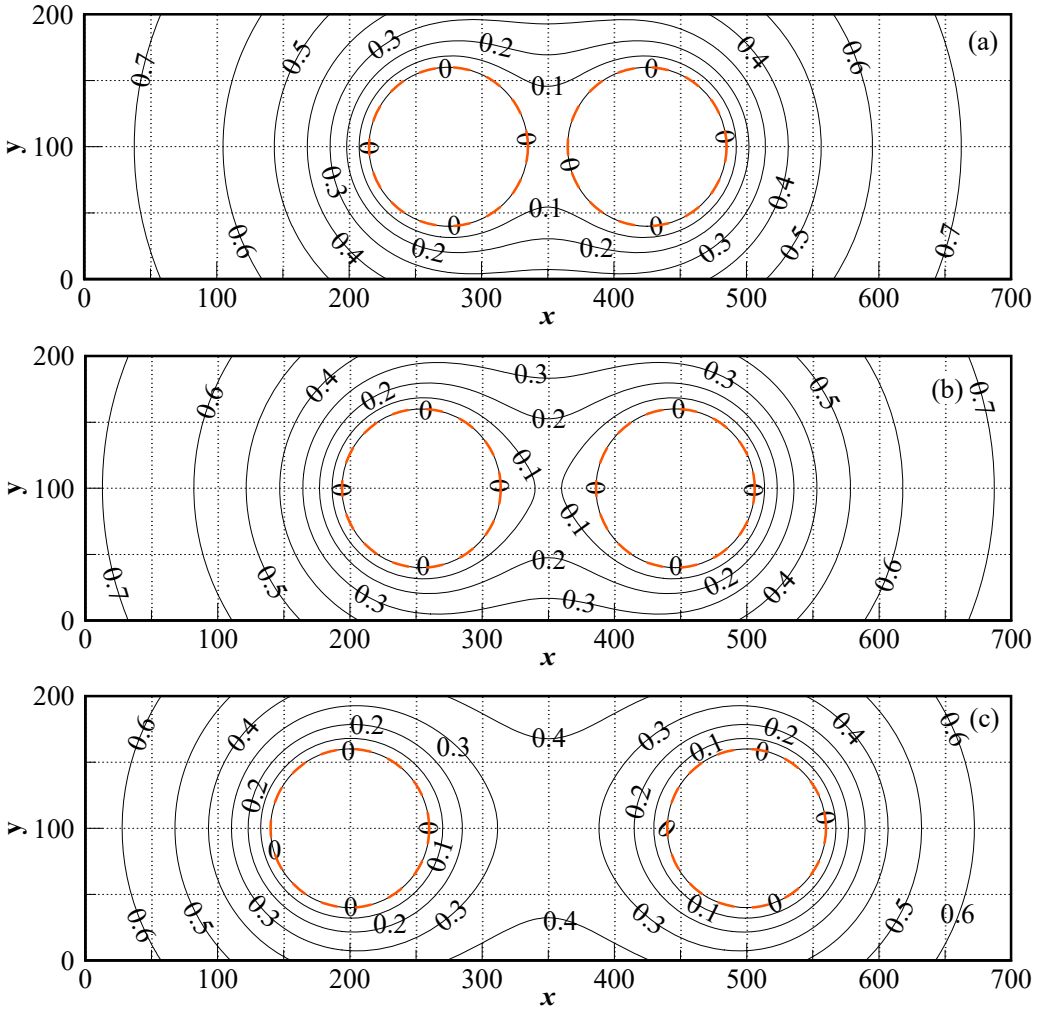

Figure 4.13 The dimensionless vapor concentration fields for a binary array predicted by DPSM. (a) d/R = 2.5; (b) d/R = 3.2; (c) d/R = 5.

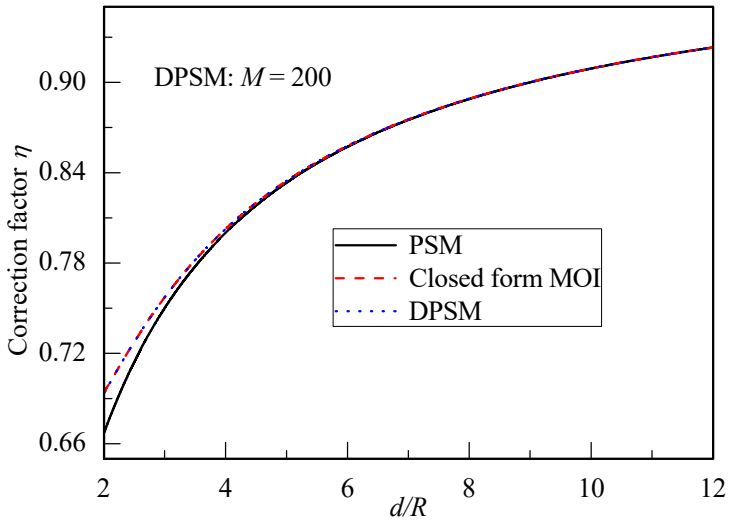

Figure 4.14 The correction factor determined by three methods for the binary array.

More deeply, the three methods are further examined in Figure 4.14 by plotting the correction factor against d/R. The value $d/R = 2$ means two droplets touch each other. In order to consider smaller inter-spacing, the number of the point sinks of one droplet in DPSM is chosen as $M = 200$ for calculating the correction factor. The predictions by the closed form MOI and DPSM closely match each other for all of the separation distances considered, even the approximately touching condition. However, the correction factors predicted by PSM increasingly deviate the exact results from the closed form MOI and DPSM with decreasing the inter-droplet spacing. The indications by the correction factor are following the results stated by the concentration field. As because of the simplification, PSM is limited to predict the relatively weak interaction when the droplets are far away each other.

4.4.3 Another simple droplet array

An additional comparison of the three methods is given in this section. Considering three different arrays having the spherical suspended droplets, the difference between the three arrays is just the droplet number surrounding the center droplet. The distance between the center droplet and the neighbors d and the droplet size R are the same and the surrounding droplets are evenly placed around the center droplet. For DPSM, the number of the point sinks for one droplet is $M = 200$, the radius of the imaginary radius is set as $R_{is} = 0.5*R$. Similar as above, the geometric progression is considered after the first four orders for MOI.

The results in Figure 4.15 are the correction factor of the centered droplet. The vertical dash lines are the converging threshold of the closed form MOI. When d/R is larger than the threshold, the infinite series in the closed form MOI is convergent; otherwise divergent. The inter-droplet interaction, corresponding to the correction factor, is enhanced with increasing number of the neighboring droplets and decreasing the inter-droplet space. Furthermore, Figure 4.15 indicates that MOI can only give the exact solution under the weak interaction. In the convergent d/R ranges, the correction factors predicted by the proposed DPSM keep in a good correspondence with that using the closed form MOI. What is worth mentioning is that the proposed DPSM can accurately capture the correction factor in the full range. From Figure 4.15, the error of PSM is gradually increased due to the enhanced interaction (the increased droplet number and the decreased separation distance), which keeps consistent with the observation above. From Figure 4.15(b) and (c), under the strong interaction, PSM produces even a negative correction factor which is totally wrong for the current mathematical model in section 4.2.

Again, in order to check the boundary condition, Figure 4.16 and Figure 4.17 compare the normalized concentration profiles of a five droplets array at $d/R = 2.2$ and $d/R = 5$ using three methods. The red dashed lines are the droplet edge. At $d/R = 2.2$, the closed form MOI is divergent, since only the results determined by PSM and DPSM are presented in Figure 4.16. The droplet array at $d/R = 2.2$ represents a very small inter-spacing, i.e. a very strong interaction. In Figure 4.16(a), the iso-concentration line by PSM clearly states the concentration value at all droplet surface is not zero. The desired boundary conditions (B. C.

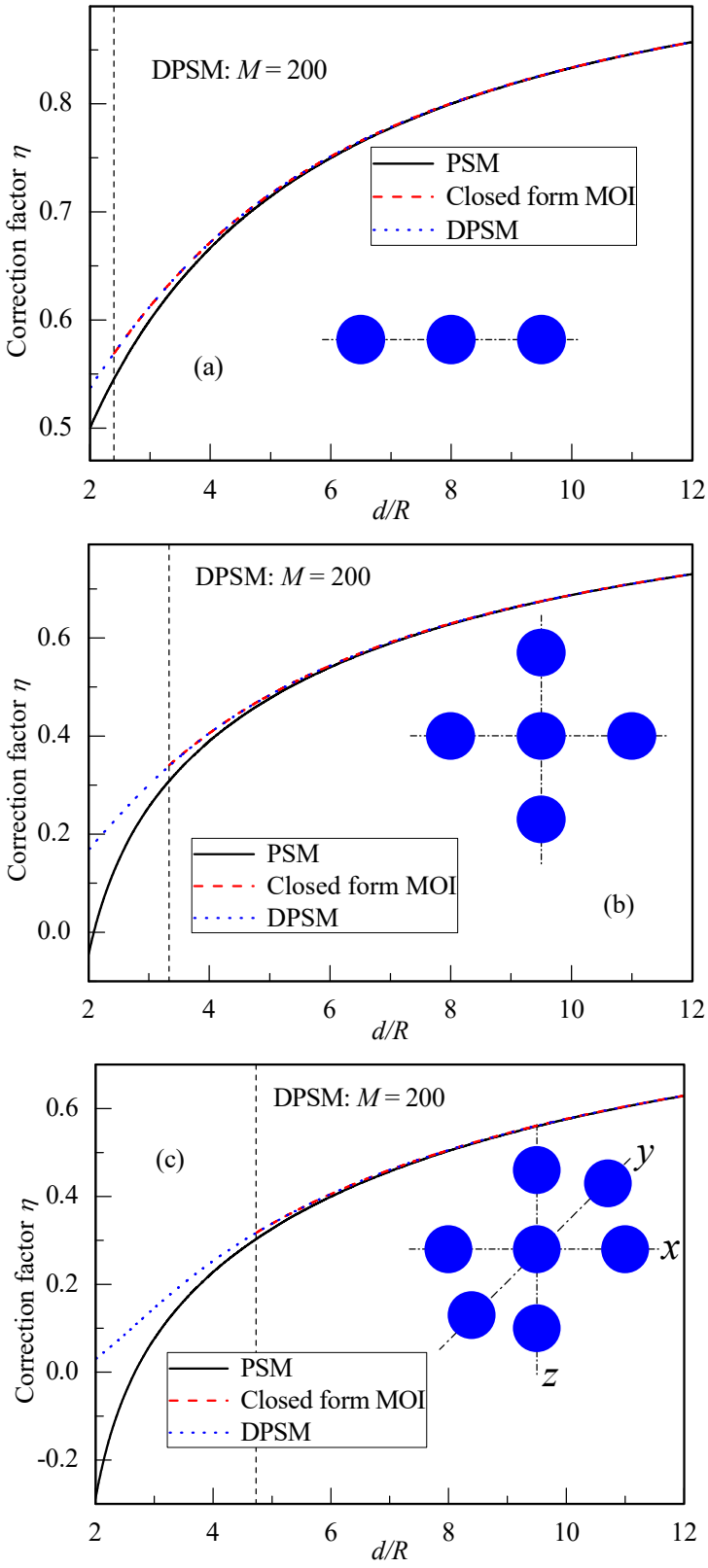

Figure 4.15 Comparison of the correction factor predicted by three methods for three arrays. (a) three droplets; (b) five droplets; (c) seven droplets.

#1) are not satisfied. And the negative region between droplets explains the correction factor predicted by PSM is smaller than the exact solution in the strong interaction. On the other hand, as shown in Figure 4.16(b), the zero iso-concentration line produced by DPSM is

accurately overlapping with the droplet profile. That means the boundary conditions can be accurately fulfilled by DPSM. Moving to the weak interaction at d/R = 5, PSM can approximately satisfy the boundary conditions from the zero iso-concentration line (see Figure 4.17(a)). Figure 4.17(b) and (c) show that the boundary conditions can be correctly prescribed by the closed form MOI and DPSM still.

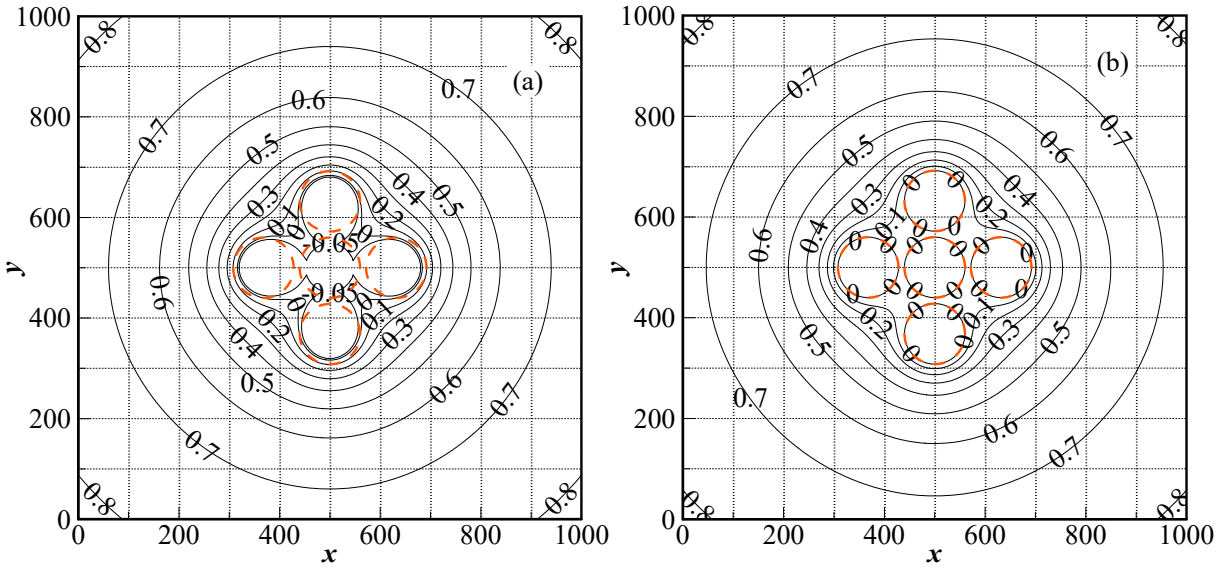

Figure 4.16 The normalized concentration field at d/R = 2.2. (a) PSM; (b) DPSM.

Aiming to evaluate the convergence efficiency of DPSM, Figure 4.18 plots the relative error of computed correction factor in different numbers of point sinks for several cases above. For all cases, the relative error is less than 1e-6 with M = 100. It can be seen that the convergence rate is depended on the droplet number and the inter-spacing. Hence the convergence rate of DPSM is depended on the strength of the inter-droplet interaction. A strong interaction (a lot of closing droplets) needs more point sinks (increasing N_s) for one droplet. For above droplet arrays (containing 2, 3, 5 droplets), the number of point sinks for one droplet M = 200 is enough to produce quite perfect result.

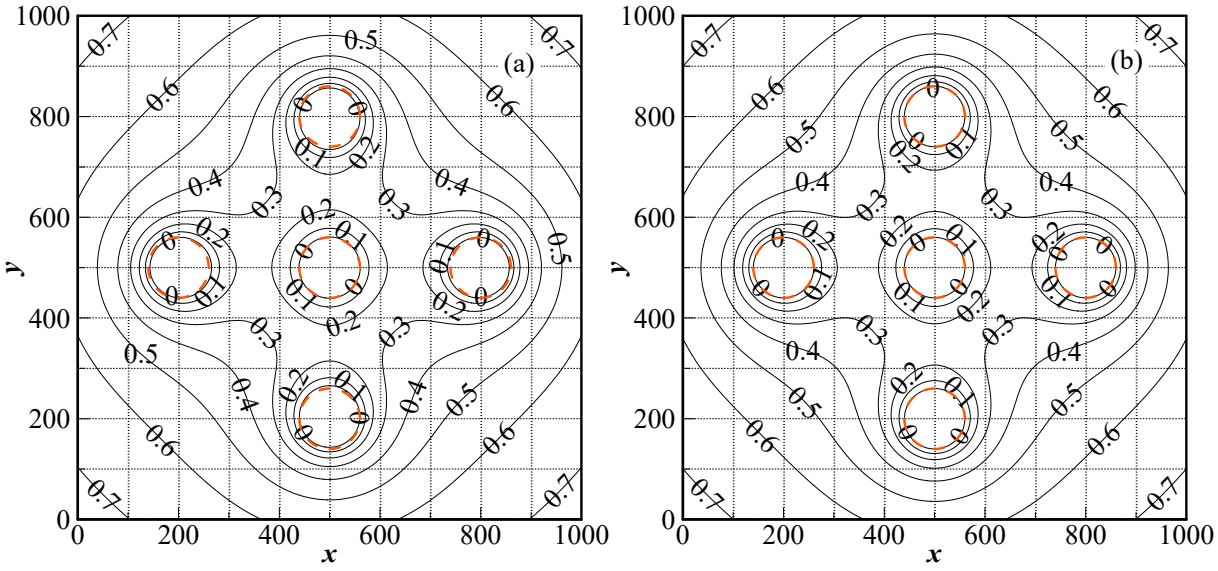

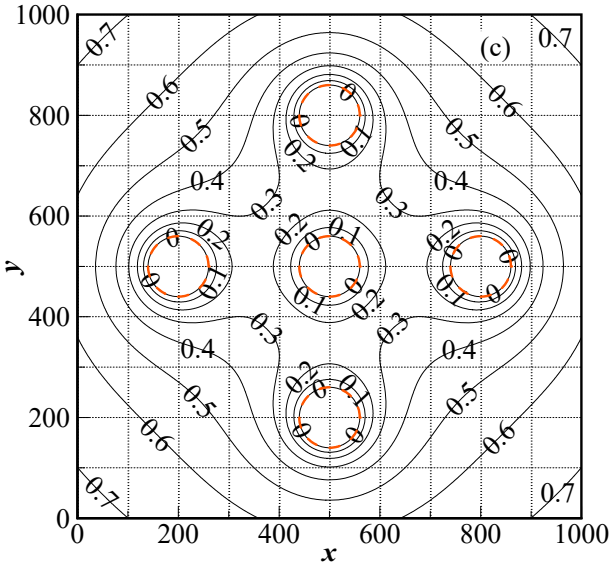

Figure 4.17 The normalized concentration field at d/R = 5. (a) PSM; (b) the closed form MOI; (c) DPSM.

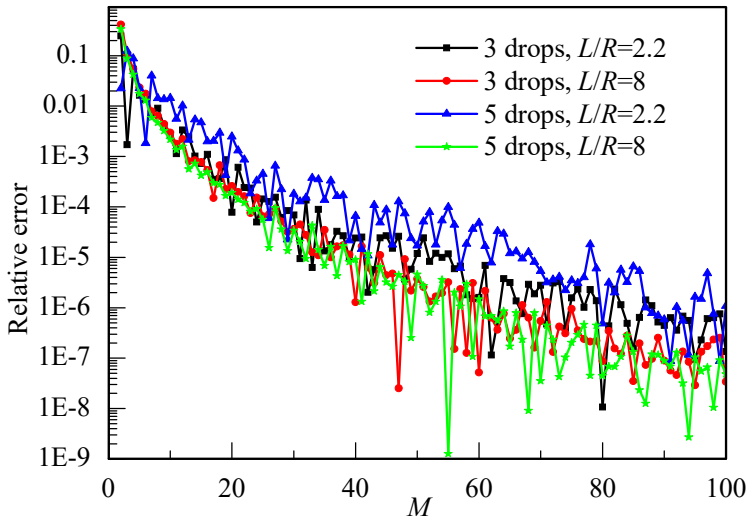

Figure 4.18 The relative error of computed correction factor in different numbers of the point sinks M.

In conclusion, the developed DPSM taking less point sinks is a powerful analytical tool in predicting the interaction between droplets over the full range inter-spacing. Due to the simplification in Eq. (4.12), PSM is essentially limited in processing the relatively weak interaction. Even though the closed form MOI can provide an exact solution, it is just suitable the weak interaction. And the point sinks in the first few orders should be considered in order to cancel the fluctuating influence of the common ratio.

4.4.4 System of multiple condensation droplets

For generality, this section considers a condensation system of multiple droplets. It contains 21 droplets randomly resting on a 1000×1000 substrate with a contact angle 90° and the droplet size widely distributed in the range 15-100. The mathematical description including

the boundary conditions for this system has been given in section 4.2. Unfortunately, for this complicated interaction MOI is divergent due to a bigger common ratio than unity in Eqs. (4.25) and (4.26). Consequently, only two analytical methods (PSM and DPSM) are implemented to model the droplet interaction. In DPSM, for each droplet 200 point sinks are evenly distributed on the imaginary half-sphere having the radius R_{is} = 0.5*R (R is the droplet radius).

Firstly, the normalized vapor concentration field from PSM is shown in Figure 4.19(a) and from DPSM in Figure 4.19(b). The red dashed circles and the red numbers are the droplet edge and its tag respectively. From Figure 4.19(a), the modeled zero iso-concentration line by PSM is totally out of order. Additionally, one can find a widely negative concentration region surrounding the droplets. The reversed direction of the concentration gradient means an evaporation flux instead of the condensation flux. By comparison, the solution by DPSM presents a closely matching between the zero iso-concentration lines and all droplet edges. According to the uniqueness theorem, the satisfied boundary conditions indicate the ability of DPSM to exactly model the droplet interaction.

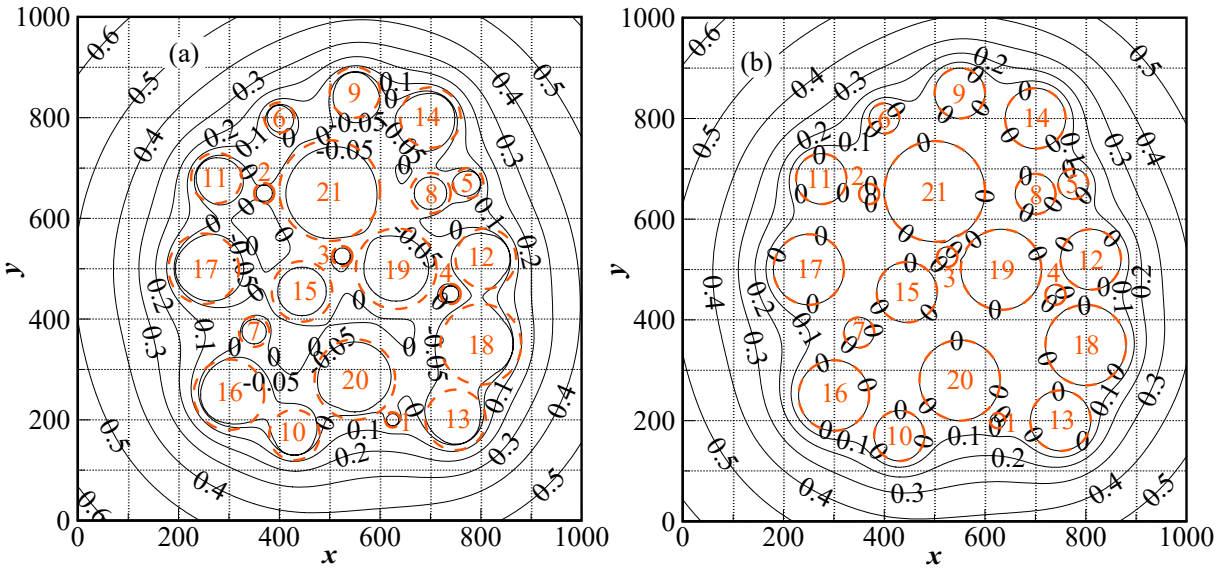

Figure 4.19 The normalized concentration field for a condensation system of multiple droplets. (a) PSM; (b) DPSM.

On the other hand, the effects of two methods in the concentration field correspond to the correction factor. With that, for both methods the correction factors of all droplets shown in Figure 4.19 are summarized in Table 4.1. It is rather remarkable that negative correction factors for droplets 3 and 4 are provided by PSM. Because the concentration distribution surrounding the droplet determines its condensation rate, the negative correction factors are the result of the negative concentration region shown in Figure 4.19(a). And droplets 3 and 4 have a strong interaction from the surrounding big droplets. On the whole, the difference is controlled less than 10% for most of the droplets. For small droplets, a strong interaction is forced by the neighboring big size droplet. The centered droplets face more strong interaction comparing with the edge droplet. The intensity of the interaction is also determined by the

number of the surrounding droplets and their inter-distance. A careful reader can find that the difference of PSM greater than 10% are those droplets facing a strong interaction (such as, droplets 2, 7, 8 and 15). Therefore, it can be concluded that PSM will introduce an unbearable error for the droplet facing a strong interaction which is in the range of DPSM ability. Actually, the correction factor defined by Eq. (4.4) denotes the improvements for the isolated growth model by PSM and DPSM. Therefore, it can be concluded that PSM and DPSM all provide a significant improvement comparing the isolated growth model. And DPSM has a higher accuracy in handling a strong interaction.

Table 4.1 The correction factor of all droplets for the droplet system shown in Figure 4.19. The difference is computed based on the results of DPSM.

Droplet No.	DPSM	PSM	Difference (%)
1	0.09462	0.09743	2.97
2	0.04579	0.01469	67.91
3	0.01165	-0.02758	336.78
4	0.01923	-0.04587	338.53
5	0.17924	0.18884	5.36
6	0.24025	0.24935	3.79
7	0.08360	0.05366	35.81
8	0.09767	0.06943	28.91
9	0.30848	0.31156	1.00
10	0.27576	0.27505	0.26
11	0.31242	0.32160	2.94
12	0.26028	0.27398	5.26
13	0.34347	0.34930	1.70
14	0.34835	0.35570	2.11
15	0.11942	0.10231	14.33
16	0.37565	0.38462	2.39
17	0.34410	0.35175	2.22
18	0.31893	0.31681	0.66
19	0.14898	0.12995	12.77
20	0.22973	0.21471	6.54
21	0.24563	0.23926	2.59

For the droplet distribution in Figure 4.19, Figure 4.20 plots the relative error of computed correction factor using DPSM in different numbers of point sinks *M*. Four droplets (Nr. 3, 6, 17 and 19) present different convergence rate. The smallest droplet 3 has the smallest convergence rate because of a strong interaction by three big neighbors (droplets 15, 19 and 21). Although equally face a strong interaction from neighbors, droplet 19 having a larger size converges more fast relatively. Locating on the edge droplets 6 and 17 suffer a relatively weak interaction which is responsible for the fast convergence. Combining with Figure 4.18, it can be concluded that the convergent rate of DPSM is decided by the interaction intensity.

For each droplet, the interaction intensity depends on its size and neighbors (size and inter-spacing). And for DPSM, the solution accuracy can be improved by using more point sinks for each droplet which also means more computation cost.

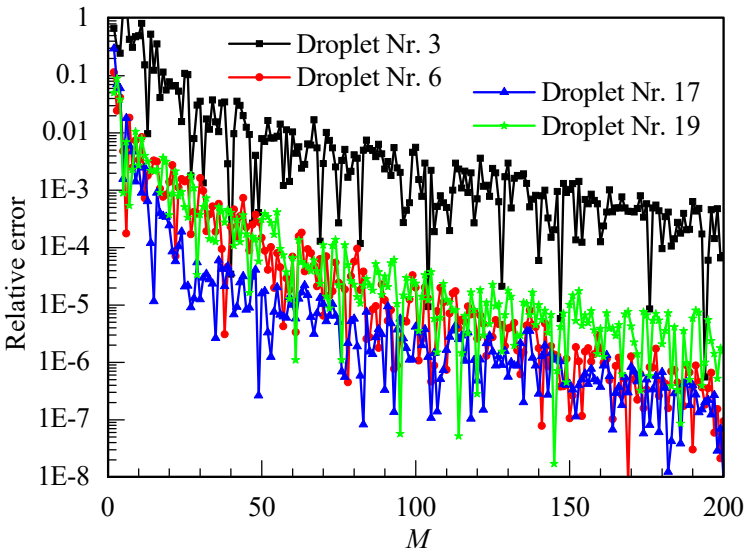

Figure 4.20 The relative error of computed correction factor for several droplets using DPSM.

4.5 Conclusions

In this chapter, the distributed point sink method is presented for predicting the interaction effects of droplets during dropwise condensation. The droplet is treated as a series of point sinks of the vapor diffusion by a spherically distribution inside the droplet. A matrix formulation based on certain boundary conditions is constructed for solving the strengths of all point sinks. Because of the distributed point sinks determined by the boundary conditions, it can satisfy the boundary conditions automatically. Actually, its ability is decided by the nature of the method of the Green's function. The proposed method makes it possible to accurately predict a strong interaction between droplets with a large number of considered droplets during dropwise condensation. The obtained correction factor can be used to improve the isolated droplet growth model as well as the accurately prediction of the condensation rate, and the solved droplets interaction can be contributed to understand the mechanism of dropwise condensation in the presence of non-condensable gas.

Chapter 5 Modeling of Heat and Mass Transfer for Dropwise Condensation with NCG

In this chapter, based on previous works, a modeling idea is launched to predict heat and mass transfer during dropwise condensation with the presence of NCG. In chapter 3, single droplet growth model is developed to predict the simultaneous heat and mass transfer through the droplet from the free steam to the droplet base. In order to consider the interaction effects between droplets, the DPSM presented in chapter 4 is applied to correct the droplet growth rate by the isolated growth model. Furthermore, the enhancement effect of convective mass transfer is also considered by the droplet Sherwood number. For re-constructing the droplet spatial distribution, a numerical algorithm is developed to reflect the droplet dynamics sufficiently detailed, including nucleation, growth, coalescence, slide-off/fall-off, re-nucleation. Combining all those aspects, for several experimental/re-constructed droplet size and spatial distributions, predictions of heat and mass transfer for dropwise condensation in case of NCG are carried out and compared with the measured results.

5.1 Literature review

As because of its extreme complexity, the direct numerical simulation for dropwise condensation is still a great challenge so far. Historically, two classical modeling ways for dropwise condensation of pure steam are developed and widely used in literature. For both of them, it is necessary to determine the droplet growth rate using the thermal resistance theory and the minimum droplet radius based on the nucleation theory, as presented by Eqs. (3.26-3.28) in chapter 3 [4, 9, 43, 80]. The difference is how to construct the droplet distribution characteristic. Typically, a method based on the population balance theory, defined as conservation of droplet number, is developed to predict the droplet size distribution density [9] under a steady state. The overall heat flux for steady-state dropwise condensation can be obtained by integrating the product of single droplet heat transfer rate and the droplet number density function [9]:

$$q_t = \int_{R_{\min}}^{R_e} Q(R) nd(R)\, dR + \int_{R_e}^{R_{\max}} Q(R) Nd(R)\, dR \tag{5.1}$$

where R_{min} and R_{max} are the minimum and maximum droplet radius respectively. The critical radius R_e depended on the nucleation site density denotes the boundary between the coalescence and non-coalescence size region. The droplet number density functions nd and Nd mean number of small and large droplets per unit area per unit size around droplet radius

R. The heat transfer rate *Q* contributed by one droplet having size *R* is derived by single droplet growth model in Eq. (3.27). Due to its direct simplicity, the integration method by Eq. (5.1) has mostly been employed to model dropwise condensation out of pure steam [44, 81-87]. Another way particularly introduced by Khandekar and Muralidhar [4] is using a mathematical algorithm to consider a consequence of the time-dependent sub-processes during dropwise condensation [61, 88-90]. The minimum radius from the nucleation theory is considered as the initial size of droplet, and then the droplet will grow with a rate resulted from the thermal resistance theory. Comparing with the integration form, the droplet dynamic characteristics can be really reflected by the mathematical algorithm. Based on those two methods, modeling of dropwise condensation under pure vapor has been investigated successfully and deeply.

In pure steam, dropwise condensation is uniquely controlled by heat transfer. Nevertheless, coupled heat and mass transfer due to the presence of NCG starts to drive dropwise condensation. Significantly, the presence of NCG introduces several important aspects related to mass transfer. The vapor diffusion resistance presented in chapter 3 corresponds to diffusion mass transfer due to the concentration gradient. The blocking effect of surrounding droplets for diffusion mass transfer introduces the interaction effect between droplets, which has been investigated in chapter 4. In mass transfer community, mass transfer can be significantly enhanced by convection (natural and forced convection) [91-92]. Based on the heat and mass transfer analogy, a famous dimensionless number the Sherwood number (*Sh*) is developed to define the ratio of the convective to diffusion mass transfer rate as the Nusselt number in heat transfer community [91-92]. In chapter 2, experiments have indicated that convective mass transfer is an unavoidable aspect for dropwise condensation heat transfer. Therefore, convective mass transfer should be considered in heat and mass transfer driven dropwise condensation, if convection is not neglected.

As we concluded in chapter 3, mechanistic understanding of dropwise condensation in the presence of NCG is far away from being complete. And the correspondingly modeling is rarely lanuched. In this chapter, based on the modeling manner for dropwise condensation of pure steam, we develop a modeling idea for dropwise condensation with the prence of NCG. In chapter 3, single droplet growth model which gives the droplet growth rate and the minimum size is proposed with the droplet growing by a isolated form. Conduction heat transfer through the liquid droplet and diffusion mass transfer outside the droplet are all considered in single droplet growth model. In chapter 4, the distributed point sink method (DPSM) is developed for the interaction effect between droplets. The influence of the interaction effect of neighbors is defined by the correction factor which is used to correct the growth rate from chapter 3. The correction factor is strongly sensitive to the droplet spatial distribution. In order to predict the correction factor accurately, a numerical algorithm as similar with it in reference [4] is constructed to produce a more realistic droplet distribution. Additionally, Sherwood number defined by the empirical correlations is also added as another correction factor for considering the convective mass transfer. Finally, the droplet growth rate

and the overall heat flux during dropwise condensation with NCG can be predicted. And the predicted results are also compared to the measurements from chapter 2. Combining the modeling and experiments, mechanistic understanding of dropwise condensation with the presence of NCG is discussed simultaneously and conclusively.

5.2 Numerical algorithm of droplet dynamics

The photographic analysis of experiments has proved that dropwise condensation is a spatio-temporal cyclic process with the consequence of time-dependent sub-processes occurring repeatedly [4]. The sub-processes of the condensation cycle become visible from the experimental images taken by the high-speed camera, as shown in Figure 5.1. Dropwise condensation begins from the formation of an initial droplet, which is the nucleation. Then these tiny droplets grow by direct condensation, until they approach a neighboring droplet and a coalescence-dominated growth take place associated with direct condensation. Once the critical size is reached, the droplets will slide from the substrate due to external forces. Beyond the first sliding, the combination of coalescence and direct condensation promote the droplet growth commonly. Due to coalescence and sliding, the exposed substrate permits new nucleation droplets to become available. That is, those individual processes interrelate in space and time to constitute a closed cycle, and dropwise condensation finally reaches a statistical dynamic steady state [4, 88, 61].

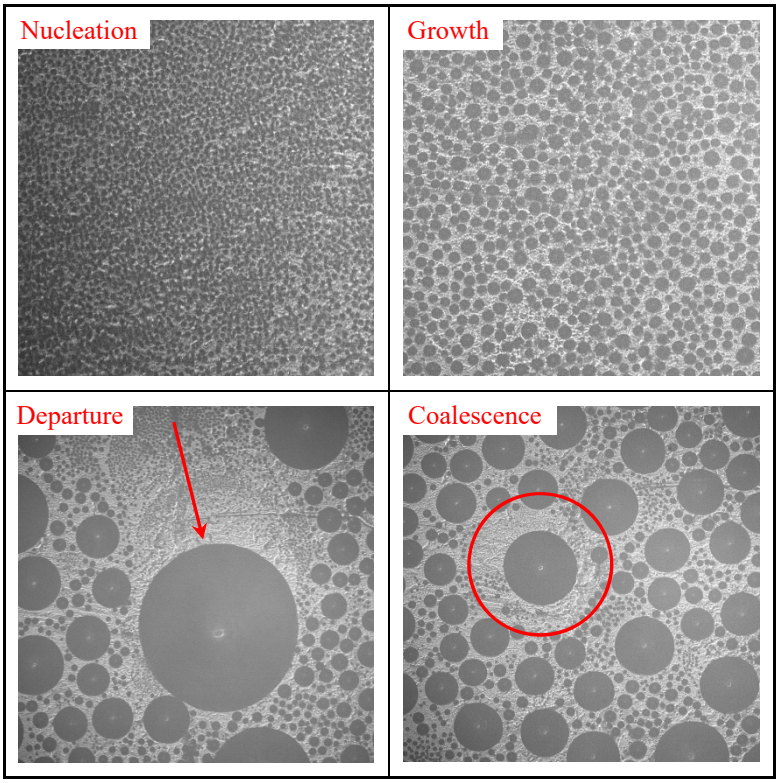

Figure 5.1 Individual sub-processes of dropwise condensation observed from experiments.

Although the growth rate depended on droplet size is provided by the proposed model in chapter 3, a mathematical algorithm is additionally required to simulate the droplet dynamics during dropwise condensation. Based on the above physical fundamentals, a numerical

algorithm considering those sub-processes is developed to simulate the droplet growth process from nucleation to departure. The main steps of the growth algorithm are listed as follows:

1. Provide all variables such as the growth rate in full size (from single droplet growth model), the nucleate size (the minimum radius from single droplet growth model), the critical size for sliding (according to the experiments), the nucleation site density, the time-step, and the total computing time.
2. Generate the nucleation sites using the random function, place the minimum radius at all sites and make sure to avoid overlaps between two neighboring droplets.
3. Scan all active droplets, find the growth rate and calculate the new radius over a time step.
4. Check the overlap and calculate the mass center before coalescence as the new center and the new radius according to the mass conservation, perform the coalescence.
5. Inactivate the nucleation sites covered by the coalesced droplets and relax the hidden nucleation sites due to coalescence.
6. Check the droplets near the substrate edges and guarantee the ingrowing.
7. Check the sliding and the falling droplets, and give a constant sliding velocity (approximate value from experiment).
8. Reactivate the nucleation site in the exposed virgin area because of the sliding and the falling.
9. Repeat step 3-9 until the simulation is terminated.

Figure 5.2 depicts the flow chart of the droplets growth algorithm for dropwise condensation at a vertical substrate. A Fortran 90 program is developed to actualize this flow chart. It is noteworthy that the algorithm at each time step needs to traverse all droplets and track every stage of droplets dynamics. Hence the open MPI is used to parallel the simulation algorithm for saving computing time. This algorithm reflects the droplet dynamics from nucleation to detectable size sufficiently detailed, including nucleation, growth/coalescence, slide-off / fall-off, re-nucleation.

5.3 Convective mass transfer

In the presence of NCG, dropwise condensation is driven by coupled heat and mass transfer. As discussed in section 5.1, mass transfer will be substantially enhanced by convection. In this work, the effect of convective mass transfer for condensation rate is taken into account by the Sherwood number which defines the ratio of the convective to diffusion mass transfer rate. Historically, different empirical correlations for droplet Sherwood number have been successfully constructed [93-98] and a great progress has been carried out [99]. In order to consider the vapor mass transfer in and out of droplet, a classical form is to correlate the experimental data by direct addition of terms representing mass transfer by pure diffusion and by forced convection [97-98]:

$$Sh_d = Sh_0 + BRe_d^{m1} Sc^{m2} \tag{5.2}$$

where Sh_0 representing the vapor diffusion under natural convection is equal to 2 commonly,

the parameters (B, m_1 and m_2) are defined by correlating the experimental data. For majority of the correlations, the exponents m_1 and m_2 on droplet Reynolds number (Re_d) and Schmidt number (Sc) are 1/2 and 3/1, respectively.

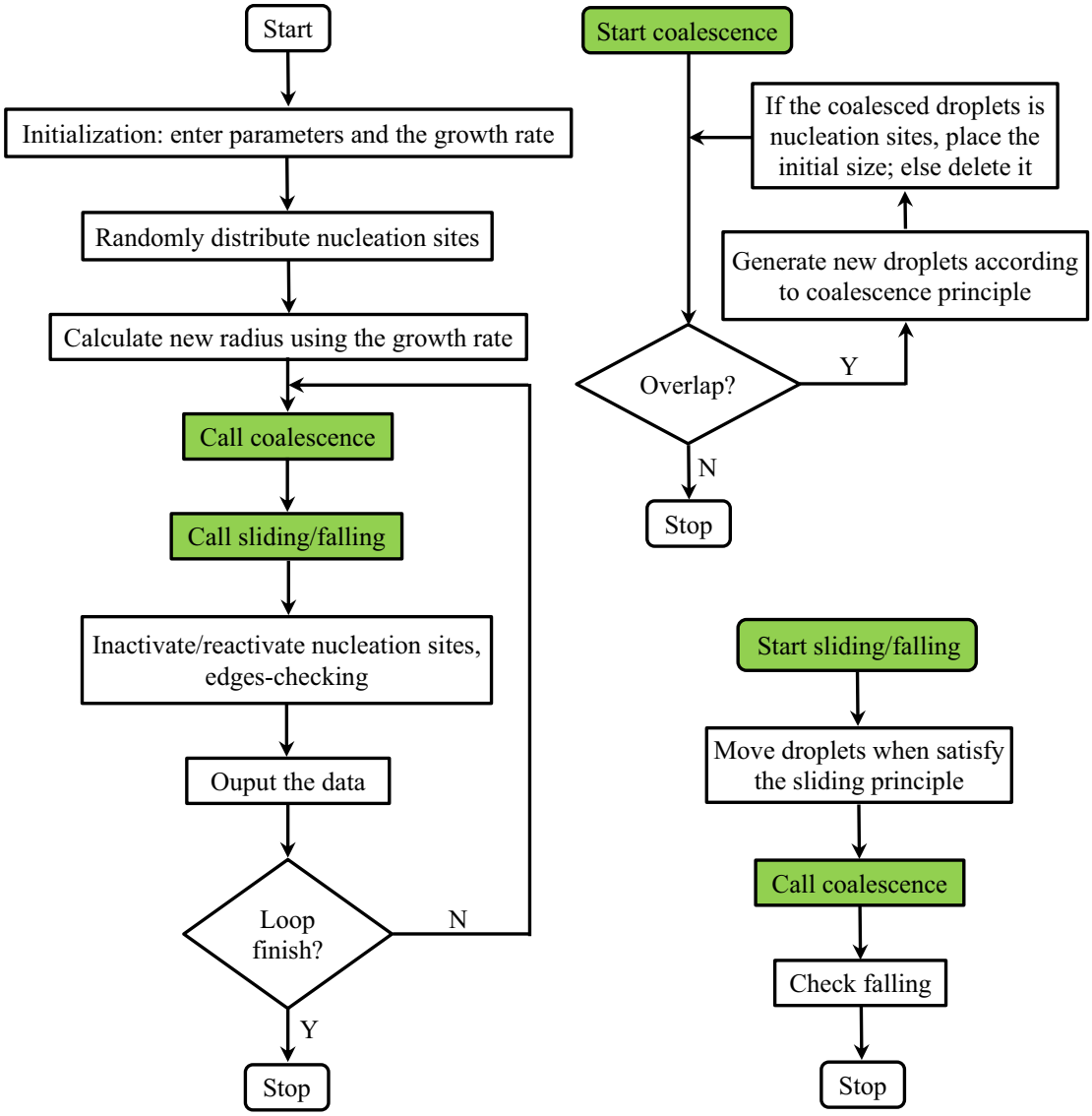

Figure 5.2 Flow chart of the droplet growth algorithm.

The classical Ranz and Marshall correlation is exactly following this form. With this form in mind, based on the experimental and theoretical investigations Schwarz and Smolik [94] and Kulmala et al. [95] developed a correlation of Sherwood number for droplet over a vertical substrate:

$$Sh_d = 2.009 + 0.514 Re_d^{1/2} Sc^{1/3} \tag{5.3}$$

where the droplet Reynolds number Re_d is calculated by the bulk flow velocity and the droplet diameter. Therefore, the droplet condensation rate under convective flow can be solved by the diffusion condensation rate corrected by the droplet Sherwood number, i.e. the diffusion condensation mass flow rate is multiplied by the droplet Sherwood number. Here, the Sherwood number by Eq. (5.3) is seen as another corrector factor to consider the convective effect for mass transfer during dropwise condensation.

With the current conditions (T_{ma} = 303.15 K, RH = 94%), the droplet Sherwood numbers at different bulk Re are plotted against its radius in Figure 5.3. It can be seen that the droplet Sherwood number is strongly sensitive to the droplet size and the bulk velocity. For larger size droplet, its Sherwood number up to 10 indicates a significantly enhanced mass transfer by forced convection. The droplet Sherwood number tends to Sh_0 = 2 which corresponds to the vapor diffusion under natural convection. Accordingly, the enhancement effect by convective mass transfer can be overlooked for the droplet smaller than 1 μm. In comparison, the larger droplet having more large surface area is instrumental in convective mass transfer between the bulk and the droplet surface.

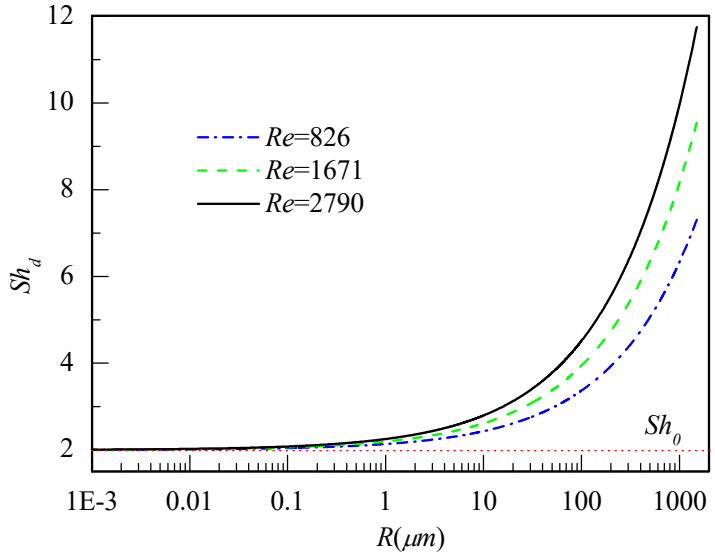

Figure 5.3 Droplet Sherwood number at different bulk Re depending on its radius.

5.4 Modeling outline for heat and mass transfer driven dropwise condensation

For present dropwise condensation, heat flow is contributed by two parts: sensible heat by forced convection heat transfer and latent heat released by vapor condensation. The sensible heat is from the convection heat transfer through the bulk flow to the droplet surface and the substrate without covering by droplets. And the droplet will also enhance the convection heat transfer due to enlarged heat transfer surface. In present convective dropwise condensation flow, heat flow is mainly contributed by condensation latent heat and the sensible heat due to the forced convection is rather secondary. For that reason the enhancement effect of droplet from sensible heat is reasonably neglected, the convection heat transfer is assumed to a fully developed laminar flow heat transfer over the whole condensation substrate. Therefore, the heat flux because of the forced convection q_{fc} can be calculated by:

$$q_{fc} = h^* \left(T_{ma} - T_w\right) = Nu^* * k_{ma} / L_s \left(T_{ma} - T_w\right) \tag{5.4}$$

where k_{ma} and L_s represent the thermal conductivity of moist air and the length of the substrate, respectively. In calculating the mean heat transfer coefficient h^*, the mean Nusselt number over the whole condensation substrate Nu^* is estimated by the empirical correlation in Eq. (2.2).

The latent heat is related to the overall condensation rate on the substrate which is attributed to the vapor condensation on all droplets surface. It is necessary to figure out the condensation rate of each droplet. For that, based on a certain modeling condition, the nucleation size and the droplet growth rate (corresponding to the droplet condensation rate) are solved by single droplet growth model in chapter 3. And then the obtained nucleation size and droplet growth rate are added into the growth algorithm for modeling the whole process from nucleation to departure of droplets. In single droplet growth model, the interaction effects between droplets and the convective mass transfer are not included. Accordingly, it is necessary to correct the condensation rate by considering those two aspects. As discussed in chapter 4, the correction factor for the interaction of droplets is strongly depended on the droplet distribution. During condensation, the droplet distribution has great changes at each step due to coalescence and growth. Because of the large number of droplets, computing the correction factor of droplets at each instant is insufferable in computing cost. It is completely unrealistic to correct the condensation rate at each step. On the other hand, the droplets distribution during steady dropwise condensation will also reach a steady state in statistic, as the droplet size distribution density presented in section 2.3.1. The droplet growth rate just change the fresh frequency during the time. The droplet distribution characteristic keeps consistency in different conditions. Thanks to those reason, after reaching steady state, different droplet spatial distributions at discrete time points from the numerical algorithm of droplet growth are chosen to consider the influence by the interaction effects of droplets and the convective mass transfer. For a certain droplet distribution, the overall condensation rate on the substrate m_t can be corrected according to:

$$m_t = \sum_{i=1}^{N} Sh_d^i \eta_i m_{iso}^i \tag{5.5}$$

where N is the droplet number over the substrate and i indexes the droplet, the droplet condensation rate m_{iso} depending on its size is solved by the isolated droplet model. The interaction effects between droplets are considered by the correction factors η which is solved by the DPSM. The term ηm_{iso} represents the droplet condensation rate due to vapor diffusion during dropwise condensation. In order to consider the enhancement effect of convective mass transfer, the droplet Sherwood number Sh_d as another correction factor is defined by Eq. (5.3). Finally, the overall condensation rate is averaged for different droplet distributions. The heat flux released by condensation at all droplet surfaces is related to the mean value of the overall condensation rate:

$$q_s = m_t^* * L / A_s \tag{5.6}$$

where L is the latent heat of condensation for water vapor and A_s means the area of the condensation substrate.

Finally, the total heat flux during convective dropwise condensation flow becomes:

$$q_t = Nu^* * k_{ma} / L_s \left(T_{ma} - T_w\right) + m_t^* * L / A_s \tag{5.7}$$

Figure 5.4 illustrates the modeling outline. More details about modeling will come soon, and also mechanism discussion.

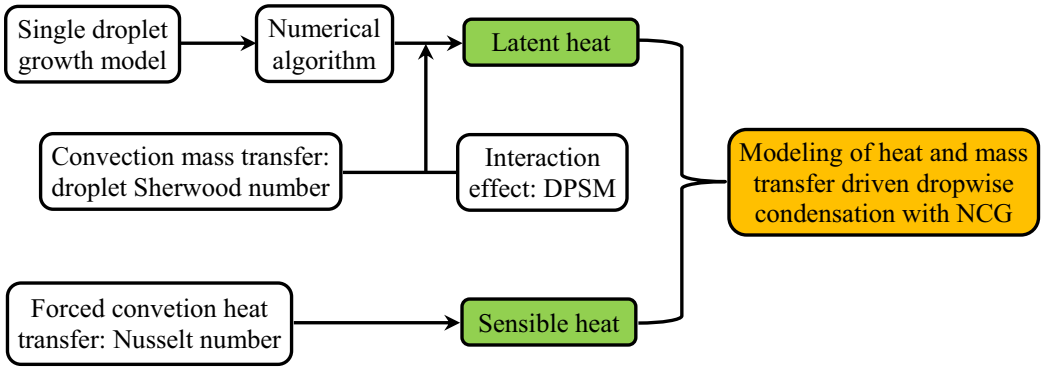

Figure 5.4 Flow chart of the modeling outline.

5.5 Results and discussion

5.5.1 Modeling details

In this part, modeling dropwise condensation in the presence of NCG is launched in details. For validation, modeling conditions are selected according to experiments in chapter 2. Moist air having the temperature 303.15 *K* and the relative humidity 94% is considered as the working fluid corresponding the dew point temperature 302.1 *K*. The wall temperature lower than the dew point is adjusted for getting different temperature differences of condensation driving. The nucleation site density is considered to be 3.7×10^8 $/m^2$ (after checking the simulated droplet size distribution with the experimental result), with 19980 nucleation sites on the simulated substrate (9×6 *mm*). Since the heat transfer performance of dropwise condensation is insensitive to the critical size for sliding, an approximately leaving radius 1.2 mm observed from the experimental images is used in the current simulation.

5.5.2 Modeling of dropwise condensation

Based on the droplet growth and the minimum size from single droplet growth model (Model B in chapter 3), this section will present modeling of dropwise condensation using the numerical algorithm in different sub-cooling. Visualization of droplet distribution from simulation, the droplet size distribution density, the area coverage ratio of substrate, the droplet number and the effect of overall heat flux will be presented and discussed.

The major processes of dropwise condensation observed in the experiment have been shown in Figure 5.1. These processes (nucleation, growth, coalescence, sliding/departure) constitute the basis of simulation for the droplet dynamics. Figure 5.5 highlights visually these sub-processes captured from the simulation of dropwise condensation. Contrary to the local phenomena (the contact angle, the contact line delay during merging, the dynamics of liquid-vapor interface seen in experiments), the perfect hemispherical droplet is assumed in the simulation. However, the major phenomena of the overall dropwise condensation at a vertical substrate are well simulated by the growth algorithm.

As a key parameter, the nucleation-site density affects the heat transfer performance of dropwise condensation evidently. Increasing the nucleation-site density leads to the reduction

of the droplet size before coalescence occurs, more virgin spaces for re-nucleation and the high population of small droplets. Unfortunately, it is almost impossible to experimentally capture the nucleation phenomenon because of the initial droplets having the order of a few nanometers. The intuitive effect from the nucleation-site density is the discontinuity between the small droplets which grow mainly by direct condensation and the big droplets which grow mainly by the coalescence [100]. Section 2.3.1 has concluded that increasing of sub-cooling causes a large nucleation-site density. It is hard to define the nucleation site density in all sub-cooling using experiments. According to this discontinuity effect, the droplet-size distribution density from the low sub-cooling experiment is considered to validate the nucleation sites density used in simulation.

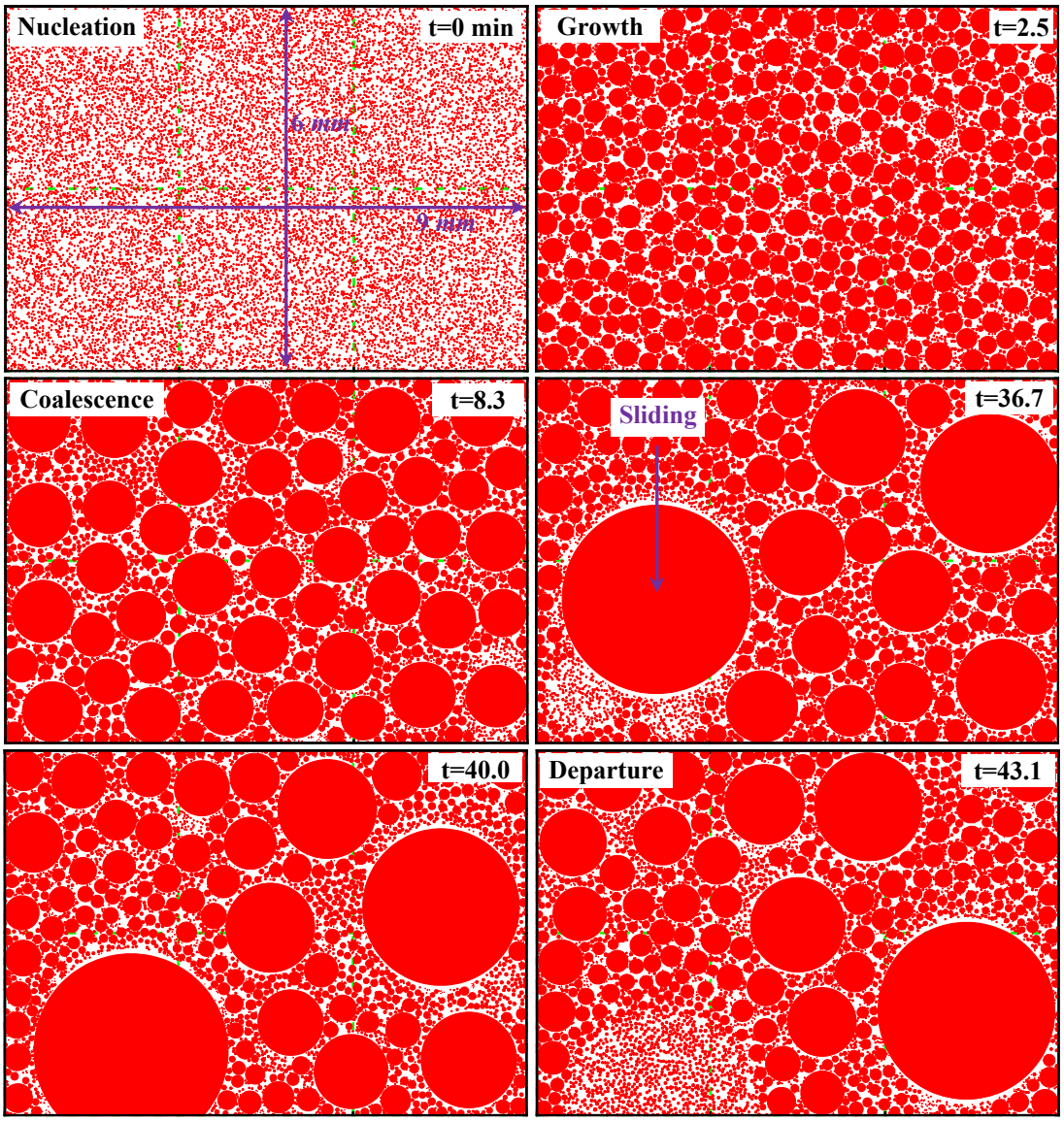

Figure 5.5 Visualization of main sub-processes captured in the simulation of dropwise condensation on the vertical substrate of area 9 mm*6 mm (ΔT_{dw}=1.0 K).

Figure 5.6 presents the droplet-size density distribution of various temporal stages in the low sub-cooling experiments and the simulation using the nucleation-site density 3.7×10^8 $/m^2$ after reaching the steady-state. Although the droplet radius less than ~10 μm cannot be

considered in checking of droplet for experimental images, the discontinuity in the sub-cooling 0.48 *K* is also nearly visible. Clearly, the simulated droplet-size density distribution accurately predicts the experimental discontinuity. Furthermore, a good fitting between the experiment and the simulation for the big droplets of the coalescence size region also confirm the used nucleation-site density in simulation. Here, the used nucleation-site density is evidently lower than the pure steam case reported in [4]. This effect is explained by Lan et al. [101]. In their works, a physical and mathematical model with respect to the molecular clustering is proposed to describe the nucleation process of vapor molecules in steam condensation with NCG. The reduced nucleation-site density attributes to the positions of vapor clusters occupied by the NCG molecules. That is the droplet size distribution density will decrease with the increasing amount of NCG.

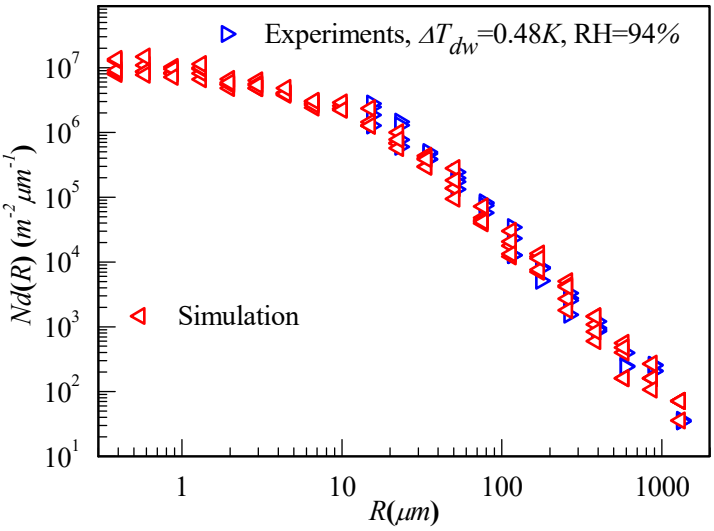

Figure 5.6 Droplet size density distribution of various temporal stages during the experiment and simulation.

Figure 5.7 shows the variation of area coverage ratio and the available droplet number against the computing time, and they also give the effect of sub-cooling. A reverse tendency for those two parameters is correspondingly presented in Figure 5.7. At the beginning of dropwise condensation, the droplets growing only by direct condensation increase the area coverage ratio ω and decrease the available droplet number N dramatically. When the coalescence starts to promote the droplet growth, the fluctuating increase of the area coverage ratio and the fluctuating decease of available droplet number are provided until the first departure. After the first droplet departing from the substrate, dropwise condensation enters a dynamic steady-state. The surface coverage ratio and the available droplet number begin to fluctuate violently as the result of the sweeping effect of sliding droplets and the coalescence. It is easy to understand that two adjacent peak and wave imply the droplet departure from the substrate. Note that the steady-state is achieved more rapidly when the degree of sub-cooling is increased. More departing droplets are found at high sub-cooling.

In view of the time-averaged value, the area coverage ratio is increased with the increasing of sub-cooling. The available droplet number behaves in an opposite fashion. This can be

ascribed to as follows: owing to the increasing of sub-cooling, the resulting higher growth rate accelerates the coalescence and the departure of droplets, the substrate is mostly covered by the big droplets and less space is left for re-nucleation. So the tendency of surface coverage ratio and available droplet number can be extrapolated. As reported in section 2.3.1, the measured surface coverage ratio located in the range 0.63 - 0.74 is slightly lower than the simulation results (0.8 - 0.87), which can be explained by the fact that smaller droplets are not accounted due to the camera limitations.

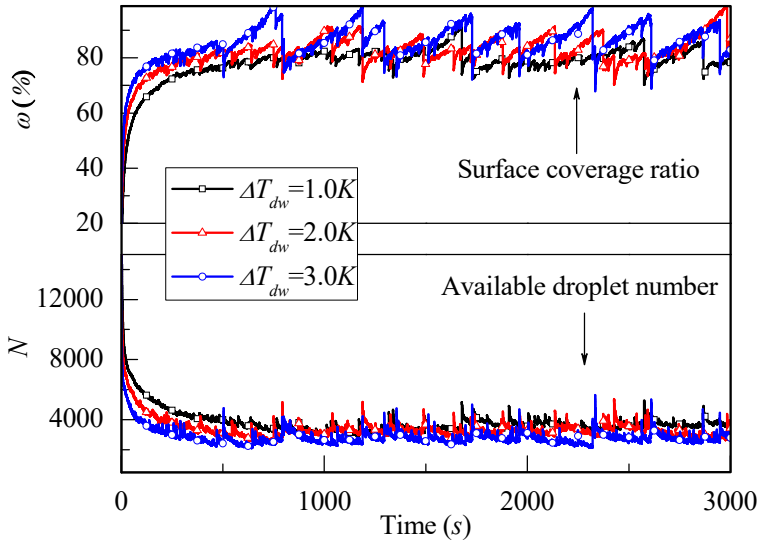

Figure 5.7 The area coverage ratio and available droplet number with respect to time and the degree of sub-cooling in 94% RH.

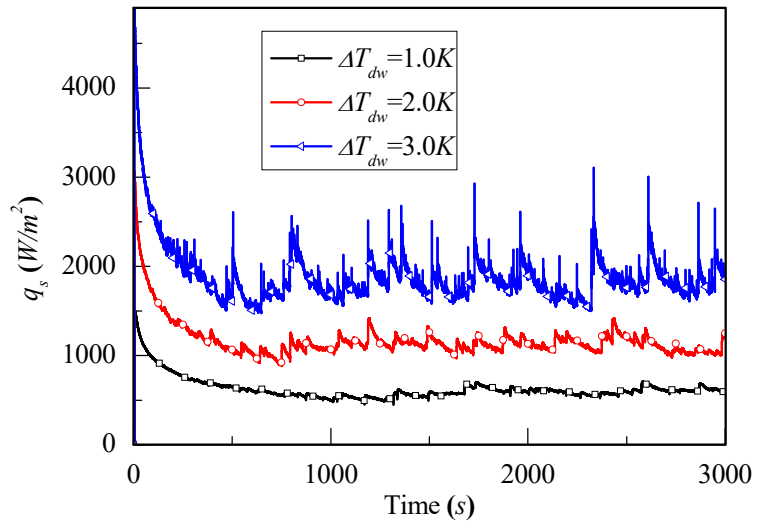

Figure 5.8 Fluctuations in the condensation heat flux as a function of computing time.

The heat transfer performance is more concerned for dropwise condensation. Accordingly, the fluctuation of the condensation heat flux in the simulation as a function of computing time is depicted in Figure 5.8 depending on the sub-cooling. It is clear that the heat transfer fluctuation is corresponded to the droplet dynamics which results in the effect of area coverage ratio and available droplet number as shown in Figure 5.7. The peak at the beginning of simulation in Figure 5.8 implies the coming departure. On the other hand, from

Figure 5.7 and Figure 5.8, it can be concluded that the droplet distribution is not depended on the sub-cooling which just changes the droplet fresh frequency on the substrate. The droplet distribution locates on a steady state in statistic for different sub-cooling. As the result of the enhanced droplet dynamics (coalescence, the sweeping of sliding droplet and the departure) and the increased driving force, the heat transfer rate of dropwise condensation is improved by the increasing of the sub-cooling degree.

What should be mentioned is that the interaction effects between droplets and the convective mass transfer are not considered in above modeling. As the reasons given in section 5.4, the droplet distributions provided by this section will be utilized to consider those two aspects as following.

5.5.3 Interaction effect between droplets

During dropwise condensation, the droplets face a strong interaction due to the closer inter-spacing and a large number of neighboring droplets. As evaluated in chapter 4, PSM is limited to the relatively weak interaction because of the simplification in deriving process. MOI is divergent meeting a strong interaction. In comparison, the proposed DPSM can accurately capture the strong interaction using a small number of the point sinks. Therefore, the proposed DPSM is adopted to analyze a characteristic spatial distribution mode of the droplets from dropwise condensation experiments, as the snapshot shown in Figure 5.9. The snapshot (9400×6800 μm) is recorded by the microscope camera. For it, 1167 droplets with the radius from 20.00 μm to 1090.69 μm are detected and marked by the red circles. The detected position and size information of the droplets are putted into DPSM for predicting the droplets interaction effect. The droplets are seen as a spherical cap having the contact angle 90 deg. For each droplet, the radius of the imaginary sphere and the point sinks number for one droplet are respectively chosen as R_{is} = 0.5*R and M = 200 considering the computation cost and the solution accuracy. Because of a large number of droplets, the solution based on the GPBiCG and TwoD algorithms is carried out on a distributed supercomputer. The numerical errors for GPBiCG and TwoD algorithms are chosen as 1e-5 and 1e-6 respectively.

Considering the droplet system in Figure 5.9, the interaction effects of all droplets are solved by DPSM. Aiming to explain the interaction intuitively, the location and size of droplets are plotted in Figure 5.10(a) and the droplets are filled by the color according to its correction factors. Figure 5.10(b) plots the correction factors of the droplets versus its radius. In Figure 5.10(b), the correction factors mean that the droplet condensation rate is 3-1000 times lower than that of single isolated droplet due to the interaction effect between droplets. On the other hand, the correction factor defined by Eq. (4.4) denotes how strong the interaction is. The droplet suffers a strong interaction by surrounding droplets if its correction factor is small; otherwise, the imposed interaction is weak. That is the correction factor is related to the intensity of the interaction. Comparing with the big size droplet, the small size droplets are easily affected by the neighbors. Thus, on the whole, small droplets have a smaller correction factor corresponding to the strong interaction. On the other hand, the

droplet correction factor (interaction intensity) is not absolutely depended on its size. As three droplets marked by numbers (1, 2 and 3), they approximately have the equal size. However the different locations result in different correction factors. As a whole, the droplets closing to the substrate edge have a weaker interaction than the droplets locating on the substrate center, as observed in experiments [42]. Actually, the droplet interaction as a complicated phenomenon is mainly depended on its own size, the number and size of the surrounding droplets and their inter-spacing.

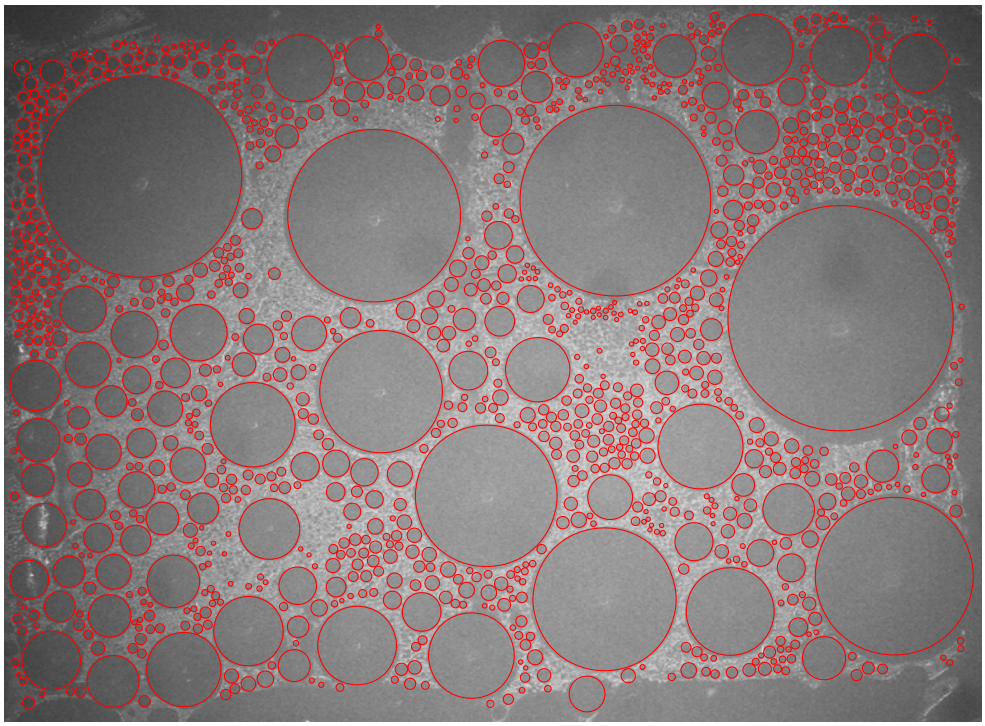

Figure 5.9 A characteristic droplet array during dropwise condensation experiments and the detected droplets.

In Figure 5.9, only the droplets having the radius greater than 20 μm are detected due to the limitation of the camera. However, dropwise condensation has a multi-scale feature as the droplet size spreads from the nucleation size of some nanometers to the maximum size at millimeter scale. For the droplets distribution in Figure 5.9, the droplets smaller than 20 μm are not included in analyzing the interaction effect using DPSM. As discussed above, the bigger size droplets are not significantly affected by small size droplets.

In order to quantify the influence of the missed small droplets, for the droplets distribution in Figure 5.9 the minimum radius of the considered droplets is gradually decreased in modeling the interaction effect using DPSM. With the decrements in the minimum radius, step by step, the number of the droplets is increased and small droplets are added in the calculation of the correction factor. During those process, we focus attention on four droplets (A, B, C and D) having different sizes as shown in Figure 5.10(a). The predicted correction factors for the droplets of interest are plotted in Figure 5.11(a), with the number of the surrounding droplets sorted in ascending order due to decreasing minimum radius of droplets considered. It is clear that the predicted corrector factors converge gradually by considering

more droplets in each calculation. The droplets in the size range 20-50 μm give an influence for the correction factor less than 10%. As more of the small droplets, the relative error between decrements in the minimum size of the considered droplets is less than 1% from Figure 5.11(b).

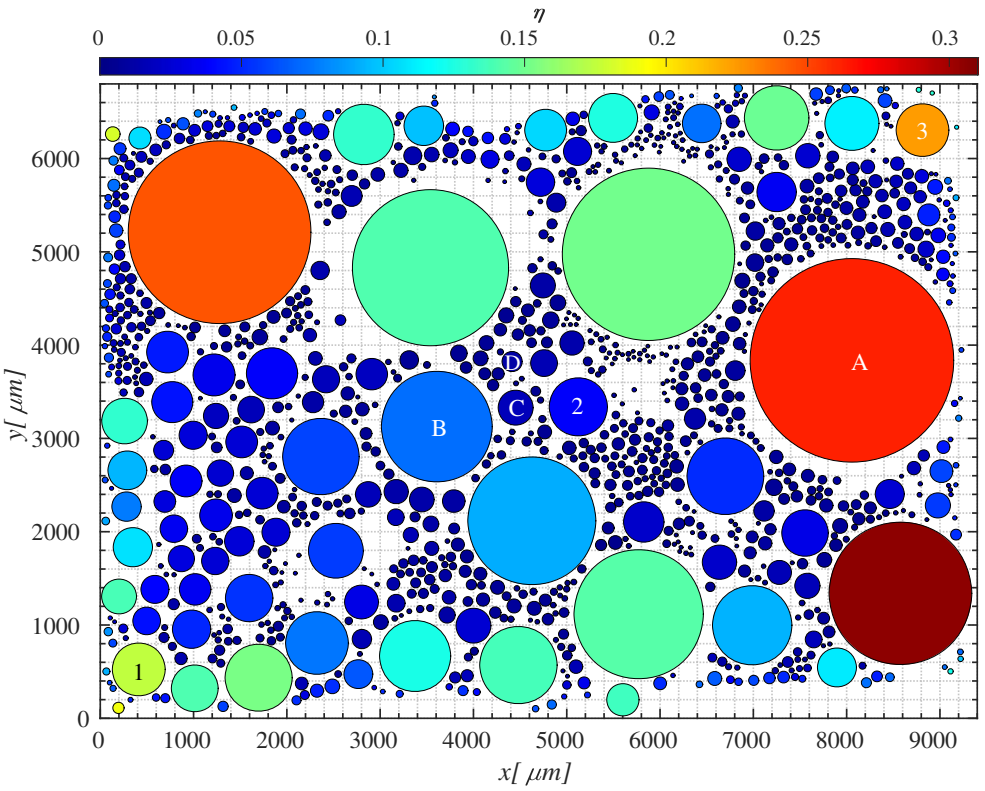

(a)

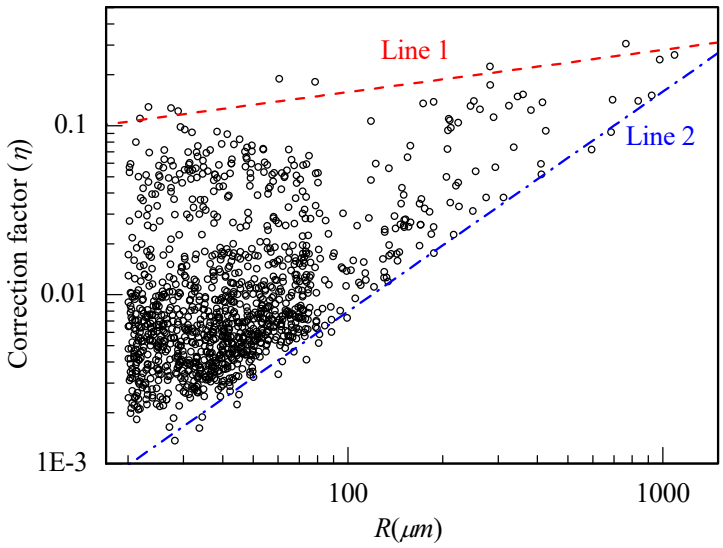

(b)

Figure 5.10 (a) the color filling the droplets according to its correction factor; (b) the correction factors of the droplets versus its radius.

In general, an accurate prediction of the interaction effects must consider all droplets over the condensation substrate. However, more droplets considered mean more computation cost.

From these results, it can be observed that the bigger size droplets contribute more for the interactions between droplets. Prediction of the interaction effects is not significantly influenced by the smaller size droplets. The minimum size of the considered droplets up to 20 μm is sufficient to accurately predict the interaction effects during dropwise condensation.

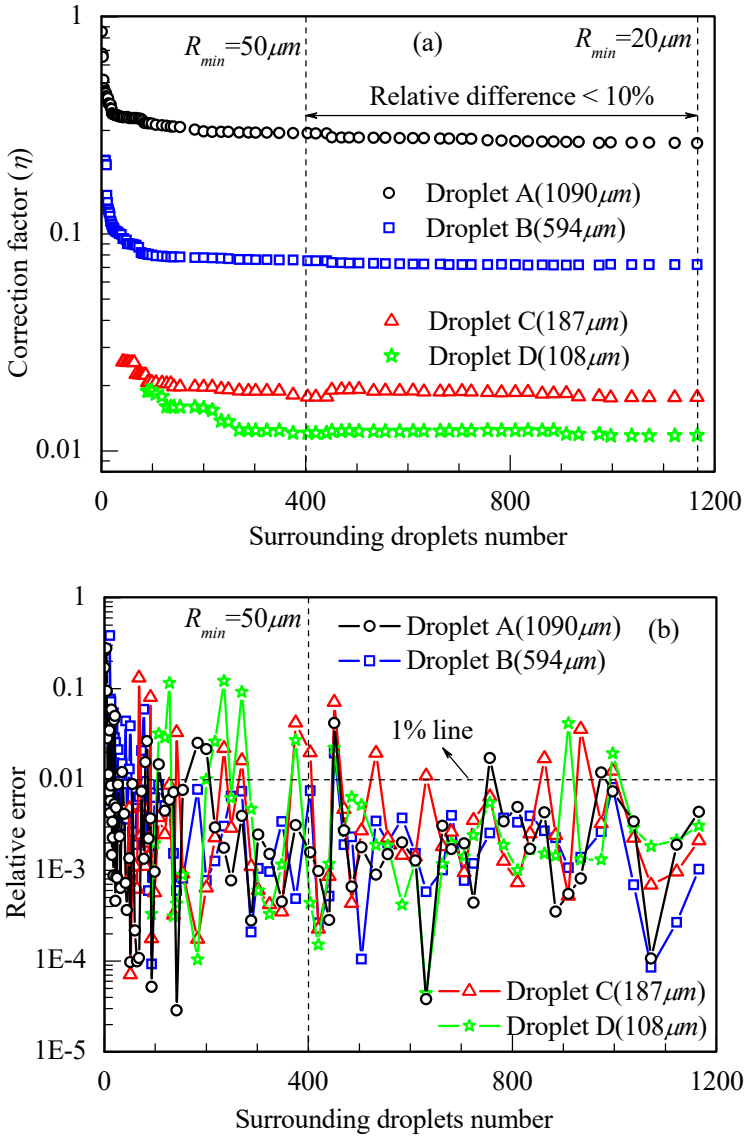

Figure 5.11 Prediction of the correction factor with a decreasing minimum size of the considered droplets. (a) the predicted correction factor for the interesting droplet; (b) the relative error between decrements in the minimum size of droplets considered.

To sum it up, the droplet interaction effects are strongly depended on the size and spatial distributions of droplets. Over the condensation substrate, as a complicated dynamic behavior the size and spatial distributions of droplets are changing constantly during condensation. In section 5.2, a numerical algorithm is developed to simulate the dynamic behaviors of droplets during dropwise condensation. The re-produced instantaneous droplet distributions have been presented in Figure 5.5 and the resulting droplet size distribution density also shows a good agreement with the experimental results in Figure 5.6. For a simulated size and spatial distributions of droplets, the interaction effects between droplets are solved using DPSM with

the minimum radius of the considered droplets 10 μm. As before, the predicted correction factors are depicted in Figure 5.12 using two manners. The results reflect the general character with that in Figure 5.10 for the experimental droplet distribution.

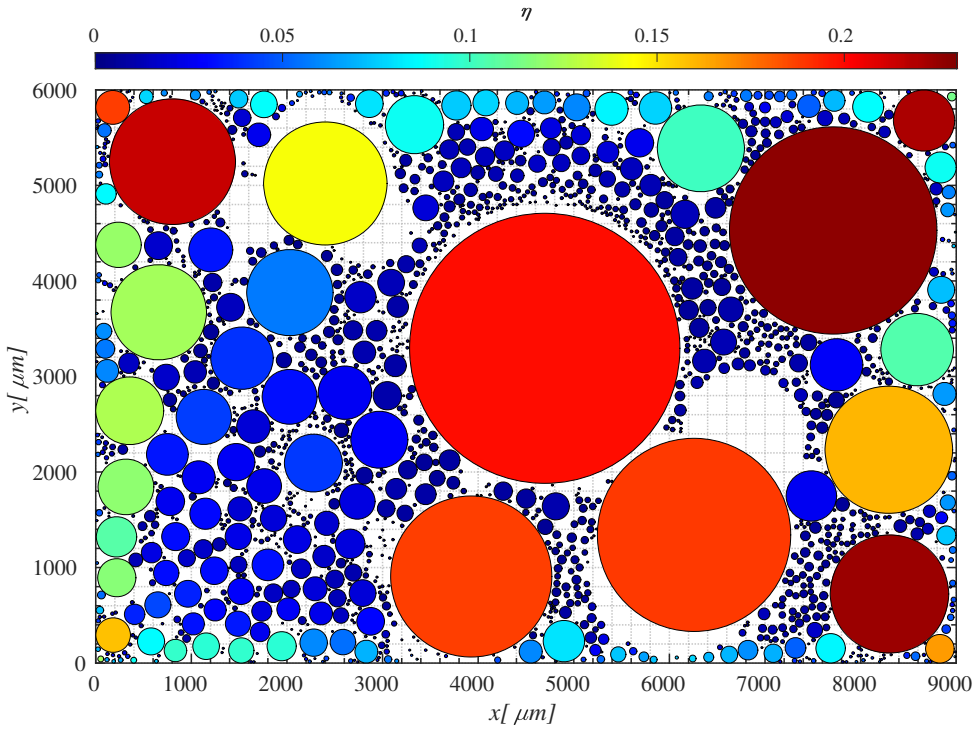

(a)

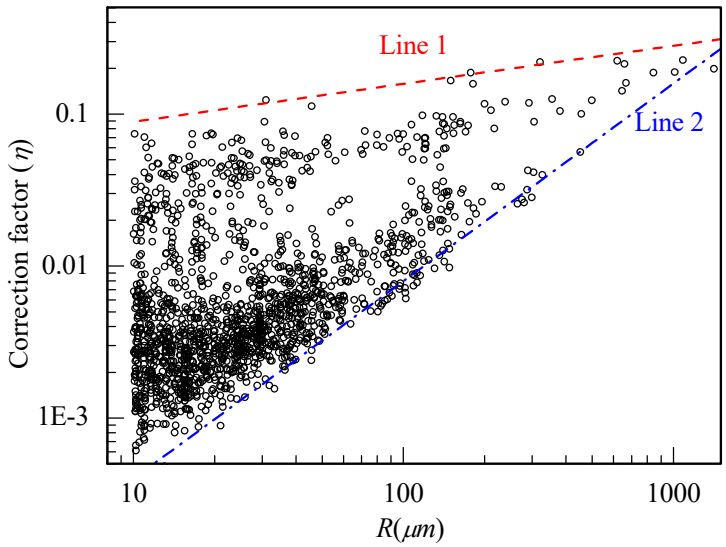

(b)

Figure 5.12 Prediction of the interaction effects for a simulated droplet distribution. (a) the color filling the droplets according to its correction factor; (b) the correction factors of the droplets versus its radius.

In addition, different droplet distributions from experiments and simulation are also considered to predict the interaction effects between droplets using DPSM. The predicted correction factors for those distributions have been presented in APPENDIX D. Although no rule for the correction factor of individual droplet can be found, the predicted correction

factors versus the droplet radius state that the correction factors are totally scattered between line 1 and line 2 for different distributions. The upper bound by line 1 denotes the weak interaction (e. g., the droplets near the substrate edge); the lower bound by line 2 represents the strong interaction (e. g., the droplets locating on the substrate center and small droplets closing larger one). Accordingly, the interaction effects of droplets during dropwise condensation have generality on the whole, and also present personality as an independent individual.

5.5.4 Evaluation of single droplet growth rate

According to section 5.4, the growth rate of single droplet during dropwise condensation dR/dt can be evaluated by including the interaction effects of droplets and the enhancing effect of convective mass transfer:

$$\frac{dR}{dt} = Sh_d * \eta * \left(\frac{dR}{dt}\right)_{iso} \tag{5.8}$$

where the droplet growth rate by the isolated droplet model as $(dR/dt)_{iso}$ is calculated by Eq. (3.22). Eq. (5.3) permits to define the droplet Sherwood number Sh_d. The point is how to accurately predict the correction factor η.

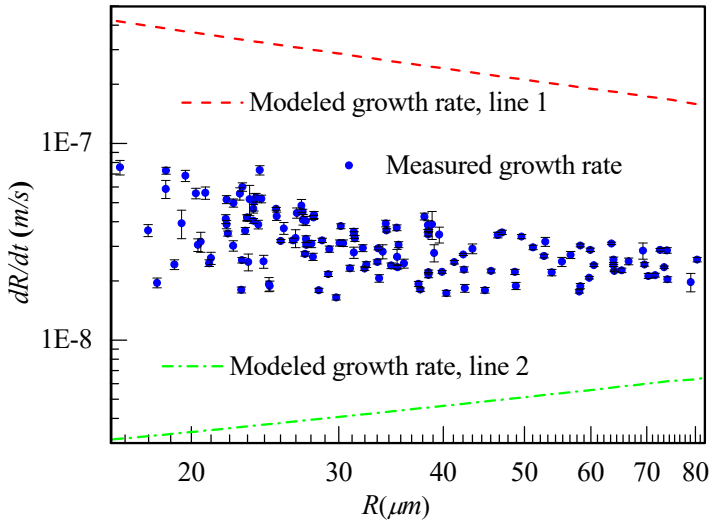

Figure 5.13 The predicted range of the droplet growth rate and the measured results.

In section 5.5.3, we have previously concluded that the interaction effect of droplets is sensitive to the size and spatial distributions of droplets. The correction factor related to the droplet interaction effect changes at all times and places. Furthermore, the correction factors for the equally size droplets differ up to two orders in different conditions. An exact definition for the correction factor depends on the accurately captured distribution of the droplets size and spatial. In chapter 2, the droplet growth rates are measured by the camera which focuses on a small part of the substrate. In spite of the measured growth rate, the droplet distribution over the whole substrate can not be captured correspondingly due to the limited view of the camera in high magnification. Therefore the direct comparison between the modeling and measured growth rates can not be released. A feasible manner is we can apply the generality

for the interaction effects, i.e. the upper and lower bounds of the correction factors by line 1 and 2 in last section. With that, one can delimit the range of the droplet growth rate. Keeping consistent with the experimental conditions, the upper and lower bounds of the droplet growth rate are defined by using the upper and lower bounds of the correction factors. The upper and lower bounds (by line 1 and 2) are depicted together with the measured data, as shown in Figure 5.13. It can be seen that the measured droplet growth rates are scattered into the predicted range. As probably noticed, the measured growth rate is far away from the predicted bounds. It is because that not all of the characteristics of the interaction effect can be captured due to the influence of the coalescence events.

5.5.5 Evaluation of the overall heat flux

Based on the predicted correction factor in Figure 5.10 and Figure .12, the total heat flow rate contributed by all droplets can be evaluated by:

$$Q_t = L\sum_{R_{\min}}^{R_{\max}} Sh_d \eta m_{iso} \tag{5.9}$$

where R_{max} is the maximum droplet radius in the droplet distribution, R_{min} is the minimum radius of the interesting droplets. Eq. (5.9) means the total heat flow contributed by the droplets locating at the size range R_{max}-R_{min}. By decreasing R_{min}, the heat flow rate due to smaller droplets is included into Q_t step by step. For two droplet distributions and the corresponding predicted correction factor as shown in Figure 5.10 and Figure 5.12, the predicted total heat flow rate is depicted against R_{min} in Figure 5.14. With more droplets considered, the total heat flow rate converges gradually. The increase is slowed down quickly and the increment thanks to the droplets between 100-10 μm is less than 6%. When R_{min} = 20 μm, the relative error of Q_t is within 0.2%. It is no doubt that the droplets having the size greater than 100 μm contribute the main heat flow rate.

In case of pure steam, it is widely accepted that heat transfer is mainly attributed to the quite small droplets. As shown in Figure 3.5, in case of pure steam the growth rates of small droplets are few orders higher than big droplets having larger thermal conduction resistance. In addition, much more large number of small droplets also makes explain. As a consequence, aiming to promote dropwise condensation heat transfer of pure steam, investigations are concentrated on enhancing the droplet dynamics and accelerating the departure of the big droplets [4, 6, 8, 11-12, 15, 18]. However, it is reversed in the presence of NCG. As resulted in Figure 5.14, the relatively larger droplets are more beneficial for dropwise condensation heat transfer with the presence of NCG. From Figure 3.5, the predicted growth rate by the isolated growth model still follows the case of pure steam that smaller droplets grow few order faster than larger droplets. The difference is the convective mass transfer and the interaction effects between droplets turn in favor of big droplets, as presented in sections 5.3 and 5.5.3. As discussed in section 5.5.2, the presence of NCG also decreases the nucleation-site density, which represents less small droplets. All those aspects together lead to the primary contribution of big droplets for dropwise condensation heat transfer in case of NCG.

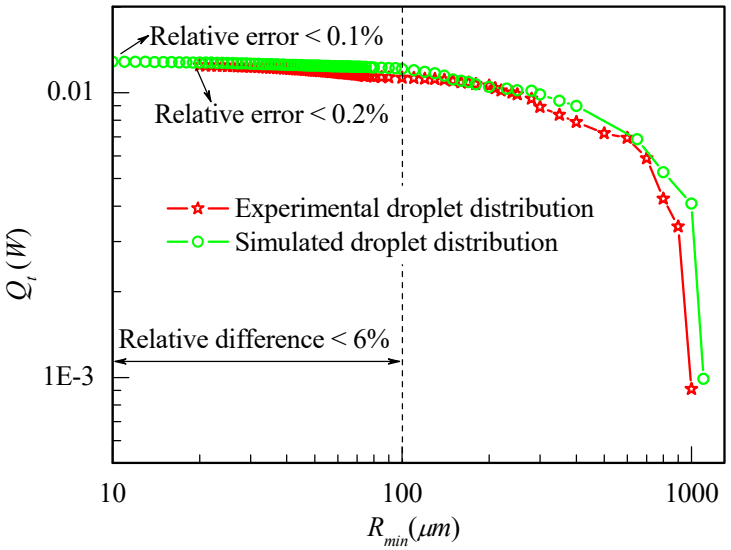

Figure 5.14 The predicted heat flow rate for the droplets of interest.

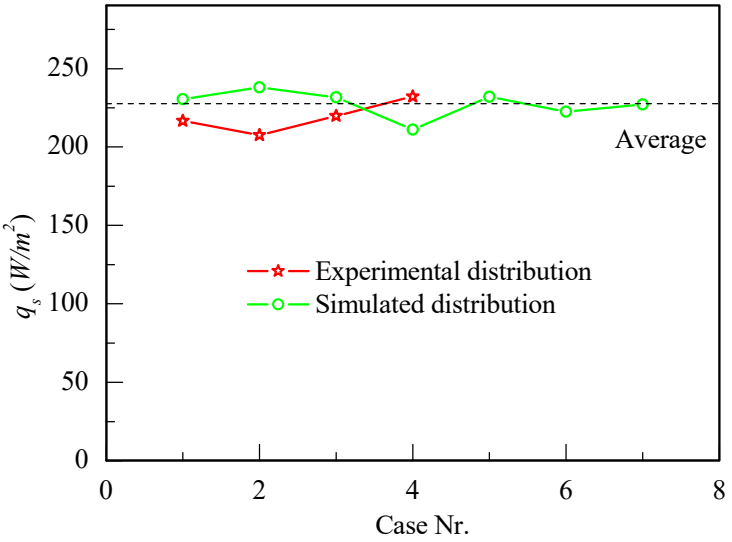

Figure 5.15 The predicted overall condensation heat flux after correcting at different time steps in simulation.

Owing to the computation cost of a certain droplet distribution by DPSM, it is impossible to correct the droplet growth rates at each time steps. For that reason the corrections considering the droplets interaction effects and convective mass transfer are applied to the droplet distribution at some discrete time points of simulation. Figure 5.15 depicts the predicted condensation heat flux after correcting q_s at Re = 1671 and ΔT_{dw} =1.0 K. The condensation heat flux for a certain droplet distribution is calculated by Eq. (5.6) using the total condensation rate by Eq. (5.5). From the beginning of this subsection, we have shown that the droplets greater than 20 μm are sufficient to accurately predict the instantaneous overall heat flux for a certain droplet distribution. Thus, the minimum droplet considered is chosen at 20 μm for all considered cases. The fluctuation of the heat flux in Figure 5.15 is normal because of different size and spatial distributions of droplets as a result of the droplet dynamics. Then, the predicted values for all cases are averaged as the final condensation heat

flux. Using Eq. (5.7), the overall heat flux q_t is the sum of the mean condensation heat flux and the heat flux by the forced convection. Finally, the predicted overall heat flux q_t at different *Re* and sub-cooling are plotted against the experimentally measured results, as shown in Figure 5.16. To sum it up, the predicted overall heat flux and the experimental data show a good agreement, which verifies the present modeling manner. Those important aspects are accurately captured in modeling.

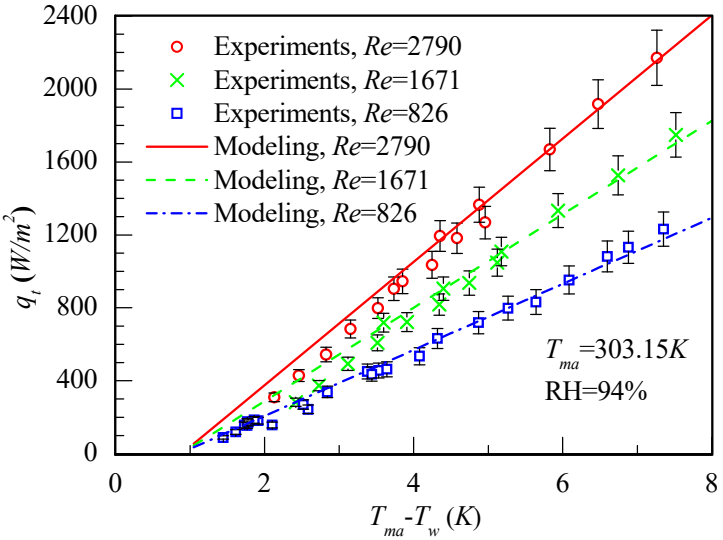

Figure 5.16 The predicted overall heat fluxes and the measured results at different *Re*.

5.6 Conclusions

In this chapter, a modeling idea is constructed for coupled heat and mass transfer driven dropwise condensation with considering NCG. The isolated growth model developed in chapter 3 is applied to predict the growth rate of droplets. The droplet size and spatial distribution is re-produced by a number algorithm which sufficiently reflects the droplet dynamics in details. The interaction effects between droplets are considered by the correction factors solved by DPSM. Additionally, the influence of convective mass transfer is included by the droplet Sherwood number. Using all those aspects, modeling of heat and mass transfer for convective dropwise condensation flow of moist air is launched. The present modeling idea is firstly evaluated by the experimentally determined droplet growth rate. And good overall agreement of the overall heat flux between the experimental and predicted results demonstrate that the current modeling idea is robust and applicable to dropwise condensation in the presence of NCG. This works also highlight the interaction effects between droplets, except the reduction of droplet growth rate by the diffusion resistance, is also responsible for the heat transfer reduction due to the presence of NCG. Nevertheless, convective mass transfer has a great potential for promoting dropwise condensation heat transfer in case of NCG. Furthermore, it is notably shown through the interaction of those aspects that in contrast to the pure steam condition the big droplets contributes more for condensation heat flow rate.

Chapter 6 Simulation by a Multi-component Multi-phase Lattice Boltzmann Model

A multi-component multi-phase thermal lattice Boltzmann model considering vapor-liquid phase change is developed to study droplet condensation with the presence of non-condensable gas. Some tests, including an isolated droplet evaporation, are conducted to verify the capability of this model in simulating multi-component multi-phase flow with vapor-liquid phase change. After that, single droplet condensation considering non-condensable gas is investigated with different mass fraction of non-condensable component and contact angles. The results show that the influence of the non-condensable gas upon droplet condensation heat transfer is depended on the growth stage and the amount of the non-condensable gas. The mass transfer of vapor and non-condensable component will tend to an equilibrium state with the droplet condensation going. Furthermore, for different contact angles, the dynamic behavior of the contact line plays a critical role in the accumulation effect of the non-condensable component. And the heat transfer of droplet condensation is enhanced by the hydrophilic substrate rather than the hydrophobic substrate as expected, no matter adding the non-condensable component or not. In different conditions, the power law, which fits the droplet radius with time, is used to define the growth rate mathematically.

6.1 Literature review

Known as a typical case of multiphase flow, dropwise condensation having the complicated dynamic behavior of the droplets (nucleation, growth, coalescence and motion) collects many difficult topics, including vapor-liquid phase change, free surface flow, coupled heat and mass transfer, multi-scale feature, interfacial behavior. Because of those difficulties, it is always a great challenge for the numerical simulation of dropwise condensation.

Computational fluid dynamics (CFD) based on solving the Reynolds-averaged Navier-Stokes (RANS) equations has shown a considerable success in simulating single-phase flow and heat transfer. For modeling multiphase flow undergoing a phase change process, many approaches based on CFD have been proposed [102, 103]. As reviewed by Kharangate and Mudawar [103], all efforts for the simulation of multiphase flow focus on the phase interface. That is exactly because the multiphase flow with phase change is complicated by the deformability and the motion of the interface. Therefore, the simulation must consider

tracking the moving interface, computing momentum, heat and mass transfer across the interface region, and hydrodynamics of the superposed flow. However, following the assumption of continuum, the conventional CFD based multiphase models neglect that the interface and the phase separation are the result of molecular interactions. It is still necessary to bridge the macroscopic phenomena and the underlying microscopic dynamic. As a fundamental approach, the microscopic numerical methods, such as molecular dynamics (MD) and direct simulation Monte Carlo (DSMC), are capable of capturing the microscopic interactions, while the high computational cost restricts their application [104].

The lattice Boltzmann (LB) method, a mesoscopic method which discretizes the original Boltzmann equation of the kinetic theory, has become a powerful simulation tool in modeling complex flows involving interfacial dynamics and complex boundaries. The kinetic and mesoscopic nature of the LB method bring its advantages, which permits it to reflect the hydrodynamic behavior at the macroscopic scale as well as the microscopic dynamics [105-107]. With the developments during the past two decades, the LB method has become to be a powerful and efficient simulation method in various phenomena and processes [108-111]. Many multiphase LB methods proposed have been deeply reviewed and summarized by Huang et al. [108] and Li et al. [109]. Especially, Li et al. [109] present the elaboration of a critical review for LB methods for multiphase flow and phase-change heat transfer. Owing to the computational efficiency and straightforward algorithm, the pseudopotential LB method devised by Shan and Chen [112-113] has developed into a very popular model in the multiphase LB community and has been adopted successfully to many problems [109, 114]. In this method, the phase separation is realized spontaneously via the introduced inter-particle pseudopotential for determining the fluid interactions. Therefore, the interface motion is simulated without utilizing any techniques to track or capture interfaces.

Besides its great progresses in single-component multi-phase flows, many efforts [115-117] are still trying to improve and complete the multi-component pseudopotential LB method. In the original pseudopotential LB model for a multi-component system, the external force is incorporated into an equilibrium velocity [112]. However, the investigation of Porter et al. [115] stated that this formulation will lead to viscosity-dependent numerical results. An explicit forcing model incorporating the external forces into the discrete Boltzmann equation for each component results in the viscosity-independent equilibrium densities and is capable for a larger kinematic viscosity ratio. In the method of Chai and Zhao [116] and Sbragaglia and Belardinelli [117], the velocity used in the equilibrium distribution function and the forcing term is just the mixture velocity based on the MRT version of Guo et al.'s forcing scheme. Most recently, some efforts [118-121] for the multi-component pseudopotential LB model have been given. Zhu et al. [118] developed a multi-component LB-MRT model in simulating multi-phase flow at a larger density ratio with small spurious current and better numerical stability. The heat transfer model for heat conduction melting is also considered by coupling the enthalpy-based method as the solid-liquid phase change term. Based on the original multi-component LB model, Li et al [119] and Zhang et al. [120] separately

constructed a multi-component multi-phase thermal LB-BGK model with vapor-liquid phase change to simulate condensation with the presence of NCG. What deserves to mention is the fresh work from Hou et al. [121]. In their study, the improvements of the single-component LB model by Li et al. [122-123] is extended to the multi-component system for realizing low spurious current, good thermodynamic consistency, viscosity-dependent densities, large density and kinematic viscosity ratios. Nevertheless, the thermal effect is not considered. As concluded in [109], the theory of multi-component pseudopotential LB method is far from being complete in spite of much progresses achieved.

In the present study, some recent improvements in LB community are adopted to develop a multi-component multi-phase hybrid thermal LB-MRT model with vapor-liquid phase change, which can achieve low spurious current, viscosity-dependent results and a large density ratio. The improvement by Li et al. [122-123] for restoring the thermodynamic consistency of the single-component LB model is extended to the present multi-component LB model, as done in reference [121]. Following the references [116-117], the mixture velocity is used in the equilibrium distribution function and the forcing term. The temperature solver in [122-123, 124] is extended for simulating heat transfer with vapor-liquid phase change in a multi-component system. After the elaboration of the validation of the present LB model, single droplet condensation in the presence of the non-condensable component is simulated considering a variety NCG concentrations and different contact angles.

6.2 Model description

6.2.1 Multi-component multi-phase pseudopotential LB-MRT model

The multi-relaxation-time (MRT) collision operator [125], which is superior over the Bhatnagar-Gross-Ktook (BGK) collision operator [126] in terms of accuracy [124, 127], model stability [127], large viscosity ratio [115] and density ratio [121-122, 128], is adopted in this work. In the two-dimensions, the multi-component multi-phase pseudopotential-based LB-MRT model for the evaluation of the density distribution function of each component can be written as [121-122, 128]:

$$f_{k,\alpha}\left(\boldsymbol{x}+\boldsymbol{e}_{\alpha}\delta_t,t+\delta_t\right)=f_{k,\alpha}\left(\boldsymbol{x},t\right)-\left(\mathbf{M}^{-1}\boldsymbol{\Lambda}\mathbf{M}\right)_{\alpha\beta}\left(f_{k,\beta}\left(\boldsymbol{x},t\right)-f_{k,\beta}^{eq}\left(\boldsymbol{x},t\right)\right)+\delta_t F'_{k,\alpha}\left(\boldsymbol{x},t\right) \quad (6.1)$$

where $f_{k,\alpha}(\boldsymbol{x},t)$ stands for the particle density distribution function of component k along the α-th direction at time t and position $\boldsymbol{x}$, $F'_{k,\alpha}$ denotes the forcing term in the discrete velocity space. In the two-dimensional nine-velocity scheme (D2Q9), the discrete lattice velocity vector $\boldsymbol{e}_{\alpha}$ can be defined as:

$$\left[\boldsymbol{e}_0,\boldsymbol{e}_1,\boldsymbol{e}_2,\boldsymbol{e}_3,\boldsymbol{e}_4,\boldsymbol{e}_5,\boldsymbol{e}_6,\boldsymbol{e}_7,\boldsymbol{e}_8\right]=lc\begin{bmatrix}0 & 1 & 0 & -1 & 0 & 1 & -1 & -1 & 1\\ 0 & 0 & 1 & 0 & -1 & 1 & 1 & -1 & -1\end{bmatrix} \quad (6.2)$$

where $lc=\delta_x/\delta_t$ is the lattice constant with the lattice spacing δ_x and the time spacing δ_t (equal to unit in this work). And $f_{k,\alpha}^{eq}(\boldsymbol{x},t)$ is the equilibrium density distribution function defined by:

$$f_{k,\alpha}^{eq}\left(\boldsymbol{x},t\right)=w_{\alpha}\rho_{k}\left[1+\frac{\boldsymbol{e}_{\alpha}\cdot\boldsymbol{u}}{lc_{s}^{2}}+\frac{\left(\boldsymbol{e}_{\alpha}\cdot\boldsymbol{u}\right)^{2}}{2lc_{s}^{4}}-\frac{\boldsymbol{u}^{2}}{2lc_{s}^{2}}\right] \tag{6.3}$$

where w_{α} are the weighting coefficients. For the D2Q9 model, w_{0}=4/9 and $w_{1\text{-}4}$=1/9 for four nearest lattices, $w_{5\text{-}8}$=1/36 for four next-nearest lattices. The lattice sound speed lc_s is set to be $lc_s = lc/\sqrt{3}$. For the present multi-component LB model, the macroscopic density ρ_k and the mixture velocity vector $\boldsymbol{u}$ can be determined via [116-117, 121]:

$$\rho_{k}=\sum\nolimits_{\alpha}f_{k,\alpha} \tag{6.4}$$

$$\boldsymbol{u}=\frac{\sum_{k}\left(\sum_{\alpha}f_{k,\alpha}\boldsymbol{e}_{\alpha}+0.5\delta_{t}\boldsymbol{F}_{k}\right)}{\sum_{k}\rho_{k}} \tag{6.5}$$

where $\boldsymbol{F}_k$ stands for the total body force acting on the fluid particle of the component k.

In Eq. (6.1), the collision matrix is defined by $(\mathbf{M}^{-1}\mathbf{\Lambda}\mathbf{M})_{\alpha\beta}$. $\mathbf{\Lambda}$ and $\mathbf{M}$ are a diagonal matrix and an orthogonal transformation matrix, respectively, and defined as below [125]:

$$\mathbf{M}=\begin{bmatrix}1&1&1&1&1&1&1&1&1\\-4&-1&-1&-1&-1&2&2&2&2\\4&-2&-2&-2&-2&1&1&1&1\\0&1&0&-1&0&1&-1&-1&1\\0&-2&0&2&0&1&-1&-1&1\\0&0&1&0&-1&1&1&-1&-1\\0&0&-2&0&2&1&1&-1&-1\\0&1&-1&1&-1&0&0&0&0\\0&0&0&0&0&1&-1&1&-1\end{bmatrix} \tag{6.6}$$

$$\mathbf{\Lambda}=diag\left(\tau_{\rho}^{-1},\tau_{e}^{-1},\tau_{\varsigma}^{-1},\tau_{j}^{-1},\tau_{q}^{-1},\tau_{j}^{-1},\tau_{q}^{-1},\tau_{\upsilon}^{-1},\tau_{\upsilon}^{-1}\right) \tag{6.7}$$

where the relaxations in Eq. (6.7), which are set as , $\tau_{\rho}^{-1} = \tau_{j}^{-1} = 1$, $\tau_{e}^{-1} = \tau_{\zeta}^{-1} = 0.8$, $\tau_{q}^{-1} = 1.1$ [121, 129], is significant to optimize the LB-MRT model. The relaxation time τ_{υ} is determined by the kinematic viscosity (υ) with $\upsilon = lc_s^2(\tau_{\upsilon}\text{-}0.5)$.

Using the transformation matrix $\mathbf{M}$, the collision process is transformed to the moment space as follows:

$$\mathbf{m}_{k}^{*}=\mathbf{m}_{k}-\mathbf{\Lambda}\left(\mathbf{m}_{k}-\mathbf{m}_{k}^{eq}\right)+\delta_{t}\left(\mathbf{I}-0.5\mathbf{\Lambda}\right)\mathbf{S}_{k} \tag{6.8}$$

where $\mathbf{I}$ is the unit tensor, the distribution functions at the moment space $\mathbf{m}_k$ and $\mathbf{m}_k^{eq}$ are derived from $\mathbf{m}_k = \mathbf{M}\mathbf{f}_k$ and $\mathbf{m}_k^{eq} = \mathbf{M}\mathbf{f}_k^{eq}$ with $\mathbf{f}_k = (f_{k,0}, f_{k,1}, \ldots, f_{k,8})^T$ and $\mathbf{f}_k^{eq} = (f_{k,0}^{eq}, f_{k,1}^{eq}, \ldots, f_{k,8}^{eq})^T$. Based on Eq. (6.3) and (6.6), the equilibrium distribution function at the moment space $\mathbf{m}_k^{eq}$ can be finally obtained:

$$\mathbf{m}_{k}^{eq}=\rho_{k}\left(1,-2+3\left|\boldsymbol{u}\right|^{2},1-3\left|\boldsymbol{u}\right|^{2},u_{x},-u_{x},u_{y},-u_{y},u_{x}^{2}-u_{y}^{2},u_{x}u_{y}\right)^{T} \tag{6.9}$$

And then the streaming process can be formulated by:

$$f_{k,\alpha}\left(\boldsymbol{x}+\boldsymbol{e}_{\alpha}\delta_{t},t+\delta_{t}\right)=f_{k,\alpha}^{*}\left(\boldsymbol{x},t\right)=\mathbf{M}^{-1}\mathbf{m}_{k}^{*} \tag{6.10}$$

For the multicomponent pseudopotential LB method, the fluid-fluid interaction force includes two parts: the intra-component interaction force $\boldsymbol{F}_{k,k}$ and the inter-component interaction force $\boldsymbol{F}_{k,\bar{k}}$, which are defined as:

$$\boldsymbol{F}_{k,k}\left(\boldsymbol{x}\right)=-G_{kk}\psi_k\left(\boldsymbol{x}\right)\sum\nolimits_{\alpha}w_{\alpha}\psi_k\left(\boldsymbol{x}+\boldsymbol{e}_{\alpha}\right)\boldsymbol{e}_{\alpha} \tag{6.11}$$

$$\boldsymbol{F}_{k,\bar{k}}\left(\boldsymbol{x}\right)=-G_{k\bar{k}}\varphi_k\left(\boldsymbol{x}\right)\sum\nolimits_{\alpha}w_{\alpha}\varepsilon_{\bar{k}}\left(\boldsymbol{x}+\boldsymbol{e}_{\alpha}\right)\boldsymbol{e}_{\alpha} \tag{6.12}$$

where w_α stands for the weights with $w_{1\text{-}4}$=1/3 for four nearest lattices and $w_{5\text{-}8}$=1/12 for four next-nearest lattices. G_{kk} and $G_{k\bar{k}}$ denote the interaction strength for the same components and different components, respectively. The pseudopotential $\psi_k(\boldsymbol{x})$ as a function of the local density is chosen below [130]:

$$\psi_k\left(\boldsymbol{x}\right)=\sqrt{\frac{2\left(p_{EOS}^{k}-\rho_k lc_s^2\right)}{lc^2G_k}} \tag{6.13}$$

where lc represents the lattice constant, the pressure p_{EOS}^{k} is determined by the non-ideal equation of state. Different from the pseudopotential $\psi_k(\boldsymbol{x})$, the empirical choice of the pseudopotential $\varepsilon_k(\boldsymbol{x})$ = $\rho_k(\boldsymbol{x})$ is employed in this work to enforce a proper component distribution [115, 117].

In this work, components 1 and 2 stand the water vapor (condensable) and non-condensable gas, respectively. For the water component, the Peng-Robinson (P-R) equation of state (EOS) is adopted as [131]:

$$p=\frac{\rho RT}{1-b\rho}-\frac{a\zeta\left(T\right)\rho^2}{1+2b\rho-b^2\rho^2} \tag{6.14}$$

$$\zeta\left(T\right)=\left[1+\left(0.37464+1.54226w-0.26992w^2\right)\left(1-\sqrt{T/T_c}\right)\right]^2 \tag{6.15}$$

with $a = 0.45724R^2T_c^2/p_c$ and $b = 0.0778RT_c/p_c$, the acentric factor w is 0.344, a = 1/49 and b = 2/21 are chosen, and R = 1. For the non-condensable component, an ideal gas equation is used:

$$p = \rho RT \tag{6.16}$$

As the ideal gas, the interaction strength G_{22} for the non-condensable component is considered as zero. Therefore, the pseudopotential $\psi_k(\boldsymbol{x})$ for the non-condensable component is meaningless. It should be noted that the interaction strength between different components $G_{12} = G_{21}$ depends on the mass fraction of NCG. A proper value $G_{12} = G_{21}$ should be adjusted to reach the immiscibility/miscibility of the binary mixture [115]. In the present work, two mass fractions of NCG (W_{NCG} = 0.5% and W_{NCG} = 1.0%) are considered. After many numerical tests, we set $G_{12} = G_{21}$ = 0.15 which can provide a suitable miscible state between the water and non-condensable components in small NCG mass fraction considered in this study.

Aiming to the thermodynamic consistency for the water component, Li et al. [122] developed an improved forcing scheme introducing an adjustable term, which is employed as follows:

$$\mathbf{S}_k = \begin{bmatrix} 0 \\ 6\left(u_x F_{k,x} + u_y F_{k,y}\right) + \dfrac{\kappa \left|\boldsymbol{F}_k\right|^2}{{\psi_k}^2 \delta_t \left(\tau_e - 0.5\right)} \\ -6\left(u_x F_{k,x} + u_y F_{k,y}\right) - \dfrac{\kappa \left|\boldsymbol{F}_k\right|^2}{{\psi_k}^2 \delta_t \left(\tau_\varsigma - 0.5\right)} \\ F_{k,x} \\ -F_{k,x} \\ F_{k,y} \\ -F_{k,y} \\ 2\left(u_x F_{k,x} - u_y F_{k,y}\right) \\ \left(u_x F_{k,y} + u_y F_{k,x}\right) \end{bmatrix} \tag{6.17}$$

where $|\boldsymbol{F}_k|^2 = F_{k,x}^2 + F_{k,y}^2$ and the parameter κ can be tuned to achieve a good thermodynamic consistency for the water component. According to our previous work [124], the adjustable parameter for the thermodynamic consistency of the water component is chosen as κ= 1.30. For the non-condensable component as the ideal gas, just set κ= 0 without considering the thermodynamic consistency [121].

For implementing the contact angle in the pseudopotential LB method, the geometric formulation approach proposed by Ding and Spelt [132] is applied which can be capable of exactly reproducing the prescribed contact angle. The formulation for numerical application is given by [133]:

$$\rho_{i,0} = \rho_{i,2} + \tan\left(\pi/2 - \theta_w^a\right)\left|\rho_{i+1,1} - \rho_{i-1,1}\right| \tag{6.18}$$

with θ_w^a is the prescribed static contact angle, and $\rho_{i,0}$ is the density of the ghost layer (i, 0) beneath the solid boundary (i, 1). The first and second subscripts represent the coordinates along the x- and y- direction, respectively. In this study, the wettability effect using Eq. (6.18) is just applied for the water component. And the NCG component is considered as the no-wetting fluid for the solid wall.

6.2.2 Energy equation for phase change

For the temperature field, the energy equation including the source term of phase change must be solved. Anderson et al. [134] have reviewed the diffuse-interface models of multiphase flow. After neglecting the viscous heat dissipation, the local balance equation of entropy is given by:

$$\rho T \frac{ds}{dt} = \nabla \cdot \left(\lambda \nabla T\right) \tag{6.19}$$

where s and λ are the entropy and thermal conductivity, respectively. And $d(\bullet)/dt = \partial_t(\bullet) + \boldsymbol{u} \cdot \nabla(\bullet)$ is the material derivative.

The thermodynamic relation of entropy has the following form [135]:

$$Tds = c_v dT + T\left(\frac{\partial p_{EOS}}{\partial T}\right)_\rho d\left(\frac{1}{\rho}\right) = c_v dT - \frac{T}{\rho^2}\left(\frac{\partial p_{EOS}}{\partial T}\right)_\rho d\rho \tag{6.20}$$

where p_{EOS} is given by the equation of state, c_v is the specific heat at constant volume. And the continuity equation is given by:

$$\frac{d\rho}{dt} = -\rho\nabla\cdot\boldsymbol{u} \tag{6.21}$$

Using Eq. (6.20) and (6.21), the energy equation (6.19) can be rewritten as [136]:

$$\partial_t T + \boldsymbol{u}\cdot\nabla T = \frac{1}{\rho c_v}\nabla\cdot(\lambda\nabla T) - \frac{T}{\rho c_v}\left(\frac{\partial p_{EOS}}{\partial T}\right)_\rho \nabla\cdot\boldsymbol{u} \tag{6.22}$$

In order to solve the energy equation using the LB equation, the target energy equation (Eq. (6.22)) is rewritten a convection-diffusion equation with a source term as follow [136]:

$$\partial_t T + \nabla\cdot(\boldsymbol{u}T) = \nabla\cdot(k\nabla T) + \frac{1}{\rho c_v}\nabla\cdot(\lambda\nabla T) - \nabla\cdot(k\nabla T) + \underline{\left[T - \frac{T}{\rho c_v}\left(\frac{\partial p_{EOS}}{\partial T}\right)_\rho\right]\nabla\cdot\boldsymbol{u}} \tag{6.23}$$

where k represents a constant having no physical meaning. Based on the pseudopotential LB model, the underlined term is incorporated into the thermal LB equation as a source term and calculated by the finite-difference scheme, another term as a convection-diffusion equation are solved using the standard LB equation. For the thermal LB model within the framework of double-distribution-function approach, two different distribution functions (the density and temperature distribution functions) are utilized for the flow and temperature fields. In order to recover the macroscopic energy equation, Li et al. [136] constructed a thermal LB model based on the MRT and SRT collision operators including the detailed Chapman-Enskog analysis. The thermal LB model has been widely used to simulate the multiphase flow with vapor-liquid phase change. However, in the thermal LB model, the forcing term in pseudopotential LB equation will introduce the addition error into the energy equation. Using the Chapman-Enskog analysis and the numerical benchmark tests, Li and Luo [137] have revealed the effect of the forcing term in the thermal LB model. For avoiding the drawback, the hybrid thermal LB model is devised subsequently. In hybrid thermal LB model, the target energy equation is directly solved by the finite-difference scheme.

Therefore, the temperature solver formulated in Ref. [128] for single component is adopted in this work, which solves the temperature equation using the finite-difference scheme. For solution, Eq. (6.22) is reorganized as [124, 128]:

$$\partial_t T = -\boldsymbol{u}\cdot\nabla T + \frac{1}{\rho c_v}\nabla\cdot(\lambda\nabla T) - \frac{T}{\rho c_v}\left(\frac{\partial p_{EOS}}{\partial T}\right)_\rho \nabla\cdot\boldsymbol{u} \tag{6.24}$$

Note that all quantities in Eq. (6.24) are for the mixture. The mixture density ρ is the summation of the two components $\rho = \rho_1 + \rho_2$. The physical properties of the mixture ϕ (namely the specific heat at constant volume c_v and the thermal conductivity λ) are defined as [138]:

$$\phi = \sum_k \rho_k\phi_k \Big/ \sum_k \rho_k \tag{6.25}$$

According to the Dalton's law of partial pressures, the term p_{EOS} in Eq. (6.24) is the summation of the equation of state for two components as shown in Eq. (6.14) and (6.16).

Using the classical second-order Runge-Kutta scheme, the time discretization for the temperature equation can be written below [124, 128]:

$$h_1 = K(T^t),\ h_2 = K(T^t + 0.5\delta_t h_1) \tag{6.26}$$

$$T^{t+\delta_t} = T^t + 0.5\delta_t\left(h_1 + h_2\right) \tag{6.27}$$

where $K(T)$ is the right-hand side of Eq. (6.24). In particular, the fluid density, velocity and thermal parameters keep fixed during the time marching for the temperature equation (6.24) using the Runge-Kutta scheme. Consequently, the solution of temperature equation is independent of the solution of the flow field by LB method. For the present forcing scheme in Eq. (6.1), LB method is second-order accuracy in space and first-order accuracy in time [109, 110]. In order to ensure high accuracy and consistency, the second-order Runge-Kutta scheme which has been commonly used in various investigations [112, 117, 119] is chosen for the time stepping of Eq. (6.24). Following the second-order isotropic difference scheme for the spatial discretization, the spatial gradient and Laplacian of an arbitrary quantity ϕ in the LB method are constructed by the Taylor series expansions [124, 128, 139]:

$$\partial_i\phi(\boldsymbol{x}) \approx \frac{1}{c_s^2\delta_t}\sum_\alpha w_\alpha\phi\left(\boldsymbol{x}+\boldsymbol{e}_\alpha\delta_t\right)\boldsymbol{e}_{\alpha i} \tag{6.28}$$

$$\nabla^2\phi(\boldsymbol{x}) \approx \frac{2}{c_s^2\delta_t^2}\sum_\alpha w_\alpha\left[\phi\left(\boldsymbol{x}+\boldsymbol{e}_\alpha\delta_t\right)-\phi(\boldsymbol{x})\right] \tag{6.29}$$

where w_α represents the weight factors, $\boldsymbol{e}_{\alpha i}$ is $\boldsymbol{e}_\alpha$ along the i-coordinate axis. Additionally, the thermal conductivity λ is set as $\lambda = \rho c_v \chi$ associated with the constant thermal diffusivity χ in this work. Consequently, the second term in the right-hand side of Eq. (6.24) must be treated with different ways [124, 136]:

$$\frac{\nabla\cdot\left(\lambda\nabla T\right)}{\rho c_v} = \begin{cases} \dfrac{\lambda}{\rho c_v}\nabla^2 T, & \lambda = \text{constant} \\ \dfrac{1}{\rho c_v}\left(\lambda\nabla^2 T + \nabla\lambda\cdot\nabla T\right), & \lambda \neq \text{constant} \end{cases} \tag{6.30}$$

6.3 Results and discussion

This section is deployed as follows. Firstly, several tests are considered to validate the present multi-component multi-phase thermal LB formulation. After the validation, the NCG influence on droplet condensation is investigated in considering the effect of the contact angle and the mass concentration of NCG. Through this work, it notes that the lattice unit (l.u.) is used for all quantities and the gravity is free.

6.3.1 Test of immiscibility/miscibility

For the single-component pseudopotential LB method, the thermodynamic consistency from the pressure tensor is crucial to define the liquid-gas coexistence densities [109]. As we

did in reference [124], the validation for the coexistence curve from the simulation and the Maxwell construction is absolutely necessary for restoring the thermodynamic consistency of the single-component system. However, the pressure tensor for the multi-component LB model is the coupled form, which is totally different from the single-component LB model according to [117]. So far, the mechanical stability condition is still keeping blank. Consequently, the thermodynamic consistency for the single-component LB model is not considered in this work. In addition, the inter-component interaction force via Eq. (6.12) will change the system thermodynamics consistency. And according to the tests, the inter-component interaction force will influence the density distribution closing the phase interface. For the multicomponent system, we cannot restore the unknown thermodynamics consistency by adjusting something. In order to minimize the deviation of the thermodynamics consistency due to the inter-component interaction force, a small W_{NCG} corresponding a small inter-component interaction force is considered here in order to make sure the reliability of the simulated results.

Firstly, we check the immiscibility/miscibility of the binary mixture in this multi-component multi-phase LB model. For that, a 2D isothermal square system (200×200 l.u.) having a static droplet with radius R_0 = 50 surrounded by the vapor/NCG mixture is considered with all periodic boundary conditions. Corresponding to the setting temperature, the coexistence densities from the analytical solution of Maxwell construction are used as the initial densities of the vapor and droplet. In the mixture, the NCG density is defined by $W_{NCG} = \rho_2/(\rho_1+\rho_2)$ based on the mass concentration W_{NCG}. Ideally, the NCG component cannot be dissolved in the liquid water, which means a zero-density region of NCG component within the water droplet. However, the zero-density region is not feasible for numerical simulation because of the discontinuities in the gradient calculation and simulation divergence. For application, the small non-zero density region is indicated as the zero-density region. Here, we initialize a much smaller NCG density within the water droplet as the zero-density region. Finally, the local density is initialized as follows:

$$\rho_k(x,y) = \frac{\rho_{k,in}+\rho_{k,out}}{2} - \frac{\rho_{k,in}-\rho_{k,out}}{2}\tanh\left[\frac{2\left(\sqrt{(x-x_0)^2+(y-y_0)^2}-R_0\right)}{W}\right] \tag{6.31}$$

where ρ_k is the density of component k, $\rho_{k,in}$ and $\rho_{k,out}$ represent the densities of component k inside and outside the droplet, (x_0, y_0) is the domain center, the initial interface thickness is set as W = 5. Simulations are carried out at the setting temperature $0.85Tc$, corresponding to the vapor density $\rho_{1,out}$ = 0.34 and the liquid density $\rho_{1,in}$ = 6.63 for the water component. Two different mass concentrations of the NCG component are considered with the NCG density $\rho_{2,out}$ = 0.00171 (W_{NCG} = 0.5%) and $\rho_{2,out}$ = 0.00341 (W_{NCG} = 1.0%).

After reaching the equilibrium state, the density distributions of the water and NCG components at W_{NCG} = 1% are presented in Figure 6.1(a). Figure 6.1(b) shows the density variation across the centerline at y = 100. The left snapshot of Figure 6.1(a) reveals that a water droplet (red region) is surrounded by the vapor (blue region) and the smooth density

region between the droplet and vapor represents the diffusion interface. Corresponding to the same lattice nodes, the homogeneous red region in the right snapshot of Figure 6.1(a) indicates the well simulated mixture system between the NCG component and the vapor (blue region in the left). Comparing with the vapor region of water component, the smaller NCG density region (blue region) in the right snapshot denotes the immiscible effect between the water and NCG components. Figure 6.1(b) quantitatively presents the mixture effect between the vapor and NCG and the immiscible state between the liquid water and NCG. In the liquid-vapor interface region, the density of water component is smoothly transited from the vapor density to the liquid density. A contrast tendency of NCG component is found in the interface region. And the NCG mass fraction has no influence for the density of the water component. In summary, Figure 1 clearly demonstrates that the present multi-component LB model is capable to simulate the immiscibility/miscibility between the water and NCG components in different phases.

Another common benchmark is the Laplace law which reflects the relationship between the pressure drop across the vapor/droplet interface Δp and the droplet radius R, and the surface tension. The system pressure for the multi-component LB model can be calculated by:

$$p = lc_s^2 \sum_k \rho_k + 0.5lc^2 \sum_k G_{kk} \psi_k^2 + 0.5lc^2 \sum_{k \neq \bar{k}} G_{k\bar{k}} \psi_k \psi_{\bar{k}} \tag{6.32}$$

Tests show a linear relationship between the simulated pressure drop across the interface and the inverse of the droplet radius at different system temperatures. Additionally, the surface tension which is determined by the slope of the fitting line is temperature dependent.

6.3.2 Wettability effect

For droplet condensation, it is necessary to consider the wettability effect of the solid wall. The present study extends the geometric formation approach via Eq. (6.18) to the multi-component pseudopotential LB model for implementing the wettability effect. Thus, we simulate a rectangle domain (200×100 l.u.) filled by the vapor-NCG mixture with W_{NCG}=1%, which has a droplet with the contact angle 90° and the radius R = 30 l.u. located at the bottom wall. The non-slip boundary condition [140] and the convective boundary condition proposed by Lou et al. [141] are implemented for the bottom solid wall and the top outflow boundary, respectively. The periodic boundary condition is considered in the x-direction. Based on the prescribed contact angle θ_w^a, the droplet finally reaches the equilibrium state over the solid wall. For different system temperatures, Figure 6.2 plots the simulated contact angle θ_w versus the prescribed contact angle θ_w^a. There is no doubt that the present contact angle adjustment method works well for the multi-component pseudopotential LB model with minor deviation at $\theta_w^a < 80°$ and $\theta_w^a > 140°$. The obtained contact angles at different temperatures are almost the same, which indicates that this method is independent with respect to the thermal variable (surface tension). Accordingly, the contact angle is approximately fixed at the described value when simulate the phase change case. The snapshots of the density distribution of the water component in Figure 6.2 illustrate the droplet profile at two prescribed contact angles after achieving a steady state.

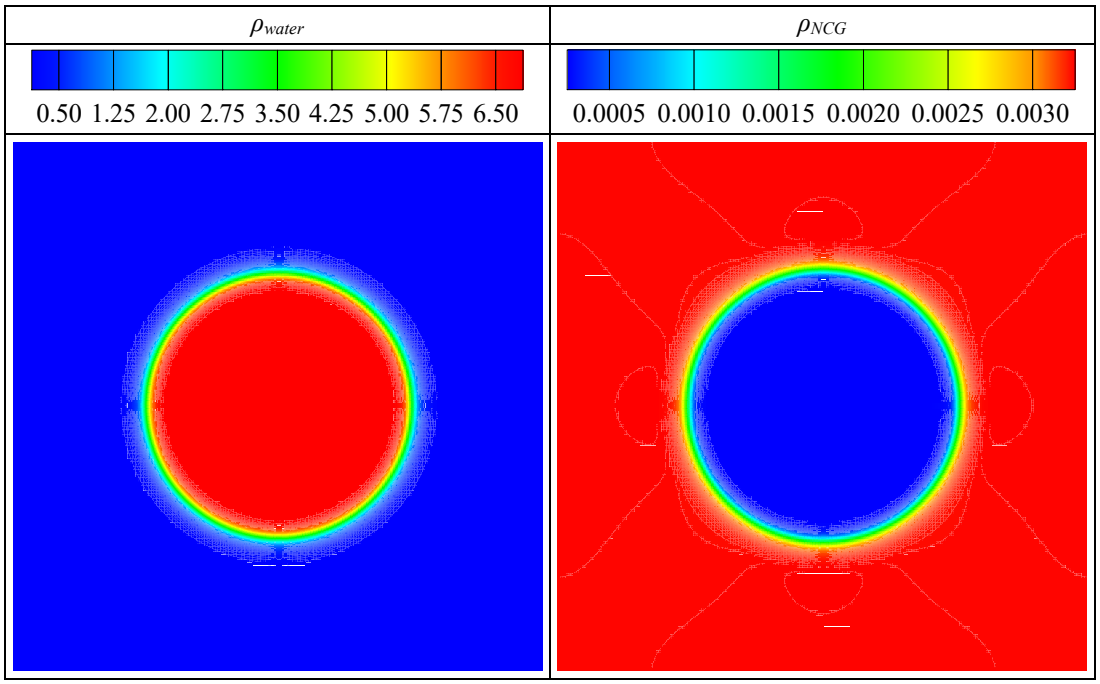

(a)

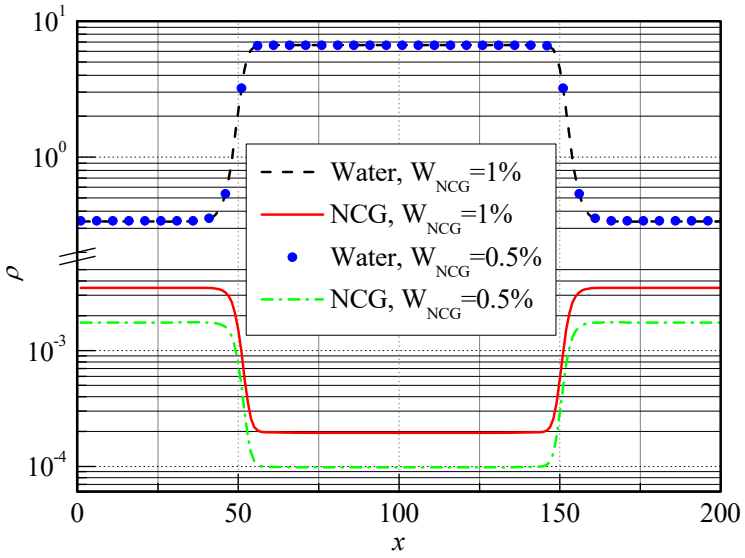

(b)

Figure 6.1 (a) The density distribution of water and NCG components at W_{NCG} = 1% after reaching a steady state; (b) the density variation of water and NCG components along the centerline (y = 100) at W_{NCG} = 0.5% and W_{NCG} = 1%.

Figure 6.3 further presents the density distribution of two components when the steady state is achieved at $T = 0.85T_c$ and $\theta_w^a = 90°$. From the density profile of the entire simulation region shown in Figure 6.3(a), the contact angle adjustment method has no influence for this LB formulation in achieving the immiscibility/miscibility between the water and non-condensable components. Furthermore, as shown in Figure 6.3(b), the density variation across the centerline at x = 100 also indicates that the water and non-condensable components densities near the wall are not influenced by the geometric formulation approach. Again the excellent ability of the geometric formulation approach in adjusting the contact angle is demonstrated

for the multi-component pseudopotential LB method.

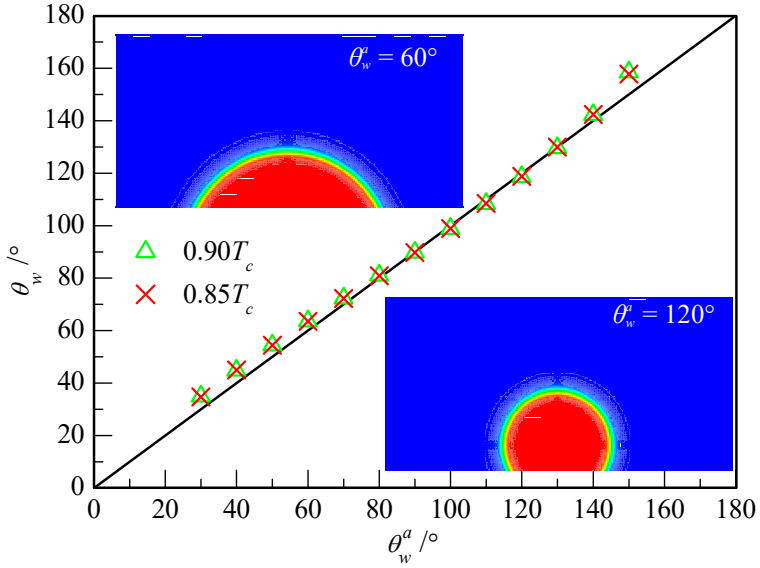

Figure 6.2 Wettability test for the geometric formulation approach with W_{NCG}=1%, τ_v = 0.8.

6.3.3 Droplet evaporation

The classical D2 law describing droplet evaporation, which predicts a linear variation of the square of the droplet radius with time, has become to be a common benchmark for validating the numerical method [136, 142]. It is instructive to give the main assumptions for establishing this law: Constant thermo-physical properties (e.g., the specific heat c_v and thermal conductivity λ), quasi-steady vapor and liquid phases, neglecting the viscous heat dissipation and buoyancy, etc. Similarly, the evaporation of an isolated droplet is simulated to evaluate the capability of our multi-component thermal LB model in simulating phase change. Simulations are carried out at a square 2D domain (200×200 l.u.). A liquid droplet with radius R = 30 l.u. is placed at the center of computational region. The droplet is surrounded by a vapor-NCG mixture with W_{NCG} = 1%. The saturation temperature 0.86T_c and a uniform temperature 1.0T_c are set to the droplet and the surrounding mixture, respectively. The temperature gradient at the interface is responsible for evaporation. The constant temperature and periodic boundary conditions are employed for all boundaries. According to the assumption, specific heat and kinematic viscosity are chosen as c_v =5.0 and υ = 0.1, respectively, for the entire computational domain. Two cases having different thermal conductivities λ = 2/3 and λ = 3/3 are considered. Additionally note that the term $\nabla\cdot(\lambda\nabla T)$ in Eq. (6.24) is simplified to $\lambda\nabla^2 T$ [119, 136] in this test.

The snapshots of the temperature field at different times for the case λ = 3/3 are shown in Figure 6.4 Figure 6.5 presents the water mass fraction field during the evaporation process. And the velocity vectors are also provided in Figure 6.4 Figure 6.5. The white dashed circle in each snapshot represents the droplet profile which is determined by the interface density. It is clear that the droplet keeps the original circular shape during evaporation. Furthermore, the radial and rotational symmetry vectors around the droplet in every snapshot declare the

consistent Stefan flow generated by evaporation as expected. Figure 6.4 shows that the droplet temperature is gradually decreased due to evaporation and the interface temperature is higher than the temperature of the droplet center. Turning to the water mass fraction profile in Figure 6.5, the decreasing fraction gradient is attributed by the decreasing evaporation rate corresponding to the temperature gradient. And the water mass fraction in the surrounding is increased with the time. The reason for this is that the vapor created by evaporation moves into the surroundings.

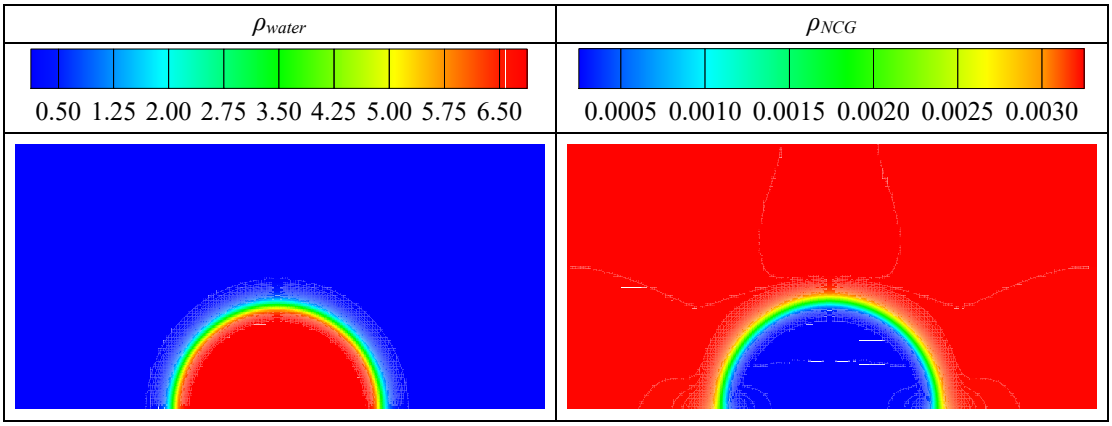

(a)

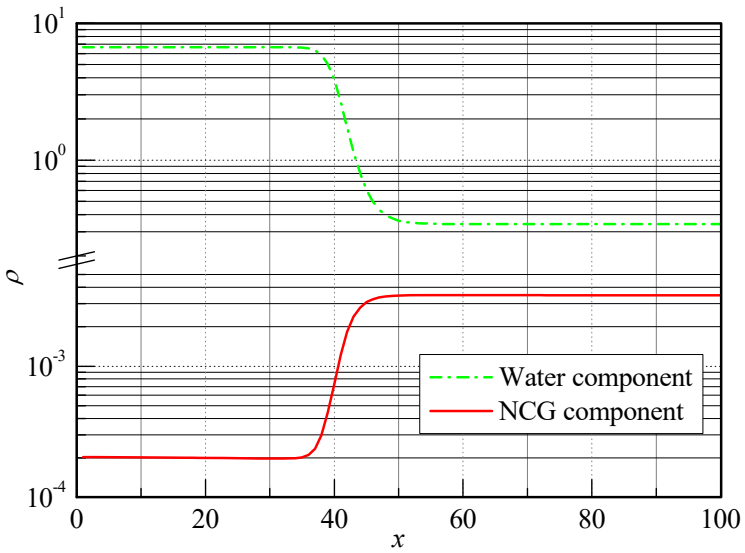

(b)

Figure 6.3 The influence of the geometric formulation approach for the density distribution. (a) the density profile of the entire system for two components; (b) the density variation across the centerline of the bottom wall.

Additionally, the normalized temperature and water mass fraction profiles across the centerline are depicted in Figure 6.6. The temperature and water mass fraction in the vicinity of the interface change rapidly. During evaporation, the decreased droplet temperature corresponds to the constant mass fraction of the water component. Eventually, the decreasing temperature and fraction gradients demonstrate the tendency in reaching the equilibrium state during evaporation. The simulated temperature and water mass fraction profiles in this work are consistent with that using the level set method, smoothed particle hydrodynamics method

and phase-field multiphase LB method [143-145]. Note that the present profile of the water mass fraction has little difference with the temperature distribution. This is because that we use the periodic boundary condition and constant temperature condition for all boundaries. As shown in Figure 6, during evaporation, the temperature on the boundary keeps constant while increasing the water mass fraction. In those three methods, the constant temperature and constant vapor mass fraction is applied as the boundary condition, which results in a consistent profile between the temperature and the vapor mass fraction.

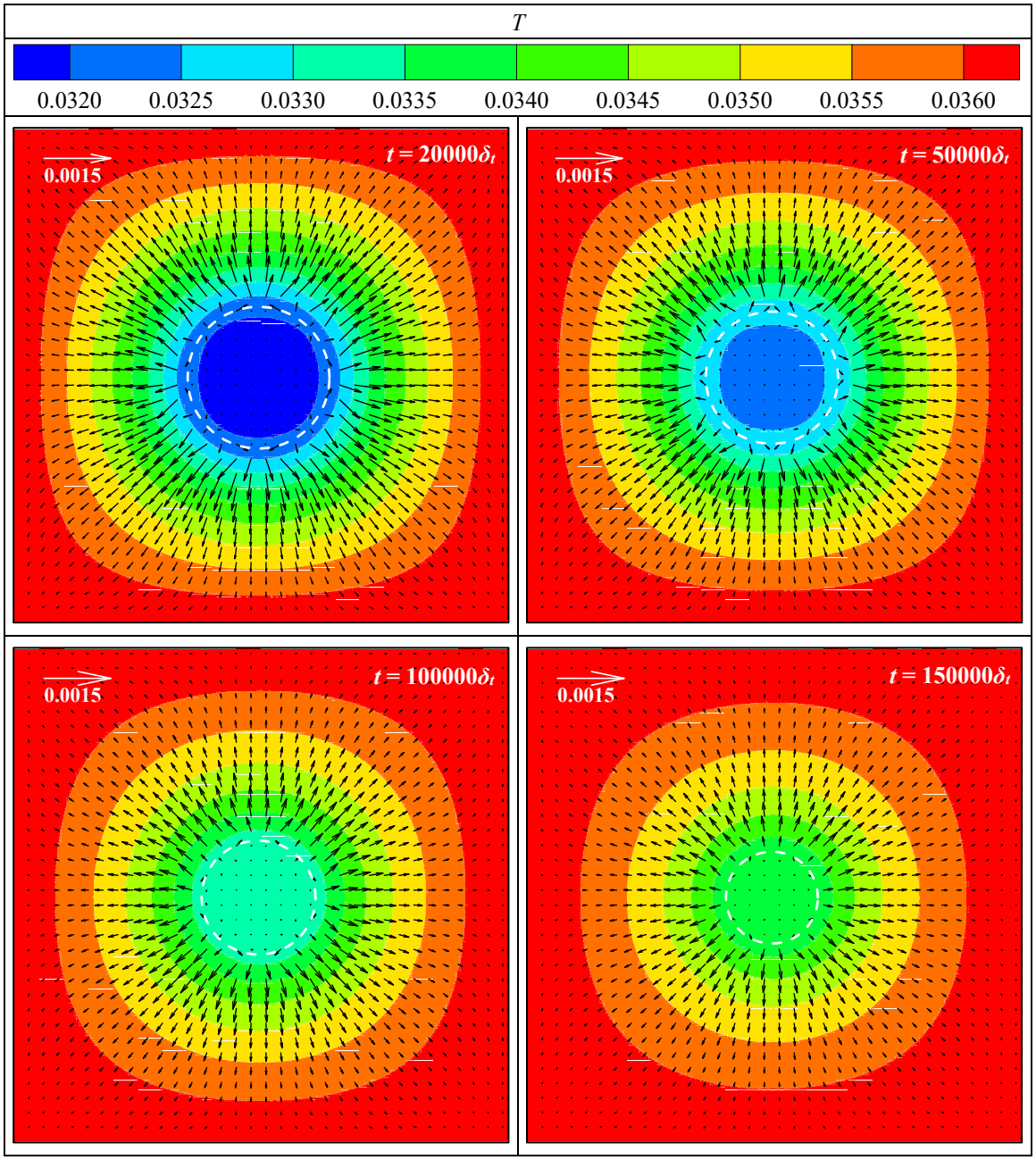

Figure 6.4 Temperature field and velocity vectors at different times for 2D droplet evaporation.

For two cases having different thermal conductivities, the variation of the reduced square radius with time is plotted in Figure 6.7. The latter one is enough to state that the numerical results of the present multi-component LB model obey the D2 law - that is the square of the

droplet radius decreases linearly over time. Moreover, the evaporation rate shows linear dependently on the thermal conductivity linearly.

In summary, the present multi-component multi-phase thermal pseudopotential LB model is capable of simulating the phase change problem in presence of NCG through several above validations. Droplet condensation in presence of NCG will be carried out next using the developed multi-component LB formulation.

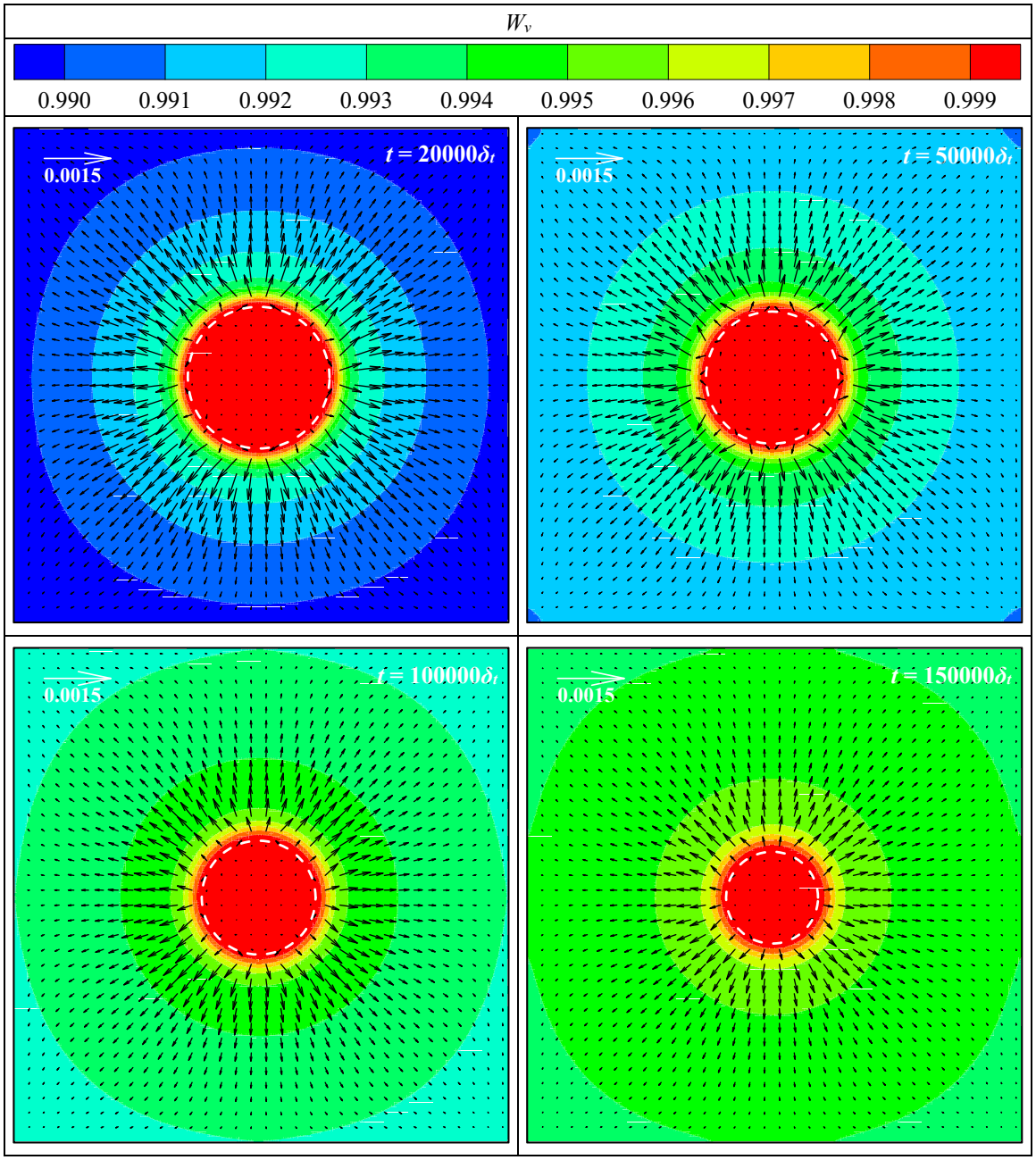

Figure 6.5 Evolution of the water mass fraction and velocity vectors during 2D droplet evaporation.

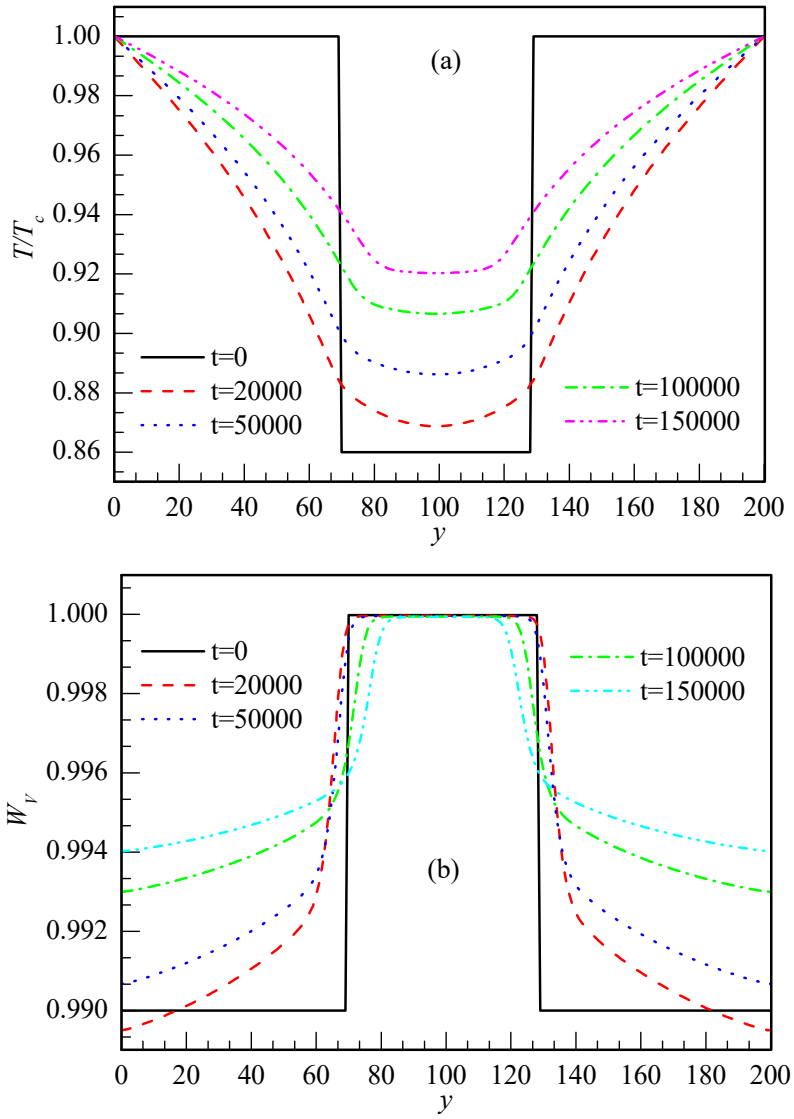

Figure 6.6 Evaluation of the normalized temperature and water mass fraction across the centerline. (a) the normalized temperature; (b) the water mass fraction.

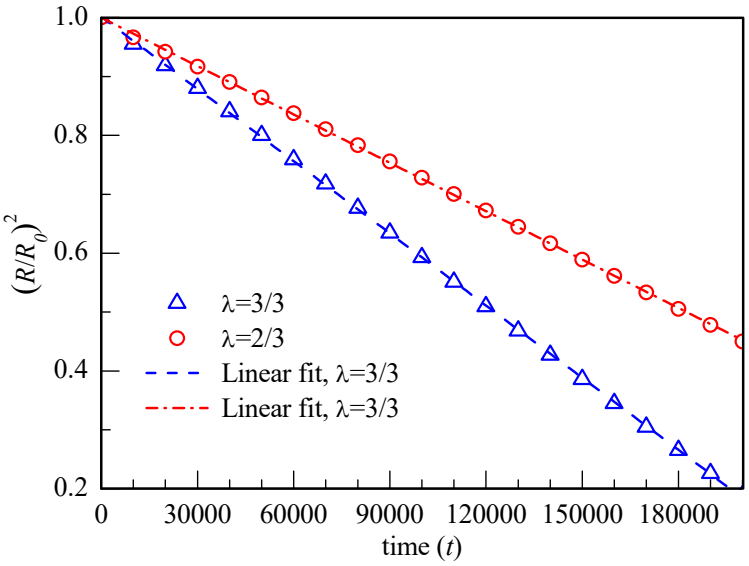

Figure 6.7 Normalized square of droplet radius versus evaporation time.

6.3.4 Single droplet condensation in presence of NCG

Aiming to investigate the mechanism of dropwise condensation with the presence of NCG, the present multi-component multi-phase thermal pseudopotential LB model is employed to simulate single droplet condensation in the vapor-NCG mixture. Firstly, the NCG mass fraction and the sub-cooling are considered to study the influence of NCG on droplet generation and growth. Finally, the effect of contact angle is also studied.

Effect of the NCG mass fraction and the sub-cooling

Initially, the computational domain is filled by a mixture of vapor and NCG at the saturation temperature $T_{sat} = 0.86T_c$. The system has the length $Lx = 400$ l.u. and the height $Ly = 200$ l.u.. The periodic boundary condition is specified in the x-direction. Moreover, the non-slip boundary condition [140] and the convective boundary condition [141] are employed for the bottom and top boundaries, respectively. At the center of the bottom wall, the clod spot (30 l.u.) having temperature T_w is appointed as the nucleation site. The temperature for all boundaries is fixed at $T = 0.86T_c$, except the cold spot where the sub-cooling for condensation is $\Delta T = T_{sat} - T_w$. The computational domain and the boundary conditions are illustrated in Figure 6.8. Furthermore, the thermal conductivity for the whole domain is chosen as $\lambda = \rho c_v \chi$ with $c_v = 3.0$ and $\chi = 0.05$. The kinematic viscosity is $v = 0.1$. In studying the effect of the NCG mass fraction and the sub-cooling, the prescribed contact angle is chosen as $\theta_w^a = 90°$.

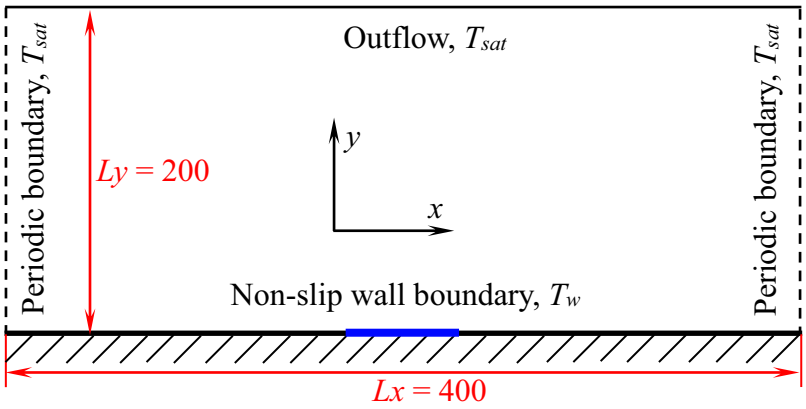

Figure 6.8 Sketch of droplet condensation with NCG on a cold spot (the blue line on the bottom wall).

Firstly, the condensation process at the sub-cooling $\Delta T = 0.19T_c$ and NCG mass fraction $W_{NCG} = 1\%$ is simulated. In Figure 6.9, we give the density distribution of two components and the temperature at the condensation time $t = 30\ 000\delta_t$. The semi-circular black line defines the droplet profile. Due to condensation of the water component, an isolated water droplet is formed at the cold spot. The Marangoni flow within the droplet and the suction flow outside the droplet are clearly presented by the streamlines. From the density profile of the NCG component in Figure 6.9(b), we can find a density gradient in the surroundings of the droplet as well as the accumulation layer of the NCG component. This is because that the NCG component cannot be dissolved in the liquid water when the phase change of the vapor occurs at the interface with the coming vapor-NCG mixture.

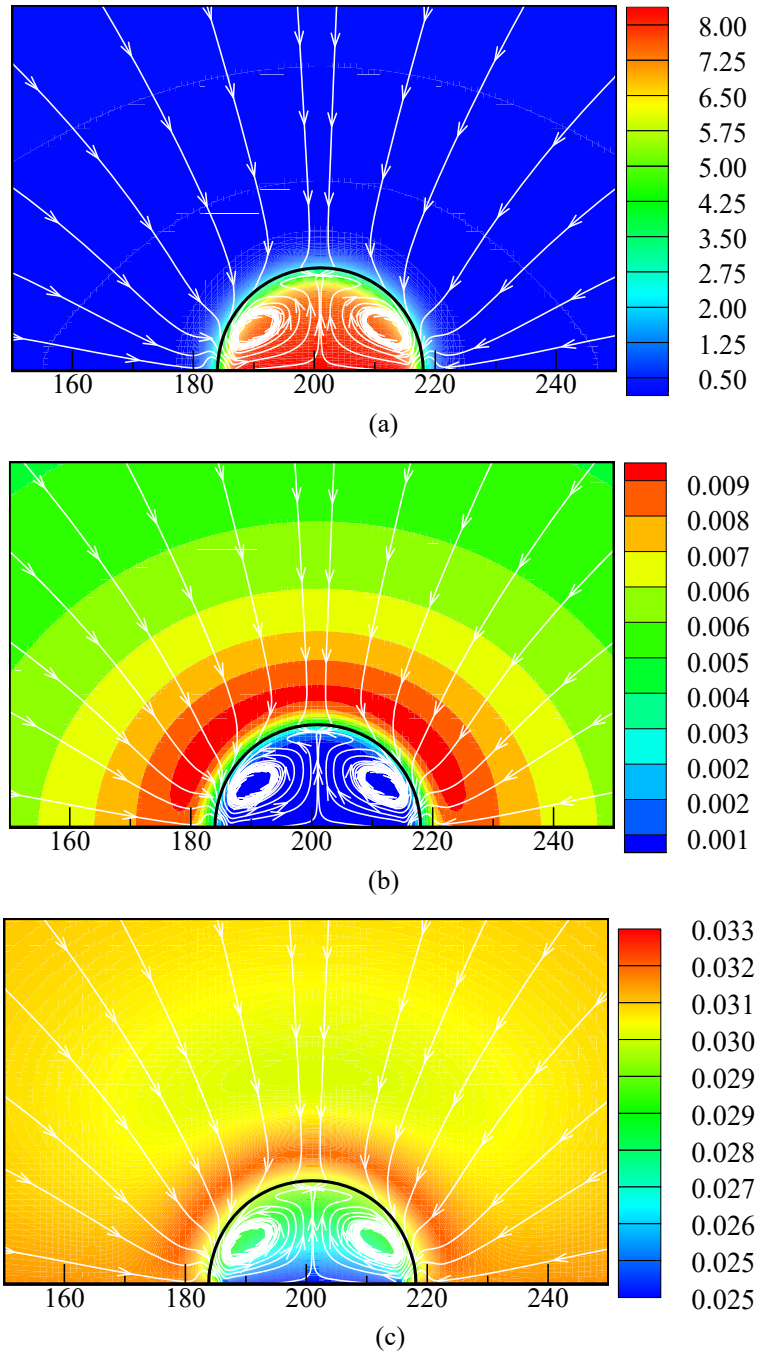

Figure 6.9 Droplet condensation with NCG on a plate at $\Delta T = 0.19T_c$, $W_{NCG} = 1\%$, $t = 30\,000\delta_t$. (a) the density distribution for water component; (b) the density distribution for NCG component; (c) the temperature profile.

Furthermore, more attentions should be given to the smaller NCG density region within the droplet which is corresponding to the immiscible effect between water and the NCG components. The droplet is generated because of condensation and is not initially placed at the bottom wall. Therefore, the immiscible effect (the smaller NCG density region) is automatically resulted by the repulsive interaction force between two components by Eq. (6.12). The temperature gradient between the droplet surface and the cold spot is the driving force for heat transfer which leads to the temperature profile inside the droplet. The temperature profile following the droplet shape is due to the larger thermal conductivity of the

water droplet.

On the other hand, a thin layer of higher temperatures is formed around the droplet. This region indicates the existence of the temperature jump between the environment and the droplet, though it is meaningless to define the interface temperature for the diffusion interface method. The latent heat released by phase change is such that the higher temperature region is formed. The physical reason for the temperature jump adjacent to the interface is discussed by Young [50] on molecular level. Outside this region, a minor temperature gradient from the surroundings towards the droplet surface is found corresponding to the saturated-temperature gradient. This is caused by the decreased gradient of the saturated-vapor density due to condensation. In the present work, the vapor contains small amounts of NCG so that the temperature gradient is very small. In order to make the temperature intuitive, the temperature variation of the centerline across the droplet from the top boundary to the bottom wall is plotted in Figure 6.10. The dotted line indicates the location of the droplet surface.

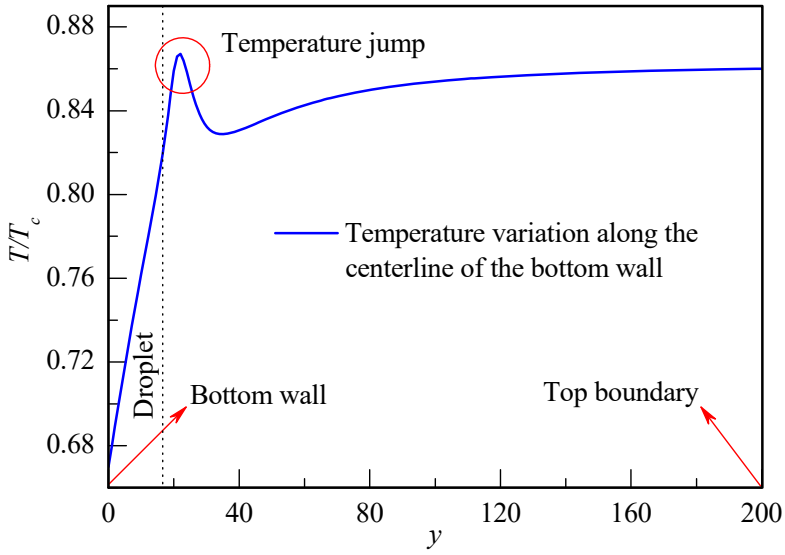

Figure 6.10 Temperature variation along the centerline of the bottom wall.

For droplet condensation, we care more about the diffusion process of vapor from the environment towards the interface and the heat transfer performance. Next, we will turn the attention to the vapor mass fraction profile, the growth process of droplet and the heat flux at different NCG mass fractions and levels of sub-cooling.

As an important aspect, the heat flux can directly reflect the influence of NCG on condensation heat transfer. Here, the influences of NCG mass fraction and sub-cooling on the heat flux are investigated as shown in Figure 6.11. Figure 6.11(a) plots the variation of the average heat flux on the cold spot with time at different NCG mass fractions. Droplet condensation in the pure vapor with W_{NCG} = 0% is simulated using the LB model from our previous LB model [124]. Even adding the NCG component, the tendency of the averaged heat flux during condensation is also following that in the pure-vapor case. Some waiting time is always necessary before onset of condensation. The lower insert plot indicates that the presence of NCG increases the waiting time before nucleation. This tendency is caused by the

fact that the position of some vapor clusters is occupied by NCG molecules. During nucleation and early condensation, the heat flux is noticeably decreased by the NCG component. The reduction effect is enhanced with increasing the NCG amount. The reason is that in the early stage the conduction resistance of the droplet is very small and adding the NCG component induces the diffusion resistance. We can conclude that the diffusion resistance is significant comparing with the small conduction resistance in the early stage. Interestingly, the NCG has a minor reduction effect for the heat transfer of droplet condensation when the droplet is grown to the large size, as shown in the upper insert plot. This is because that the condensation resistance is more duo to the conduction resistance for large sized droplets. In this work, we just consider to addition of small concentrations of NCG, which corresponds to a small diffusion resistance. Thus the effect of the diffusion resistance will be minor when compared with the higher conduction resistance for larger droplets. Based on our results, the influence of small amounts of NCG on droplet condensation heat transfer is significantly difference with that in reference [119]. In reference [119], the heat flux in the whole stage of droplet condensation is seriously reduced by the non-condensable component even at small amount. Here, our conclusion is that the presence of NCG significantly reduces the heat transfer of droplet condensation in early condensation, while for the larger droplets the influence of NCG is depending on the amount of NCG. Therefore, the reduction effect of the NCG component for droplet condensation heat transfer depends on the growth stage and the NCG amount. For dropwise condensation on a cold substrate, the experiments indicate that even small amounts of NCG can significantly decrease its heat transfer coefficient. The present results give the explanations that adding non-condensable components seriously decreases the heat flux for the early stage of condensation, which contributes the main heat transfer performance for dropwise condensation. Figure 6.11(b) gives the effect of sub-cooling. Out of questions, the wall sub-cooling has an enhancing effect for heat transfer in droplet condensation in presence of NCG. And higher sub-cooling decreases the waiting time of nucleation, as well as the advancing condensation.

On the other hand, the variation of the droplet radius with time, which can reflect the droplet growth rate during condensation, is plotted in Figure 6.12. Both, the NCG mass fraction and the wall sub-cooling are considered. The experimental and theoretical investigations have revealed that the isolated droplet radius during condensation obeys the power law $R = a*t^b$ [146, 147], where the pre-factor a and exponent b control the droplet growth rate. The growth rate can be determined by the derivation of the power law function $dR/dt = a*b*t^{b-1}$. Thus, the numerical results are fitted using the power law, as shown in Figure 6.12. From Figure 6.12(a), the exponent b is increased with adding the NCG component and increasing the NCG amount. However, the pre-factor a presents an opposite tendency compared with the exponent b. The effect of NCG on the parameters a and b gives the growth rate which can be determined by the derivation of the fitted power law function. Increasing the wall sub-cooling also results in the opposite effect for the parameters a and b, as seen from Figure 6.12(b).

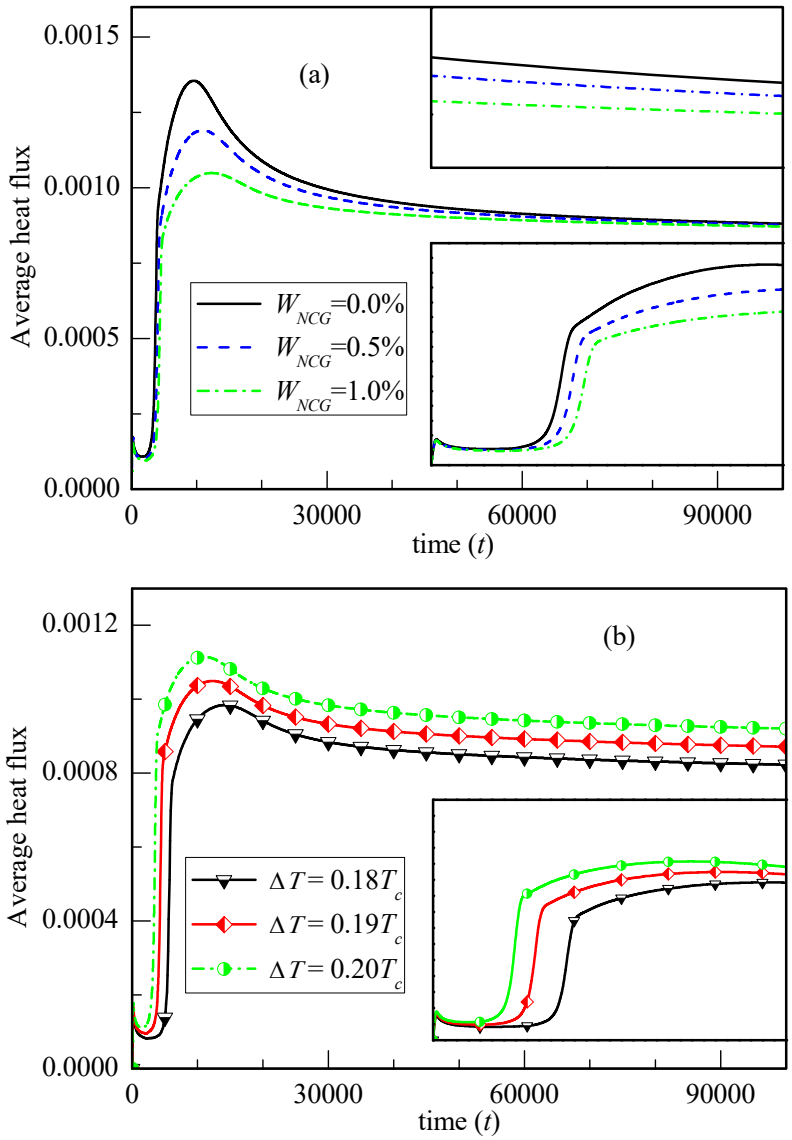

Figure 6.11 The average heat flux over the whole cold spot versus the condensation time. (a) the effect of the NCG mass fraction at $\Delta T = 0.19T_c$; (b) the sub-cooling effect at W_{NCG}=1%.

In order to analyze the accumulation effect of NCG qualitatively, Figure 6.13 presents the mass fraction distribution of the water component during condensation. The left and right sides show the results at W_{NCG} = 0.5% and W_{NCG} = 1.0%. The profile of the water mass fraction is corresponding to the NCG mass fraction distribution. The red region having the water mass fraction close to 1.0 represents the liquid droplet which has a small quantity of NCG inside. The lower mass fraction of the water component reflects the accumulation effect of the NCG component neighboring the droplet surface. Through the formed concentration layer, the density gradient derives the mass transfer of vapor from the surroundings to the interface, while the NCG component diffuses far away from the interface. For an isolated droplet on the plane, the profile of the concentration boundary layer presents a radial diffusion. With growing of the droplet, the NCG accumulation effect becomes weakened due to the reduced condensation rate. Furthermore, the concentration boundary layer is enlarged as more and more vapor components condensate on the interface and the NCG component diffuses to the surrounding. The extended conclusion is that the mass transfer of the vapor and

NCG will reach an equilibrium state. These results from Figure 6.13 are consistent with our former discussions about the average heat flux.

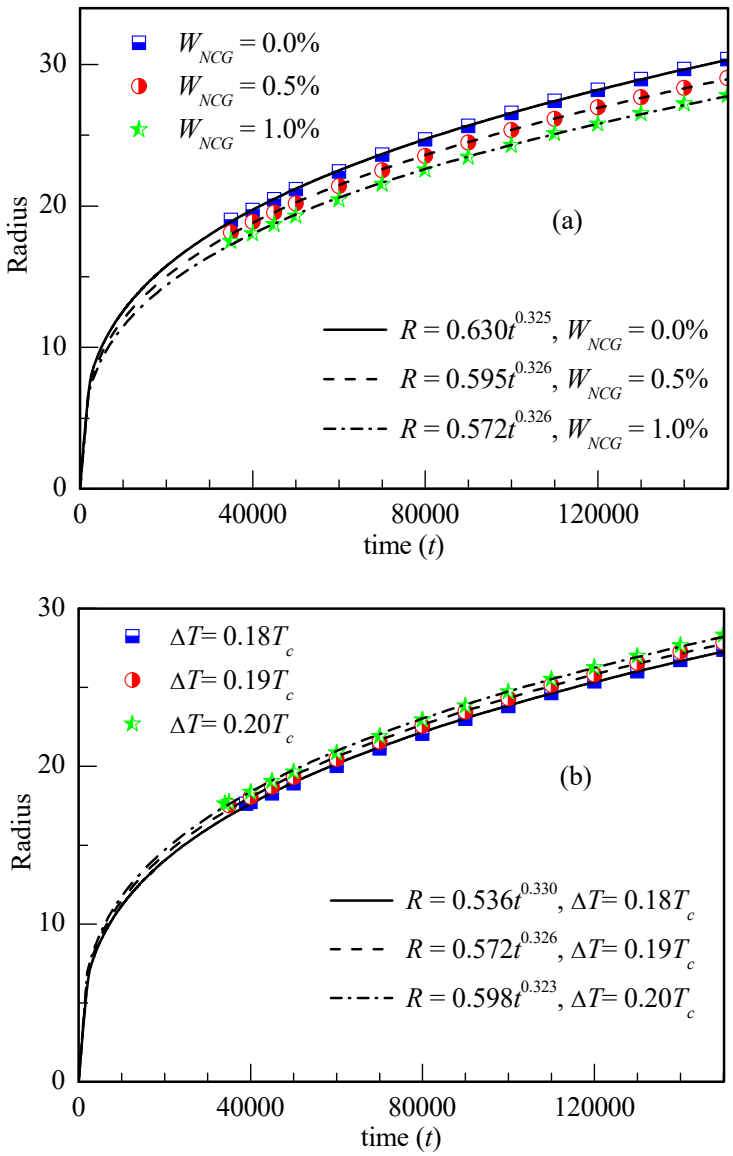

Figure 6.12 Condensation droplet radius with time. (a) the effect of the NCG mass fraction at $\Delta T = 0.19T_c$; (b) the sub-cooling effect at W_{NCG} = 1%.

According to the results and discussions in Figure 6.11 and Figure 6.13, the mechanism for droplet condensation considering NCG is carried out. During nucleation and early growth, the diffusion resistance is dominant as the barrier of condensation. Thus, the heat transfer is noticeably weakened by adding the NCG component even at a small amount. A strong accumulation effect of NCG (small density gradient) is caused because of the fast condensation. With the condensation going on, the growing droplet marks an increased conduction resistance of the droplet. The proportion of the conduction and diffusion resistances is changed; nevertheless, the proportion is also depended on the NCG amount. For the small amount of NCG in the present work having a small diffusion resistance, the conduction resistance significantly controls the condensation rate for the larger sized droplet. In this stage, a smaller density gradient is due to weak condensation.

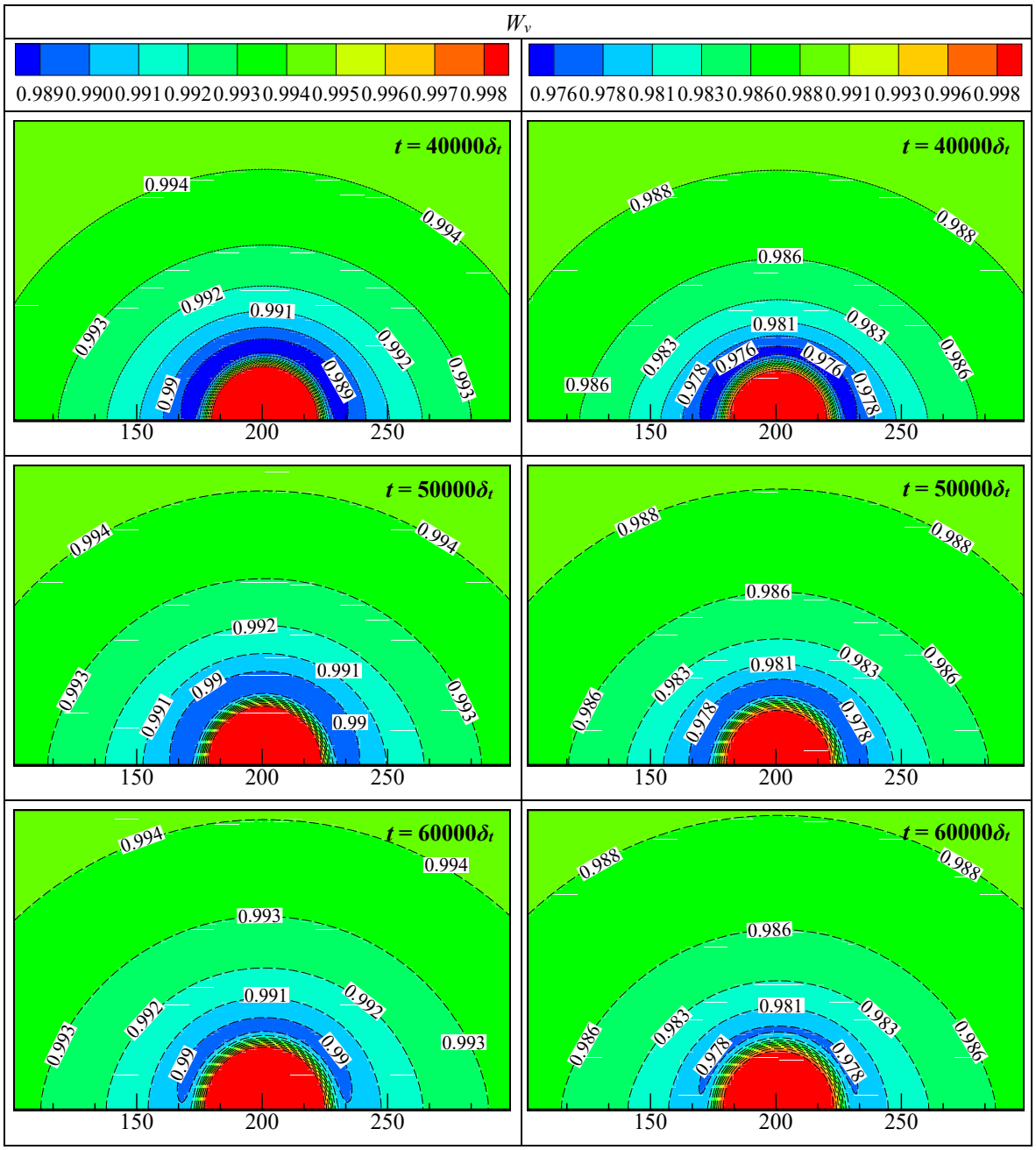

Figure 6.13 The distribution of the mass fraction of the water component during condensation at W_{NCG} = 0.5% (left side) and W_{NCG} = 1.0% (right side).

Effect of the contact angle

In this section, the contact angle effect is considered for droplet condensation. At a certain wall sub-cooling, Figure 6.14 gives the average heat flux at droplet condensation with and without a NCG component at different contact angles. Figure 6.14(a) and Figure 6.14(b) indicate clearly that the wettability does have the same influence for droplet condensation with and without a non-condensable component. The larger contact angle slightly increases the waiting time for nucleation. Significantly, no matter adding the NCG component or not, the heat transfer of droplet condensation is enhanced by the hydrophilic substrate rather than the hydrophobic one, particularly in the early stage of condensation. This phenomenon is resulted by the combined action of the droplet height and base which control conduction

resistance and heat transfer area, respectively.

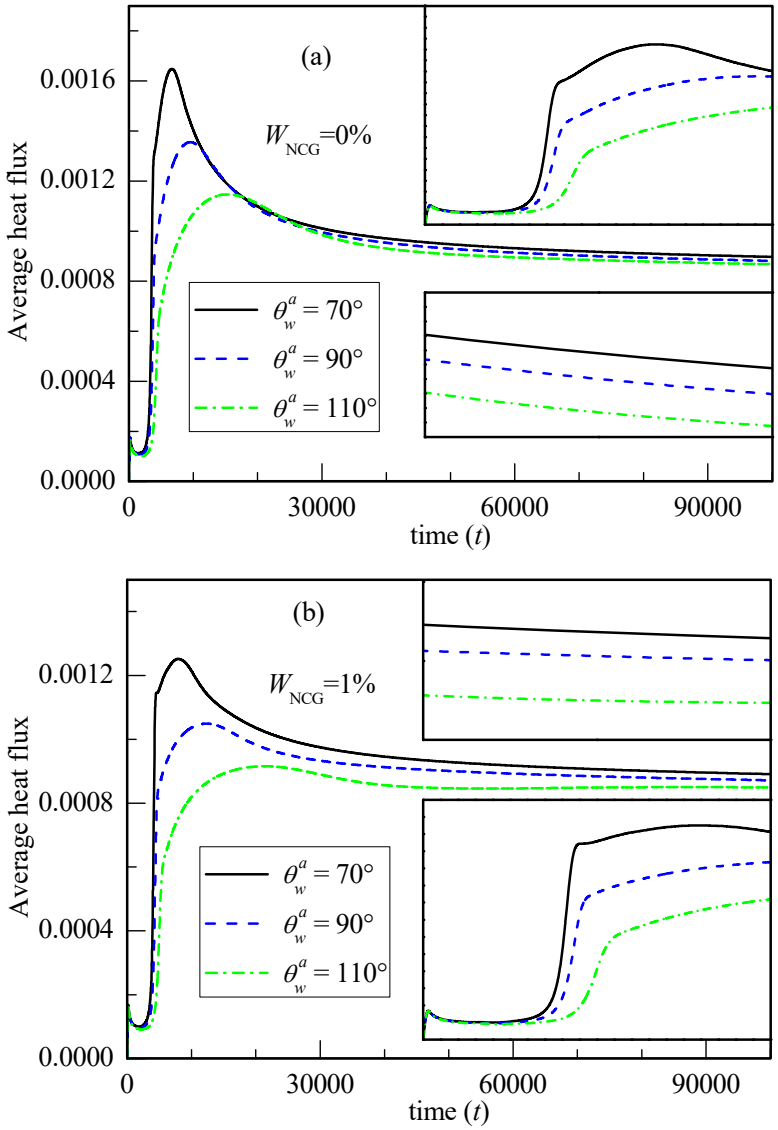

Figure 6.14 Evaluation of the average heat flux at different contact angles and $\Delta T = 0.19T_c$. (a) the pure vapor; (b) the NCG mass fraction $W_{NCG} = 1\%$.

On the other hand, the evaluation of the power law for the droplet growth rate at different contact angles is investigated. Corresponding to Figure 6.14, the droplet radius over time is plotted in Figure 6.15 for different contact angles. The slope of the fitting line which is the derivation of the power law function represents the growth rate of the droplet. The effect of the contact angle on the droplet growth rate follows that of the heat flux.

For the fitted power law function, the pre-factor a and the exponent b are important in controlling the growth rate. Accordingly, the fitting coefficients a and b at different contact angles and NCG mass fractions are summarized in Table 6.1. Using the fitting coefficient, the droplet growth rate at different conditions can be evaluated mathematically. Furthermore, the waiting time for nucleation can be also included into the power law function. In the present study, the factor for the waiting time is neglected because of the short waiting time.

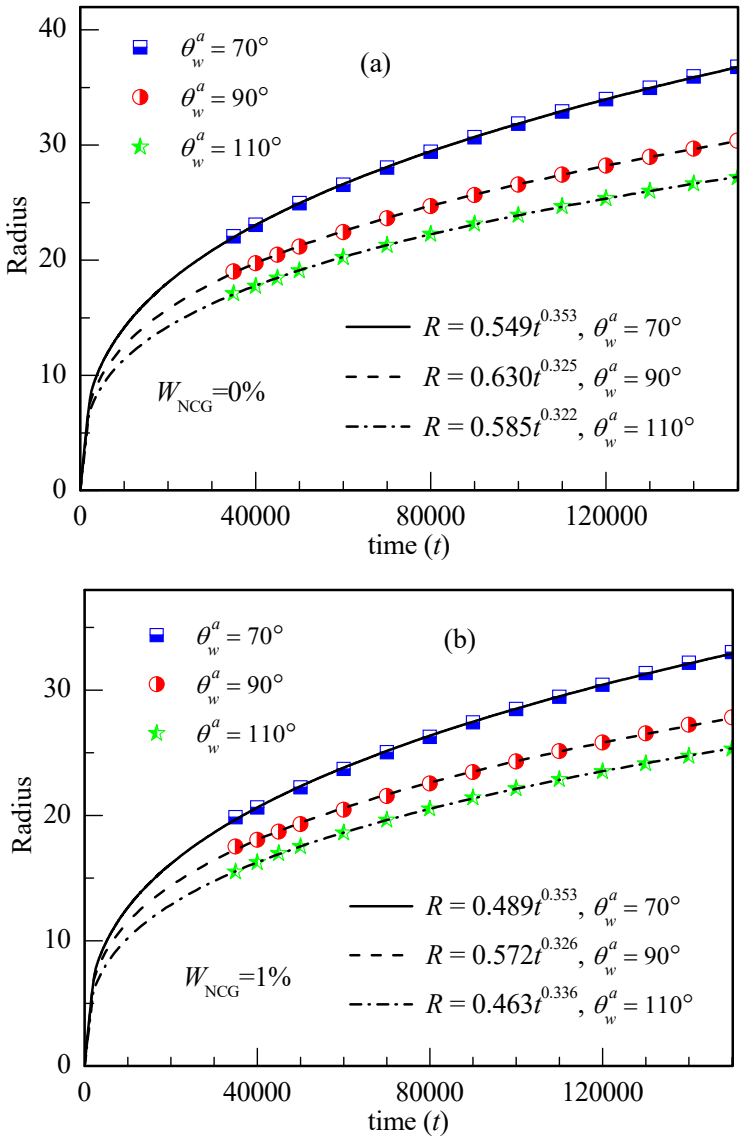

Figure 6.15 Evaluation of the power law for the droplet growth rate during condensation at different contact angles and $\Delta T = 0.19T_c$. (a) the pure vapor; (b) the NCG mass fraction W_{NCG} = 1%.

Turning to the accumulation effect of the non-condensable component, Figure 6.16 presents the distribution of the mass fraction of the water component for different contact angles and two W_{NCG}. Combining the results for $\theta_w^a = 90°$ in Figure 6.13, we can investigate the influence of the contact angle on the accumulation effect of the NCG component. Naturally, we do not care about the NCG distribution within the droplet. It is clear that the contact angle has a serious influence for the NCG accumulation around the interface. For $\theta_w^a = 70°$, the non-condensable component prefers to accumulate on the top of the droplet. However, a strong accumulation is observed at the corners adjacent to the wall for $\theta_w^a = 110°$. These different accumulation effect are attributed to the dynamic behavior of the contact line in different contact angles. With growing of the droplet, the contact angle deviates from the equilibrium contact angle causing an unbalanced force toward outside which leads to the contact line motion for reaching the equilibrium contact angle. This phenomenon is the dynamic behavior of the contact line during droplet condensation at the mode of the constant contact angle.

More details about this phenomenon can be found in references [148-149]. Comparing with the bigger contact angle, the smaller contact angle brings a more strong dynamic behavior of the contact line. The motion of the contact line will introduce an extrusion effect for the mixture at the corners, thus influencing the mass transfer of NCG around the droplet.

Table 6.1 Power law, 0.19Tc.

W_{NCG}	$\theta_w^a = 70°$		$\theta_w^a = 90°$		$\theta_w^a = 110°$	
	a	b	a	b	a	b
0.0%	0.5493	0.3527	0.6304	0.3250	0.5847	0.3222
0.5%	0.5180	0.3527	0.5950	0.3260	0.5237	0.3284
1.0%	0.4893	0.3531	0.5720	0.3257	0.4629	0.3359

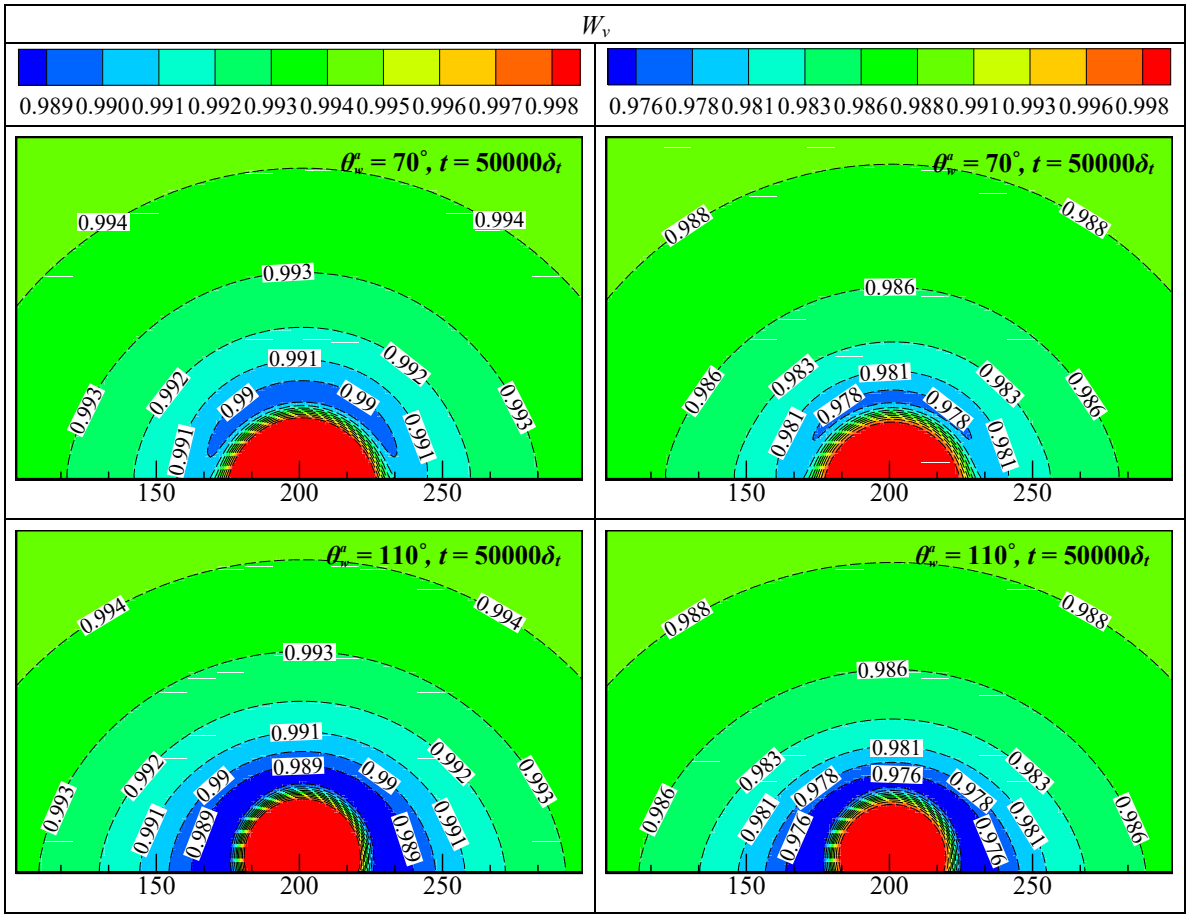

Figure 6.16 The distribution of the mass fraction of the water component in two contact angles for the NCG mass fraction W_{NCG} = 0.5% (left side) and W_{NCG} = 1.0% (right side), ΔT = 0.19T_c, t =500 00δ_t.

In practice, the distance between the contact point and the droplet center denotes the radius. Consequently, the contact line movement can be evaluated by the droplet growth rate during the time. In above, we have concluded that the droplet radius is a power law function of the condensation time $R = a*t^b$. After fitting, the parameters a and b under different conditions have been listed in Table 6.1. In order to clarify the dynamic behavior of the contact line in different contact angle, the droplet growth rate (dR/dt) versus the considering time is plotted in Figure 6.17 at W_{NCG} = 1% and ΔT = 0.19T_c. The growth rates at different contact angles

demonstrate intuitively the relationship between the contact line dynamics and the contact angles discussed above.

In conclusion, the strong dynamic behavior of the smaller contact angle during droplet condensation enhances the mass transfer of the NCG component far away from the interface, i.e. attenuating the NCG accumulation.

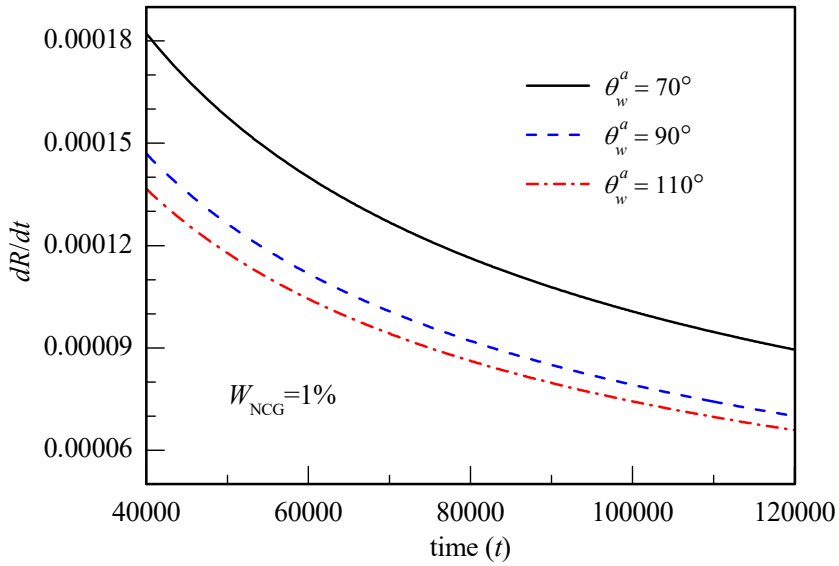

Figure 6.17 The evaluation of the contact line dynamics in different contact angles by the droplet growth rate at $W_{NCG} = 1\%$ and $\Delta T = 0.19T_c$.

6.4 Conclusions

Trying to simulate dropwise condensation considering the non-condensable component, a multi-component multi-phase thermal pseudopotential lattice Boltzmann method is developed in realizing the stable and viscosity-independent physical results. After validation of this method using several numerical benchmarks, numerical simulation for single droplet condensation with non-condensable gas is carried out including the effects of mass fraction of non-condensable component and contact angle.

During droplet condensation, the heat transfer in the nucleation and early stage is seriously reduced by the non-condensable gas. For the large size droplet, the small amount of non-condensable gas brings a weak reduction for the condensation heat transfer. The waiting time of nucleation is increased with the amount of non-condensable component increasing. The influence of the non-condensable gas for the heat transfer of droplet condensation is depended on the growth stage and the amount of the non-condensable gas.

The smaller contact angle having more strong dynamic behavior of the contact line will promote the mass transfer of non-condensable component far away from the corner near the wall. As expected, the heat transfer of droplet condensation in the presence of non-condensable gas or not can be enhanced by the hydrophilic substrate rather than the hydrophobic substrate.

Chapter 7 Summary and Future work

7.1 Summary

In the present thesis, dropwise condensation in case of NCG is both experimentally and numerically investigated. A series of vital aspects are evaluated after concerning NCG. Correspondingly, Mechanistic understanding is also released on the basis of this work.

In the experimental investigations, dropwise condensation experiments are performed at a constant relative humidity and different sets of bulk flow velocity and sub-cooling degree. Using the microscope camera, the defined droplet size distribution density declares that the droplet distribution during dropwise condensation is a steady state in statistic. In addition, it is observed that the droplet growth rate is not depended on its size uniquely. The local depletion of the vapor concentration field resulted by neighbors (i.e. the interaction effects between droplets) is testified by the present experiments. Notable that the forced convection even at a quite low level should be regarded as a vital factor for promoting dropwise condensation in case of NCG.

With the object of modeling dropwise condensation, parts of the thesis are dedicated to the modeling method for the case of several vital aspect. The overarching issue is the coupled heat and mass transfer during droplet condensation. For that, an isolated droplet growth model, which incorporates three regions (the continuum region, the Knudsen layer and the region of liquid droplet) by matching the mass flow and energy flow rates, is developed to evaluate the droplet growth rate. However, a crucial parameter the accommodation coefficient is introduced by the Knudsen layer for considering the multi-scale feature of droplet size. Considering the dispute definition for the accommodation coefficient, a simplified model is correspondingly presented. Different models with different considered resistances are compared together including the droplet growth model for the case of pure steam. The quantitative growth rates demonstrate that for single droplet the case of pure steam is reduced more than one order by the vapor diffusion resistance. Hence, the induced diffusion resistance is a key factor for the decrements in heat transfer.

Further, as another important factor, the interaction effects between droplets must be considered to correct the growth rate from the isolated droplet growth model. For capturing the strong interaction during dropwise condensation, the DPSM method is creatively proposed. The correction factor reflecting the interaction intensity can be determined and favorable to correct the results of the isolated form growth model. It is notably shown through the predictions for some droplet distributions that the reduction of the growth rate by the interaction effects can be rated as dramatic comparing with the effect of the diffusion resistance. For the droplets smaller than 10 μm, the growth rate can be decreased up to three

orders thanks to the interaction effect of droplets. In comparison, the big droplets suffer a relatively weaker interaction. Actually, the interaction effects between droplets are strongly depended on the size and spatial distributions of droplets. To sum it up, for the interaction effects between droplets, the generality on the whole coexists with the personality as an independent individual.

Considering the influence of convective mass transfer for droplet growth rate, the droplet Sherwood number as another correction factor is also included by an empirical correlation. The enhancement effects of convective mass transfer present great difference for different size droplets. It is found that the increment of the condensation rate can be up to 10 times for big droplets. For small droplets, the enhancement effect can be overlooked.

Withal, not to forget that the interaction effects of droplets are sensitive to the droplet size and spatial distributions. Therefore, a numerical algorithm reflecting the droplet dynamics behaviors is developed to re-construct the droplet distribution over the substrate. The developed numerical algorithm is quantitatively and qualitatively evaluated by the experimental results for the case of droplet dynamics characteristics. Finally, taking the simulated droplet distribution, the condensation behaviors of droplets are predicted by combining all aspects. The growth rates of all droplets from the isolated droplet growth model is corrected by the correction factors related to the interaction effects between each others and their Sherwood number corresponding to the enhancement effect of convective mass transfer. The predicted results including single droplet growth rate and the overall heat flux all keep a good agreement with the measured data. It is no doubt that the current modeling idea is robust and applicable to predict heat and mass transfer driven dropwise condensation in the presence of NCG.

Significantly, this thesis highlights the mechanistic understanding on the influence of NCG for dropwise condensation. Firstly, the NCG induces the vapor diffusion resistance which seriously slows down the droplet condensation rate. But more important, the blocking effects of neighboring droplets for the vapor diffusion is another significantly negative factor for condensation. Conversely, convection (natural and forced convention) can be seen as an enhancing factor due to the case of convective mass transfer. However, the blocking effects between droplets and convective mass transfer turn in favor of big droplets from the point of heat transfer. As a consequence, different with the case of pure steam, heat transfer of dropwise condensation with the presence of NCG is primarily dedicated by the quite big droplets.

Aiming to advance the direct numerical simulation for dropwise condensation, a multi-component multi-phase thermal pseudopotential-based LB model is developed to simulate droplet condensation. Due to the limitation of the model, only small mass fraction of non-condensable component and one droplet are considered in simulation. Nevertheless, some significant results are provided. Droplet condensation is simulated starting from nucleation and the waiting time of nucleation is increased with adding non-condensable component. In addition, the influence of NCG for heat transfer of droplet condensation is depended on both

the growth stage and its amount. In case of the isolated form, the droplet growth can be evaluated by the power law. Investigations of different contact angles demonstrate that the smaller contact angle having strong dynamic behavior of the contact line will promote mass transfer of NCG far away from the corner near the wall. From this point, heat transfer of droplet condensation considering NCG can be enhanced by the hydrophilic substrate rather than the hydrophobic substrate.

7.2 Future work

Knowing the fact that the NCG is key factor for dropwise condensation heat transfer, it is still necessary to investigate the basic mechanism of droplet condensation with the presence of NCG using different methods. Firstly, the thermal conduction resistance inside the droplet and the diffusion resistance of vapor outside the droplet should be figured out more details in the forthcoming future work. Secondly, as the enhancement effect of convective mass transfer, it can be possible to improve the blocking effect of neighbors for vapor diffusion. On the other hand, there is no doubt that the present developed isolated growth model with a proper accommodation coefficient can accurately describe the droplet growth in case of NCG. Due to the complexity of the corresponding physical mechanisms and the limitation of measurement technology, the accommodation coefficient in the presence of NCG is still a subject of dispute. An exact definition of the accommodation coefficient is necessary in future. Further, DPSM in predicting the interaction effects of droplets is expensive in time, which limits the solution in each time step. It is heuristic that we found the interaction effects of droplets having generality on the whole. Accordingly, it is desired that in future a kind of correlation can be found based on the prediction of DPSM. From numerical simulation, significant efforts are still required to improve the multi-component pseudopotential LB method theoretically in future. And the present developed LB method need to be extended in 3D and parallel computation. There have been other methods to study the vapor diffusion in the interfacial region such as the molecular dynamics simulation that can be implemented into the future work. And the molecular dynamics simulation can be applied to investigate condensation mechanism from the molecular level.

Appendix A: Uncertainty analysis

The uncertainty analysis is carried out according to the guide to the expression of uncertainty in measurement (GUM) [33]. The heat flux through the block sensor is calculated using the measured value:

$$q_t = \gamma\, k_s \left(T_{fs}^* - T_{bs}^*\right) \Big/ \delta_s \tag{A.1}$$

The uncertainty in heat flux by Eq. (A1) can be calculated by:

$$u_q = \sqrt{\left(c_k u_k\right)^2 + \left(c_\delta u_\delta\right)^2 + \left(c_\gamma u_\gamma\right)^2 + \left(c_{T_{fs}} u_{T_{fs}}\right)^2 + \left(c_{T_{bs}} u_{T_{bs}}\right)^2} \tag{A.2}$$

with the sensitivity coefficients c for different variables:

$$c_k = \partial q_t / \partial k_s = \gamma \left(T_{fs}^* - T_{bs}^*\right) \Big/ \delta_s \tag{A.3}$$

$$c_\delta = \partial q_t / \partial \delta_s = -\gamma k_s \left(T_{fs}^* - T_{bs}^*\right) \Big/ \delta_s^2 \tag{A.4}$$

$$c_\gamma = \partial q_t / \partial \gamma = k_s \left(T_{fs}^* - T_{bs}^*\right) \Big/ \delta_s \tag{A.5}$$

$$c_{T_{fs}} = \partial q_t \Big/ \partial T_{fs}^* = \gamma k_s / \delta_s \tag{A.6}$$

$$c_{T_{bs}} = \partial q_t \Big/ \partial T_{bs}^* = -\gamma k_s / \delta_s \tag{A.7}$$

These sensitivity coefficients defined the partial derivatives describe how the output estimate varies with changes in the values of the input estimates. The mean temperature at front and back side from the thermocouple readings can be seen as a Type A uncertainty. The uncertainty for the thickness δ_s is considered zero. The thermal conductivity k_s and the correction factor γ are considered as Type B uncertainty are estimated with the accuracy ±2.0 $W\ m^{-1}\ K^{-1}$ and ±0.1, respectively. Table A.1 lists the relative fractional uncertainties for all measured values. Considering a coverage factor 2, the relative expanded uncertainties of the overall heat flux for convection and condensation experiments are located in a range 6.9%-10.6% and 14.5%-17.0%.

Table A.1 The relative fractional uncertainties.

Input variable	Type	Uncertainty u (%)
Thermal conductivity k_s	B	2.9
Correction factor γ	B	5.8
Front side temperature T_{fs}^*	A	0.025-1.2
Back side temperature T_{bs}^*	A	0.012-0.37

Appendix B: The incoming and outing mas flow rate of vapor molecules

The droplet itself is supposed to be in internal equilibrium. Finally, all molecules evaporating and reflecting from the droplet surface are considered having a Maxwellian velocity distribution with the temperature T_{ds}. The velocity distributions of vapor molecules are specified as follows:

$$f_{+v} = \frac{\rho_{v,ds}}{\left(2\pi R_v T_{ds}\right)^{3/2}} \exp\left\{-\left[\frac{\beta_r^2 + \beta_\xi^2 + \beta_\varphi^2}{2R_v T_{ds}}\right]\right\} \tag{B1}$$

where (β_r, β_ξ, β_φ) are the velocity components of vapor molecules in the spherical coordinate system (r, ξ, φ). The outgoing mass flow rate of vapor from the droplet surface can be calculated using the integration of the Maxwellian velocity distribution over the hemispherical surface of droplet:

$$m_{+v} = 2\pi R^2 \left(1-\cos\theta\right) \int_0^\infty \int_{-\infty}^\infty \int_{-\infty}^\infty \beta_r f_{+v} d\beta_r d\beta_\xi d\beta_\varphi = 2\pi R^2 \left(1-\cos\theta\right) \rho_{v,ds} R_v T_{ds} \Big/ \sqrt{2\pi R_v T_{ds}} \tag{B2}$$

However, the vapor in the continuum region outside the Knudsen layer is in a non-equilibrium state, and hence the Maxwellian velocity distribution for the equilibrium state cannot be well approximated for the molecules velocity distribution. As a good representation of the real molecules velocity distribution, a much better approximation in continuum region is the Grad distribution, which can also work at the interface i between the Knudsen layer and the continuum region. When the Knudsen layer is considered as a collision-free zone, the molecules velocity distribution arriving at the droplet surface corresponds to that at the interface. Thus, the velocity distribution of incoming molecules at the droplet surface can be written as the Grad distribution function:

$$\begin{aligned} f_{-v} = \frac{\rho_{v,i}}{\left(2\pi R_v T_i\right)^{3/2}} \Bigg\{ & 1 - \frac{q_{v,i}\left(\beta_r - u_{b,i}\right)}{p_{v,i} R_v T_i}\left[1 - \frac{(\beta_r - u_{b,i})^2 + \beta_\xi^2 + \beta_\varphi^2}{5R_v T_i}\right] \\ & + \frac{v_{v,i}\left(\beta_r - u_{b,i}\right)}{R_v T_i}\left[3.5 - \frac{(\beta_r - u_{b,i})^2 + \beta_\xi^2 + \beta_\varphi^2}{2R_v T_i}\right]\Bigg\} \exp\left\{-\left[\frac{\left(\beta_r - u_{b,i}\right)^2 + \beta_\xi^2 + \beta_\varphi^2}{2R_v T_i}\right]\right\} \end{aligned} \tag{B3}$$

where $u_{b,i}$ is the bulk velocity, $v_{v,i}$ is the diffusive velocity of vapor, $q_{v,i}$ is the contribution of the vapor molecules for the radial heat flux. Likewise, the incoming mass flow rate of vapor at the droplet surface can be got by substituting Eq. (B3). The final form is obtained using some assumption and approximation, and the total mass flow rate m:

$$\begin{aligned} m_{-v} &= 2\pi R^2 \left(1-\cos\theta\right) \int_{-\infty}^0 \int_{-\infty}^\infty \int_{-\infty}^\infty \beta_r f_{-v} d\beta_{vr} d\beta_\xi d\beta_\varphi \\ &\approx -2\pi R^2 \left(1-\cos\theta\right) \frac{\rho_{v,i} R_v T_i}{\sqrt{2\pi R_v T_i}} \left[1 - \frac{\left(u_{b,i} + v_{v,i}\right)\sqrt{\pi}}{\sqrt{2R_v T_i}}\right] \\ &\approx -2\pi R^2 \left(1-\cos\theta\right) \frac{\rho_{v,i} R_v T_i}{\sqrt{2\pi R_v T_i}} + \frac{R^2}{2R_i^2} m \end{aligned} \tag{B4}$$

Appendix C: GPBiCG algorithm

A general linear system is written as:

$$\boldsymbol{A}\boldsymbol{x} = \boldsymbol{b} \tag{C1}$$

where the coefficient matrix $\boldsymbol{A}$ is an square matrix, $\boldsymbol{b}$ and $\boldsymbol{x}$ are a column vector with same order. The GPBiCG algorithm as an iterative method is developed to solve a non-symmetric linear system [76-78]. The algorithm is proceeding below [76-78]:

1: let $\boldsymbol{r}_0$ be an initial guess, and take $\boldsymbol{r}_0 = \boldsymbol{b}\text{-}\boldsymbol{A}\boldsymbol{x}$ here

2: chose a arbitrary vector $\boldsymbol{r}^*$ such that $(\boldsymbol{r}^*, \boldsymbol{r}_0) \neq 0$, e.g. $\boldsymbol{r}^* = \boldsymbol{r}_0$

3: other vectors and scalars using next is initialized with zero vector and constant zero

4: **for** k=1, 2, …, until $\| \boldsymbol{r}_k \| \leq tol$

5: $\boldsymbol{p}_k = \boldsymbol{r}_k + \beta_{k-1}\left(\boldsymbol{p}_{k-1} - \boldsymbol{u}_{k-1}\right)$; $\boxed{\boldsymbol{q}_k = \boldsymbol{A}\boldsymbol{p}_k}$

6: $$\alpha_k = \frac{\left(\boldsymbol{r}^*, \boldsymbol{r}_k\right)}{\left(\boldsymbol{r}^*, \boldsymbol{q}_k\right)}$$

7: $\boldsymbol{t}_k = \boldsymbol{r}_k - \alpha_{k-1}\boldsymbol{q}_k$; $\boxed{\boldsymbol{s}_k = \boldsymbol{A}\boldsymbol{t}_k}$

8: **if** (k=1) **then**

9: $$\zeta_k = \frac{\left(\boldsymbol{s}_k, \boldsymbol{t}_k\right)}{\left(\boldsymbol{s}_k, \boldsymbol{s}_k\right)}$$

10: $\boldsymbol{u}_k = \zeta_k \boldsymbol{q}_k$

11: $\boldsymbol{z}_k = \zeta_k \boldsymbol{r}_k - \alpha_k \boldsymbol{u}_k$

12: $\boldsymbol{r}_{k+1} = \boldsymbol{t}_k - \zeta_k \boldsymbol{s}_k$

13: **else**

14: $$\eta_k = \frac{\left(\boldsymbol{s}_k, \boldsymbol{s}_k\right)\left(\boldsymbol{y}_k, \boldsymbol{t}_k\right) - \left(\boldsymbol{y}_k, \boldsymbol{s}_k\right)\left(\boldsymbol{s}_k, \boldsymbol{t}_k\right)}{\left(\boldsymbol{s}_k, \boldsymbol{s}_k\right)\left(\boldsymbol{y}_k, \boldsymbol{y}_k\right) - \left(\boldsymbol{y}_k, \boldsymbol{s}_k\right)\left(\boldsymbol{s}_k, \boldsymbol{y}_k\right)}$$

15: $$\zeta_k = \frac{\left(\boldsymbol{y}_k, \boldsymbol{y}_k\right)\left(\boldsymbol{s}_k, \boldsymbol{t}_k\right) - \left(\boldsymbol{y}_k, \boldsymbol{t}_k\right)\left(\boldsymbol{s}_k, \boldsymbol{y}_k\right)}{\left(\boldsymbol{s}_k, \boldsymbol{s}_k\right)\left(\boldsymbol{y}_k, \boldsymbol{y}_k\right) - \left(\boldsymbol{y}_k, \boldsymbol{s}_k\right)\left(\boldsymbol{s}_k, \boldsymbol{y}_k\right)}$$

16: $\boldsymbol{u}_k = \zeta_k \boldsymbol{q}_k + \eta_k\left(\boldsymbol{t}_{k-1} - \boldsymbol{r}_k + \beta_{k-1}\boldsymbol{u}_{k-1}\right)$

17: $\boldsymbol{z}_k = \zeta_k \boldsymbol{r}_k + \eta_{k-1}\boldsymbol{z}_{k-1} - \alpha_k \boldsymbol{u}_k$

18: $\boldsymbol{r}_{k+1} = \boldsymbol{t}_k - \eta_k \boldsymbol{y}_k - \zeta_k \boldsymbol{s}_k$

19: **end if**

20: $\beta_k = \dfrac{\alpha_k}{\zeta_k} \dfrac{\left(\boldsymbol{r}^*, \boldsymbol{r}_{k+1}\right)}{\left(\boldsymbol{r}^*, \boldsymbol{r}_k\right)}$

21: $\boldsymbol{x}_{k+1} = \boldsymbol{x}_k + \alpha_k \boldsymbol{p}_k + \boldsymbol{z}_k$

22: $\boldsymbol{w}_{k+1} = \boldsymbol{s}_k + \beta_k \boldsymbol{q}_k$

23: **end**

In the algorithm, the small bolds mean the vector, the big bolds represent the matrix, the Greek symbols are the scalar. Here the convergence criterion is less than *tol*=1e-5 of the residual $||\boldsymbol{r}_k||$. Moreover, notation ($\boldsymbol{x}$, $\boldsymbol{y}$) denotes the inner product of two vectors. The computing cost for the inner product of vectors can be ignored comparing with matrix-vector multiplication. Therefore, only the matrix-vector multiplication (namely the computation for $\boldsymbol{q}$ and $\boldsymbol{s}$) is paralleled in our program. The above symbols in this subsection are just suitable to illustrate the solution of a linear system.

Appendix D: Additional figures for the prediction of the interaction effects

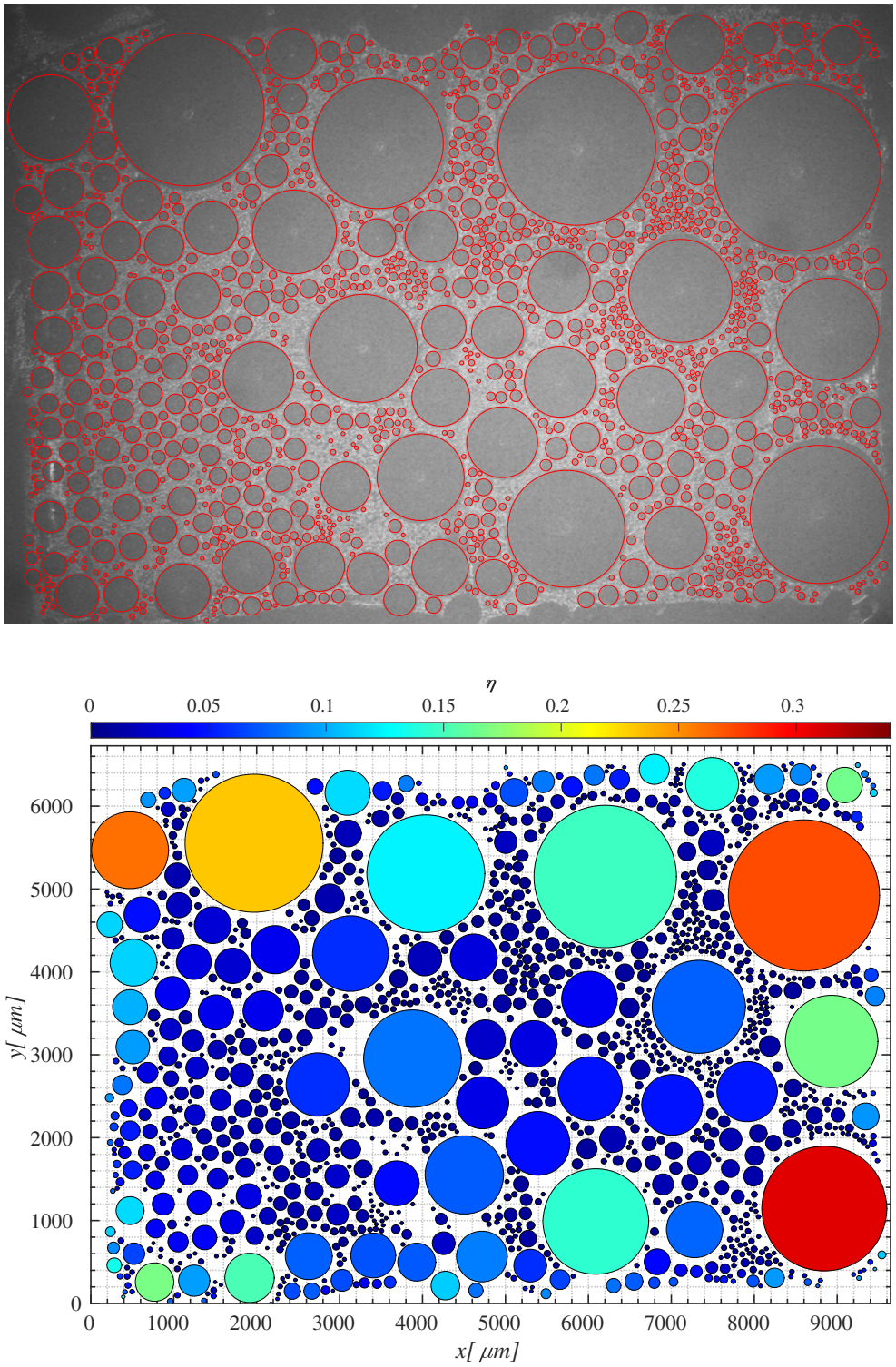

Figure D-1 Prediction of the interaction effects between droplets for the experimentally detected droplet distribution: Case E1.

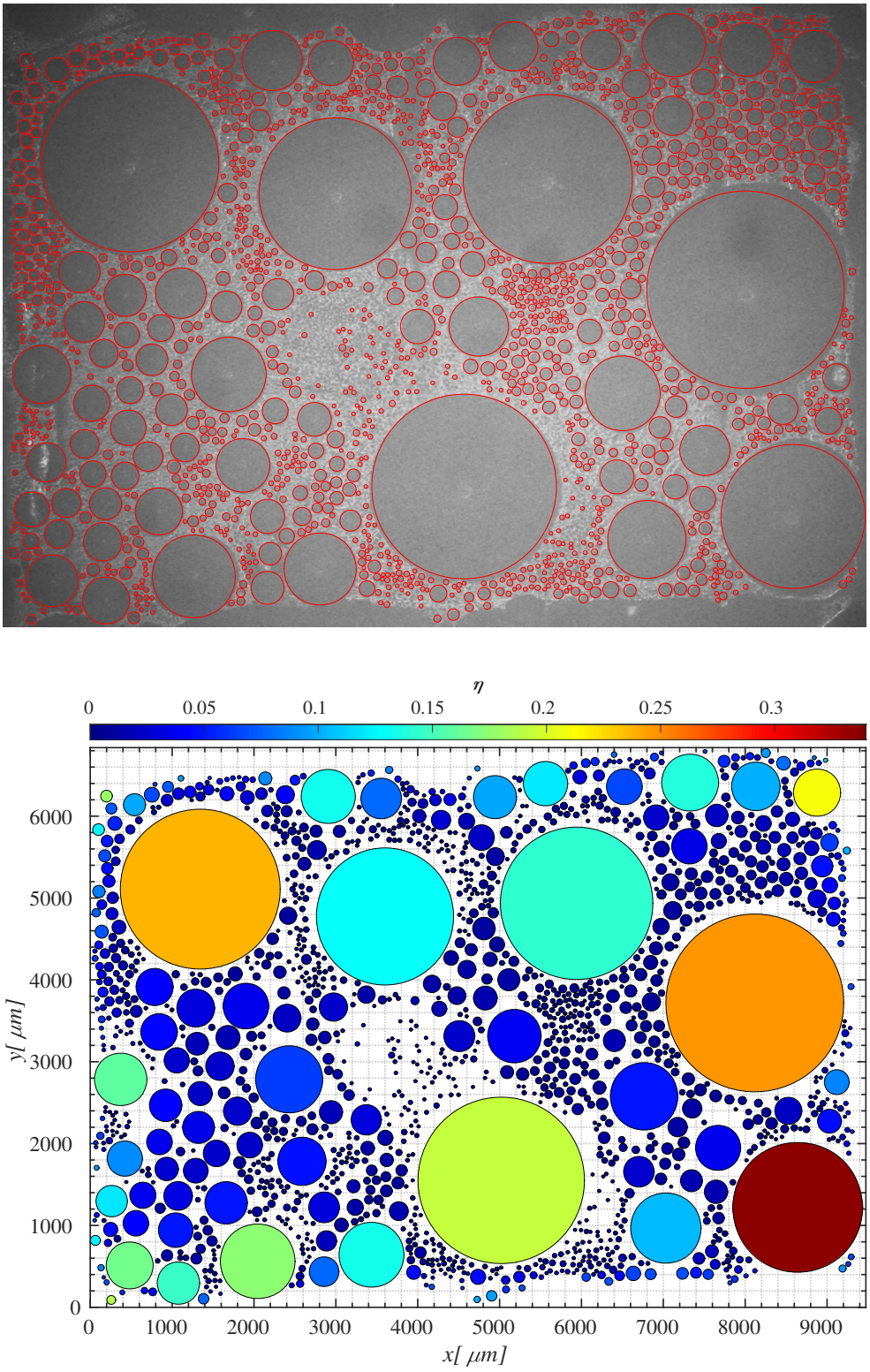

Figure D-2 Prediction of the interaction effects between droplets for the experimentally detected droplet distribution: Case E2.

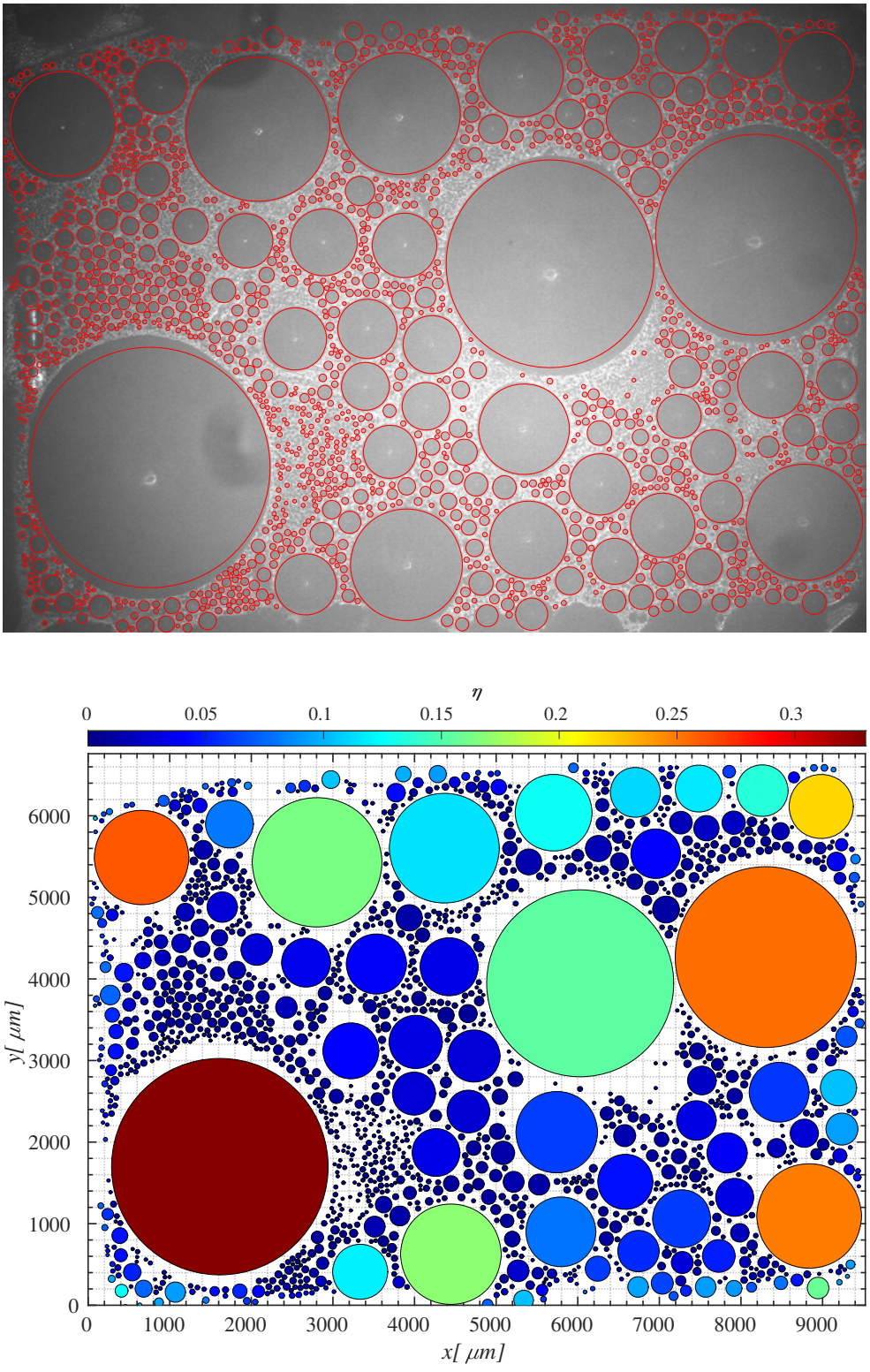

Figure D-3 Prediction of the interaction effects between droplets for the experimentally detected droplet distribution: Case E3.

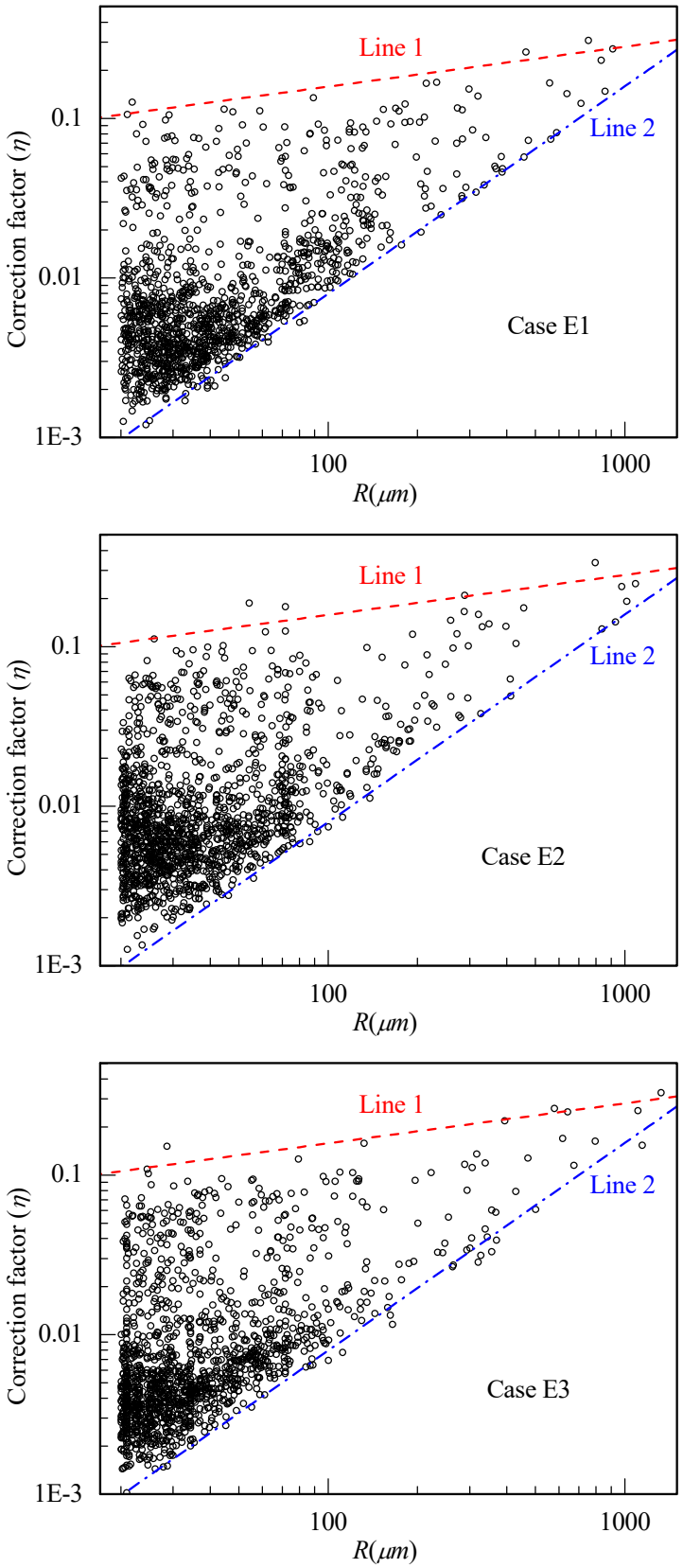

Figure D-4 The predicted correction factors of droplets with respect to its radius.

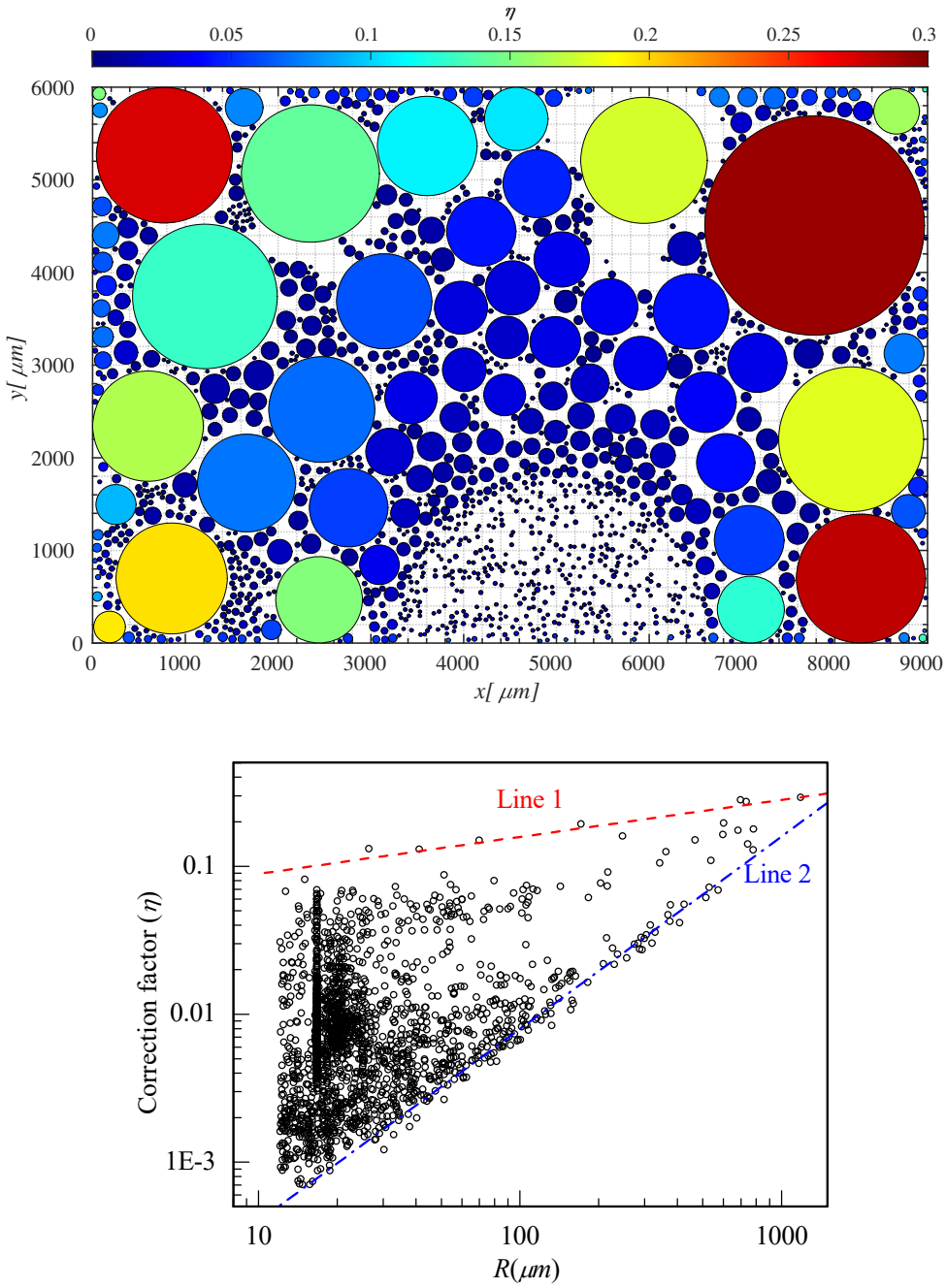

Figure D-5 Prediction of the interaction effects between droplets for the simulated droplet distribution: Case S1.

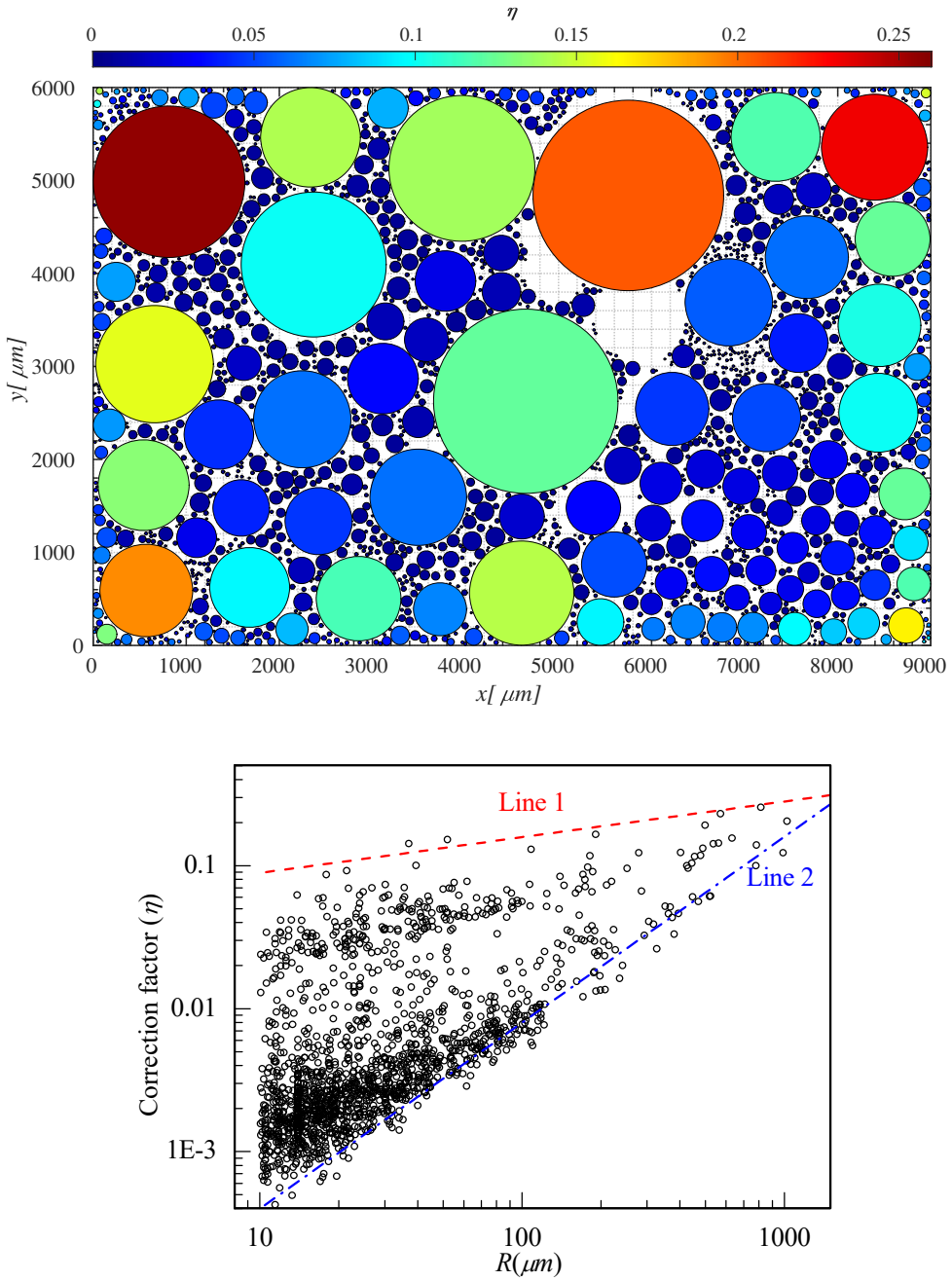

Figure D-6 Prediction of the interaction effects between droplets for the simulated droplet distribution: Case S2.

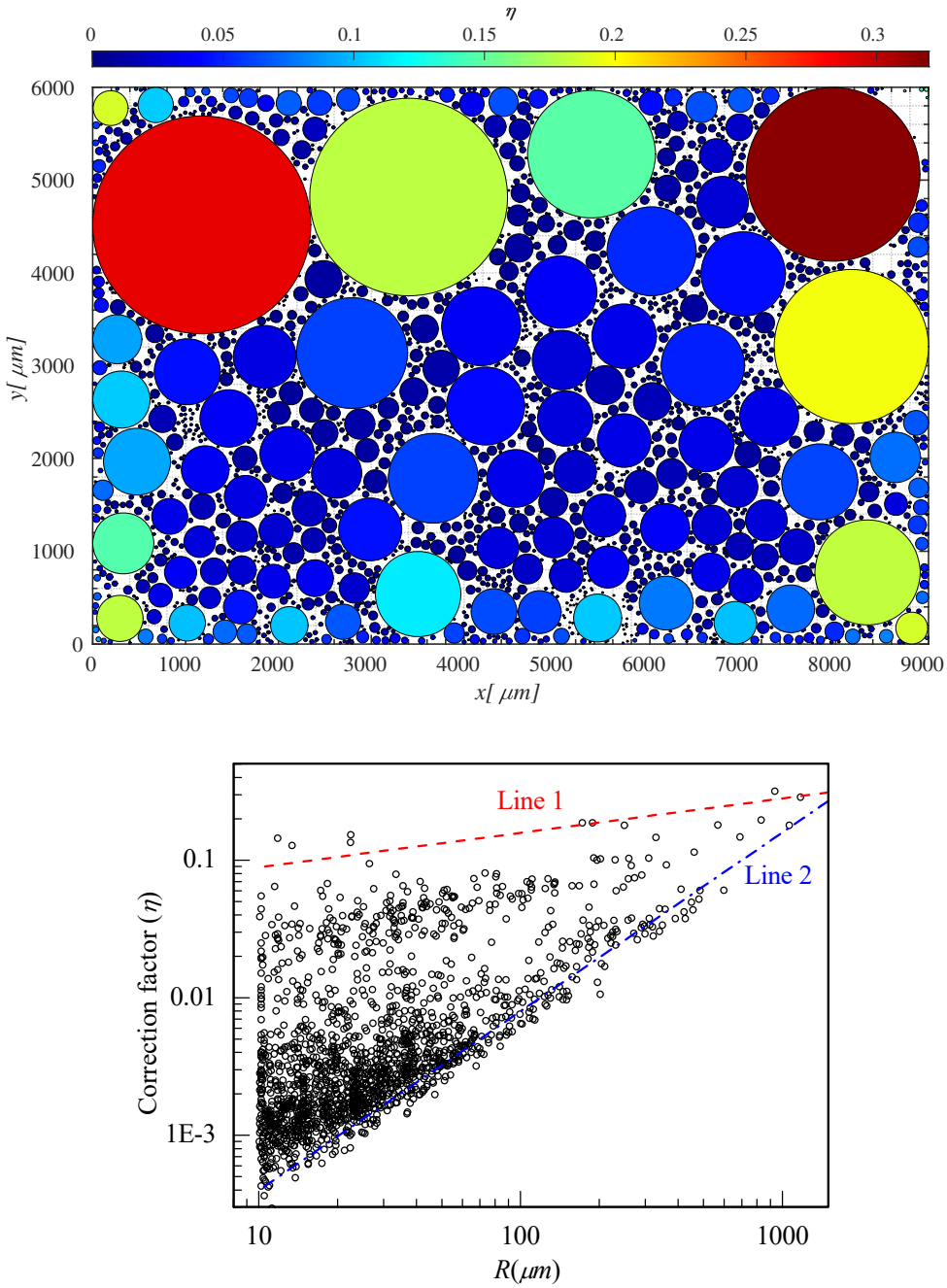

Figure D-7 Prediction of the interaction effects between droplets for the simulated droplet distribution: Case S3.

References

[1] www.pinterest.de

[2] J. G. Collier and J. R. Thome, Convective boiling and codensation, Oxford University Press, New York, 1994.

[3] F. T. Malik, R. M. Clement, D. T. Gethin, W. Krawszik and A. R. Parker, Nature's moisture harvesters: a comparative review, Bioinspir. Biomim. 9 (2014) 031002.

[4] S. Khandekar and K. Muralidhar, Dropwise condensation on inclined textured surfaces, Springer, New York, 2014.

[5] N. Miljkovic, R. Enright, Y. Nam, K. Lopez, N. Dou, J. Sack and E. N. Wang, Jumping-droplet-enhanced condensation on scalable superhydrophobic nanostructured surfaces, Nano Lett. 13 (2013) 179-187.

[6] J. W. Rose, Dropwise condensation theory and experiment: a review, Proc. Inst. Mech. Eng., Part A: J. Power Energy 216 (2002) 115-128.

[7] E. Schmidt, W. Schurig and W. Sellschop, Versuche uber die Kondensation von Wasserdampf in film- und tropfenform, Technische Mechanik und Thermodynamik 1 (1963) 53-63.

[8] J. Huang, J. X. Zhang and L. Wang, Review of vapor condensation heat and mass transfer in the presence of non-condensable gas, Appl. Therm. Eng. 89 (2015) 469-484.

[9] M. Abu-Orabi, Modeling of heat transfer in dropwise condensation, Int. J. Heat Mass Transfer 41 (1) (1998) 81-87.

[10] N. Miljkovic and E. N. Wang, Condensation heat transfer on superhydrophobic surfaces, MRS BULL. 38 (5) (2013) 397-406.

[11] D. Attinger, C. Frankiewicz, A. R. Betz, T. M. Schutzius, R. Ganguly, A. Das, C. J. Kim and C. M. Megaridis, Surface engineering for phase change heat transfer: a review, MRS Energy & Sustainability 1 (2014) E4.

[12] P. Zhang and F. Y. Lv, A review of the recent advances in superhydrophobic surfaces and the emerging energy-related applications, Energy 82 (2015) 1068-1087.

[13] H. Jeremy Cho, D. J. Preston, Y. Zhu and E. N. Wang, Nanoengineered materials for liquid-vapor phase-change heat transfer, Nat. Rev. Mater. 2 (2016) 16092.

[14] R. Wen, S. Xu, X. Ma, Y. C. Lee and R. Yang, Three-dimensional superhydrophobic nanowire networks for enhancing condensation heat transfer, Joule 2 (2) (2018) 269-279.

[15] S. A. Khan, F. Tahir, A. A. Bozdar Baloch and M. Koc, Review of micro-nanoscale surface coatings application for sustaining dropwise condensation, Coatings 9 (2) (2019) 117.

[16] K. C. Park, P. Kim, A. Grinthal, N. He, D. Fox, J. C. Weaver and J. Aizenberg, Condensation on slippery asymmetric bumps, Nature 531 (2016) 78-82.

[17] H. Chen, P. Zhang, L. Zhang, H. Liu, Y. Jiang, D. Zhang, Z. Han and L. Jiang, Continuous directional water transport on the peristome surface of Nepenthes alata, Nature 532 (2016) 85-89.

[18] C. Hao, Y. Liu, X. Chen, J. Li, M. Zhang, Y. Zhao and Z. Wang, Bioinspired interfacial materials with enhanced drop mobility: from fundamentals to multifunctional applications, Small 12 (14) (2016) 1825-1839.

[19] X. Dai, N. Sun, S. O. Nielsen, B. B. Stogin, J. Wang, S. Yang and T. S. Wong, Hydrophilic directional slippery rough surfaces for water harvesting, Sci. Adv., 4 (3) (2018) eaaq0919.
[20] J. Li, J. Li, J. Sun, S. Feng and Z. Wang, Biological and engineered tpological droplet rectifiers, Adv. Mater. 31 (2019) 1806501.
[21] D. W. Tanner, C. J. Potter, D. Pope and D. West, Heat transfer in dropwise condensation-part I: the effect of heat flux, steam velocity and non-condensable gas concentration, Int. J. Heat Mass Transfer 8 (3) (1965) 419-426.
[22] D. W. Tanner, D. Pope, C. J. Potter and D. West, Heat transfer in dropwise condensation at low steam pressures in the absence and presence of non-condensable gas, Int. J. Heat Mass Transfer 11 (2) (1968) 181-190.
[23] B. J. Chung, S. Kim, M. C. Kim and M. Ahmadinejad, Experimental comparison of filmwise and dropwise condensation of steam on vertical flat plates with the presence of air, Int. Commun. Heat Mass Transfer 31 (8) (2004) 1067-1074.
[24] S. X. Wang and Y. Utaka, An experimental study on the effect of non-condensable gas for solutal marangoni condensation heat transfer, Exp. Heat Transfer 18 (2) (2005) 61-79.
[25] X. H. Ma, X. D. Zhou, Z. Lan, Y. M. Li and Y. Zhang, Condensation heat transfer enhancement in the presence of non-condensable gas using the interfacial effect of dropwise condensation, Int. J. Heat Mass Transfer 51(7-8) (2008) 1728-1737.
[26] D. F. Othmer, The condensation of steam, Ind. Eng. Chem. 21(6) (1929) 577-583.
[27] M. H. M. Grooten and C. W. M. van der Geld, Dropwise condensation from flowing air-steam mixtures: diffusion resistance assessed by controlled drainage, Int. J. Heat Mass Transfer 54 (2011) 4507-4517.
[28] M. H. M. Grooten and C. W. M. van der Geld, Surface property effects on dropwise condensation heat transfer from flowing air-steam mixtures to promote drainage, Int. J. Therm. Sci. 54 (2012) 220-229.
[29] J. E. Castillo, J. A. Weibel and S. V. Garimella, The effect of relative humidity on dropwise condensation dynamics, Int. J. Heat Mass Transfer 80 (2015) 759-766.
[30] S. Danilo, C. Dominique and P. Frederic, Experimental dropwise condensation condensation of unsaturated humid air – influence of humidity level on latent and convective heat transfer for fully developed turbulent flow, Int. J. Heat Mass Transfer 102 (2016) 846-855.
[31] F. Eimann, S. Zheng, C. Philipp, T. Fieback and U. Gross, Convective dropwise condensation out of humid air inside a horizontal channel-experimental investigation of the condensate heat transfer resistance, Int. J. Heat Mass Transfer 127 (2018) 448-464.
[32] Y. Zhao, D. J. Preston, Z. Lu, L. Zhang, J. Queeney and E. N. Wang, Effects of millimetric geometric features on dropwise condensation under different vapor conditions, Int. J. Heat Mass Transfer 119 (2018) 931-938.
[33] BIPM, IEC, IFCC, ILAC, ISO, IUPAC, IUPAP AND OIML, Evaluation of measurement data-guide to the expression of uncertainty in measurement, JCGM 100:2008, GUM 1995 with minor corrections, 2008.

[34] J. P. Holman, Heat transfer, 10th ed., McGraw-Hill, London, 2010.
[35] V. Gnielinski, Heat transfer in pipe flow, in: Sec. Ed., VDI Heat Altas, Springer, Heidelberg, 2010.
[36] N. Watanabe, M. Aritomi and A. Machida, Time-series characteristics and geometric structures of drop-size distribution density in dropwise condensation, Int. J. Heat Mass Transfer 76 (2014) 467-483.
[37] M. F. Mei, F. Hu, C. Han and Y. H. Cheng, Time-averaged droplet size distribution in steady-state dropwise condensation, Int. J. Heat Mass Transfer 88 (2015) 338-345.
[38] E. J. Le Fevre and J. W. Rose, A theory of heat transfer by dropwise condensation, in: Proceedings of 3rd International Heat Transfer, Chicago, USA, 2 (1966) 362-375.
[39] J. L. McCormick and J. W. Westwater, Nucleation sites for dropwise condensation, Chem. Eng. Sci. 20 (12) (1965) 1021-1036.
[40] H. J. Seltman, Experimental design and analysis, Carnegie Mellon University, Pittsburgh, PA, 2018.
[41] R. N. Leach, F. Stevens, S. C. Langford and J. T. Dickinson, Dropwise condensation: experiments and simulations of nucleation and growth of water drops in a cooling system, Langmuir 22 (2006) 8864-8872.
[42] M. G. Medici, A. Mongruel, L. Royon and D. Beysens, Edge effects on water droplet condensation, Phys. Rev. E 90 (6) (2014) 062403.
[43] J. W. Rose, Some aspects of condensation heat transfer theory, Int. Commun. Heat Mass Transfer 14 (4) (1988) 449-473.
[44] X. Chen and M. M. Derby, Droplet departure modeling and a heat transfer correlation for dropwise flow condensation in hydrophobic mini-channels, Int. J. Heat Mass Transfer 125 (2018) 1096-1104.
[45] A. Ghosh, S. Beaini, B. J. Zhang and C. M. Megaridis, Enhancing dropwise condensation through bioinspired wettability patterning, Langmuir 30 (43) (2014) 13103-13115.
[46] I. O. Ucar and H. Y. Erbil, Use of diffusion controlled drop evaporation equations for dropwise condensation during dew formation and effect of neighboring droplets, Colloids Surf. A: Physicochem. Eng. Asp. 411 (2012) 60-68.
[47] J. Guadarrama-Cetina, R. D. Narhe, D. A. Beysens and W. Gonzalez-Vinas, Droplet pattern and condensation gradient around a humidity sink, Phys. Rev. E 89 (1) (2014) 012402.
[48] J. E. Castillo and J. A. Weibel, A point sink superposition method for predicting droplet interaction effects during vapor-diffusion-driven dropwise condensation in humid air, Int. J. Heat Mass Transfer 118 (2018) 708-719.
[49] G. Gyarmathy, The spherical droplet in gaseous carrier streams: review and synthesis, Multiphase Sci. Technol. 1 (1-4) (1982) 99-279.
[50] J. B. Young, The condensation and evaporation of liquid droplets in a pure vapor at arbitrary Knudsen number, Int. J. Heat Mass Transfer 34 (7) (1991) 1649-1661.
[51] J. B. Young, The condensation and evaporation of liquid droplets at arbitrary Knudsen number in the presence of an inert gas, Int. J. Heat Mass Transfer 36 (11) (1993) 2941-2956.

[52] F. Peters and K. A. J. Meyer, Measurement and interpretation of growth of monodispersed water droplets suspended in pure vapor, Int. J. Heat Mass Transfer 38 (17) (1995) 3285-3293.
[53] P. Peeters, C. C. M. Luijten and M. E. H. van Dongen, Transitional droplet growth and diffusion coefficients, Int. J. Heat Mass Transfer 44 (1) (2001) 181-193.
[54] X. Luo, Y. Fan, F. Qin, H. Gui and J. Liu, A new model for the processes of droplet condensation and evaporation on solid surface, Int. J. Heat Mass Transfer 100 (2016) 208-214.
[55] I. Langmuir, The dissociation of hydrogen into atoms. [Part II.] calculation of the degree of dissociation and the heat of formation, J. Am. Chem. Soc. 37 (3) (1915) 417-458.
[56] E. J. Davis, and G. Schweiger, The airborne microparticle: its physics, chemistry, optics and transport phenomena, First Ed., Springer, Heidelberg, 2002.
[57] V. A. Zagaynov, V. M. Nuzhny, T. A. Cheusova and A. A. Lushnikov, Evaporation of water droplet and condensation coefficient: theory and experiment, J. Aerosol Sci. 31 (suppl. 1) (2000) 795-796.
[58] R. Marek and J. Straub, Analysis of the evaporation coefficient and the condensation coefficient of water, Int. J. Heat Mass Transfer 44 (1) (2001) 39-53.
[59] R. Holyst, M. Litniewski, D. Jakubczyk, K. Kolwas, M. Kolwas, K. Kowalski, S. Migacz, S. Palesa and M. Zientara, Evaporation of freely suspended single droplets: experimental, theoretical and computational simulations, Rep. Prog. Phys. 76 (3) (2013) 034601.
[60] M. Z. Jacobson, Fundamentals of atmospheric modeling, second ed., Cambridge University Press, New York, 2005.
[61] S. Zheng, F. Eimann, C. Philipp, T. Fieback and U. Gross, Modeling of heat and mass transfer for dropwise condensation of moist air and the experimental validation, Int. J. Heat Mass Transfer 120 (2018) 879-894.
[62] C. Graham and P. Griffith, Drop size distributions and heat transfer in dropwise condensation, Int. J. Heat Mass Transfer 16 (2) (1973) 337-346.
[63] M. Sokuler, G. K. Auernhammer, C. J. Liu, E. Bonaccurso and H-J. Butt, Dynamics of condensation and evaporation effect of inter-drop spacing, EPL 89 (2010) 36004.
[64] J. E. Castillo and J. A. Weibel, Predicting the growth of many droplets during vapor-diffusion-driven dropwise condensation experiments using the point sink superposition method, Int. J. Heat Mass Transfer 133 (2019) 641-651.
[65] K. Annamalai, W. Ryan and S. Chandra, Evaporation of multicomponent drop arrays, J. Heat Transfer 115(3) (1993) 707-716.
[66] K. Annamalai and W. Ryan, Interactive process in gasification and combustion. Part I: liquid drop arrays and clouds, Prog. Energy Combust. Sci. 18 (1992) 221-295.
[67] W. A. Sirignano, Advances in droplet array combustion theory and modeling, Prog. Energy Combust. Sci. 42 (2014) 54-86.
[68] M. Labowsky, The effects of nearest neighbor interactions of the evaporation rate of cloud particles, Chem. Eng. Science, 31 (1976) 803-813.

[69] M. Labowsky, Transfer rate calculations for compositionally dissimilar interacting particles, Chem. Eng. Science, 35 (1980) 1041-1048.
[70] J. D. Jackson, Classical electrodynamics, 3rd ed., John Wiley & Sons, New York, 1998.
[71] P.T. Metzger, J.E. Lane, Electric potential due to a system of conducting spheres, Open Appl. Phys. J. 2 (2009) 32–48.
[72] M. Labowsky, Comments arising from "effect of multiple particle interactions on burning droplets" by M. Marberry, A. K. Ray, and K. Leung, Combust. Flame 57:237 (1987), Combust. Flame, 65 (1986) 367-369.
[73] A. H. Reis, Constructal view of scaling laws of river basins, Geomorphology 78 (3) (2006) 201-206.
[74] D. Placko and T. Kundu, DPSM for modeling engineering problems, John Wiley & Sons Inc., New Jersey, 2007.
[75] J. Cheng, W. Lin and Y. Qin, Extension of the distributed point source method for ultrasonic field modeling, Ultrasonics 51 (5) (2011) 571-580.
[76] S. L. Zhang, GPBi-CG: Generalized product-type methods based on Bi-CG for solving nonsymmetric linear systems, SIAM J. Sci. Comput. 18 (2) (1997) 537-551.
[77] S. Fujino, GPBiCG(*m*, *l*): a hybrid of BiCGSTAB and GPBiCG methods with efficiency and robustness, Appl. Numer. Math. 41 (2002) 107-117.
[78] S. X. Zhu, T. X. Gu and X. P. Liu, Minimizing synchronizations in sparse iterative solvers for distributed supercomputer, Comput. Math. Appl. 67 (2014) 199-209.
[79] L. F. Shampine, MATLAB program for quadrature in 2D, Appl. Math. Comput. 202 (2008) 266-274.
[80] M. Singh, N. D. Pawar, S. Kondaraju and S. S. Bahga, Modeling and simulation of dropwise condensation: a review, J. India Inst. Sci. 99 (1) (2019) 157-171.
[81] S. Kim and K. J. Kim, Dropwise condensation modeling suitable for superhydrophobic surfaces, ASME J. Heat Transfer 133 (2011) 081502.
[82] N. Miljkovic, R. Enright and E. N. Wang, Modeling and optimization of superhydrophobic condensation, ASME J. Heat Transfer 135 (2013) 111004.
[83] B. Peng, X. Ma, Z. Lan, W. Xu and R. Wen, Analysis of condensation heat transfer enhancement with dropwise-filmwise hybrid surface: droplet size effect, Int. J. Heat Mass Transfer 77 (2014) 785-794.
[84] X. Liu and P. Cheng, Dropwise condensation theory revisited part II. droplet nucleation density and condensation heat flux, Int. J. Heat Mass Transfer 83 (2015) 842-849.
[85] D. Liu, L. Guo, H. W. Hu and G. H. Tang, Dropwise condensation heat transfer model considering the liquid-solid interfacial thermal resistance, Int. J. Heat Mass Transfer 112 (2018) 333-342.
[86] M. Singh, S. Kondaraju and S. S. Bahga, Mathematical model for dropwise condensation on a surface with wettability gradient, ASME J. Heat Transfer 140 (2018) 071502.
[87] Y. Shang, Y. Hou, M. You and S. Yao, Modeling and optimization of condensation

heat transfer at biphilic interface, Int. J. Heat Mass Transfer 122 (2018) 117-127.
[88] B. M. Burnside and H. A. Hadi, Digital computer simulation of dropwise condensation from equilibrium droplet to detectable size, Int. J. Heat Mass Transfer 42 (16) (1999) 3137-3146.
[89] B. S. Sikarwar, N. K. Battoo, S. Khandekar and K. Muralidhar, Dropwise condensation underneath chemically textured surfaces: simulation and experiments, ASME J. Heat Transfer 133 (2011) 021501.
[90] P. M. Somwanshi, K. Muralidhar and S. Khandekar, Dropwise condensation patterns of bismuth formed on horizontal and vertical surfaces, Int. J. Heat Mass Transfer 122 (2018) 1024-1039.
[91] H. D. Baehr and K. Stephan, Heat and mass transfer, second ed., Springer, Heidelberg, 2006.
[92] R. Byron Bird, W. E. Stewart and E. N. Lightfoot, Transport phenomena, second ed., John Willey & Sons, New York, 2002.
[93] W. Ranz and W. Marshall, Evaporation from drops: Part I. Chem. Eng. Prog. 48 (3) (1952) 141-146.
[94] J. Schwarz and J. Smolik, Mass transfer from a drop-I. experimental study and comparison with existing correlations, Int. J. Heat Mass Transfer 37 (14) (1994) 2139-2143.
[95] M. Kulmala, T. Vesala, J. Schwarz and J. Smolik, Mass transfer from a drop-II. theoretical analysis of temperature dependent mass flux correlation, Int. J. Heat Mass Transfer 38 (9) (1995) 1705-1708.
[96] S. K. Aggarwal and F. Peng, A review of droplet dynamics and vaporization modeling for engineering calculations, J. Eng. Gas Turbines Power 117 (1995) 453-461.
[97] A. Kumar and S. Hartland, Correlations for prediction of mass transfer coefficients in single drop systems and liquid-liquid extraction columns, Chem. Eng. Res. Des. 77 (1999) 372-384.
[98] M. Wegener, N. Paul and M. Kraume, Fluid dynamics and mass transfer at single droplets in liquid/liquid systems, Int. J. Heat Mass Transfer 71 (2014) 475-495.
[99] D. Brutin, Droplet wetting and evaporation: from pure to complex fludis, Elsevier, 2015.
[100] W. H. Wu and J. R. Maa, On the heat transfer in dropwise condensation, Chem. Eng. J. 12 (3) (1976) 225-231.
[101] Z. Lan, R. F. Wen, A. L. Wang and X. H. Ma, A droplet model in steam condensation with noncondensable gas, Int. J. Therm. Sci. 68 (2013) 1-7.
[102] S. S. Sazhin, Advanced models of fuel droplet heating and evaporation, Prog. Energy Combust. Sci. 32 (2006) 162-214.
[103] C. R. Kharangate and I. Mudawar, Review of computational studies on boiling and condensation, Int. J. Heat Mass Transf. 108 (2017) 1164-1196.
[104] K. H. Luo J. Xia and E. Moncao, Multiscale modeling of multiphase flow with complex interactions, J. Multiscale Modell. 1 (2009) 125-156.
[105] S. Chen and G. D. Doolen, Lattice Boltzmann method for fluid flows, Annu. Rev.

Fluid Mech. 30 (1998) 329-364.
[106] S. Succi, The lattice Boltzmann equation for fluid dynamics and beyond, Clarendon Press, Oxford, 2001.
[107] M. C. Sukop and D. T. Thorne, Lattice Boltzmann modeling: an introduction for geoscientist and engineers, Springer, Berlin, 2006.
[108] H. Huang, M. C. Sukop and X. Y. Lu, Multiphase lattice Boltzmann methods: theory and application, John Wiley & Sons, Oxford, 2015.
[109] Q. Li, K. H. Luo, Q. J. Kang, Y. L. He, Q. Chen and Q. Liu, Lattice Boltzmann methods for multiphase flow and phase-change heat transfer, Prog. Energy Combust. Sci. 52 (2016) 62-105.
[110] T. Krüger, H. Kusumaatmaja, A. Kuzmin, O. Shardt, G. Silva and E. M. Viggen, The lattice Boltzmann method: principles and practice, Springer, Switzerland, 2017.
[111] A. Xu, W. Shyy and T. Zhao, Lattice Boltzmann modeling of transport phenomena in fuel cells and flow batteries, Acta Mehc. Sin. 33 (3) (2017) 555-574.
[112] X. Shan and H. Chen, Lattice Boltzmann model for simulating flows with multiple phases and components, Phys. Rev. E 47 (1993) 1815-1820.
[113] X. Shan and H. Chen, Simulation of nonideal gases and liquid-gas phase transitions by the lattice Boltzmann equation, Phys. Rev. E 49 (1994) 2941-2948.
[114] L. Chen, Q. Kang, Y. Mu, Y. L. He and W. Q. Tao, A critical review of the pseudopotential multiphase lattice Boltzmann model: methods and applications, Int. J. Heat Mass Transf. 76 (2014) 210-236.
[115] M. L. Porter, E. T. Coon, Q. Kang, J. D. Moulton and J. W. Carey, Mulicomponent interparticle-potential lattice Boltzmann model for fluids with large viscosity ratios, Phys. Rev. E 86 (2012) 036701.
[116] Z. H. Chai and T. S. Zhao, A pseudopotential-based multiple-relaxation-time lattice Boltzmann model for multicomponent/multiphase flows, Acta Mech. Sin. 28 (4) (2012) 983-992.
[117] M. Sbragaglia and D. Belardinelli, Interaction pressure tensor for a class of multicomponent lattice Boltzmann models, Phys. Rev. E 88 (2013) 013306.
[118] W. Zhu, M. Wang and H. Chen, Study on multicomponent pseudo-potential model with large density ratio and heat transfer, Int. Commun. Heat Mass Transfer 87 (2017) 183-191.
[119] M. Li, C. Huber, Y. Mu and W. Tao, Lattice Boltzmann simulation of condensation in the presence of noncondensable gas, Int. J. Heat Mass Transfer 109 (2017) 1004-1013.
[120] C. Zhang, P. Cheng and W. J. Minkowycz, Lattice Boltzmann simulation of forced condensation flow on a horizontal cold surface in the presence of a non-condensable gas, Int. J. Heat Mass Transfer 115 (2017) 500-512.
[121] Y. Hou, H. Deng, Q. Du and K. Jiao, Multi-component multi-phase lattice Boltzmann modeling of droplet coalescence in flow channel of fuel cell, J. Power Sources 393 (2018) 83-91.
[122] Q. Li, K. H. Luo and X. J. Li, Lattice Boltzmann modeling of multiphase flows at

large density ratio with an improved pseudopotential model, Phys. Rev. E 87 (2013) 053301.
[123] Q. Li and K. H. Luo, Achieving tunable surface tension in the pseudopotential lattice Boltzmann modeling of multiphase flows, Phys. Rev. E 88 (2013) 053307.
[124] S. Zheng, F. Eimann, T. Fieback, G. Xie and U. Gross, Numerical investigation of convective dropwis condensation flow by a hybrid thermal lattice Boltzmann method, Appl. Therm. Eng. 145 (2018) 590-602.
[125] P. Lallemand and L.-S. Luo, Theory of the lattice Boltzmann method: dispersion, dissipation, isotropy, Galilean invariance, and stability, Phys. Rev. E 61 (2000) 6546-6562.
[126] Y. H. Qian, D. D'Humieres and P. Lallemand, Lattice BGK models for Navier-Stokes equation, Europhys. Lett. 17 (1992) 479-484.
[127] L. S. Luo, W. Liao, X. Chen, Y. Peng and W. Zhang, Numeric of the lattice Boltzmann method: effects of collision models on the lattice Boltzmann Simulations, Phys. Rev. E 83 (2011) 056710.
[128] Y. Yu, Q. Li C. Q. Zhou, P. Zhou and H. J. Yan, Investigation of droplet evaporation on heterogeneous surfaces using a three-dimensional thermal multiphase lattice Boltzmann model, Appl. Therm. Eng. 127 (2017) 1346-1354.
[129] Q. Li, Y. Yu, P. Zhou and H. J. Yan, Enhancement of boiling heat transfer using hydrophilic-hydrophobic mixed surfaces: a lattice Boltzmann study, Appl. Therm. Eng. 132 (2018) 490-499.
[130] X. He and G. D. Doolen, Thermodynamic foundations of kinetic theory and lattice Boltzmann models for multiphase, J. Sta. Phys. 107 (2002) 309-328.
[131] P. Yuan and L. Schaefer, Equations of state in a lattice Boltzmann model, Phys. Fluids 18 (2006) 042101.
[132] H. Ding and P. D. M. Spelt, Wetting condition in diffuse interface simulations of contact line motion, Phys. Rev. E 75 (2007) 046708.
[133] L. Wang, H. B. Huang and X. Y. Lu, Scheme for contact angle and its hysteresis in a multiphase lattice Boltzmann method, Phys. Rev. E 87 (2013) 013301.
[134] D. M. Anderson, G. B. McFadden and A. A. Wheeler, Diffuse-interface method in fluid mechanics, Ann. Rev. Fluid Mech. 30 (1998) 139-165.
[135] G. Hazi and A. Markus, On the bubble departure diameter and release frequency based on numerical simulation results, Int. J. Heat Mass Transfer 52 (2009) 1472-1480.
[136] Q. Li, P. Zhou and H. J. Yan, Improved thermal lattice Boltzmann model for simulation of liquid-vapor phase change, Phys. Rev. E 96 (2017) 063303.
[137] Q. Li and K. H. Luo, Effect of the forcing term in the pseudopotential lattice Boltzmann modeling of thermal flows, Phys. Rev. E 89 (2014) 053022.
[138] M. R. Kamali, J. J. J. Gillisse and H. E. A. van den Akker, Lattice-Boltzmann-based two-phase thermal model for simulating phase change, Phys. Rev. E 88 (2013) 033302.
[139] T. Lee and C. L. Lin, A stable discretization of the lattice Boltzmann equation for simulation of incompressible two-phase at high density ratio, J. Comput. Phys. 206 (2006) 16-47.
[140] Q. Li, K. H. Luo, Q. J. Kang and Q. Chen, Contact angles in the pseudopotential

lattice Boltzmann modeling of wetting, Phys. Rev. E 90 (2014) 053301.
[141] Q. Lou, Z. Guo and B. Shi, Evaluation of outflow boundary condition for two-phase lattice Boltzmann equation, Phys. Rev. E 87 (2013) 063301.
[142] C. K. Law, Recent advances in droplet vaporization and combustion, Prog. Energy Combust. Sci. 8 (1982) 171-201.
[143] S. Tanguy, T. Ménard and A. Berlemont, A level set method for vaporizing two-phase flows, J. Comput. Phys. 221(2007) 837-853.
[144] X. Yang and S. C. Kong, Smoothed particle hydrodynamics method for evaporating multiphase flow, Phys. Rev. E 96 (2017) 033309.
[145] H. Safari, M. H. Rahimian and M. Krafczyk, Consistent simulation of droplet evaporation based on the phase-field multiphase lattice Boltzmann method, Phys. Rev. E 90 (2014) 033305.
[146] J. L. Viovy, D. Beysens and C. K. Knobler, Scaling description for the growth of condensation patterns on surfaces, Phys. Rev. A 37 (1988) 4965-4970.
[147] D. Beysens, The formation of dew, Atmos. Res. 39 (1998) 215-237.
[148] Y. Sui, H. Ding and P. D. M. Spelt, Numerical simulations of flows with moving contact line, Annu. Rev. Fluid Mech. 46 (2014) 97-119.
[149] Q. Li, P. Zhou and H. J. Yan, Pinning-depinning mechanism of the contact line during evaporation on chemically patterned surfaces: a lattice Boltzmann study, Langmuir 32(2016) 9389-9396.

Publications

Journal:

[1] **S. Zheng**, F. Eimann, C. Philipp, T. Fieback and U. Gross, Dropwise condensation in the presence of non-condensable gas: interactions effect of the droplet array using the distributed point sink method, Int. J. Heat Mass Transfer 141(2019): 34-47.

[2] **S. Zheng**, F. Eimann, T. Fieback and U. Gross, Single droplet condensation in the presence of non-condensable gas by a multi-component multi-phase thermal lattice Boltzmann model Int. J. Heat Mass Transfer 139(2019): 254-268.

[3] **S. Zheng**, F. Eimann, C. Philipp, T. Fieback and U. Gross, Modeling of heat and mass transfer for dropwise condensation of moist air and the experimental validation, Int. J. Heat Mass Transfer 120(2018): 879-894.

[4] **S. Zheng**, F. Eimann, T. Fieback, G. Xie and U. Gross, Numerical investigation of convective dropwise condensation flow by a hybrid thermal lattice Boltzmann method, Appl. Therm. Eng., 145(2018): 590-602.

[5] **S. Zheng**, F. Eimann, C. Philipp, T. Fieback and U. Gross, Experimental and modeling investigations of dropwise condensation out of convective humid air flow, Int. J. Heat Mass Transfer, submitted on 21st August 2019.

Conference:

[1] **S. Zheng**, F. Eimann, C. Philipp, T. Fieback and U. Gross, The interaction effects between droplets condensing from moist air using a distributed point sink method, The 12th International Conference on Computational Heat, Mass and Momentum Transfer, September 3-6, 2019, Rome, Italy.

[2] **S. Zheng**, F. Eimann, C. Philipp and U. Gross, Single droplet growth model for Dropwsie Condensation considering non-condensable gas, Proceedings of the 16th International Heat Transfer Conference, August 10-15, 2018, Beijing, China.

[3] **S. Zheng**, F. Eimann, T. Fieback and U. Gross, Numerical study of the effect of forced convective flow on dropwise condensation by thermal LBM simulation, The 11th International Conference on Computational Heat, Mass and Momentum Transfer, May 21-24, 2018, Cracow, Poland.

[4] **S. Zheng**, F. Eimann, T. Fieback and U. Gross, Numerical simulation of dropwise condensation by a hybrid thermal lattice Boltzmann method, Surface Wettability Effects on Phase Change Phenomena Workshop, May 17-18, 2018, Brighton, UK.

[5] **S. Zheng**, F. Eimann, C. Philipp, U. Gross and T. Fieback, Single Droplet Model for Dropwsie Condensation of Moist Air and the Experimental Validation, Thermodynamik-Kolloquium, September 27-29, 2017, Dresden, Germany.